

Alma Mater Studiorum – Università di Bologna

DOTTORATO DI RICERCA IN
GEOFISICA

Ciclo XXIX

Settore Concorsuale di afferenza: 04/A4 – GEOFISICA

Settore Scientifico disciplinare: GEO/10 – GEOFISICA DELLA TERRA SOLIDA

Propagation and Scattering of Seismic Waves in Complex Media
at Different Scales

Presentata da: Marcello Serra

Coordinatore Dottorato

Prof. Nadia Pignardi

Relatore

Prof. Gaetano Festa

Esame finale anno 2017

1	Introduction.....	1
2	Mechanics of elastic waves.....	6
2.1	Elements of continuum mechanics.....	6
2.1.1	The strain tensor.....	7
2.1.2	The stress tensor.....	11
2.2	The linear elasticity: the elastodynamic equation.....	12
2.3	Wave-like solution.....	14
2.4	P- and S- waves.....	15
2.5	Surface waves.....	17
2.5.1	Rayleigh waves.....	17
2.5.2	Love waves.....	24
2.5.3	Dispersion of surface waves.....	25
2.5.4	Phase and group velocity measurements.....	29
2.6	Attenuation of seismic waves.....	34
2.6.1	Single scattering model.....	35
2.6.2	Radiative transfer model.....	38
2.6.3	Diffusive model.....	39
2.6.4	Anealstic attenuation.....	40
3	The Solfatara.....	48
4	RICEN.....	57
4.1	Data processing.....	61
4.2	S-wave model for the Solfatara.....	66
4.2.1	Phase and Group velocity measurement.....	70
4.2.2	Inversion of the dispersion curve.....	77
4.3	Scattering properties at Solfatara.....	95
5	Interferometry.....	115
5.1	Damage detection in a masonry bridge.....	121
5.2	The Irpinia fault system.....	146
6	Conclusion.....	166
7	References.....	168

1 Introduction

Huge improvements in seismology were driven in the last centuries by the availability of powerful computers and by the progress in the digital technology, which permitted to verify complex mathematical models and to analyze a large amount of data with the modern approaches of signal processing. Recently, a further burst to this discipline, was given by the installation of high-quality permanent and mobile digital networks of seismic stations displaced all over the world.

While in the past seismologists theoretical, numerical and experimental approaches from other disciplines, today seismology is not only aimed at understanding physics of the earthquakes, but their methods are exported in oil/gas industry to seek for natural reservoirs, in the structural engineering, to build structures that can avoid or limit the damage due to the ground shaking, and also for monitoring purposes. Moreover, concepts developed in seismology can be found in applications where non-invasive approaches are required, e.g. in echography, where the image of the inner parts of the human body are retrieved from the backscattered wave field, in aerospace industry to detect some micro fractures and small defects not observable at visual inspection, in helioseismology, where the sun can be investigated from noise cross-correlation. (Dainty et al., 1981). All these disciplines share a similar mathematical framework concerning waves of different nature, propagating inside complex media, and the knowledge of the propagating speed and how this deforms the wave amplitude is a common road to learn about the structure of the medium crossed by the waves and its time variation.

One of the most important applications in seismology is the monitoring of natural areas, or structures. In the first case, a dense network of receivers is displaced around the region of interest and using a continuous data acquisition, variations in the waveforms are analyzed to track changes in the physical properties of the medium. For instance, before and after an earthquake occurrence the wave velocity into the medium might change, owing to the interaction between the

rupture and the surrounding medium. If some physical conditions vary when the faulting zone is approaching to the failure, such variations can be used as a proxy for the earthquake occurrence (Brenquier et al., 2008). Many efforts are made to apply monitoring methods in volcanic areas to detect variations in the physical state of magmatic chamber. However, this application is a great challenge, because the magmatic chamber is a multiphase system and it is not straightforward to associate variations in some parameters to the magma ascent. Moreover the magma chamber is a low-velocity zone with respect to the surrounding medium, and its exploration could suffer of poor ray coverage, which decreases the quality of the information (Brenquier et al., 2008).

At shallower depths, the subsoil monitoring is intimately connected with the energy production. Oil extraction of, the natural gas storage, and geothermal energy imply the injection of over pressured fluids that can induce earthquakes with a magnitude as large as 5.0 or more. The aim of the monitoring is the detection of a critical state of the system that may approach to the failure, allowing to stop or reduce the extraction activity. The structural monitoring deserves to detect variations in the health status of a structure by means of thermal, ultrasonic or electromagnetic methods (Doherty et, 1987), which highlight structural anomalies. In addition, methods typical of the seismology such as the coda wave interferometry or the measurement of the ambient noise can be applied to track variations in the wave velocity that reflects the presence of damage in specific areas of the building.

In this framework, the experiment RICEN (Repeated and InduCED Earthquake and Noise) has been designed at Solfatara (Festa, 2015), to monitor and track the variations in the elastic properties of the medium through repeated observations over the time. The Solfatara is a volcano of the Campi Flegrei caldera, where there is a strong hydrothermal activity, whose intensity varies over the time. Because of the volcanic nature of the investigated area, the Solfatara is a highly heterogeneous medium, where scattering properties are expected to be dominant. Indeed the application of standard imaging techniques may be limited, and methods exploiting data from dense array are more suitable. In this experiment, the source-receiver configuration involved 240 receivers and about 100 sources. The large number of sources and receivers allow for data gathering

to obtain an enhancement in the signal to noise ratio and a more robust estimator for the average properties of the medium. Moreover, the density of the network allows to recover small wavelengths, which are more sensitive to the anomalies embedded in the medium and to their variations.

The scientific results presented in this thesis are mostly oriented to the discussion about the experiment RICEN, although some connected activities, which use similar methods are also discussed. The thesis is composed of four parts:

- In the first chapter, we provide some elements of the continuum mechanics. We start with the definition of the strain and stress tensors, through the second principle of the dynamics, and after introducing the elasticity, we write the elastodynamic equation. We discuss the solutions of the equation, their properties, and how they interact with the interfaces. We describe the surface waves their dispersion characteristics, and how it is possible to estimate the phase and group velocity dispersion curves. Once the generation and the propagation of the seismic waves has been addressed, we focus on what can modify a propagating wave. Therefore, we dedicate a section to the scattering and the inelastic attenuating properties of the medium. From the scattering properties of the medium we describe the physical processes involved in the seismic coda generation and the different scattering regimes, which can be met in a more or less heterogeneous medium.
- In the second chapter, we will describe the volcanic system located close the city of Naples: the Campi Flegrei caldera. We specifically focus on one of the most active points of such a volcanic area: the Solfatara. This place is the top of the hydrothermal system and therefore a large amount of gas emission is recorded. Moreover, since the Solfatara is a highly heterogeneous medium, it is a suitable place where testing non-standard imaging techniques which make use of ballistic waves. We focus on this area because here the RICEN experiment was performed. In this chapter, we will summarize all the information we have on this place.

- In the third chapter, the experiment RICEN is explained. Moreover, the different phases are shown, from the data acquisition to the data processing to retrieve the Green's function. After, we describe the different steps required to determine a three-dimensional model in term of S -waves velocity of the investigated area. Since receivers and sources are located at the surface, the seismograms are dominated by surface waves, therefore we measure the dispersion curves for the phase and the group velocities. We face the problem of splitting the receiver grid in smaller subgrids where it is possible to apply a 1D approximation. In this way, using the software GEOPSY (Whatelet et al., 2004), we recover layered models for each subgrid. The collection of all these models provides the three-dimensional structure of such area.

The Solfatara is a highly heterogeneous medium because of the presence of gas and water sacks, stratification of rocks having different elastic properties and a seismic wave propagating in such medium it is subjected to numerous scattering events. In such a medium, it is not possible to localize the scatterers but we are able to compute some statistical parameters of the scattering process. We discuss the estimate of the mean free path (MFP), from the ratio between the coherent and incoherent intensities (Roux and De Rosny, 2001), and the transport mean free path (TMFP). We also infer some mechanical properties of the scatterers through the inversion of the MFP curve as a function of the frequency using the theoretical model of a cylindrical anomaly.

- In the fourth chapter, we will face the interferometry. In the first section we will introduce the coda wave interferometry (CWI), starting with the definition and the properties of the seismic coda. We will see that the coda is not a completely random process, but it is composed by waves which travelled for longer times into the medium, and becoming sensitive to the smallest variations occurred into the medium (Snieder, 2006). We can take advantage from these properties and use them to measure the variations in the wave velocity of a monitored structure. Specifically, we measure and quantify the velocity variations suffered by a progressively damaged bridge (Ratdomopurbo and Poupinet, 1995).

Subsequently, we briefly discuss the theory of the ambient noise cross-correlation and the assumptions under which the cross-correlation function converges to the Green's function between a couple of stations (Shapiro and Campillo, 2004). We cross-correlate three year of ambient noise acquired at the stations of the seismic network ISNet (Iannaccone et al., 2010). Moreover, from the recovered Green's function, we measure the group velocity and finally we retrieve a three-dimensional model of the investigated area.

2 Mechanics of elastic waves

2.1 Elements of continuum mechanics

Different materials form the Earth, most of which are silicates, iron, nickel and chemical compounds of these elements, subjected to different pressure and temperature. They behave in a different way under external load. In general, the Earth responds elastically if the load perturbation acts for a small time, as in the case of earthquakes, whereas it has viscous behavior if long period forces are considered, e.g. the convection in the mantle. Earthquakes are transient phenomena, at least far from the source: particles crossed by seismic waves move from their equilibrium position and start to oscillate around it, the amplitude of the oscillations decay with the time because of the inelastic attenuation. Therefore, it is possible to assert that the Earth behaves as an elastic solid at in the whole time scale of earthquakes, ranging from several seconds (body waves) up to some days after the occurrence of the earthquake (free oscillations of the Earth), this latter being the case of the earthquakes having higher magnitude ($M > 8$).

The easiest way to describe elastic phenomena is the well-known Hooke's law. It establishes a linear relationship between the force acting on the considered body and the associated small deformations, through a constant depending on the material. The Hooke's law is not able to take into account the different conditions that single particle can undergo along different directions. The particles could be stretched and compressed at the same time, moreover also the elastic response of the body could be different along the different directions. To fully describe such kind of physical phenomena, a new tensor formulation for the elastic deformations has been developed. This formulation makes use of the formalism of the continuum mechanics with the Lagrangian approach, where a particle is labelled at the initial time and its evolution followed. This approach is the most natural for seismology because the seismogram, that is the prince object of this

discipline, is the recorded motion of the Earth particle on which the instrument is located.

2.1.1 The strain tensor

The motion of a rigid body is fully determined knowing the motion of the mass center and how the Euler angles evolve with time; six parameters are sufficient for this description because a rigid body can undergo rotations and translations. In the case of a deformable body, we should know the position of each point constituting it, this making the problem cumbersome and unsolvable also using modern calculators. This situation can be duped thanks to the theory of the elasticity.

The elasticity takes into account the internal deformation of the body; to describe the deformation we need to know the relative position of two points in the initial, B_0 , and final configurations, B_t . We can identify with ξ and $\xi+d\xi$ two near points in B_0 and with \mathbf{x} and $\mathbf{x}+d\mathbf{x}$ the same points in B_t (Figure 2-1). If we call χ , the transformation from the initial configuration to the actual one, we have:

$$\mathbf{x} = \chi(\xi) \quad \mathbf{x} + d\mathbf{x} = \chi(\xi + d\xi) \quad (2.1)$$

therefore, the differential $d\mathbf{x}$ as function of $d\xi$ is:

$$dx_i = \frac{\partial \chi_i}{\partial \xi_j} d\xi_j \quad (2.2)$$

i and j are the coordinate axes: 1, 2 and 3. The lengths of the elements $d\mathbf{x}$ and $d\xi$ are respectively dl and dL , so using the relation (2.2) and posing $F = \partial \chi_i / \partial \xi_j$:

$$(dl)^2 - (dL)^2 = dx_i dx_i - d\xi_j d\xi_j = (F_{ik} F_{il} - \delta_{kl}) d\xi_l d\xi_k \quad (2.3)$$

posing again $C = F^T F$, the previous relation can be written as:

$$(dl)^2 - (dL)^2 = (C_{kl} - \delta_{kl}) d\xi_l d\xi_k \quad (2.4)$$

where C is called Cauchy right tensor. If $C = I$ there is no deformation.

Instead of considering the position of two points and their evolution, we can evaluate the displacement \mathbf{u} :

$$\mathbf{u} = \mathbf{x} - \boldsymbol{\xi} \Rightarrow \mathbf{x} = \boldsymbol{\xi} + \mathbf{u} \quad (2.5)$$

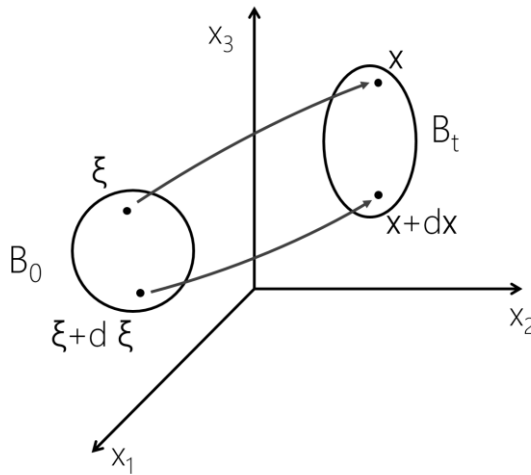


Figure 2-1: Representation of a deformable body in the initial, B_0 , and actual configuration B_t .

Deriving it, making use of the relation (2.2), calling $H = \partial u_i / \partial \xi_j$ the equation becomes:

$$\mathbf{F} = \mathbf{I} + \mathbf{H} \quad (2.6)$$

This last relationship allows us to rewrite \mathbf{C} as function of \mathbf{H} :

$$\mathbf{C} = \mathbf{F}^T \mathbf{F} = (\mathbf{I} + \mathbf{H}^T)(\mathbf{I} + \mathbf{H}) = \mathbf{I} + \mathbf{H} + \mathbf{H}^T + \mathbf{H}^T \mathbf{H} \quad (2.7)$$

In the approximation of small deformations, which works well in most of practical applications, we can neglect higher order terms, therefore:

$$\mathbf{C} - \mathbf{I} = \mathbf{H} + \mathbf{H}^T \quad (2.8)$$

Moreover, the following relationship also holds:

$$\frac{\partial u_i}{\partial \xi_j} = \frac{\partial u_i}{\partial x_k} \frac{\partial x_k}{\partial \xi_j} = \frac{\partial u_i}{\partial x_k} \left(\frac{\partial u_k}{\partial \xi_j} + \delta_{kj} \right) \approx \frac{\partial u_i}{\partial x_j} \quad (2.9)$$

The small deformation approximation allows us to replace the derivation with respect to $\boldsymbol{\xi}$ with that with respect to \mathbf{x} . This statement is fundamental in the formulation of the deformation because we can define the strain tensor in the actual configuration:

$$\varepsilon_{ij} = \frac{1}{2} \left(\frac{\partial u_i}{\partial x_j} + \frac{\partial u_j}{\partial x_i} \right) \quad (2.10)$$

the equation (2.4) can be reviewed as follows:

$$(dl)^2 - (dL)^2 = 2\varepsilon_{ij} d\xi_i d\xi_j \quad (2.11)$$

Starting from the eq. (2.10), we can analyze the components of $\boldsymbol{\varepsilon}$. We choose two vectors $d\boldsymbol{\alpha}$ and $d\boldsymbol{\beta}$ respectively along the directions 1 and 2:

$$d\boldsymbol{\alpha} \equiv (d\alpha_1, 0, 0) \quad d\boldsymbol{\beta} \equiv (0, d\beta_2, 0) \quad (2.12)$$

following the relation (2.2), in the actual configuration the vectors are:

$$da_i = \frac{\partial \chi_i}{\partial \alpha_1} d\alpha_1 \quad db_i = \frac{\partial \chi_i}{\partial \beta_2} d\beta_2 \quad (2.13)$$

and in term of components for the (2.6) we can write:

$$d\mathbf{a} = \left(1 + \frac{\partial u_1}{\partial \alpha_1}, \frac{\partial u_2}{\partial \alpha_1}, \frac{\partial u_3}{\partial \alpha_1} \right) d\alpha_1 \quad d\mathbf{b} = \left(\frac{\partial u_1}{\partial \beta_2}, 1 + \frac{\partial u_2}{\partial \beta_2}, \frac{\partial u_3}{\partial \beta_2} \right) d\beta_2 \quad (2.14)$$

Now we can compute the square modulus of the vector $d\mathbf{a}$ and neglect the terms to second order:

$$|d\mathbf{a}|^2 = d\mathbf{a} \cdot d\mathbf{a} = \left(1 + 2 \frac{\partial u_1}{\partial \alpha_1} \right) (d\alpha_1)^2 \quad (2.15)$$

using the Taylor expansion, it descends:

$$|d\mathbf{a}| = \left(1 + 2 \frac{\partial u_1}{\partial \alpha_1} \right)^{\frac{1}{2}} d\alpha_1 = (1 + \varepsilon_{11}) d\alpha_1 \quad (2.16)$$

or more explicitly:

$$\varepsilon_{11} = \frac{|d\mathbf{a}| - d\alpha_1}{d\alpha_1} \quad (2.17)$$

ε_{11} represents the relative compression or stretching along the 1-st direction. Of course the same discussion can be repeated for the other components; therefore the diagonal elements ε_{ii} represent the relative compression or stretching along the 1-st, 2-nd or 3-rd directions respectively. To understand the elements out of the diagonal we can use the same approximation as before and compute the scalar product:

$$d\mathbf{a} \cdot d\mathbf{b} = 2\varepsilon_{12} d\alpha_1 d\beta_2 \quad (2.18)$$

We also know that alternatively the scalar product can be written involving the cosine of the angle between the two vectors, therefore:

$$d\mathbf{a} \cdot d\mathbf{b} = |d\mathbf{a}| |d\mathbf{b}| \cos \theta_{12} = (1 + \varepsilon_{11})(1 + \varepsilon_{22}) d\alpha_1 d\beta_2 \cos \theta_{12} \quad (2.19)$$

comparing the equations (2.18) and (2.19), and neglecting higher order term:

$$\cos \theta_{12} = \frac{2\varepsilon_{12}}{1 + \varepsilon_{11} + \varepsilon_{22}} \quad (2.20)$$

Finally, we can expand the denominator obtaining:

$$\varepsilon_{12} = \frac{1}{2} \cos \theta_{12} \quad (2.21)$$

The same holds for other components, and in conclusion the elements out of the diagonal, ε_{ij} with $i \neq j$, are related to the shear deformation of the body since they are proportional to the cosine of the angle between the i -th and the j -th direction. By definition, $\boldsymbol{\varepsilon}$ is symmetric.

2.1.2 The stress tensor

Two kinds of forces act on a deformable body: body forces and contact forces. The first ones arise from the presence of an external force field, e.g. gravitation and electromagnetic fields; they are indeed proportional to the volume of the body; Contact forces act at the surfaces of a body and are linked to the molecular interaction, therefore they are short-range forces. We can subdivide the body in small elements of volume dV having small external surfaces ΔA , on which the force ΔF acts. We can define the traction vector as:

$$\mathbf{T}(\hat{\mathbf{n}}) = \lim_{\Delta A \rightarrow 0} \frac{\Delta \mathbf{F}}{\Delta A} = T_1 \hat{\mathbf{x}}_1 + T_2 \hat{\mathbf{x}}_2 + T_3 \hat{\mathbf{x}}_3 \quad (2.22)$$

It is a force acting on the surface element of the volume dV having normal $\hat{\mathbf{n}}$. Choosing a suitable reference system, we define:

$$\begin{aligned} \sigma_{11} &= \lim_{\Delta A_1 \rightarrow 0} \frac{\Delta F_1}{\Delta A_1} \\ \sigma_{12} &= \lim_{\Delta A_1 \rightarrow 0} \frac{\Delta F_2}{\Delta A_1} \\ \sigma_{13} &= \lim_{\Delta A_1 \rightarrow 0} \frac{\Delta F_3}{\Delta A_1} \end{aligned} \quad (2.23)$$

where σ_{ij} are the components of the stress tensor $\boldsymbol{\sigma}$ and the elements of the force are defined as:

$$\Delta \mathbf{F} = \Delta F_1 \hat{\mathbf{x}}_1 + \Delta F_2 \hat{\mathbf{x}}_2 + \Delta F_3 \hat{\mathbf{x}}_3 \quad (2.24)$$

The first subscript in σ_{ij} is related to the direction of the normal at the considered surface, i , whereas the second one, j , is the force direction (Figure 2-2). It is possible to demonstrate, starting from the forces balance acting on a tetrahedron with three faces parallel to the coordinate planes, that the relationships linking the traction acting on a surface and the normal of the same surface are:

$$T_i(\mathbf{x}, \hat{\mathbf{n}}, t) = \sigma_{ij} n_j \quad (2.25)$$

it means that the traction \mathbf{T} and normal at the surface $\hat{\mathbf{n}}$ are linked by the stress tensor σ . Finally, it is also possible to observe, using the conservation of the angular momentum, that σ is symmetric (Lay and Wallace, 1995).

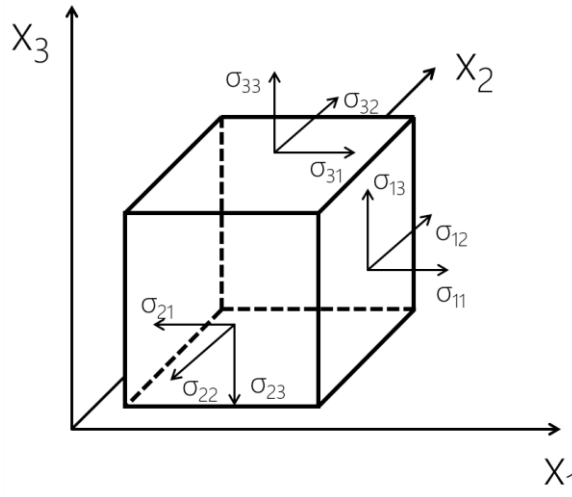


Figure 2-2: Components of the stress tensor acting on the element of volume dV .

2.2 The linear elasticity: the elastodynamic equation

We can imagine a continuous body like a discrete medium composed by a large number of small elements of volume dV . The second principle of dynamics for a continuous medium is:

$$\frac{d}{dt} \int_V \rho \mathbf{v} dV = \int_V \mathbf{f} dV + \int_S \mathbf{T} dS \quad (2.26)$$

The force contribution is split in a term of body forces acting on the volume dV (\mathbf{f}) and in a term of forces acting on the surface of the elements of volume (\mathbf{T}). In the equation (2.26) we can substitute the traction \mathbf{T} with the (2.25). Considering the density ρ not dependent on time, the Stokes's theorem and assuming that the equation is verified for any volume, we obtain:

$$\rho \frac{d\mathbf{v}}{dt} = \mathbf{f} + \nabla \cdot \boldsymbol{\sigma} \quad (2.27)$$

This equation is called the equation of motion for a continuum system. In order to derive the equation that governs the elastodynamic phenomena we need to introduce a relationship where the displacement or its derivatives appear. In literature, many laws relating the stress tensor to the strain one are present, usually indicated as constitutive laws. They are more or less complicated relations, in order to explain the different behavior of materials due to pressure, temperature, saturation and the past history of the material. In general, for our applications, if we want study phenomena away from the seismic source and under small deformations a linear elastic behavior holds. The term "elastic" means that a body under a load is instantaneously deformed, after removing the load, it instantaneously returns to the initial configuration. The most simple and general constitutive law is:

$$\boldsymbol{\sigma} = \mathbf{c} : \boldsymbol{\varepsilon} \quad (2.28)$$

or in term of components:

$$\sigma_{ij} = c_{ijkl} \varepsilon_{kl} \quad (2.29)$$

where c_{ijkl} is a fourth order tensor called the stiffness tensor; it should have 81 independent components, but from the symmetry of $\boldsymbol{\sigma}$, $\sigma_{ij} = \sigma_{ji}$, we have $c_{ijkl} = c_{jikl}$, from the symmetry of $\boldsymbol{\varepsilon}$, $\varepsilon_{kl} = \varepsilon_{lk}$, we have $c_{ijkl} = c_{jilk}$, and from the symmetry of elastodynamic energy form we also have $c_{ij} = c_{klij}$. Finally c is symmetric with respect to the exchange of all the indices and only has 21 independent components. For most of the rocks modelled in geophysics the isotropy approximation can be assumed, with this further simplification we only have 2 independent coefficients, with the exception of the Earth mantle where 8 coefficients are required. The independent constants λ and μ are the Lamé coefficients and allow to write the (2.29) as follows:

$$\sigma_{ij} = \lambda \varepsilon_{kk} \delta_{ij} + 2\mu \varepsilon_{ij} \quad (2.30)$$

The first one coefficient λ has no physical meaning, whereas the second coefficient μ is the shear modulus and it is the link between the shear stress and

the shear deformation: $\sigma_{ij}=2\mu\epsilon_{ij}$ with $i \neq j$. For a fluid $\mu=0$ because no resistance to the shear stress is observed, whereas the higher μ the smaller the deformation. From combination of λ and μ , other parameters can be defined, such as the Young's modulus, the Poisson's ratio and the bulk modulus.

To obtain the elastodynamic equation, we have to introduce the elasticity condition in the equation of the dynamics. Therefore we can put the generalized Hook's law (2.30) in the eq. (2.27). Considering a homogenous medium, where the Lamé constants are independent of the considered point, and using the vector identity $\nabla^2(\mathbf{u}) = \nabla(\nabla \cdot \mathbf{u}) - \nabla \times \nabla \times (\mathbf{u})$, we obtain the elastodynamic equation:

$$\rho \ddot{\mathbf{u}} = \mathbf{f} + (\lambda + 2\mu)\nabla(\nabla \cdot \mathbf{u}) - \mu\nabla \times (\nabla \times \mathbf{u}) \quad (2.31)$$

The elastodynamic equation is valid for the theory of the linear elasticity and it describes the motion of a particle in a homogeneous and isotropic body under small deformation.

2.3 Wave-like solutions

To understand to which kind of motion are submitted particles whose evolution in time is described by the elastodynamic equation we need to manipulate equation (2.31). Moreover, since we are interested in the motion after it has been induced by the source, we will focus on the propagation of the energy, while discarding the forcing term and considering the homogeneous equation.

Applying the divergence at both members of the (2.31), considering the properties of the nabla operator: $\nabla \cdot \nabla = \nabla^2$ and $\nabla \cdot (\nabla \times \mathbf{u}) = \mathbf{0}$, and under appropriate regularity assumptions, we can invert the order of spatial with the temporal derivation:

$$\frac{\partial^2(\nabla \cdot \mathbf{u})}{\partial t^2} = \frac{\lambda + 2\mu}{\rho} \nabla^2(\nabla \cdot \mathbf{u}) \quad (2.32)$$

Now, applying the curl operator at the equation (2.31), and using $\nabla \times \nabla \mathbf{u} = \mathbf{0}$ property, we can recover:

$$\frac{\partial^2 (\nabla \times \mathbf{u})}{\partial t^2} = \frac{\mu}{\rho} \nabla^2 (\nabla \times \mathbf{u}) \quad (2.33)$$

The equations (2.32) and (2.33) are respectively the scalar wave equation and the vector wave equation. Since these results directly descend from the elastodynamic equation, in an uniform, infinite isotropic solid is loaded by an external perturbation, the energy propagates inside the medium as two wave- modes with different velocities.

2.4 P- and S-waves

In this section, we want to study the nature of the motion associated to the propagation of the energy inside the medium. We are authorized to use as a test solution, as discussed in the previous section, a wave-like solution; moreover, without loss of generality and to simplify the mathematical treatment, far away from the source, we can approximate the wave front as a plane wave:

$$\mathbf{u}(\mathbf{x}, t) = \mathbf{U} e^{i(\omega t - \mathbf{k} \cdot \mathbf{x})} \quad (2.34)$$

The above solution represents a monochromatic wave propagating along \mathbf{k} direction. We can substitute it in the (2.31), yielding an algebraic equation in the domain of the frequencies, (ω), and wave numbers, (\mathbf{k}). This equation is reached using the relations:

$$\nabla \cdot \mathbf{u} = -i\mathbf{k} \cdot \mathbf{u}; \quad \nabla \mathbf{u} = -i\mathbf{k} \otimes \mathbf{u}; \quad \nabla \times \mathbf{u} = -i\mathbf{k} \times \mathbf{u}; \quad (2.35)$$

The symbol \otimes refers to the tensor product. Than we obtain:

$$\rho \omega^2 \mathbf{U} = [(\lambda + \mu)\mathbf{k} \otimes \mathbf{k} + \mu k^2 \mathbf{1}] \mathbf{U} \quad (2.36)$$

which can be easily connected to an eigenvalues problem:

$$\frac{1}{\rho} [(\lambda + \mu)\hat{\mathbf{k}} \otimes \hat{\mathbf{k}} + \mu \mathbf{1}] \mathbf{U} = c^2 \mathbf{U} \quad (2.37)$$

where $c = \omega/|\mathbf{k}|$ and $\hat{\mathbf{k}} = \mathbf{k}/|\mathbf{k}|$.

Choosing a coordinate system with the x-axis along the propagation direction of the plane wave, the unit vector of the wave number is reduced to $\hat{\mathbf{k}} = (1,0,0)$, and remembering that $\mathbf{a} \otimes \mathbf{b} = \mathbf{a}^T \mathbf{b}$, the first member of the equation in matrix form can be written as follows:

$$\frac{1}{\rho} \begin{pmatrix} \lambda + \mu & 0 & 0 \\ 0 & 0 & 0 \\ 0 & 0 & 0 \end{pmatrix} + \frac{1}{\rho} \begin{pmatrix} 1 & 0 & 0 \\ 0 & 1 & 0 \\ 0 & 0 & 1 \end{pmatrix} = \frac{1}{\rho} \begin{pmatrix} \lambda + 2\mu & 0 & 0 \\ 0 & \mu & 0 \\ 0 & 0 & \mu \end{pmatrix} \quad (2.38)$$

We have a first mode along the direction of propagation of the wave (x-axis) and a second one with double degeneration, orthogonally to the propagation direction (y and z-axes). Moreover for the properties of the vector product $\mathbf{k} \times \mathbf{u} = 0$ and the scalar one $\mathbf{k} \cdot \mathbf{u} = 0$, using the analogy between the wave numbers domain and the space one it is verified that the first solution is curl free, while the second one is divergence free. We can define:

$$\nabla \times \mathbf{u}_p = \mathbf{0} \quad \nabla \cdot \mathbf{u}_s = 0 \quad (2.39)$$

and replace the two field of displacement, \mathbf{u}_p and \mathbf{u}_s , separately in the (2.31), leading to:

$$\frac{\partial^2 \mathbf{u}_p}{\partial t^2} = \frac{(\lambda + 2\mu)}{\rho} \nabla^2 \mathbf{u}_p \quad \frac{\partial^2 \mathbf{u}_s}{\partial t^2} = \frac{\mu}{\rho} \nabla^2 \mathbf{u}_s \quad (2.40)$$

They both satisfy the wave equation and propagate inside the medium, hence they are referred to as body waves (Figure 2-3). Looking at the two wave equations, the longitudinal waves propagate inside the medium faster than the transversal ones. It is well known that after an earthquake, far enough from the source, the P-waves arrive first at a given target point, this characteristic being exploited in all the earthquakes early warning systems, to mitigate the damages due to the more energetic late S-waves. Furthermore, the double degeneration of S-waves means that they can induce displacements in two mutually orthogonal directions. These directions are also orthogonal to the direction of propagation of the wave. They are called SV and SH waves: The SV wave propagates in the vertical plane containing the source and receiver, while the SH in the direction orthogonal to the vertical plane.

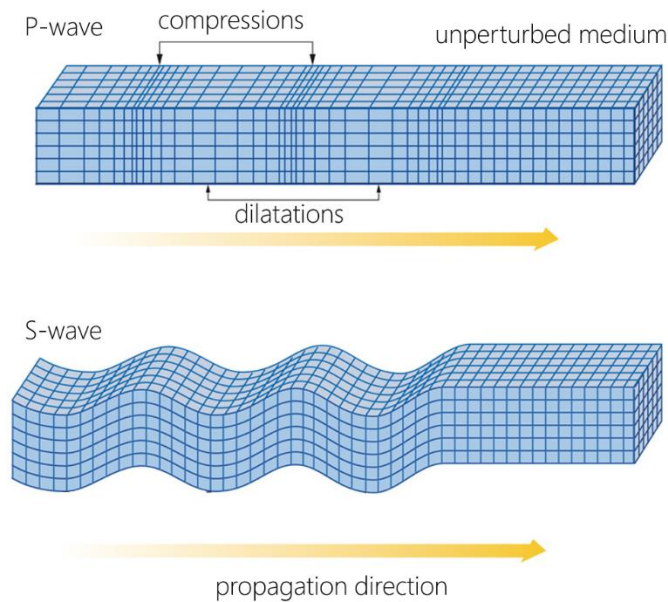


Figure 2-3: Longitudinal (on the top) and transversal (on the bottom) deformations induced by the P-wave and the S-wave respectively on a material block.

2.5 Surface waves

2.5.1 Rayleigh waves

The wave front is the set of points of the space reached by the perturbation at the same time. To follow the propagation of a wave rather than looking at the wave front it is possible to draw locally the curve normal to the wave front; this curve is referred to as the ray. In agreement with the ray theory when a P-wave meets an interface between two materials with different velocity of propagation, it is reflected and transmitted as P-wave and converted in S-wave, in order to preserve the boundary conditions at the interface (continuity of the traction and the displacement). The same occurs for the S wave. To describe the behavior of

a seismic ray at the interface, the well-known law of the geometrical optics, the Snell law holds:

$$\frac{\sin(i)}{c} = k \quad (2.41)$$

Here i is the incident angle defined with respect to the normal to the interface, c is the propagation velocity of the wave in the medium and k is a constant. It is trivial to demonstrate, that incident and reflected P-waves (S-waves) have the same angle with respect to the normal. In the case of converted/refracted phases the ray approaches or moves away from the normal if the wave velocity is higher or lower than the incident one, respectively (Figure 2-4). Following the same argumentation as before, in a medium where the velocity increases with depth, rays will move away from the normal, when they deepen, while they approach it when going toward the free surface. This situation is typical in the Earth; because of the lithostatic load, the Lamé constants increase faster than the density; this also explains the characteristic shape of seismic rays and why P-waves have a dominant component on the vertical component of seismometers and S-waves on the horizontal ones.

Let us consider the free surface of the Earth, the velocity of the P-waves in the Earth is higher than in the air and in this last there are not S-waves. If an SV-wave arrives at the surface, a reflected SV-wave is generated with an angle that is the same of the incident wave. The converted P-wave deepens with a larger angle.

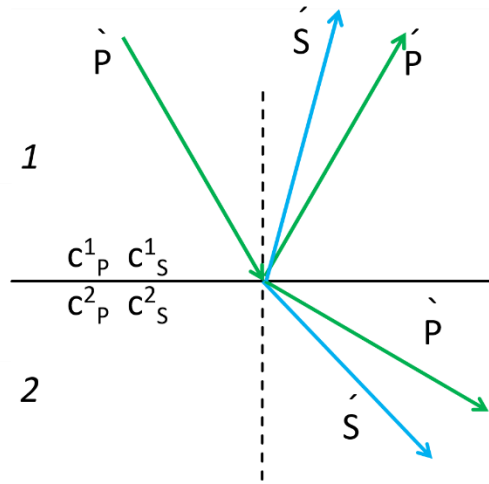


Figure 2-4: P- and S-waves rays approach or move away from the normal passing from a slower (1) to a faster (2) medium. With c we indicated the velocity, with the subscripts the kind of waves and with the superscript the medium.

Therefore, there is a critical angle for the existence of the P-wave:

$$\frac{\sin(\alpha_i^S)}{c_S} = \frac{\sin(\pi/2)}{c_P} \Rightarrow \alpha_i^S = \arcsin\left(\frac{c_S}{c_P}\right) \quad (2.42)$$

Beyond this angle, conversion in evanescent surface waves takes place. To investigate the properties of the surface waves we can consider a monochromatic plane wave, $\mathbf{u}(\mathbf{x}, t) = \mathbf{U}e^{i(\mathbf{k}\mathbf{x} - \omega t)}$. This representation is general because any wave can be considered as linear combination of plane waves:

$$\mathbf{u}(\mathbf{x}, t) = \int_{-\infty}^{+\infty} u(\mathbf{x}, \omega) e^{-i\omega t} d\omega \quad (2.43)$$

In a reference system like figure 2-5 \mathbf{k} is decomposed as:

$$\mathbf{k} = \frac{\omega}{c} (\sin(\alpha_i), \cos(\alpha_i)) = \omega(p_x, \eta) \quad (2.44)$$

where we have used the relationships: $c = \lambda v$ then $c = \omega/k$, and we have defined:

$$p_x = \frac{\sin(\alpha_i)}{c} \quad \eta = \frac{\cos(\alpha_i)}{c} \quad (2.45)$$

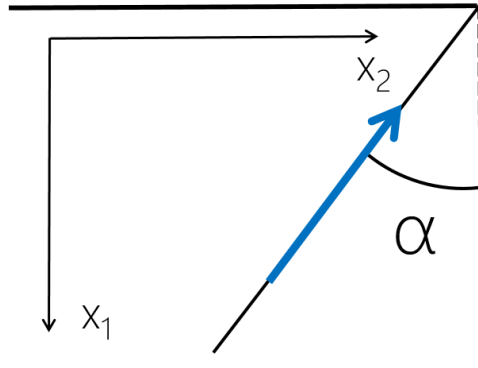


Figure 2-5: Wave number projection in a system having the x_1 -axis parallel to the interface and the x_3 -axis orthogonal to the interface. α is the incident angle between \mathbf{k} and the normal to the surface.

As stated by the Lamé theorem, we can represent the P and S-wave propagation by means of a scalar and vector potentials ϕ and ψ . To satisfy the propagation of the S-wave in the vertical plan, the potential must have component just along y-axis, such that:

$$\boldsymbol{\psi} = \mathbf{U} e^{i\omega(p_x x + \eta_S z - t)} \quad (2.46)$$

Therefore, remembering that $\mathbf{u}_S = \nabla \times \boldsymbol{\psi}$ we have:

$$\mathbf{u}_{Si} = i\omega \mathbf{U}(p_x, \eta_S) e^{i\omega(p_x x - \eta_S z - t)} \quad \mathbf{u}_{Sr} = i\omega \mathbf{U}(p_x, -\eta_S) e^{i\omega(p_x x + \eta_S z - t)} \quad (2.47)$$

respectively for the incident and reflected S-wave. Similarly it is possible to define the scalar potential in order to recover the displacement induced by the converted P-wave:

$$\phi = C e^{i\omega(p_x x + \eta_P z - t)} \quad \mathbf{u}_{Pc} = i\omega C(p_x, \eta_P) e^{i\omega(p_x x + \eta_P z - t)} \quad (2.48)$$

Looking at (2.42) if α_i^S is greater than the critical angle, it does not admit solution in the real field, therefore the value:

$$\eta = \frac{\cos(\alpha_i)}{c} = \sqrt{\frac{1 - \sin^2(\alpha_i)}{c^2}} = \sqrt{\frac{1}{c^2} - p_x^2} \quad (2.49)$$

For the P-wave becomes imaginary:

$$\eta_p = \sqrt{\frac{1}{c_p^2} - p_x^2} = i \sqrt{p_x^2 - \frac{1}{c_p^2}} = i \hat{\eta}_p \quad (2.50)$$

And substituting it in the (2.48):

$$\phi = C e^{i\omega(p_x x + \eta_p z - t)} = C e^{i\omega(p_x x - t)} e^{-\omega \hat{\eta}_p z} \quad (2.51)$$

we obtain the expression of a P-wave propagating along the direction of the interface but decaying exponentially along the z-direction. It is possible to demonstrate that such kind of P-wave exists until incident S-waves feed it with the same angle. We are interested in waves that can propagate independently of the continuous activation of their source. We indeed investigate the possibility than an evanescent wave comes from a combination of P and SV-waves. The scalar and vector potential associated to the evanescent wave are, respectively:

$$\phi = P e^{i\omega(p_x x - t)} e^{-\omega \hat{\eta}_p z} \quad \psi = S e^{i\omega(p_x x - t)} e^{-\omega \hat{\eta}_s z} \quad (2.52)$$

The displacement will be a combination of the two ones: $\mathbf{u} = \mathbf{u}_P + \mathbf{u}_S = \nabla \phi + \nabla \times \psi$, where explicating the previous expressions:

$$\mathbf{u}_P = P \omega (i p_x, -\hat{\eta}_p) e^{i\omega(p_x x - t)} e^{-\omega \hat{\eta}_p z} \quad \mathbf{u}_S = S \omega (\hat{\eta}_s, i p_x) e^{i\omega(p_x x - t)} e^{-\omega \hat{\eta}_s z} \quad (2.53)$$

and it has to satisfy the boundary conditions of free surface, that is, $\sigma_{zz}|_{z=0} = 0$ and $\sigma_{xz}|_{z=0} = 0$.

The first request, paying attention to divide by the density, yields:

$$\sigma_{zz}|_{z=0} = \lambda \frac{\partial u_x}{\partial x} + (\lambda + 2\mu) \frac{\partial u_z}{\partial z} \Big|_{z=0} = P(2c_s^2 p_x^2 - 1) - 2c_s^2 i S \hat{\eta}_s p_x = 0 \quad (2.54)$$

in the same way for the off-diagonal component of the stress tensor:

$$\sigma_{xz}|_{z=0} = \mu \left(\frac{\partial u_x}{\partial z} + \frac{\partial u_z}{\partial x} \right) \Big|_{z=0} = 2P i p_x \hat{\eta}_p + S(\hat{\eta}_s^2 + p_x^2) = 0 \quad (2.55)$$

The two equations admit a solution different from the trivial one if the determinant of the system is zero:

$$\begin{bmatrix} 2c_s^2 p_x^2 - 1 & -2c_s^2 i \hat{\eta}_s p_x \\ 2i p_x \hat{\eta}_p & \hat{\eta}_s^2 + p_x^2 \end{bmatrix} \quad (2.56)$$

Using the link between P and S velocity through the Lamé constants, the determinant is:

$$\left[(\lambda + 2\mu) \hat{\eta}_p^2 - \lambda p_x^2 \right] (\hat{\eta}_s^2 + p_x^2) - 4\mu \hat{\eta}_s \hat{\eta}_p p_x^2 = 0 \quad (2.57)$$

It is also called Rayleigh denominator because in the analysis to the interaction between surface waves and the free surface of the Earth, it is possible to demonstrate that it appears at the denominator of the free surface reflection coefficients. We can solve the previous equation looking for a solution of p_x , if such a solution exists, it is the slowness of the horizontally propagating wave at the interface: $p_x = 1/c_R$. So, replacing $\hat{\eta}_p$ and $\hat{\eta}_s$ for the corresponding expressions as a function of p_x we have:

$$\left(2 - \frac{c_R^2}{c_s^2} \right)^2 - 4 \sqrt{1 - \frac{c_R^2}{c_p^2}} \sqrt{1 - \frac{c_R^2}{c_s^2}} = 0 \quad (2.58)$$

To simplify the (2.58), we can pose $\alpha_R = \frac{c_R}{c_p}$ and $\beta_R = \frac{c_R}{c_s}$, and in order to search for its solutions we can solve it using the hypothesis of Poissonian medium: $c_p^2 = 3c_s^2$, therefore:

$$3\beta_R^8 - 24\beta_R^6 + 56\beta_R^4 - 32\beta_R^2 = 0 \quad (2.59)$$

We can further simplify the equation as follows:

$$3x^3 - 24x^2 + 56x - 32 = 0 \quad (2.60)$$

where $x = \beta_R^2$, the equation has 3 solutions:

$$x_1 = 4 \quad x_2 = 2 + \frac{2}{\sqrt{3}} \quad x_3 = 2 - \frac{2}{\sqrt{3}} \quad (2.61)$$

Just the third one is a solution of the problem, because it is the only one providing a value smaller than 1. We remember that in order to have an evanescent wave, $\hat{\eta}_s$ has to be imaginary, it means:

$$p_x > \frac{1}{c_S} = \frac{1}{c_R} > \frac{1}{c_S} \Rightarrow \beta_R < 1 \quad (2.62)$$

and therefore the only solution satisfying this condition is:

$$c_R = 0.919c_S \quad (2.63)$$

It is demonstrated that c_R ranges between $0.9c_S$ and $0.85c_S$ for Poisson's ratio between 0.2 and 0.4. Furthermore, since the equations of the system (2.56) are dependent (the determinant is zero), from one of these two equations it is possible to write the ratio of the amplitude of S wave with respect to the P wave component:

$$\frac{S}{P} = -\frac{2ip_x\hat{\eta}_P}{\hat{\eta}_S^2 + p_x^2} = -\frac{2i\sqrt{1-\alpha_R^2}}{2\beta_R^2 + 1} \quad (2.64)$$

For a Poissonian medium $S = -iP\gamma_{PS}$ with $\gamma_{PS} = 1.47$. Therefore we can express the displacement induced by a Rayleigh wave as:

$$\mathbf{u} = P\omega e^{i\omega(p_x x - t)} (ip_x e^{-\hat{\eta}_P z} - i\hat{\eta}_S \gamma_{PS} e^{-\hat{\eta}_S z}, -\hat{\eta}_P e^{-\hat{\eta}_P z} + p_x \gamma_{PS} e^{-\hat{\eta}_P z}) \quad (2.65)$$

The relationship shows a shift of $\pi/2$ between the horizontal and the vertical components, therefore we can indicate the displacement (except for a common normalization constant) along the axis as follows:

$$\begin{aligned} x &= c_1(z)\omega \sin\left(\frac{x}{c_R} - t\right) \\ z &= c_2(z)\omega \cos\left(\frac{x}{c_R} - t\right) \end{aligned} \quad (2.66)$$

At the surface $c_1 = -0.42$ and $c_2 = 0.62$, as said before the ratio between the vertical and the horizontal components is 1.47 indeed, indicating that the wave has an elliptical polarization with the major axis along the vertical axis (Figure 2-6). The motion is *retrograde* near the surface, the coefficient changes its sign with depth and the motion becomes *prograde*. The inversion happens at about 1/5 of the wavelength of the Rayleigh wave (Lay and Wallace, 1995).

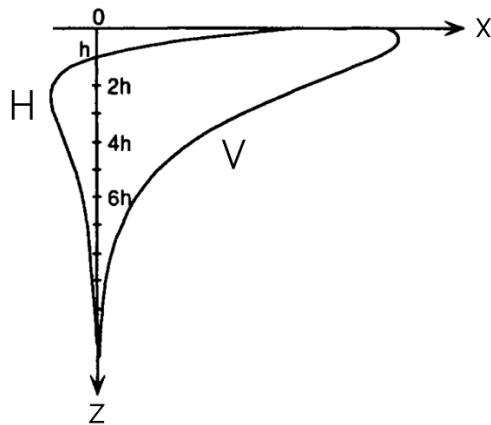


Figure 2-6: Normalised horizontal (H) and vertical (V) displacement amplitude of a Rayleigh wave in a homogenous half-space.

2.5.2 Love waves

Let us consider now the S-wave propagating in the horizontal plane, to which we referred to as SH-wave. In a homogenous medium, for the boundary condition, an SH-wave cannot be converted into a P-wave, therefore such waves are not generated. In order to have horizontally polarized S waves confined below the surface, the presence of a waveguide is required. In the case of the Earth, we are thinking to a horizontally stratified medium. To understand the crucial points of the Love wave propagation, we can consider a simplified Earth model where we have a layer in which SH-waves propagate with velocity c_1 , above an half space with higher velocity c_2 : $c_1 < c_2$. In a such kind of medium a wave reflected at the free surface and that after meets the interface between the layer and half space, according to the Snell law (2.41), moves away from the normal. As for the Rayleigh waves, it exists a critical angle for which the wave is trapped in the low-velocity layer, and it is evanescent in the half space. Such waves are demonstrated to propagate with velocity between the S wave of the two media, and in general faster than Rayleigh waves.

The motion induced by Rayleigh and Love waves is shown in the figure 2-7.

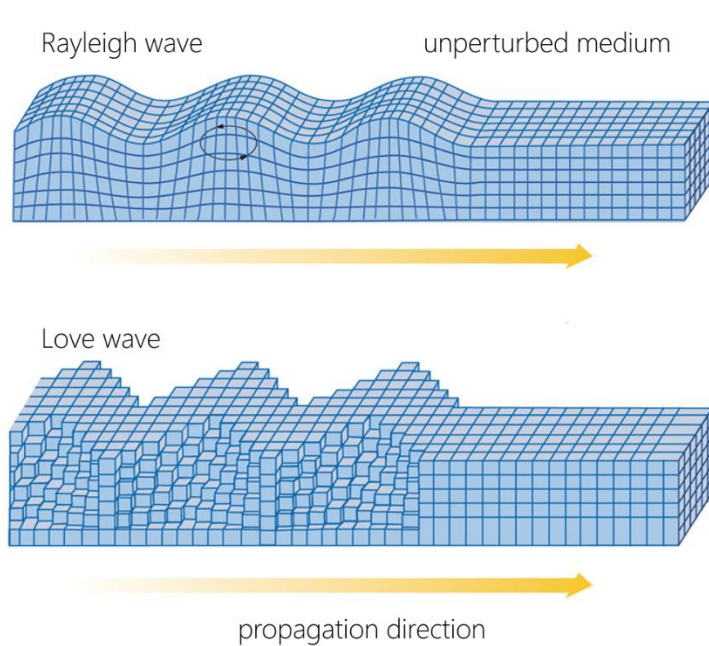


Figure 2-7: Deformations induced by the Rayleigh-wave and the Love-wave, respectively on the top and on the bottom, in a material block.

2.5.3 Dispersion of surface waves

If a heterogeneous medium is taken into account, Rayleigh and Love waves are dispersive, that is, their velocity depends on the frequency $c(\omega)$. Now, the phase and the group velocity characterize the propagation of the surface waves. To understand the meaning of these two velocities, we can start looking at the propagation of two monochromatic signals. We choose signals having frequencies and wavenumbers close to each other, propagating along the x direction. The ratio between the angular frequency and the modulus of the wavenumber is still a velocity, referred to as the phase velocity. With this choice, the two signals are:

$$u_1 = \cos(\omega_1 t - k_1 x) \quad u_2 = \cos(\omega_2 t - k_2 x) \quad (2.67)$$

and their superimposition (Figure 2-8):

$$u = u_1 + u_2 = \cos(\omega_1 t - k_1 x) + \cos(\omega_2 t - k_2 x) \quad (2.68)$$

Using Simpson's formulas, we can handle the (1.68) in order to highlight important characteristics of the solution:

$$u = \cos\left(\frac{\omega_1 + \omega_2}{2} t - \frac{k_1 + k_2}{2} x\right) \cos\left(\frac{\omega_2 - \omega_1}{2} t - \frac{k_2 - k_1}{2} x\right) \quad (2.69)$$

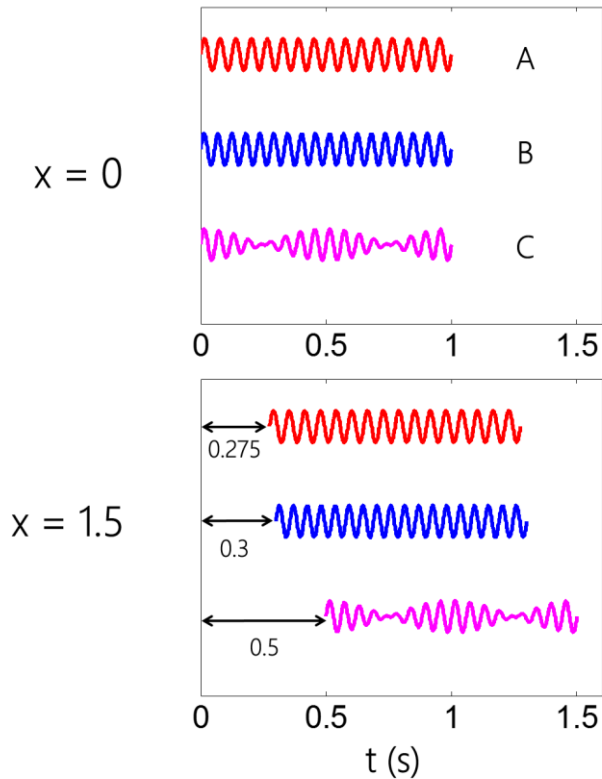


Figure 2-8: Two monochromatic waves (A and B) and their superimposition (C) at the two position $x=0$ km and $x=1.5$ km. We can notice that the envelope propagates slower than the single waves.

The total displacement is the product of two periodic functions, one with pulsation and wavenumber computed as the average of the initial ones and a second one having pulsation and wavenumber, being the semi-difference of the initial ones. From inspection of Figure 2-6 the resulting signal has an intermediate frequency between the initial ones, which are very close each other, modulated by a low-frequency wave. Again, looking at Figure 2-8, the sum of the signals is still a periodic signal. We can define the period and the wavelength of this signal, by measuring the distance between two maxima (minima) in time ($\Delta\omega$) and in the space (Δk), respectively. Finally, we can define the velocity:

$$C_g = \frac{\Delta\omega}{\Delta k} \quad (2.70)$$

In the limit of superimposing signals with very close frequency, the previous relationship is the group velocity:

$$c_g = \lim_{\Delta k \rightarrow 0} \frac{\Delta\omega}{\Delta k} = \frac{d\omega}{dk} \quad (2.71)$$

In general, we do not deal with the superimposition of discrete monochromatic waves; the acquired signals are deriving from a continuous superimposition of waves. Signals emitted by the Earth (Earthquakes and noise) have a wide spectrum and also if signals are filtered, we never isolate a single frequency contribution to the seismic wave but we always maintain a wave packet. The filtered signal can be written as:

$$u = A \int_{\omega_0 - \Delta\omega/2}^{\omega_0 + \Delta\omega/2} \cos(\omega t - k(\omega)) d\omega \quad (2.72)$$

Here ω_0 is the central frequency of the filter and $\Delta\omega$ is the bandwidth of the filter. The amplitude of the single monochromatic signals can be considered independent of the frequency and therefore carry out of the integration. The more valid this approximation, the smaller the filter bandwidth. The wavenumber is a function of the frequency and can be expanded as a Taylor summation around ω_0 at the first order:

$$k(\omega) = k_0 + \left(\frac{dk}{d\omega} \right)_{\omega=\omega_0} (\omega - \omega_0) \quad (2.73)$$

We can put the above relationship in the (2.72):

$$u = A \int_{\omega_0 - \Delta\omega/2}^{\omega_0 + \Delta\omega/2} \cos \left[\omega \left(t - \frac{dk}{d\omega} x \right) - \left(k_0 - \frac{dk}{d\omega} \omega_0 \right) x \right] d\omega \quad (2.74)$$

Integrating the equation and manipulating it through the prosthaphaeresis formulas, we obtain:

$$u = \Delta\omega A \cos(\omega_0 t - k_0 x) \text{sinc} \left[\frac{\Delta\omega}{2} \left(t - \frac{dk}{d\omega} x \right) \right] \quad (2.75)$$

The displacement is a monochromatic wave having frequency equal to the central frequency of the filter, modulated by the sine cardinal function having propagation velocity equal to the group velocity (Figure 2-9).

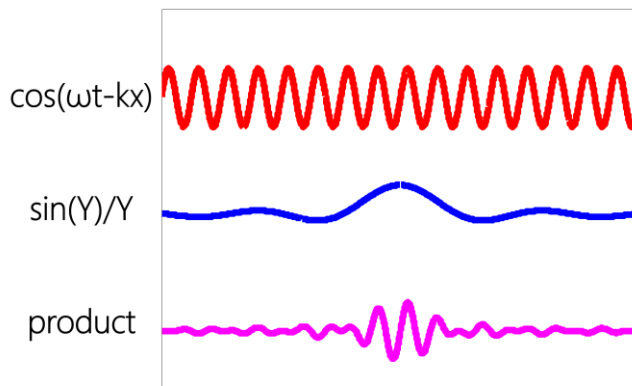


Figure 2-9: A monochromatic wave (red curve) is multiplied for a sinc function (blue curve). The result is a wave packet (magenta curve).

Considering the definition of the group velocity, we have that:

$$c_g = \frac{d\omega}{dk} = \frac{d(kc)}{dk} = c + \frac{dc}{dk} \quad (2.76)$$

there is a relation between the group velocity and the phase velocity. Focusing on the second term of the second member, it can be rewrite as:

$$\frac{dc}{dk} = \frac{dc}{d\lambda} \frac{d\lambda}{dk} = \frac{dc}{d\lambda} \frac{d(2\pi/k)}{dk} = -\frac{2\pi}{k^2} \frac{dc}{d\lambda} = -\frac{\lambda^2}{2\pi} \frac{dc}{d\lambda} \quad (2.77)$$

and therefore, the relationship between group and phase velocity is:

$$c_g = c - k \frac{\lambda^2}{2\pi} \frac{dc}{d\lambda} \quad (2.78)$$

Since, in the Earth it is observed that the S wave velocity, to which surface waves are more sensitive, is increasing with depth, waves with larger wavelengths propagate deeply in the subsoil and travel faster, therefore the term $dc/d\lambda > 0$, and consequently the group velocity is smaller than the phase velocity.

2.5.4 Phase and group velocity measurement

From the equation (2.78) the phase and the group velocities are therefore both dependent on the P and S wave velocity models of the subsoil; measuring the dispersion curves it is possible to infer the elastomechanical properties of the medium. The dispersion curve is the curve of the phase or group velocity as a function of the frequency.

The measure of the group velocity is more intuitive, because it is directly linked to the velocity at which the energy propagates. In the case of the surface waves, a filtered signal at different receivers appears as wave packet propagating among stations. Therefore, if the distance between two stations is known, the ratio between the distance and the arrival time of the wave packet is the group velocity; changing the filter band, we obtain the measure of the group velocity as a function of the frequency (Figure 2-10). Some precautions must be taken in order to have an accurate measure of the group velocity: the previous approach works if the stations are aligned with the source, if it is not the case, we obtain the measure of the apparent velocity, which is larger than the real speed; therefore the wave front has to be projected along the direction between the two stations. It is also possible to measure the group velocity using one station.

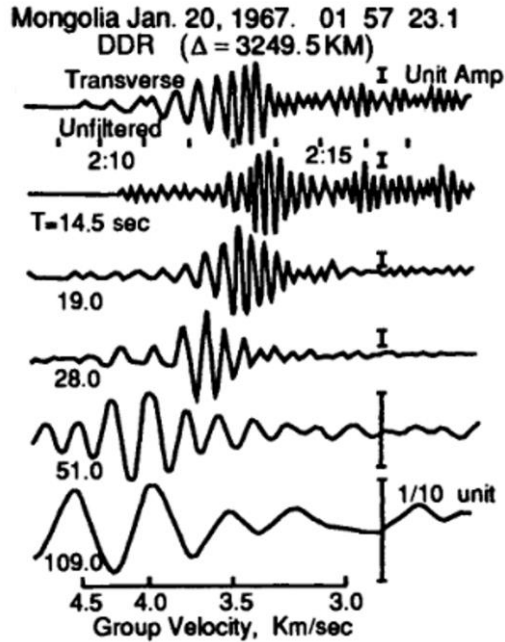


Figure 2-10: Seismograms of the Mongolia earthquake 1967, filtered in several decreasing narrow frequency bands. For each trace is indicated the central period of the band. On the top there is the unfiltered trace. Each trace look like a wave packet.

On a sphere, when an earthquake happens, the surface waves spread in two directions with respect to the considered receiver, the shorter path between the source and the receiver is the minor arc, while the longer path is the major arc. In the literature the minor arc arrivals are indicated with odd numbers: R_1, R_3, R_5, \dots whereas the even passages are related to the major arc: R_2, R_4, R_6, \dots . In all of these cases, the distance between one passage and the next one is the maximum circumference of the Earth (Figure 2-11).

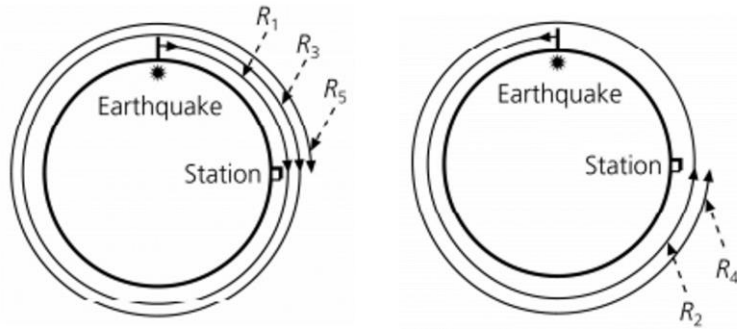


Figure 2-11: Representation of the minor (R_1, R_3, R_5) and major (R_2, R_4) arcs. The earthquake location is indicated with star, the station with box.

The measure of the phase velocity can be performed roughly in the case of a very dispersed seismogram. In that case, we are able to recognize the arrival times of the single phases, this procedure is possible only if the different frequencies do not envelope each other (Figure 2-12). Another way is computing the Fourier transform of the seismogram:

$$u = \int_{-\infty}^{\infty} A(x, \omega) e^{i\left(\omega t - \frac{\omega}{c(\omega)}x + \phi_0(\omega)\right)} d\omega \quad (2.79)$$

and focusing on the phase spectrum:

$$\phi = \omega t - \frac{\omega}{c(\omega)}x + \phi_0(\omega) + 2\pi N \quad (2.80)$$

The terms in the phase are: $\phi_0(\omega)$ the phase at the source and $2\pi n$ the periodicity of the function. The difference of the phase spectrum of two signals acquired at two stations on the same circumference, or at the same station at successive passages of the wave is:

$$\phi_1(\omega) - \phi_2(\omega) = \omega(t_1 - t_2) - \frac{\omega}{c(\omega)}(x_1 - x_2) + 2\pi M \quad (2.81)$$

in this way the knowledge of the phase at the source is no longer required, and it is possible to recover the dispersion relationship for the phase velocity:

$$c(\omega) = \frac{x_1 - x_2}{(t_1 - t_2) + T \left[M - (1/2\pi)(\phi_1(\omega) - \phi_2(\omega)) \right]} \quad (2.82)$$

M is the cycles difference in term of 2π (Lay, et al., 1995).

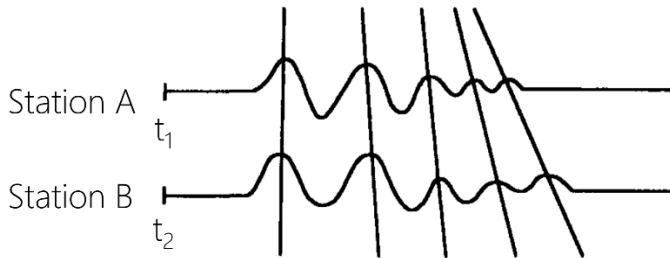


Figure 2-12: Representation of very well dispersed seismogram. The tilted line connect the same maxima acquired at two stations. The slope of the lines is the phase velocity.

Nowadays due to the large availability of sensors, techniques based on arrays have been developed. MASW (multichannel analysis of surface waves) methods make use of Rayleigh waves to recover the dispersion curve, and today they are widely used for the characterization of the first meters of the subsoil. There are different criteria to transform the space parameters in order to obtain the best parametrization for the curve of the energy in the frequency domain. Here we briefly discuss two algorithms that are exploited for this goal: the f - k transform and the τ - p transform. For the first method the original space is transformed into the frequency wavenumber f - k domain and then the dispersion relationship $v=f/k$ pointing to the phase velocity is recovered. This procedure suffers of low quality. The τ - p algorithm is composed by two transformations, the first is to represent data in the space of the ray parameters p and τ , where $\tau=t-px$. The second transformation is a Fourier transform. This method is preferable to the first one because is not sensitive to the preliminary data processing. The Fourier transform is required for the decomposition of the acquired wave field in plane waves after a linear move-out and the traces are summed over the offset axis. This procedure is also known as the slant stack transform. The transformation is:

$$S(p, \tau) = \sum_x P(x, \tau + px) \quad (2.83)$$

Where $S(p, \tau)$ is the monochromatic wave having ray parameter $p = \sin\theta/v$. The complete mapping of the τ - p domain is computed by changing p . In such a way, the asymptotic behavior of the hyperbola in the t - x domain, which is the velocity of the considered wave, $p = 1/v$, is mapped in the vertical tangent to the curve in the τ - p domain (Figure 2-13) (Yilmaz, 2001). Another technique, which uses more than two stations is the spatial autocorrelation method, SPAC, introduced by Aki (Aki, 1957). Aki showed that if the wave field is stationary both in time and space the following relationship is valid:

$$\bar{\rho}(r, \omega) = J_0\left(\frac{\omega r}{c(\omega)}\right) \quad (2.84)$$

where:

$$\bar{\rho}(r, \omega) = \int_0^\pi \rho(r, \omega, \theta) d\theta \quad (2.85)$$

is the azimuthal average spatial autocorrelation for couple of stations separated by the distance r , and J_0 is the Bessel function of the first kind and zero order. With this relation is possible to recover the dispersion curve for the phase velocity $c(\omega)$ by the measured spatial autocorrelation coefficients. A good array configuration would be a semicircular array with a receiver in the middle.

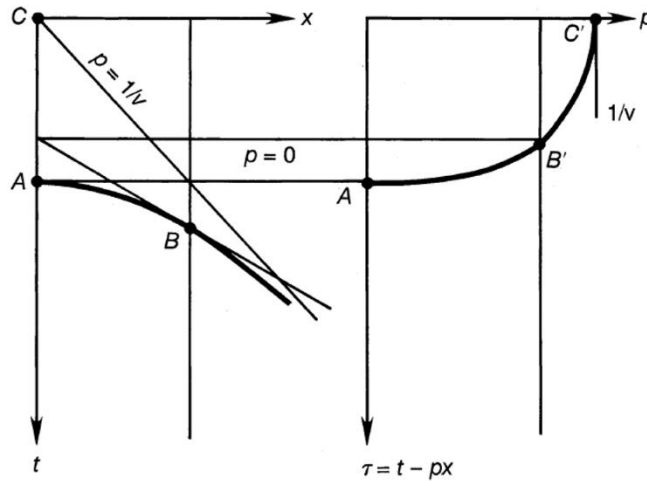


Figure 2-13: In this figure is represented a wave-front in the natural offset-time domain, and how it appears in the τ - p domain.

The knowledge of the dispersion curves of the phase and the group velocity allows for the determination of the structure of the medium crossed by seismic waves. The stronger the velocity gradient of the medium the larger the dispersion. Usually, phase velocity curves are monotonic, whereas group velocity curves can have a minimum. The group velocity is strictly linked to the propagation of the energy therefore, the presence of a minimum implies the simultaneous arrival of a big amount of energy increasing interference effects. This condition is called the Airy phase.

2.6 Attenuation of seismic waves

Up to now, we described the Earth as a perfect elastic body, and the amplitude attenuation of the signals, in all the previous formulas, was conceived just due to the geometric attenuation; ideally once a perturbation was produced it propagates indefinitely in a bounded elastic medium. Of course, that situation is not experimentally observed, but the seismic waves attenuate due to the mechanism of energy conversion in heat and spreading of the energy along directions different from the initial one. A seismogram do not only consists of direct P, S and surface waves, but it englobes a multitude of arrivals that cannot

only be explained in terms of reflections, refractions, conversions at interfaces present in the propagation medium. The one-dimensional description is not enough to understand the complexity of the real data, since it is able to explain a limited quantity of energy in waves. The scattering of the seismic waves with small-scale heterogeneities produces most of the late arrivals; they are gathered under the name of coda. At each scattering event, waves change their direction, and continue to propagate in the medium until their energy is completely converted in heat due to friction. To understand its importance, we can compare the records of a "moonquake" with an earthquake. The acquisitions on the Moon show highly spindle shaped signals that last for a long time, on the Earth the coda waves are weaker. This difference is interpreted by considering the Moon as a medium poorly attenuating but highly scattering (Dainty et al., 1981).

A lot of attempts were performed in order to explain the coda waves, but early, it was clear that coda waves are not waves directly coming from the source but they are scattered waves coming from all directions. These waves cannot be explained using the classical deterministic approaches such as the ray theory, but they need of a theory that can take into account the scattering events, wither produced by single or multiple scatterers turning into radiative or diffusive regimes.

2.6.1 Single scattering model

Here we do not want to provide a deep mathematical description of the scattering theory but just some elements, in order to understand the problem. If we consider the simple problem of the energy propagation in an inhomogeneous infinite medium, we can define the amount of energy through the solid angle $d\Omega$ per unit time as J_0 , and in the same way the scattered energy with J_1 . Therefore the differential scattering cross-section is defined as:

$$\frac{d\sigma}{d\Omega} = \frac{J_1}{J_0} r^2 \quad (2.86)$$

Where $r^2 d\Omega$ is the surface element at a distance r from the source of the radiation. The medium in which waves propagate can be assumed as homogenous, having

propagation velocity v_0 , filled with randomly distributed point-like scatterers, having density n . It follows that the scattering power per unit volume for the considered medium is:

$$p = 4\pi n \frac{d\sigma}{d\Omega} \quad (2.87)$$

p has the dimension of the inverse of a length and it is related to the differential scattering cross section. Integrating the (2.87) on all the possible directions:

$$p_0 = \frac{1}{4\pi} \int g d\Omega = n \int \frac{d\sigma}{d\Omega} d\Omega = n\sigma_0 = \frac{1}{l} \quad (2.88)$$

Where σ_0 is the total scattering cross-section, and l is called mean free path. This parameter gives a statistical global description of the medium, indicating the average path travelled by a wave between two scattering events. Aki and Chouet (Aki and Chouet, 1975) gave the first description for the scattering through the theory of the single backscattering model. In a three-dimensional medium a scatterer is located at distance r from the source of radiation of the energy W . Because of the geometry of the problem, the energy propagates along spherical wavefronts. The scatterer is reached by the energy flux density equal to:

$$P = \frac{W}{4\pi r^2} \delta\left(t - \frac{r}{v_0}\right) \quad (2.89)$$

where the geometrical spreading and the delay time are taken into account. In such kind of model, the single backscattered energy flux density is:

$$P_\pi = \frac{W}{4\pi r^2} \delta\left(t - \frac{2r}{v_0}\right) \frac{1}{r^2} \frac{d\sigma}{d\Omega} \Big|_\pi \quad (2.90)$$

Now the time delay is twice that of the formula (2.89) because we have to consider the round trip between source and receiver and the subscript π is used to indicate the angle at which energy comes back at the source. Starting from the (2.90), considering a medium with randomly distributed scatterers and dividing by the

velocity of the medium, we can recover the energy density of the single backscattered wavefield:

$$E = \int_V \frac{W}{4\pi|\mathbf{r}|^2} \delta\left(t - \frac{2|\mathbf{r}|}{v_0}\right) \frac{n}{|\mathbf{r}|^2} \frac{d\sigma}{d\Omega} \Bigg|_{\pi} \frac{1}{v_0} dV \quad (2.91)$$

Replacing the (2.87) into the above equation and integrating in the spherical coordinate system, yield:

$$E = \frac{Wg_{\pi}}{2\pi v_0^2 t^2} H(t) \quad (2.92)$$

$H(t)$ is the Heaviside function. In this example, we considered the origin of our system located at the source, but with the same considerations we can achieve the solution of a more general problem where the source and receivers are in generic points of the space:

$$E = \frac{Wg_0}{2\pi|\mathbf{r}|^2} K\left(\frac{v_0 t}{|\mathbf{r}|}\right) H(v_0 t - |\mathbf{r}|) \quad (2.93)$$

We have introduced the function $K(v)$ with $v = v_0 t / |\mathbf{r}|$ which is defined as:

$$K(v) = \int_{-1}^1 \frac{1}{v^2 - w^2} dw = \frac{1}{v} \ln \frac{v+1}{v-1} \quad (2.94)$$

in a prolate spheroidal system where (w, v, ϕ) are the coordinates. Dealing with surface waves the solution for a two-dimensional medium is more useful. If the source is at the origin of the reference frame, we have:

$$E = \frac{Wg_0}{2\pi|\mathbf{r}|} \frac{H(v_0 t - |\mathbf{r}|)}{\sqrt{(v_0 t / |\mathbf{r}|)^2 - 1}} \quad (2.95)$$

In the three-dimensional approach the root mean square of the coda, in the same point, is attenuating as t^2 , whereas in a two-dimensional medium it attenuates as t (Sato, et al. 2012).

2.6.2 Radiative transfer model

The single scattering approximation can be used if we are close to the source or if a small lapse time is considered, otherwise multiple scattering becomes dominant and the interference effects of incoherent waves destroy the phase information. The transition from the single scattering regime to the multiple one is not a threshold phenomenon but we can have a superimposition of them. Typically, we can split the process of multiple scattering in radiative and diffusive behaviors. The radiative transfer model is the solution of the Boltzmann equation also known as radiative transfer equation; its long time limit is the diffusive solution. Hemmer (Hemmer, 1971.) gave the solution of this equation in one-dimension, whereas exact solutions were founded in the Fourier space for a two or four-dimensional medium; finally numerical results are available for three-dimensional media. For sake of simplicity will give just the two-dimensional solution. The expression of the solution of the Boltzmann equation in the Fourier space for a two-dimensional medium is:

$$I_N(k, \omega) = \frac{l}{c} \left[(1 - i\omega l / c)^2 + k^2 l^2 \right]^{-(N+1)/2} \quad (2.96)$$

$I(\mathbf{r}, t)$, in the real space, is defined as the sum of the partial intensities I_N :

$$I(\mathbf{r}, t) = \sum_{N=0}^{\infty} I_N(\mathbf{r}, t) \quad (2.97)$$

that is, the total intensity is obtained summing the separate contributions coming from $N=0,1,2,3,\dots$ scattering events. To write the solution in the real space we invert the relationship (2.96), without taking into account the ballistic wave contribution, $N=0$. This term is modelled as a delta function shifted in time, and will be added to the solution later. Therefore, the intensity in the real space for a generic n-th scattering event is:

$$I_N(\mathbf{r}, t) = \frac{e^{-ct/l}}{2\pi l^2} \frac{1}{(N-1)!} \left(\frac{ct}{l} \right)^{N-2} \left(1 - \frac{r^2}{c^2 t^2} \right) H(ct - r) \quad (2.98)$$

for $N \geq 1$, and, summing over N contributions and adding the direct wave, we can write:

$$I_N(\mathbf{r}, t) = \frac{e^{-ct/l}}{2\pi|\mathbf{r}|} \delta(ct - r) + \frac{1}{2\pi lct} \left(1 - \frac{r^2}{c^2 t^2}\right)^{-1/2} e^{\frac{\sqrt{c^2 t^2 - r^2} - ct}{l}} H(ct - r) \quad (2.99)$$

The first term of the solution is the ballistic wave, whereas in the last term is contained the long time term, when the solution tends to the diffusive regime (Paasschens, 1997).

2.6.3 Diffusive model

Following the previous discussion, it is possible to affirm that in a medium with randomly distributed scatterers, having small l or when waiting for enough time, the energy originated by an impulsive source function diffuses in the medium following the diffusion equation:

$$\frac{\partial E(\mathbf{x}, t)}{\partial t} - D \nabla^2 E(\mathbf{x}, t) = W \delta(\mathbf{x}) \delta(t) \quad (2.100)$$

The coefficient D is called the diffusivity and is related to the mean free path through the relationship $D = v_0 l / d$, and d is the dimensionality of the system in which we are solving the problem. The solution of the equation is:

$$E(\mathbf{x}, t) = \frac{W}{(4\pi Dt)^{d/2}} H(t) e^{-\left(\frac{|\mathbf{r}|^2}{4Dt}\right)} \quad (2.101)$$

The energy decays slower than in the previous cases, and the large number of scattering events destroy the direct waves arrivals, such that they are no longer detectable on the seismograms and a smoother coda is observed (Sato et al., 2012).

2.6.4 Anelastic attenuation

The energy during the propagation process is converted from mechanical one to heat, owing to internal friction. We gather in this expression a large variety of complex molecular processes, which we don't want to individually interpret because we are interested at their collective effects at larger scale. The simplest model of the anelastic attenuating process is an oscillating mass on a spring that moves on a plane with friction.

We start considering a mass m , attached to a spring having spring constant k , without friction between the plane and mass. The equation of the motion is:

$$m\ddot{x} + kx = 0 \quad (2.102)$$

This is a second order differential equation, and its general solution is:

$$x = Ae^{i\omega_0 t} + Be^{-i\omega_0 t} \quad (2.103)$$

Where $\omega_0 = \sqrt{k/m}$ and, A and B are two constants that can be determined solving the related Cauchy problem. The (2.102) does not involve any attenuating term, and it describes an oscillating motion with natural frequency ω_0 that continues indefinitely. If we add a damping force, the equation (2.102) becomes:

$$m\ddot{x} + \gamma\dot{x} + kx = 0 \quad (2.104)$$

γ accounts for the friction which opposes the motion. The solution is:

$$x(t) = A_0 e^{-\varepsilon\omega_0 t} \sin(\omega_0 t \sqrt{1 - \varepsilon^2}) \quad (2.105)$$

where $\varepsilon = \gamma/m\omega_0$ and the term $A_0 e^{-\varepsilon\omega_0 t}$ is the amplitude of the oscillation, if $\varepsilon=0$ no attenuation is present. The damping factor ε can be expressed in term of the so called quality factor Q :

$$\frac{1}{Q} = -\frac{\Delta E}{2\pi E} \quad (2.106)$$

which is a measure of the energy loss per cycle. From this definition, large Q values imply small attenuation, whereas low Q values imply high attenuation. The relationships that links ε and Q is:

$$\varepsilon = \frac{1}{2Q} \quad (2.107)$$

therefore, the amplitude becomes:

$$A(t) = A_0 e^{-\frac{\omega_0 t}{2Q}} \quad (2.108)$$

The energy is proportional to the square of the amplitude of the waves, and the fractional energy loss can be written as:

$$\frac{\Delta E}{E} = 2 \frac{\Delta A}{A} = -\frac{2\pi}{Q} \Rightarrow -\frac{\pi}{Q} \quad (2.109)$$

If we consider the variation of the amplitude on the distance equal to the wavelength λ :

$$\frac{dA}{\lambda} = \frac{\Delta A}{\lambda} = -\frac{A\pi}{\lambda Q} \Rightarrow \frac{1}{Q} = -\frac{1}{\pi} \frac{\lambda}{A} \frac{dA}{dr} \quad (2.110)$$

From the equation (2.110) and using the dispersion relationship $\lambda=2\pi c/\omega$ we obtain:

$$A = A_0 e^{-\frac{\omega r}{2cQ}} = A_0 e^{-\frac{\omega t}{2Q}} \quad (2.111)$$

that is a generalization of the (2.108) for all the frequencies. The amplitude A_0 refers to the time $t=0$ or alternatively, to the position $r=0$. It is evident that higher frequencies attenuate faster than the lower ones, since in a given interval time, higher frequencies complete more cycles and loose more energy.

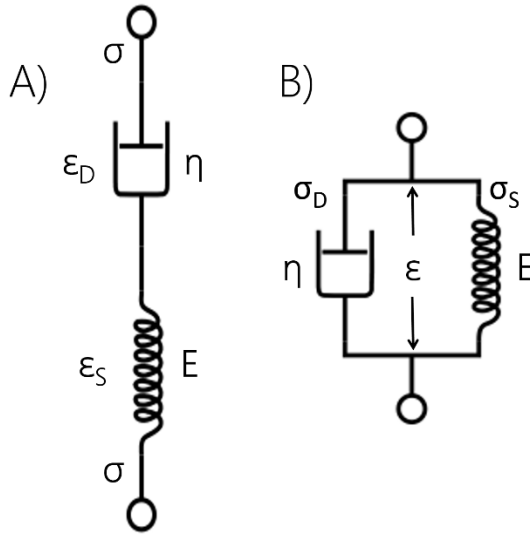


Figure 2-14: Representation of the Maxwell (A) and Kelvin-Voigt material (B). The letters ϵ , σ indicates respectively the deformation and the stress, the subscripts D and S referred to the dashpot and the spring.

The previous relationships indicate a Q frequency independent; it is true in the frequency range 0.001 to 1 Hz, but at higher frequencies it has been experimentally showed to be a function of the frequency. To understand the nature of this relation we have to introduce the standard linear solid model (SLS). This model is used to represent from a mathematical point of view the viscoelastic behavior of rocks. It is a one-dimensional mechanical model composed by a spring and a dashpot, coupling the elastic with the viscous behavior. Before focusing on the SLS model, we deal with two simpler models. Although a combination of spring and dashpot will be considered, the dynamics of the total system can be obtained from the constitutive law of the single elements. This two elements can be combined in series or in parallel, resulting in a Maxwell material or Kelvin-Voigt material (Figure 2-14) models, respectively. In the Maxwell material the total stress and strain are:

$$\begin{aligned}\sigma_T &= \sigma_D = \sigma_S \\ \epsilon_T &= \epsilon_D + \epsilon_S\end{aligned}\tag{2.112}$$

the subscript D indicates stress and strain related to the dashpot, D , the equivalent S is for the spring. Taking the derivative of the strain with respect to time, we obtain the constitutive law:

$$\dot{\varepsilon}_T = \dot{\varepsilon}_D + \dot{\varepsilon}_S = \frac{\sigma}{\eta} + \frac{\dot{\sigma}}{E} \quad (2.113)$$

E is the elastic modulus and η is the viscosity. If this material is suddenly deformed, the stress decays with a characteristic time, η/E , and if a sudden stress is applied, the elastic element instantaneously responds whereas the viscous one accommodates it at constant rate. It is important to notice that if the stress is released at the time t^* the presence of the dashpot doesn't permit to the spring to come back at the rest position. Therefore the energy associated to the dashpot deformation, $t^* \sigma_0 / \eta$, is lost. If the spring and the dashpot are connected in parallel, we get the Kelvin-Voigt model. Due to this configuration, the strain for the two elements is the same, whereas the stress is the sum of the ones for the single elements:

$$\begin{aligned} \varepsilon_T &= \varepsilon_S = \varepsilon_D \\ \sigma_T &= \sigma_S + \sigma_D \end{aligned} \quad (2.114)$$

From these equations, we can achieve the relationship that governs the stress and strain variation with the time:

$$\sigma(t) = E\varepsilon(t) + \eta \frac{d\varepsilon}{dt} \quad (2.115)$$

As discussed before if a sudden stress is applied, the body approaches to the deformation of a pure elastic body with an exponential growth:

$$\varepsilon(t) = \frac{\sigma_0}{E} \left(1 - e^{-\frac{E}{\eta} t} \right) \quad (2.116)$$

Differently from the previous case, if the stress is released the system comes back to initial position in a certain characteristic time, E/η and the deformation is reversible.

The Maxwell model doesn't expect recovery, whereas the Kelvin-Voigt model is lacking in describing the stress relaxation. The SLS better describes the real materials, taking into account both the phenomena. This system is built connecting in parallel a Maxwell arm with a spring (Figure 2-15). The relationships which link stress and strain in the global system are:

$$\begin{aligned}
 \sigma_T &= \sigma_M + \sigma_{S1} \\
 \varepsilon_T &= \varepsilon_M = \varepsilon_{S1} \\
 \sigma_M &= \sigma_D = \sigma_{S2} \\
 \varepsilon_M &= \varepsilon_D + \varepsilon_{S2}
 \end{aligned}
 \tag{2.117}$$

The subscript M identifies the Maxwell arm, S_1 and S_2 are related to springs 1 and 2. Combining these relationships and their derivatives, we can recover the equation that describes the system:

$$\frac{d\varepsilon}{dt} = \frac{1}{E_1 + E_2} \left(\frac{d\sigma}{dt} + \frac{E_2}{\eta} \sigma - \frac{E_1 E_2}{\eta} \varepsilon \right)
 \tag{2.118}$$

The physical behavior of the SLS is easily predictable, if the mass is shifted, the system instantaneously responds with a restoring force, generated by the springs. If the mass is hold shifted from the rest position, the restoring force diminishes with time owing to the dashpot action. The energy spent in the relaxation of the dashpot is not recoverable, therefore, this system is anelastic. The dynamics of the system is contained in the complex elastic moduli defined as:

$$M^* = M_R + \delta M \frac{\omega^2 \tau_\sigma^2}{1 + \omega^2 \tau_\sigma^2} + \frac{i \Delta M \omega \tau_\sigma}{1 + \omega^2 \tau_\sigma^2}
 \tag{2.119}$$

Where $\Delta M = M_U - M_R$, $M_U = \tau_\varepsilon M_R / \tau_\sigma$, M_R is the relaxed elastic moduli, τ_σ are τ_ε are the stress and strain relaxation time. From this relationship is also possible to obtain an equation for Q :

$$\frac{1}{Q(\omega)} = \frac{\Delta M}{M_R} \frac{\omega \tau_\sigma}{1 + \omega^2 \tau_\sigma^2}
 \tag{2.120}$$

The equation presents a peak, known as Debay peak, in a limited frequency range, around $\omega\tau_0=1$, and attenuates for higher or lower frequencies (Lay and Wallace, 1995).

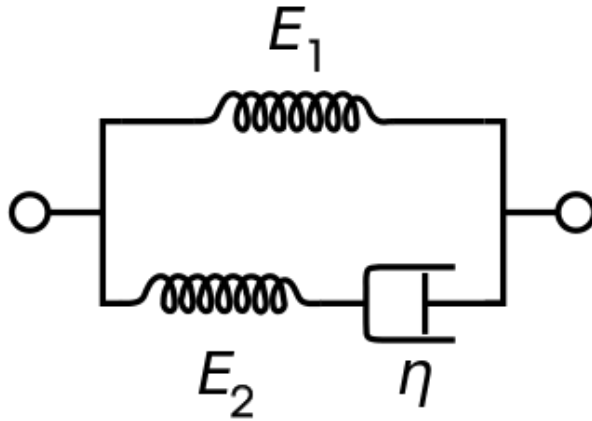


Figure 2-15: The standard linear solid is a composition in parallel of a Maxwell arm and a spring

The Q value measure can be performed in the time or frequency domains; in both cases the measure is obtained looking at the signals acquired at different distances. If we identify a particular phase in a seismogram and we follow it during its propagation, in the time domain, the main effect of the attenuation is the reduction of the amplitude of the signal and the dispersion of the phase, when increasing the source receiver distance. For a point-like source the relationship between the half duration of an attenuated pulse and Q is:

$$\tau = \tau_0 + C(Q) \frac{t}{Q} \quad (2.121)$$

where τ_0 is the half duration of the pulse at the source, t is the propagation time to the considered receiver and $C(Q)$ is a coefficient depending on the source time function. Repeating this measure at different distances, it is possible recover the Q value by means of a linear regression. In the time domain the measure of Q is also inferred looking at the envelope of the seismograms at difference distances. As showed in the (2.111) , the amplitude is exponentially attenuated; if we take the logarithm of the amplitude of a seismogram, the coda attenuates as a linear

function. The slope obtained from the linear regression is related to the Q value. Since the attenuation is a parameter typical of the investigated area, the envelope of a multitude of seismograms acquired in the same area would almost show the same envelope decay in the coda, better constraining the final estimate.

In the spectral domain, the spectrum of a seismic phase is computed and it is analyzed as a function of the distance and the frequency. A station close to the source, less polluted by the attenuation effect, can be assumed to provide the spectrum at the source:

$$|A(r_0, \omega)| \approx k |S(\omega)| \quad (2.122)$$

At a generic distance r from the source, the spectrum amplitude is:

$$|A(r_1, \omega)| = k |S(\omega)| \cdot |Q(t_1, \omega)| = k |S(\omega)| e^{-\frac{\pi\omega t_1}{Q}} \quad (2.123)$$

and therefore, the ratio of the previous equations in a log scale is:

$$\ln \frac{|A(r_1, \omega)|}{|A(r_0, \omega)|} = k - \frac{\pi t_1}{Q} \omega \quad (2.124)$$

k is a constant which takes into account the source effects. Through a linear regression, we can infer the Q value from the slope of the best fit curve. We can also exploit the functional form of the displacement spectrum for an earthquake:

$$|S_0(\omega)| = \frac{\Omega_0}{1 + \left(\frac{\omega}{\omega_c}\right)^n} \quad (2.125)$$

Ω_0 is the amplitude of the spectrum at lower frequencies, ω_c is the corner frequency and n is a value ranging from 2 and 3. For small earthquakes, for which the corner frequency is enough large, the spectrum level diminishes in agreement with the attenuation of the medium:

$$|S(r_1, \omega)| \approx k e^{-\frac{\pi\omega t_1}{Q}} \Rightarrow \ln(|S(r_1, \omega)|) = \ln k - \frac{\pi t_1}{Q} \omega \quad (2.126)$$

again, from the slope of the best fit linear curve we can estimate the Q value.

Finally, it is worth to note that usually we are not able to distinguish the effects of the scattering attenuation from the anelastic one and they will be mixed and appear as one single Q value. Nevertheless, they are two completely different phenomena: the scattering properties of the medium allow a transfer of the energy from the ballistic to the coda waves, so it can be considered as an effect of energy redistribution; whereas, the second one is just an energy loss (Zollo and Emolo, 2011).

3 The Solfatara

The Campi Flegrei caldera is a resurgent and restless volcano located on the western coast of Southern Italy, close the city of Naples, a densely inhabited region. It covers an area of about 400 km² and it is one of the two active volcanic systems in the south of the Italian peninsula. In the last years, this area has shown uplift events, variations in gas composition of fumaroles and variable seismicity linked to the ground deformation. For such a reason the alert level has increased and the area has become object of numerous studies. Analysis of gravity data, geoelectric and geomagnetic surveys, seismological active or passive campaigns with dense networks of instruments have been performed. Some of them were realized in conjunction with other ones, some others independently, but all of them were aimed to understand the shallow or the deep structure of the volcanic area, the fluids circulation, the sources of ambient noise and in general the variation over the time of the physical properties governing the volcanic system.

During its past history, the Campi Flegrei area has experienced an intense eruptive activity. There are different interpretations to explain the actual conformation of the caldera, but the idea of two big eruptions is generally accepted. The Campanian Ignimbrite eruption occurred about 39 kyr ago, when 300 km³ of magma where erupted, and the Neapolitan Yellow Tuff eruption occurred about 15 kyr ago, producing 40 km³ of pyroclastic material (Figure 3-1) (Orsi et al., 2004; Acocella, 2008; Fedele et al., 2008; Pappalardo & Mastrolorenzo 2012). Furthermore, to understand the potentiality of such a volcano, we report that the Campanian Ignimbrite eruption is the biggest one in Europe in the last 200 kyr (Costa et al. 2012).

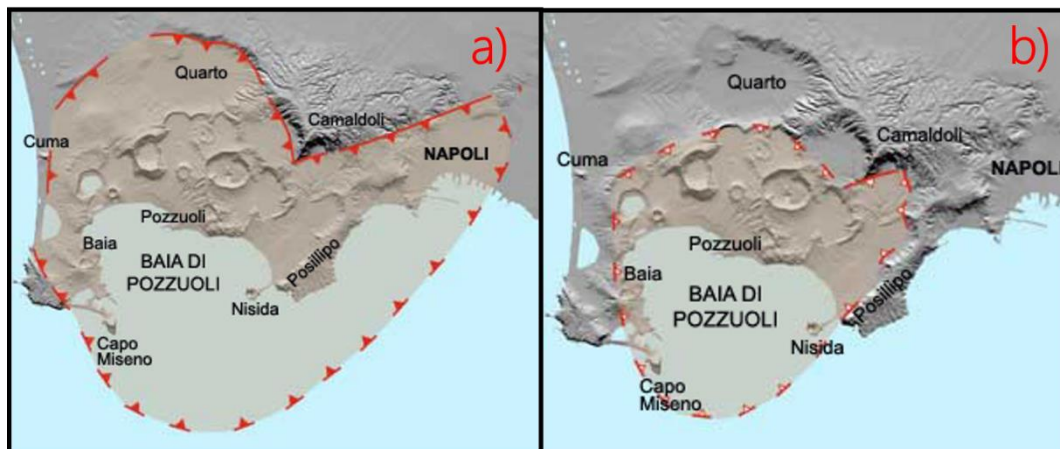


Figure 3-1: Satellite images of the Pozzuoli bay where the rims of the Ignimbrite Campana caldera (a) and Neapolitan Yellow tuff caldera (b) are highlighted (red lines).

After the Neapolitan Yellow Tuff eruption, geologists have recognized traces of more than 70 smaller eruptions (Di vito et al., 1999; Di Rienzo et al., 2011). The last eruption is dated 1538 and produced the Monte Nuovo tuff cone (Guidoboni & Ciuccarelli, 2011). In the periods 190-72 and 1982-84 two major bradyseismic crises occurred (Del Gaudio et al., 2010) with a cumulative uplift of about 3.5 m. They were associated to the magma intrusion from depth (D'Auria et al., 2015; Trasatti et al., 2015). Due to the ground deformation, also a small seismic activity was observed during the first episode of bradyseism, whereas it was intense in the second one. The deformation of the soil, the temperature increase and the rising of the table water is never turned at the levels before the crisis of the seventies and eighties years. Today, the activity consists mainly in fumaroles, due to the interaction between heat coming from depth and meteoric water, and a ground uplift that started around 2000.

In general, the large scale structure of the Campi Felgrei caldera is pretty well known. The shallower part of the area was investigated by means of local earthquakes, gravity, magnetelluric experiments, while the temperature profile was recovered through boreholes analysis (De Lorenzo et al., 2001). Geophysical data consistently agree with the presence of a layer at about 3 km depth, that separates the older caldera from saturated rocks. In the zone above this interface,

there are fractured rocks saturated with supercritical fluids, also recognized to be the barrier of the hydrothermal system (Zollo et al. 2008; Vanorio et al., 2005), whose effects are clearly visible at Pisciarelli and Solfatara. To have a global knowledge of the caldera, in the 2001, the seismic survey SERAPIS was realized in the bays of Naples and Pozzuoli. The geometrical source receiver setup permits to obtain tomographic images of a volume of $13 \times 13 \times 5 \text{ km}^3$ (Judenerch and Zollo, 2004). Results showed that at 8 km depth there is a partial melting zone where the V_P decreases from about 6 km/s to 3 km/s, but at the same time the ratio V_P/V_S increases up to about 2.5. Active seismic analysis (AVO) also showed that this layer has an areal coverage of 30 km^2 and about 1 km of thickness. Moreover, despite of the different magma composition it is supposed that this layer could also feed the Vesuvius volcano (Zollo et al. 2008). It is established that different temperatures, velocities and different settle times can generate differentiation in the magma at Campi Flegrei (De Lorenzo et al. 2006). From gravity data, in the area under Pozzuoli a negative anomaly was founded, interpreted as the buried caldera of a huge volcano filled with marine and continental sediments; in agreement with other surveys, also gravity puts the bottom of the caldera at about 3 km (Fedi et al. 1991). Gravity data coming from different campaigns were then assembled (Capuano et al. 2013) to refine the geostructural conformation of the area and to infer the variation in the thermal and gravitational maps of the area which are expected to be a proxy of the underlying volcanic activity because such variations are associated to fluid injection from depth. Through a P-wave attenuation tomography obtained from SERAPIS data, an arch-like structure was individuated with Q_P of about 70. In the light of seismic analysis, this structure can be interpreted as the rim of the Campi Flegrei caldera. Bodies having Q_P values of 30 have also be found, indicating a strongly attenuating medium correlated to unconsolidated pyroclastic material filling the caldera (Serlenga et al., 2016).

The Solfatara volcano is one of the dozens craters of the Campi Flegrei caldera, it is a 600 m tuff cone located at 100 m above the sea level. Here the most of the fumarolic activity is centered. About 3000 tons/day of CO_2 and gas mixture are released in the atmosphere. Solfatara is assumed to be the top of the hydrothermal system located in the shallower part of the caldera (Chiodini et al., 2001). The Solfatara volcano is not a medium with simple structural signatures, it

is a mixture of different materials subjected to different physical extreme conditions, which can also alter their chemical composition. It is noteworthy that the soil temperature at just 30 cm depth can reach temperatures of 80 °C, because of the latent heat due to the condensation of the large amount of ascending steam. The understanding of the Solfatara feeding system is also important for the hazard assessment; due to the morphological complexity and the large heterogeneity of the medium, it is a place where new experimental techniques can be developed and evaluated.

In general, electromagnetic and electrical data are more sensitive to the fluids saturation therefore, they can be advantageously operated to distinguish different rock phases. From the resistivity point of view, the Solfatara area can be roughly split in two domains, one with higher resistivity in the northwestern part of the crater, which became thinner and thinner going toward the central zone of the Solfatara, where the Fangaia is located. The Fangaia is a mud pool where the water outcrops at the surface and a continuous stream of fluids and gas generates bubbling. Magnetotelluric data can penetrate deeply, showing that the region rich in water extends down to 400 m under the Solfatara (Figure 3-2a). Below the conductive body the resistivity increases, this observation being interpreted as a volume where there is a more important gas presence (Bruno et al. 2007). The great conductive body is split by an area having high resistivity, this anomaly has been interpreted as an ensemble of faults or fractures, which are exploited by gases to reach the surface. The injection of gas at high pressure and temperature push off the water from these degassing patterns and an increasing of the resistivity and of the seismic waves velocity was observed. Looking more in detail and shallower (Figure 3-2b) we can observe that the conductive body in the central part of the profile becomes thinner due to the presence of an anomaly resistivity zone, which again it has been interpreted as a volume where there is a more important gas presence (Bruno et al., 2007).

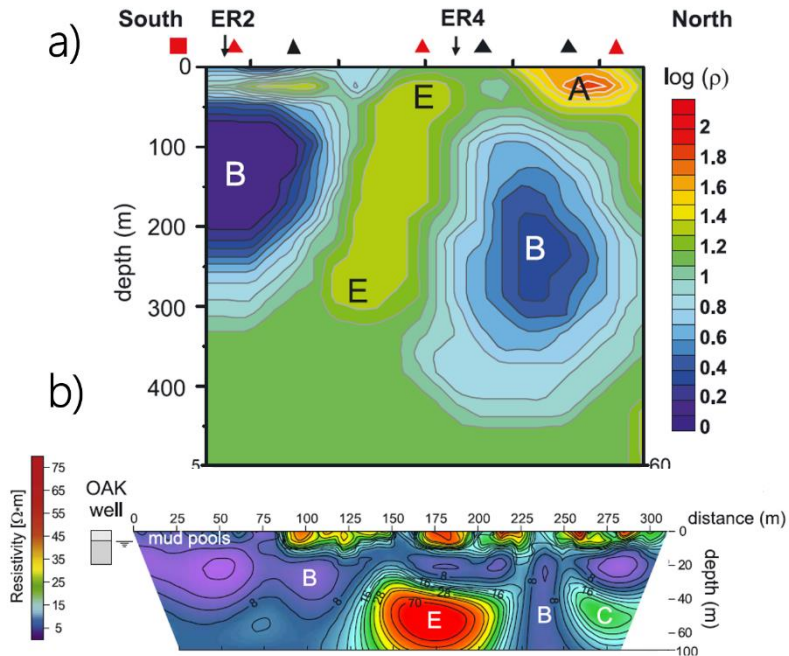


Figure 3-2: The figure on the top (a) shows the clear splitting of the conductive body (B) by means of the presumed fractured degassing pattern (E). On the bottom (b) we can follow the progressive thinning of the resistive shallower layer going toward the “Fangaia” and also the presence of the resistive anomaly (E) again associated to a more rich in gas volume.

Letort et al. 2012 reported similar phenomena; they performed a surface wave analysis, measuring the dispersion curve of the group velocity and deriving an S-wave velocity model for the area. In their results, strong lateral variations were found. Additionally, at 6 m depth, there is a zone where they observed a drop in the S-wave velocity in correspondence of a strong gradient of temperature, being interpreted as indicative of a fractured zone such as a fault that is filled by hot gas, which arrives at the surface (Figure 3-3).

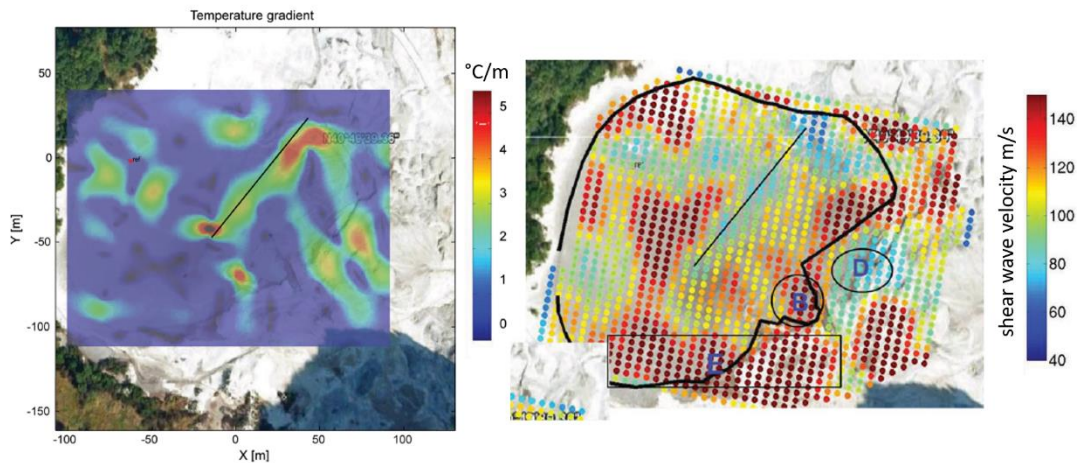


Figure 3-3: Gradient of temperature on the left and S-wave velocity value on the right. From the comparison of the two figures it is possible to observe that the points where higher temperature variations are found are the same ones where slower shear velocity are measured. These common features can be jointly explained by imaging the presence of a fault (black solid line).

Seismic refraction profiles in this area do not bring information at depths higher than 30 m, this depth being only reached in central part of the investigated area. At the edges of the model it is not possible to interpret results due to the lower ray coverage. The analysis is limited in depth because of the reduced array aperture, and because of the low velocity propagation in the shallow part of the medium which doesn't allow to follow coherent phases along the complete profile. In general, due to the very low mechanical properties of the medium, very low P-waves velocities are recovered. There is a shallower layer having velocity ranging from 300-800 m/s and a deeper one ranging from 1000-2600 m/s (Bruno et al. 2007). Low P velocity value possibly indicates that the rocks inside the layer are unconsolidated. In the second layer the velocity is higher, comparable to P-wave speed in the water, but anyway is low with respect to other rocks at the same depth.

The noise analysis shows that there is a strong correlation with the cycle of the hydrothermal system, the activity is strongly variable and it is easily evaluable also from a visual inspection of the area (Vandemeulebroeck et al. 2005). The noise activity is mostly concentrated in two hot spots of the Solfatara: Bocca Grande

and Bocca Nuova. The variations happen during the day and over the time scale of a year. Consequently if gas emissions change, because of a different water level or a different temperature, also the noise activity changes. During the RICEN experiment (we will discuss widely about it in the next section) the noise analysis was performed using data related to stations spread over the whole area of the Solfatara, which acquired data for a week. Through the cross-correlations of vertical data the Green's functions were obtained (Pilz et al., 2016). A low velocity S-wave profile was obtained and the presence of a shallower soft layer was highlighted. In this analysis, S-waves velocities range from 120 m/s in north-eastern part, up to 200 m/s in the south-western part. Moreover, they observe a velocity increasing below this first soft layer around 10-20 m. Consistently with other works, at around 35 m the S-wave velocity increases up to an average value of between 850 m/s and 1200 m/s. Again, the investigated volume is split in two domains one having higher velocity, where most of the visible gas emission is located, and another one with lower velocity. Furthermore Petrosino et al. (2016) showed, for the array of smaller dimension, which have a better resolution at shallow depths, that there is a very thin shallow layer of unconsolidated material. For arrays having wider spacing, results showed that velocity at larger depth can reach values larger than 1500 m/s. De Landro et al. (2016) produced a tomographic model in terms of P-waves. Starting from the data acquired during the RICEN experiment, they used a multiscale approach in order to achieve a high-resolution three-dimensional image of the subsoil of the region close the Fangaia. They found low P-wave velocity for the first 10-15 m, ranging from 200-700 m/s and corresponding to values typical of tephra, and going deeper velocity increases up to 1800 m/s that can be associated to more consolidated tephra owing to the lithostatic load. The value of 1800 m/s is reached in a high velocity anomaly, located at 25-30 m depth, which authors relate to a degassing structure. They also recovered the dual trends of the P-waves, which well match with results from the geoelectric profiles obtained in the same area during the same survey. P-waves and S-waves velocity decrease toward the Fangaia (Figure 3-4), where at the same time geoelectrics shows materials having more conductive properties with respect to the area toward North-East, where both the velocity and the resistivity increase. Also if between the more or less saturated zones there is not

a physical barrier, the variation in the abovementioned parameters in some point is abrupt.

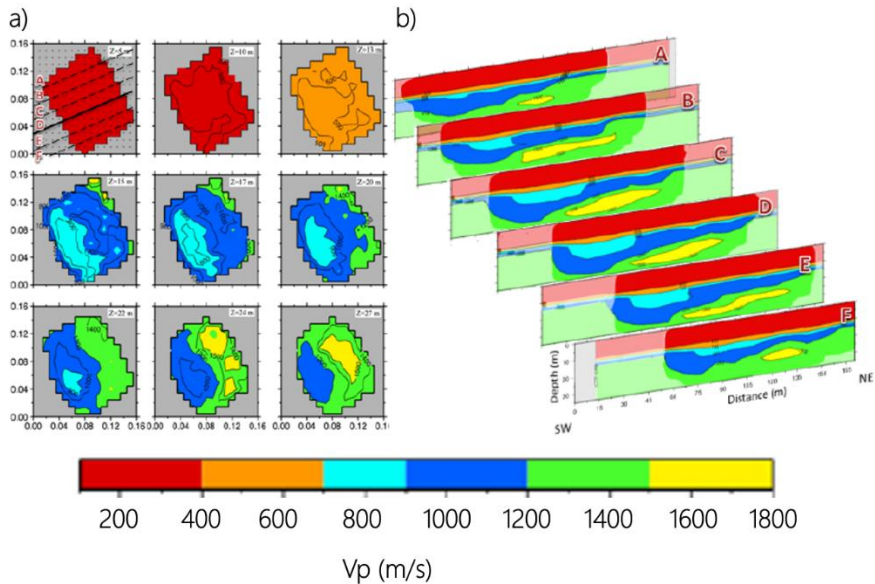


Figure 3-4: The P-wave analysis shows general very low velocity values at the surface which increase going deeper. At the same time the dual nature of the investigated domain is clear. The lowest velocity are recovered closer the Fangaia.

The actual ground deformation of Campi Flegrei caldera, is governed by an uplift with a total displacement of about 0.40 m and an accelerating trend. The deformation started in the last decades, and were correlated to magma injection, the idea being supported by the variations in the chemical contents of the emissions. The CO flux which is sensitive to the temperature changes, increased in fumaroles and at the same time, also the H₂O fraction shows the same trend. Chiodini et al. (2016) simulated the injection of magma fluids subjected to typical conditions of the Campi Flegrei hydrothermal system and analyzed the production of CO and H₂O. They observed that the increasing trend of the CO emission follows the measured temperature trend, and when magma reaches the critical degassing pressure, more water is released. The water content seems to be a crucial parameter in such kind of eruptions because the heat convection

becomes more efficient and furthermore the water dramatically alters the rocks rheology, by decreasing the rock mechanical resistivity and increasing the fluid permeation. Therefore, the Campi Flegrei caldera could be approaching to the tipping point as already verified for other volcanoes in the world. This expectation is however questioned other effect that could change completely the final scenario are not taken into account (Figure 3-5).

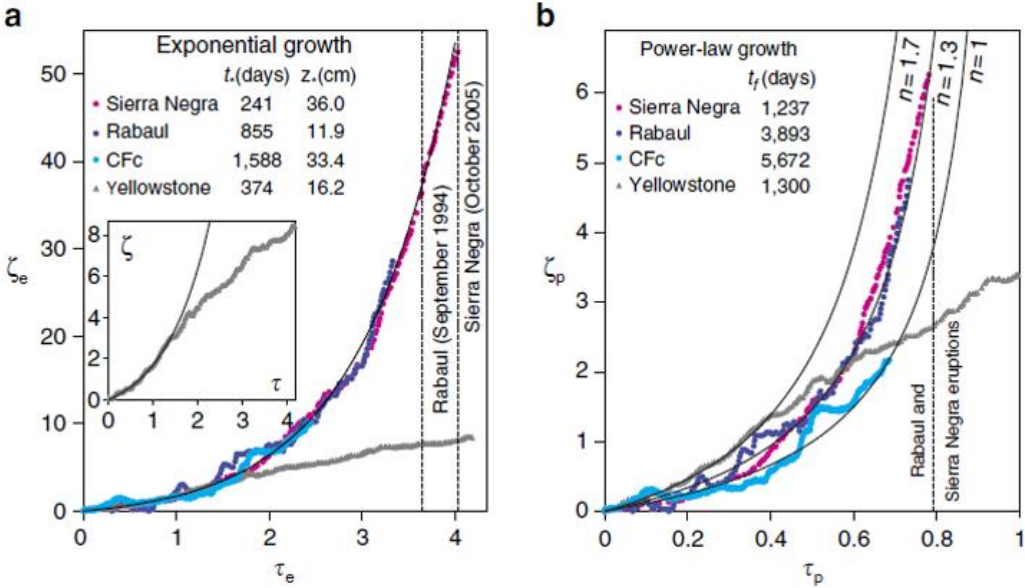


Figure 3-5: In this figure are showed the vertical displacement as function of the dimensionless time, fitted (black solid line) using an exponential law on the left (a), or a power law (b). The colored curves are the measured data at different volcanoes in the world located in hydrothermal areas. With the vertical dashed line is indicated the failure time.

4 RICEN

RICEN is the acronym of Repeated and Induced Earthquakes and Noise; it is an active and passive interdisciplinary survey. It involved geoelectric, magnetotelluric, active and passive seismic surveys and gas emissions measurements. The experiment was aimed to study the variations in the elastic properties of the medium, through repeated observations over the time. In the case of the seismic acquisition, the basic idea is that if we repeat the experiments in the same source-receiver configuration the variations in the recorded waveforms are directly imputable to variations happened in the medium. There are several reasons to choose the Solfatara as investigation target, but it was principally selected because since the 2000 a slow but accelerating uplift was observed (Figure 3-5). This was also accompanied with an increasing gas emission having critical variations in the chemical composition. Therefore, more accurate analysis are required, using the modern techniques and thus bringing new information. Furthermore, the Solfatara is a strongly heterogeneous medium where standard imaging techniques are not applicable or the quality of the retrieved models can result critically lowered. Therefore this is a suitable place where refine existing techniques or apply new methodologies which make use of the information carried by the backscattered wave field and not from the ballistic waves.

One of the most appreciable effects at Solfatara is the variation in fumarolic emissions at the scale of one day and one year. The activity is related to the interaction between the rainwater and the heat coming from depth. The mechanical propagation properties can vary significantly if the water content of the medium changes, therefore repeating the experiment with different weather conditions could produce different signatures in the acquired signals. The experiment is composed of three acquisition campaigns, spread over a period of two years. The initial phase was held from the 23rd to the 26th September 2013; this initial step was conceived in order to give preliminary results and to understand the feasibility, the repeatability of the experiment and the spatial resolution of the resulting velocity model. If we had not selected an adequate source-receiver spacing, we could be not able to resolve the different structures

in the investigated area, but we could obtain too big wavelengths, which smoothen the medium and cover the spatial heterogeneities. In this phase of the experiment, a regular grid of 240 vertical mono-component sensors was displaced on an area of $115 \times 90 \text{ m}^2$ in front of the Fangaia. They were arranged in 10 lines spaced by 10 m each other (cross-line distance) and in each line, there were 24 receivers spaced by 5 m each other (in-line direction). In each line, the geophones were linked to the acquisition system Geode G24, having a dynamic range of 24 bits and a full-scale voltage of 2.8 V. We have the possibility to set the sampling frequency: for our purpose taking into account the spectrum of the source, we set it to 1 kHz. As the active source, the Vibroseis truck was used (Figure 4-1). This device is equipped with a metal plate that can be lowered on the soil, sustaining the weight of the truck, and can oscillate. We opted for such kind of source because the oscillation is completely controlled in duration and frequency contents. In our case the oscillation lasted for 15 s and as a source function a linear sweep was used.



Figure 4-1: The Vibroseis showed in the figure is of the same kind we used during the RICEN experiment.

The linear sweep is a vibration where the frequency content linearly increases with the time; in our case it was set to start at a frequency of 5 Hz and to stop at 125 Hz. About 100 energizations were performed following the distribution of an equally spaced grid by 10 m along the two directions; the source grid was staggered and it was internal with respect to the receivers grid (Figure 4-2);

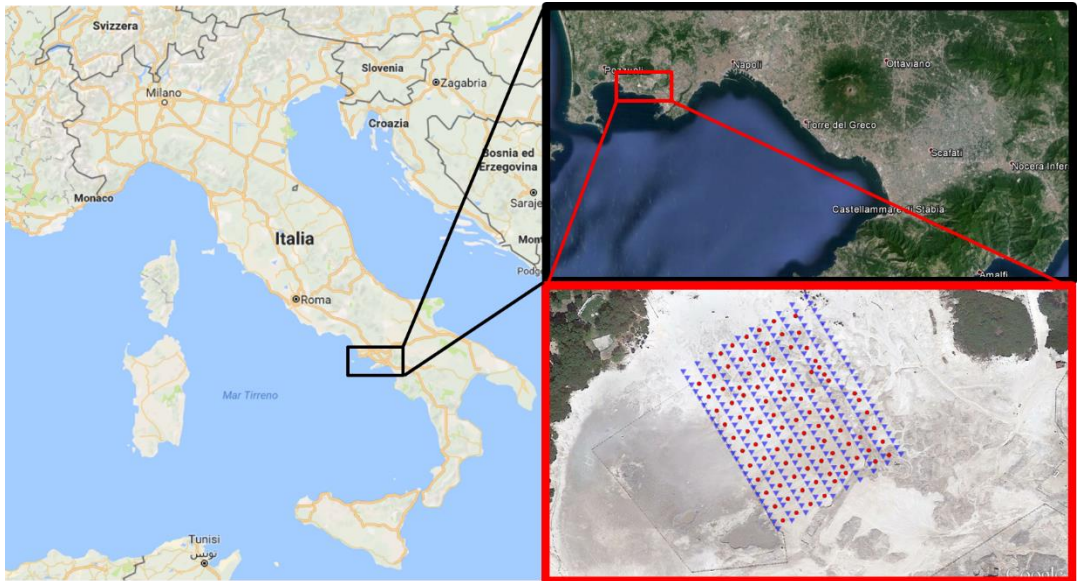


Figure 4-2: From the recursive zooms, it is possible to define the location in the space of the Solfatara. In the figure with red edges, it is displayed the source-receiver configuration of the RICEN experiment, with red circles we represent the shots positions and with blue triangle the stations positions.

We tried to follow the described configuration as closely as possible but in some cases we had logistic problems. In the case of the receivers, the major problem was related to the presence of some hot spots. They made impossible to install stations in the specific points due to the high temperature or the gas emission that could damage the instrument in a short time. Anyway, this event occurred few times, so the experimental receiver grid was very similar to the designed one. the source grid was not as regular as the receiver one, the drawbacks were related to the irregular Solfatara floor, which made impossible for the Vibroseis to reach some areas. Therefore there are some differences between the real and the

designed grids and in some small regions we have a lower source coverage. In each vibration point, three energizations were realized in order to increase the signal to noise ratio. The vibrating plate is lowered and oscillates; at the end of the oscillation the plate stays on the soil and after a break time it performs a new vibration. Since the source function is controlled by a PC, it is ever the same, and the medium in such a short time has not changed, therefore the same signal is expected. Indeed, seismograms related to the same excitation point are automatically stacked. The acquisition system is completely radio-controlled, to ensure correct timing for all of the sensors. When the Vibroseis starts to energize the soil, at the same time a radio signal is sent to the stations, in this way all of them start to record exactly at the same moment. The differences in the arrival times, of the considered seismic phases among stations, were due to the propagation of the seismic waves across the receiver network. At the same time, to record the seismic noise, 54 three-component stations were displaced in the whole area of the Solfatara crater and they acquired for a total duration of about 16 h.

The second and the third phases of the experiment were realized respectively from the 19th to the 23rd May 2014 and from the 10th to the 14th November 2014. In these two cases, the source-receiver grid was positioned in the same points of the first phase of the experiment, and the noise acquisition was performed using 50 DSS-CUBE stations. The stations for the noise acquisition had a different layout in each of the three acquisition campaigns and for the second and third surveys, they continuously recorded for the whole duration of the experiment also during the night, when a lower anthropic noise is expected. Moreover, in the last two campaigns also two additional one-dimensional arrays were realized. They were 400 m long, the stations were spaced by 2 m and the Vibroseis shots by 4 m. The arrays were not repeated along the same direction: in the second phase, the array was displaced in the NE-SW direction, whereas in the final experiment it was displaced orthogonally to the first one, along the NW-SE direction. Globally the experiment produced a huge amount of data, more than 75000 waveforms were collected during the whole experiment. They have been, checked, processed and stored on a ftp server under the University of Napoli "Federico II" responsibility.

4.1 Data Processing

In general, in all the modern digital instruments, we do not directly measure the physical quantity of interest, but we have a measure in voltage. By means of conversion factors we can obtain the appropriate units, these factors are typical of the used instruments and the construction company furnishes them. Moreover, it is crucial to know the behavior of the instruments at different frequencies, because we could have amplification or damping in the signal that are not related to the medium. The characterization of the instrument is summarized in the response curve; to have the response of the medium to a given solicitation, the acquired signals have to be corrected for the response curve. Such curve is given by the factory that built the device, and in our case, we have not a single curve for each instrument but an average curve including all of them. For the geophones GS-11D 4.5 Hz, the response curve is flat above the cut-off corner frequency at 4.5 Hz. Since the source has a cut-off at 5 Hz, therefore in our case this correction is just a constant.

The recorded signal at a given position \mathbf{x} is the convolution of the source function, $S(\xi, t)$ acting at the position ξ , and the Green's function of the medium $G(\mathbf{x}, t; \xi)$:

$$v(\mathbf{x}, t) = S(\mathbf{x}, t) * G(\mathbf{x}, t; \xi) \quad (4.1)$$

we used the symbol $*$ to refer to the convolution product. Since we are interested in the properties of the medium, we need to recover the Green's function. We should then remove the source function from the acquired signal, either by deconvolving the source function or by cross-correlating the signal for its source function and there are advantages and disadvantages for both techniques. This problem has been widely studied in literature, the Vibroseis is used in the industry oil and many efforts have been made in order to preserve the high frequency content in the data, since the higher the frequency content the better the resolution.

The deconvolution is the most intuitive procedure to remove the source function, because the equation (4.1) thanks to the deconvolution theorem in the frequency domain is:

$$v(\mathbf{x}, \omega) = G(\mathbf{x}, \omega; \xi)S(\xi, \omega) \quad (4.2)$$

and therefore, the Green's function can be retrieved through:

$$G(\mathbf{x}, \omega; \xi) = \frac{v(\mathbf{x}, \omega)}{S(\xi, \omega)} \quad (4.3)$$

This procedure is correct from a theoretical point of view and it is appropriate if we consider a noise free acquisition, since in the spectrum of the recorded signal we find just the frequency content produced by the source, therefore no division by 0 is conceivable. If we take into account the seismic noise, its contribution is additive, therefore the recovered Green's function is:

$$G(\mathbf{x}, \omega; \xi) = \frac{v(\mathbf{x}, \omega)}{S(\xi, \omega)} + \frac{N(\mathbf{x}, \omega)}{S(\xi, \omega)} \quad (4.4)$$

In such a case the noise is amplified and other processing is required in order to reduce it. Basically, this procedure can be performed following different ways: before the division, by means of a bandpass filter we have to remove the frequencies that are not excited by the source or alternatively, we have to add a small noise percentage to the sweep function or we can perform the water level regularization. The suggested methods are aimed to avoid the division by 0, removing in one case or adding some artificially frequencies in the other ones.

The second method to remove the source function is the cross-correlation of the acquired signal with its associate source:

$$v(\mathbf{x}, t) \otimes S(\xi, t) = G(\mathbf{x}, t; \xi) * S(\xi, t) \otimes S(\xi, t) = G(\mathbf{x}, t; \xi) * K(\xi, t) \quad (4.5)$$

The symbol \otimes denotes the cross-correlation and the function $K(\xi, t)$ (Figure 4-3) is the autocorrelation of the source function, which is called the Klauder wavelet (Sheriff, 1990).

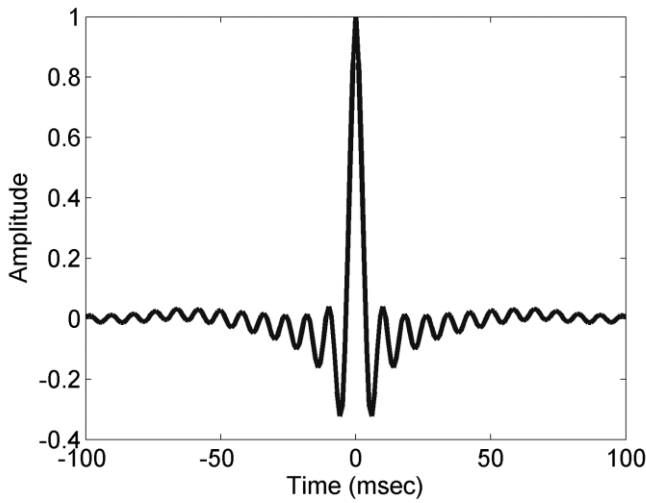


Figure 4-3: Autocorrelation of a sweep function by itself: the Klauder wavelet.

The basic idea of this approach is that the cross-correlation is a measure of similarity between two functions, where one of the two ones is shifted in time; in the case of the autocorrelation the maximum is reached at zero shift time. Therefore, looking at the (4.5), the cross-correlation with the sweep function is equal to the convolution of the Green's function with the Klauder wavelet, which acts as a filter because only the frequencies in the source spectrum are found in the final function, the other ones are rejected. As we did before, if we consider the problem adding some noise, we have:

$$v(\mathbf{x}, t) \otimes S(\xi, t) = G(\mathbf{x}, t; \xi) * K(\xi, t) + N(\mathbf{x}, t) \otimes S(\xi, t) \quad (4.6)$$

The noise is present in the final waveform but it is not amplified and it is automatically band pass filtered (Brittle, et al., 2001). The lower and upper corner frequencies are those set from the range of the sweep function (Figure 4-4).

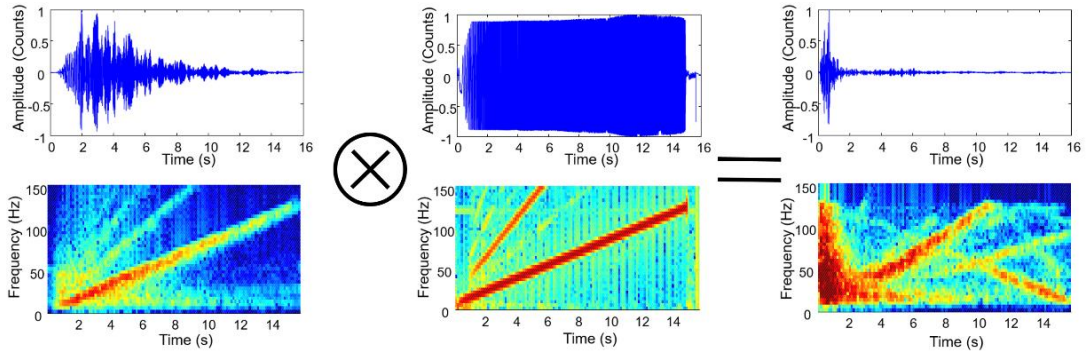


Figure 4-4: In this figure the processing applied to the data is summarized. On the left, there are the acquired traces, in the middle, the sweep function and on the right, the results of the processing. For each trace, the related spectrogram is also shown.

The Klauder wavelet is a zero-phase filter, while the Earth behaves as low pass filter, that is, a minimum phase filter which preserves the causality in the data. These two filters result together combined in a mixed-phase wavelet. Therefore we need to remove the zero-phase filter by means of a minimum phase equivalent to the Klauder wavelet (Gibson, et al., 1984). The sweep function is directly recorded on the vibrating plate, therefore looking at this seismogram it is possible to evidence if coupling problems between the soil and the platform occurred or other kinds of drawbacks arose. It is relatively simple to discover problems in the sweep function because they show anomalous amplitudes or interruption in the temporal sequence (Figure 4-5); such kind of sweep functions cannot be employed for the cross-correlation procedure because they would pollute the propagation function. This problem is easily overcome, considering that the function injected in the soil is the same at each shot and in each position, therefore we can substitute the wrong one with a sweep function obtained averaging the right ones.

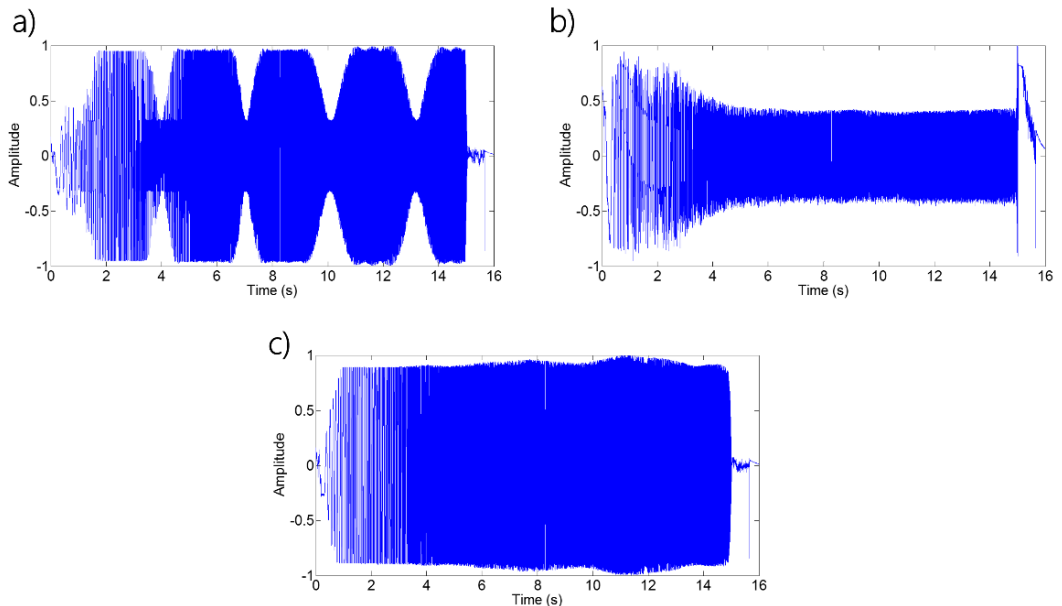


Figure 4-5: Three sweep functions, the figure a) and b) are relative to functions which presents some problems due to the coupling with the soil or due to the sensor located on the plate. In the figure c) a regular sweep function is plotted.

With the cross-correlation operation, we obtain a filtered Green's function but the Klauder wavelet is an acausal filter. To preserve the causality in the data the introduction of a minimum phase filter is required. We also checked if there were relevant differences before and after the minimum phase filter. Data were superimposed in the first P-wave arrival and in the others more energetic seismic phases, but they showed a satisfactory matching. Finally, each trace is normalized by the maximum of its absolute value. We can adopt this kind of normalization because in the following analysis we will be interested in the phase coherency of the signal rather than in their absolute amplitude. This ensemble of procedures has been applied at each trace of the final dataset, for the data of the grid and also for those ones of the arrays.

4.2 S-wave model for the Solfatara

To recover information about the medium composition in terms of velocity of the surface waves, we can use the simple assumption that waves related to lower frequencies can penetrate deeper in the medium, whereas higher frequencies are associated to waves which have travelled in shallower layers. Moreover, since both receivers and sources are located at the surface and the directions of the source and of the records are both vertical, signals are dominated by surface waves, therefore it is more suitable to use an approach that exploits the characteristics of the Rayleigh waves. To measure the dispersion curves for the phase and the group velocity of the Rayleigh waves, we need to adopt a method, which can take advantage from the large number of the recorded signals. The idea is to use a method similar to those of the section 2.5.4, according to which we stack the signals to increase the signal to noise ratio and to suppress the small-scale variability that we are not able to resolve in our velocity models. In this way, we also observe an enhancement in the coherence of the signals that allows us to follow emergent phases for longer distance. Since the stack can be performed over couples of source and receivers located at the same distance, such strategy works for horizontally layered media and for isotropic sources, since travelling waves meet the same interfaces along the path and therefore the deterministic part of the acquired signals is the same, whereas the random incoherent one will be reduced. The Vibroseis is an isotropic source also compared to the size of the investigated area, but the 1D approximation of the medium deserves a deeper discussion.

In this approximation, we can sum all traces that have the same offset regardless of their locations in the space. The Solfatara, however, is not a one-dimensional medium since we observe a great variability in the arrival times, also when considering the seismic section filtered in the lowest frequency band used in this study (7-10 Hz), where most of the heterogeneities appear smoothed. Nevertheless, the coherence at short distance is verified (Figures 4-6 and 4-7). In general in the figures, we can notice the dispersivity and the heterogeneity of the medium, indeed, the wave packet is wider and wider when the source-receiver distance is increasing. Moreover, we are able to recognize the arrivals of the P

and the more energetic Rayleigh waves, but it is also clear that increasing the frequency band there are large variations in the arrival times even for the closest stations. To have a good estimator representative of the average signal, the sum over a great number of signals is required; at the same time, if signals come from different regions of the investigated area, they appear too different and they will interfere destructively. We have to find a compromise between the number of traces to be stacked and the area which can be assumed as a one-dimensional structure.

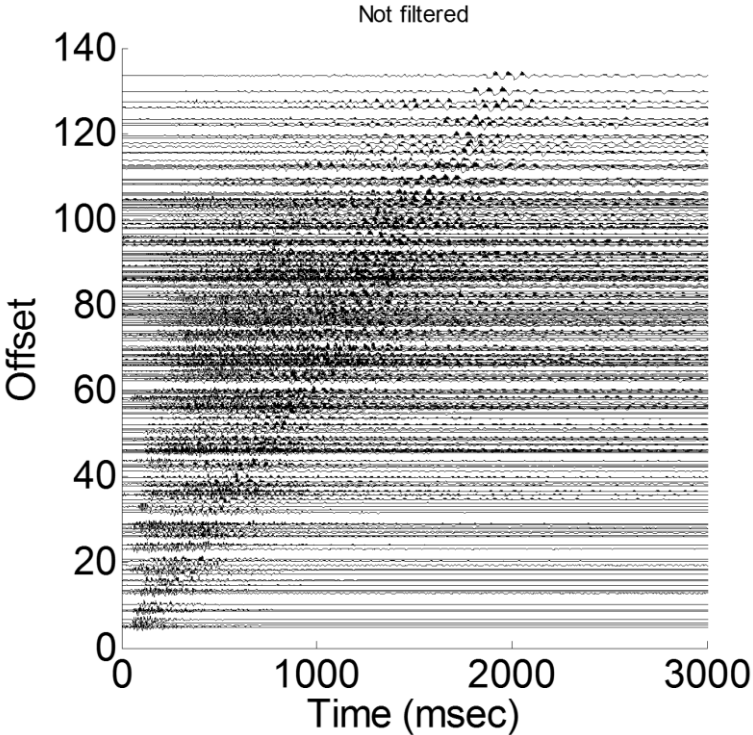


Figure 4-6: Seismic section of one shot acquired at all the stations of the network. In this figure traces are not filtered. It is evident the dispersion of the seismic waves going farther and farther from the source.

Moreover, when working with high frequency we face with smaller and smaller wavelengths and therefore they are more sensitive to small, local scale anomalies embedded in the medium. We then expect that if the coherency holds for high

frequencies, it will also hold for low frequencies (Figure 4-7 and 4-9). To evaluate the minimum grid size, for which the 1D approximation applies, we did several attempts starting with subgrids sized from 20×20 m² up to 90×90 m². The last choice was obliged by the size of the whole grid. Ideally we would like to stack traces located at the same offset, but this is not possible because source and receivers are organized to form a rectangle, therefore, we divided the distance in smaller intervals, bins, and we computed the mean among traces falling in the same bin.

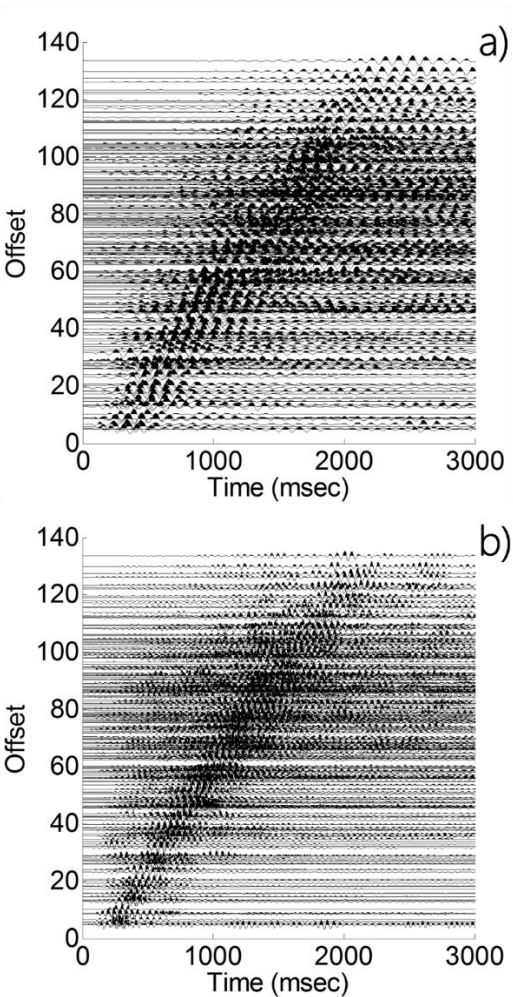


Figure 4-7: The same seismic section as in Figure 4-6 but filtered in the lowest frequency band (7-10 Hz) on the top (a) and the highest frequency band (17.7-25.3 Hz) on the bottom (b). When

increasing the frequency band, the medium appears more heterogeneous determining widely dispersed traces and different arrival times for contiguous stations.

Also the dimension of the bin is important, because depending on the number of traces falling within the same bin: the smaller the bin the smaller the number of the traces in the stack but the more robust the average. Finally, we decide to select subgrids of $40 \times 40 \text{ m}^2$ where we obtain a coherent signal for source-receiver distances up to 20 m (Figure 4-9), and a binning of 1 m that allows to have more than 10 traces for most of the bins (Figure 4-8).

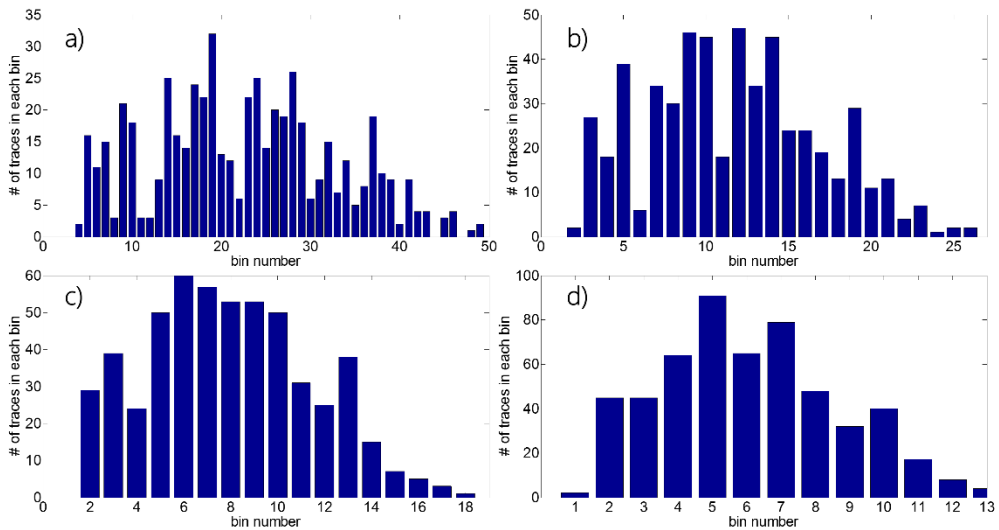


Figure 4-8: Number of traces falling in each bin as a function of the bin dimension for 1 m (a), 2 m (b), 3 m (c) and 4 m (d). When increasing the bin dimension, more traces fall in the same bin producing destructive interference.

Since the size of the subgrids is smaller than the whole grid, to investigate the entire medium covered by the stations, we considered 96 overlapping subgrids. The grids were obtained by shifting of 5 m the subgrid in the in-line direction and 10 m in the cross-line direction.

4.2.1 Phase and Group velocity measurement

The phase and group velocities were then measured in each subgrid as a function of the frequency. After selecting a subgrid, we collect the data acquired at all the stations and generated by sources both belonging to the considered subgrid. Given the subgrid dimension, we have at maximum 45 receivers and 20 shots within this subgrid and therefore, we dealt with 900 signals at maximum. We filtered the data and gathered the traces according their bin distance. The frequency bands were selected following the criterion that the ratio between the width of the band and the central frequency is constant. Since we lose any coherent phase in the binned seismic section beyond 25 Hz, we selected 14 overlapping frequency bands, which central frequencies ranging from 8.5 Hz up to 21.5 Hz (Figure 4-9).

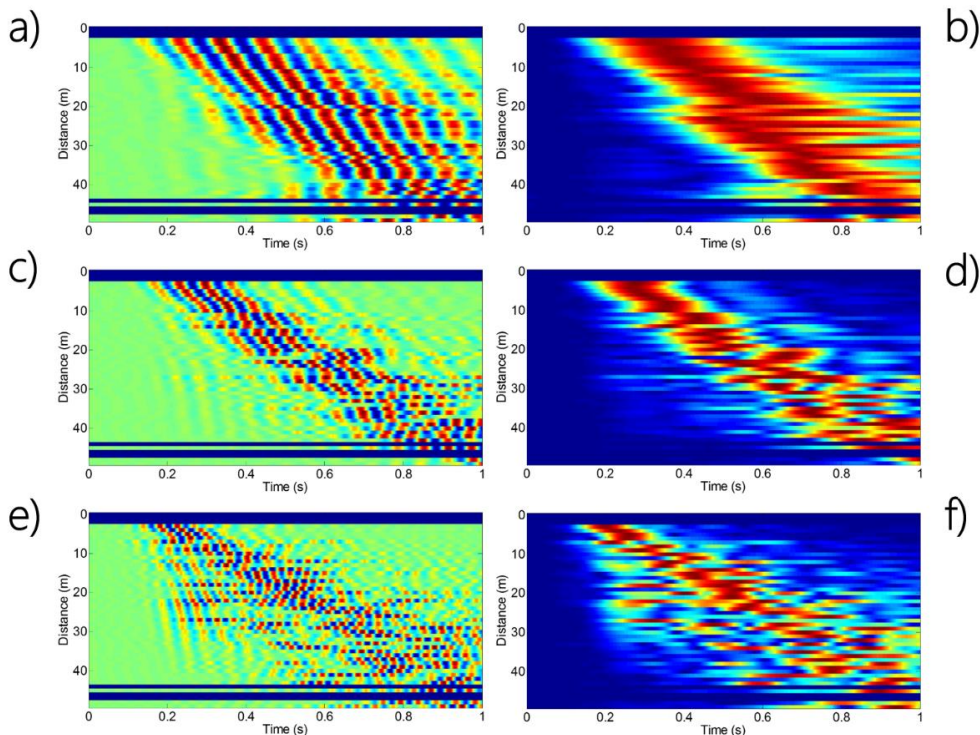


Figure 4-9: Seismic sections for the phase (a, c, e) and group velocity (b, d, f) measurements, in three frequency bands. Starting from the top where lowest band is considered, it is clear how it is more and more difficult to follow the coherent profile of the surface waves when increasing the frequency.

The phase velocity was estimated along the seismic section as the speed providing the best alignment of the traces along the section. To find this speed we tested velocity values covering the interval 35-300 m/s with a step of 5 m/s. For each velocity value we shifted the traces along the seismic section for a time given by the ratio between the source-receiver distance and the test velocity, and we stacked all the traces (Figure 4-10). In order to smooth the stack function we performed the envelope of the stack, and we select the maximum of the stack function as representative of the quality of the stack for that test velocity. We repeated this processing for all the velocities in the considered interval, to build up a stack-quality function of the test velocity (Figure 4-10). Since we apply a filter in a narrow frequency band, the traces present a monochromatic shape: because of the destructive interference, the curve of the maxima of the stack as a function of the velocity presents a peak and decreases to very small values far from it. We then assumed the phase velocity as the velocity value at which this quality function has its maximum.

For the estimation of the group velocity, that represent the speed of the propagating wave packet, we performed the envelope of the signals before the binning procedure. The related seismic section is plotted in Figure 4-11. As before, we searched for the group velocity as the speed at which we get the best alignment of the enveloped seismic section. A grid search was performed in a lower velocity range with respect the previous case, being the range 20-210 m/s with step of 5 m/s; this because the group velocity is generally smaller than the phase velocity. For each tested value, we aligned the traces, we computed the stack on the move-out section, and we took the maximum of the stack function (Figure 4-11). We collected all the maxima as a function of the tested velocity and finally we assumed the group velocity as the absolute maximum of this quality function. In this case, when we performed the envelope of the signals we obtained a positive function. Therefore in the binning procedure and in the stack function after the realignment, we do not observe destructive interference. Nevertheless, when signals are not in phase their stack will present a smaller value with respect to the effective group velocity. This is reflected in the quality function of the stack,

that has not a definite peak but it often exhibits a plateau region around the effective group velocity of the considered subgrid (Figure 4-11).

This analysis is repeated in each subgrid for different frequency bands, in order to compute the space distribution and variability of the dispersion curves for the phase and the group velocities (Figure 4-12). The phase velocity shows a monotonic decreasing and it is always larger than the group velocity, which is almost constant, with the presence of few spatially localized maxima and minima. The difference in the phase and group velocity values is indicative of a layered medium with increasing velocity with the depth, as shown in the relation (2.78). We expect that the determination of the phase velocity is better constrained with respect to the group velocity, but we also found cases where its determination was not simple. The waveforms quality degrades as the central frequency of the band increases, therefore bimodal or multimodal stack functions, with comparable amplitudes of the maxima, occur in some subgrids (Figure 4-13). Since, we adopted overlapping subgrids, when we moved from one grid to another one we changed a small number of stations and sources, therefore we did not expect a great difference in the velocity values among contiguous subgrids. The same applies for increasing frequency band, because also the selected bands are overlapping. In such cases, we add a smoothness condition on the velocity as an additional constraint, which guarantees smoother velocity variations in space and with frequency. In figure 4-14 the phase and group velocity maps are represented. The maps are not associated to specific depths but they are put in columns simply considering that lower frequencies are related to longer wavelengths and as a consequence, to deeper layers with respect to the higher frequencies.

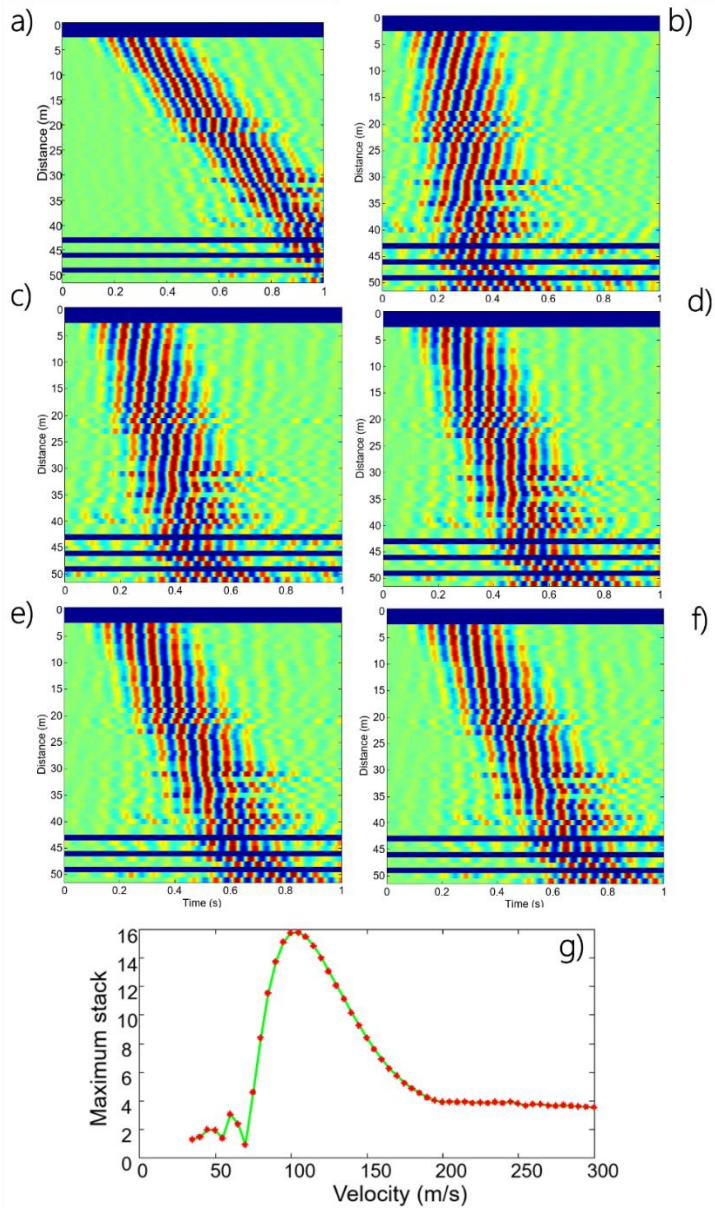


Figure 4-10: Processing used for the phase velocity estimation. In panel a) we represent the filtered seismic section, whereas in the following ones, we have the same section but shifted in time in agreement with several test velocities (70 m/s, 85 m/s, 105 m/s, 125 m/s and 140 m/s). The estimated value of the phase velocity is 105 m/s, in correspondence of which we have the best realignment of the section. Finally, in panel g) the maximum of the stack function is represented as a function of the test velocity.

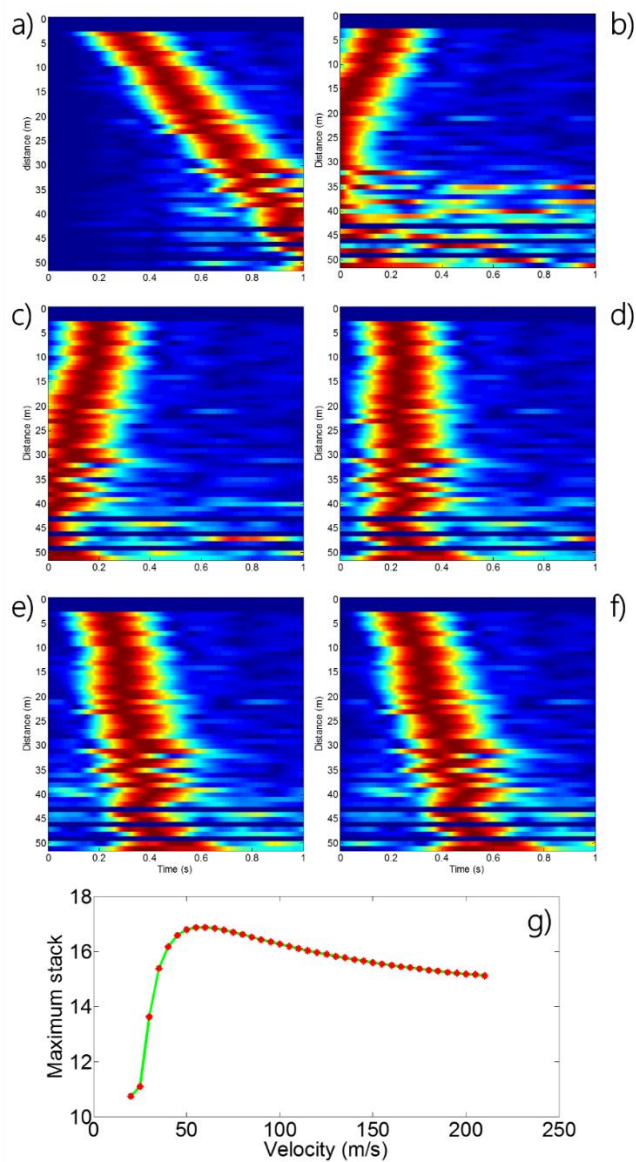


Figure 4-11: Processing used for the group velocity estimation. In panel a) we represent the filtered seismic section, whereas in the following ones, we have the same section but shifted in time in agreement with several test velocities (50 m/s, 60 m/s, 75 m/s, 90 m/s and 105 m/s). The estimated value of the phase velocity is 75 m/s, in correspondence of which we have the best realignment of the section. Finally, in panel g) the maximum of the stack function is represented as a function of the test velocity.

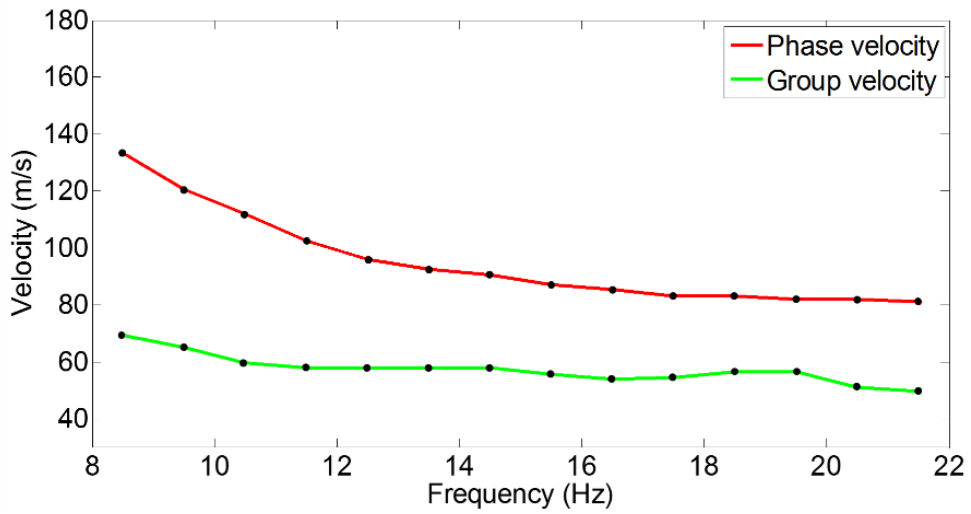


Figure 4-12: Dispersion curves for a specific subgrid. The phase velocity is monotonically decreasing, whereas the group velocity curve is always below the phase velocity curve and it is almost constant.

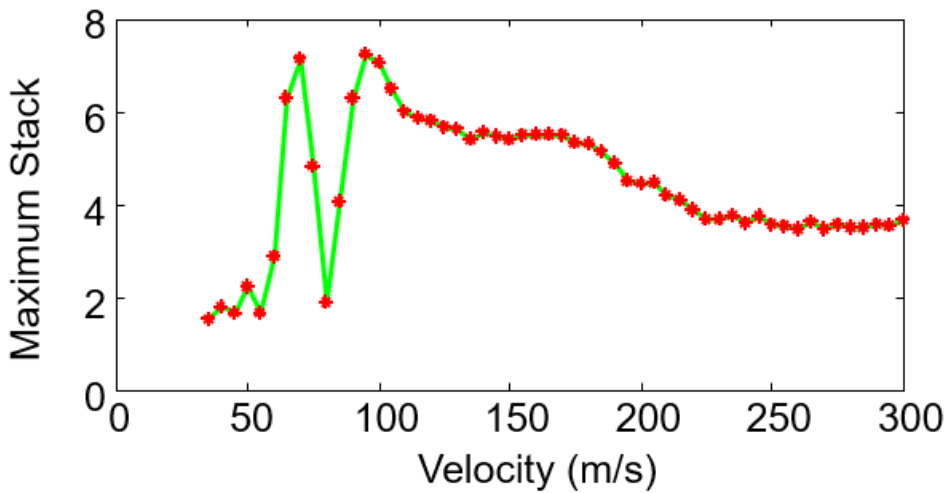


Figure 4-13: Increasing the frequency band, the signals are more sensitive to the heterogeneities of the medium and therefore the coherence of the signals is reduced. Such reduction determines a reduction in the stack coherence and, in turns, it may produce equivalent alignments of the seismic section for different values of the velocity.

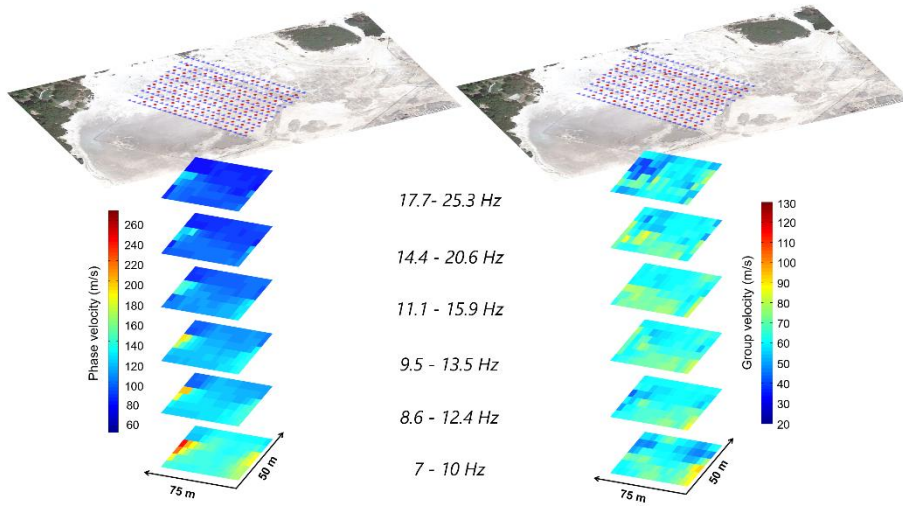


Figure 4-14: Areal maps of the phase on the left and group velocities on the right. The two anomalies in the phase velocity maps are evident at the boundaries of the investigated area. We can also recognize the separation of the region in a faster domain and a slower domain.

Looking at the phase velocity maps, the most significant features are the two anomalies at the boundaries of the investigated region. The one located at NW also corresponds to the highest measured phase velocity value and it is clearly recognizable in the whole frequency range, even if its presence is more important in depth. The SE anomaly has almost the same shape but with smaller velocity values. It is visible at lower frequency and it seems to disappear beyond 17.5 Hz. The group velocity maps are more constant but they have a maximum at low frequency that seems to correspond to the SE anomaly retrieved in the phase velocity maps. In general, from the comparison of the figures we can affirm that the medium presents a separation in two areas, with the NE region faster than the SW one. This situation is more appreciable at higher frequencies. In the same area, in the past, another experiment was performed using different experimental approach for the recovering of the phase velocity dispersion curves (Petrosino, et al., 2012) and the retrieved velocities well superimpose on average to our values. The comparison is possible in a limited overlapping frequency range 7-12 Hz, since they used more distant stations and noise measurements, which investigate lower frequencies, with a lesser capability to resolve small-scale anomalies.

4.2.2 Inversion of the dispersion curves

We can use the information contained in the phase and group velocities and in their behavior at different frequencies, to determine a velocity model of the investigated area. This purpose is achievable jointly inverting the dispersion curves. Specifically, we computed a one-dimensional model in each subgrid, and we interpolated the 96 one-dimensional models to obtain a three dimensional model of the area. For the retrieving of the one-dimension model, we used the Geopsy software (Wathelet, et al., 2004). The software searches for the best horizontally layered P-wave and S-wave models that fit the dispersion curves using the Neighborhood algorithm (Sambridge, 1999). The code requires in input the number of layers, the range of variability for the P-wave and S-wave speeds and the density of the medium. Starting from these parameters the algorithm subdivides the parameter space in Voronoi's cells, where each cell is characterized by a set of parameters. The software use such parameters to construct a one-dimensional layered medium and from this model, it computes the dispersion curves. The theoretical dispersion curves are compared with the real ones,

through a misfit function. The misfit is given by $\sqrt{\sum_{i=0}^{n_F} \frac{(x_{di} - x_{ci})^2}{\sigma_i^2 n_F}}$ where x_{di} is the

measured velocity at the frequency f_i , x_{ci} is the computed velocity at the frequency f_i , σ_i is the uncertainty on the measurement of the considered frequency and n_F is the number of frequency samples we have in our problem. At this point to optimize the search process to find the best-fit solution, the algorithm refines the parameter space only into the cells where the misfit is smaller, and the procedure continues until either the number of iterations is reached or the misfit function is reduced below a fixed threshold (Figure 4-15).

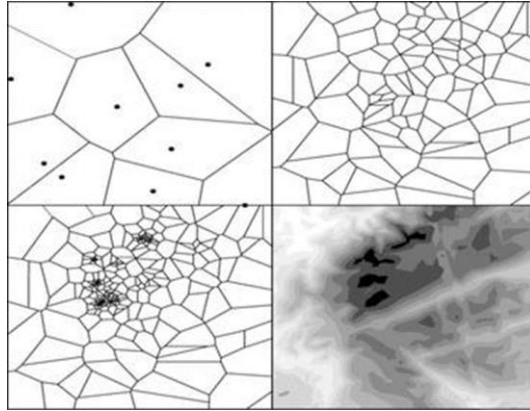


Figure 4-15: Schematic representation of the parameter space, as subdivided in Voronoi's cells and the further refining in that cells where a lower misfit function is computed.

In our case the parameters are initially set as follows: the density to 1500 kg/m^3 , the S-wave velocity interval to 50-1250 m/s, the P-wave interval is linked to the S one through the Poisson's ratio, which is allowed to range from 0.2 up to 0.5. They were chosen in agreement with literature values (Letort et al., 2012). The setting of the number of layers deserves more attention. We performed several tests to correctly set the number of layers and the maximum penetration depth of the Rayleigh waves. We started from a two-layered medium up to consider a four-layered model. This latter resulted in being the best choice, because the misfit between the simulated and expected dispersion curves significantly reduces up to one order of magnitude, whereas there is no further significant reduction when the number of layers is increased beyond this value (Figure 4-16). Of course, a further layer improves the misfit since it would be able to fit better and better the slope breaks that occur in some dispersion curves (Figure 4-17). Nevertheless, an additional layer does not justify such a small gain in the misfit function.

The solutions are insensitive to the P-wave model (Figure 4-16). All the models around the best-fit solution provide a large range of P wave velocities. The S-wave models are more constrained; therefore, the exploration was further limited to the to the S-wave velocity values and to the identification of the interfaces. Since our goal is to determine a single velocity profile for each subgrid, we need

of a criterion to choose which is the model that can be assumed as the best one. We have indeed many models with misfit comparable to the lowest one.

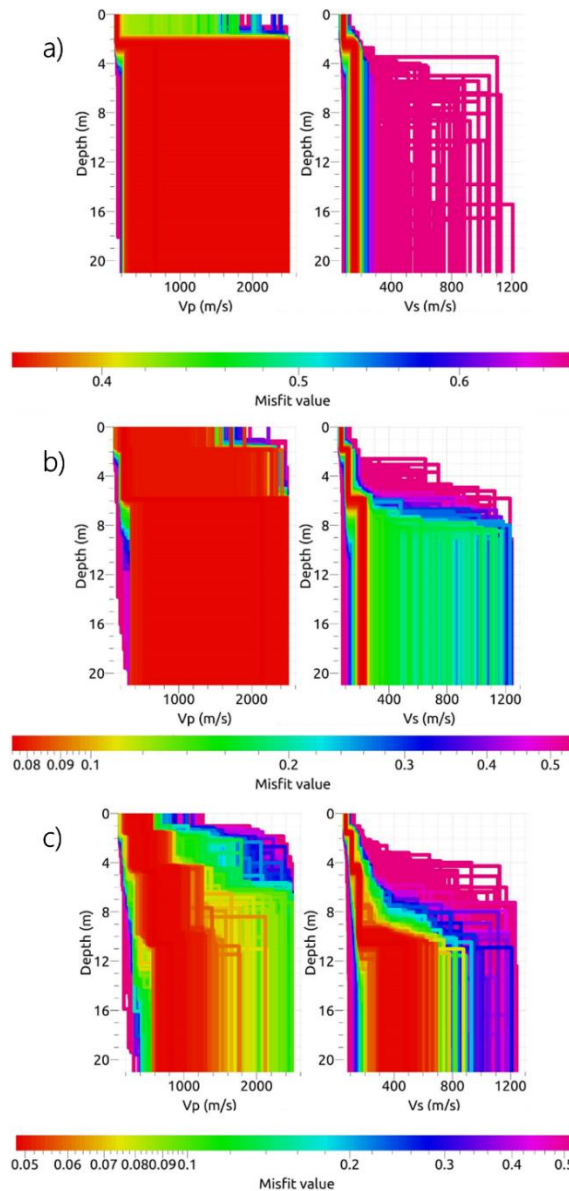


Figure 4-16: Recovered P- (on the left) and S-wave (on the right) velocity models when increasing the number of layers. The reduction of the misfit function is large moving from 2 (a) to 3 (b) layers, and it is smaller but still relevant from 3 to 4 (c) layers. Different colors correspond to different misfit value.

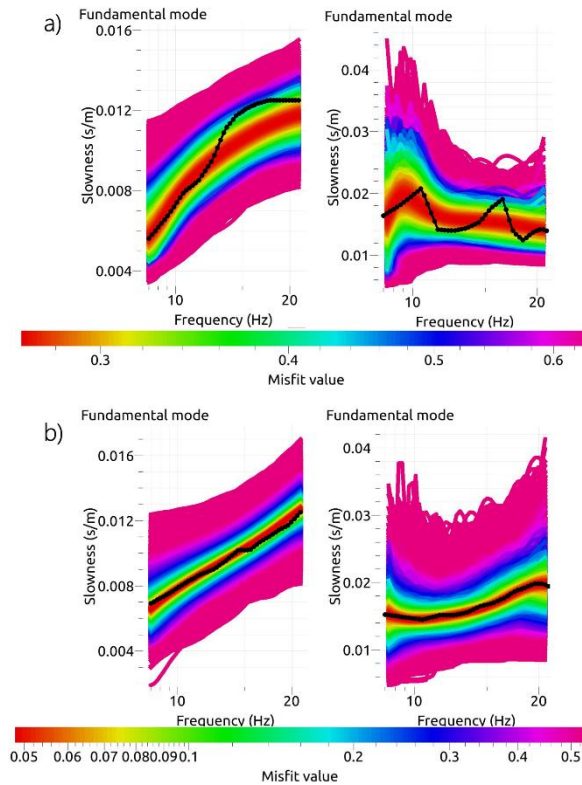


Figure 4-17: Comparison between the measured dispersion curves for the phase (on the left) and the group velocities (on the right), represented with the solid black lines and the set of curves recovered by the software Geopsy. Such curves have a different behavior when compared to those shown in figure 4-12 because here the slowness is the quantity represented in the plots.

Therefore, we did not select the best-fit model as the final model, but we extracted an ensemble of profiles having a misfit difference smaller than the 15% with respect to the minimum misfit. We assumed as the final model, which is representative of the one-dimensional medium, the average among the selected models. It is worth to note that the average profile is a smoother solution of the problem because, referring to the figure 4-16, all the models in the average are close to each other and they differ either by the velocity values or by the depth of the interfaces. On the contrary, if the selected family solutions had been spread in the parameter space, resulting in models with different patterns having close

misfit values, the average model would not have been a good estimator of the 1D model because the average would have been a model having different characteristics from the initial ones and possibly falling in an area where models with high misfit were founded.

As a consequence, the average models are no longer layered, but they present an almost continuous variation of the velocity with depth. Finally, combining the 96 velocity profiles of each subgrid we obtained the three-dimensional model, in term of S-wave velocity, of the medium by interpolation. The figure 4-18 is a slice representation of the S-wave model at fixed depth; in the same figure, we compare the resistivity model.

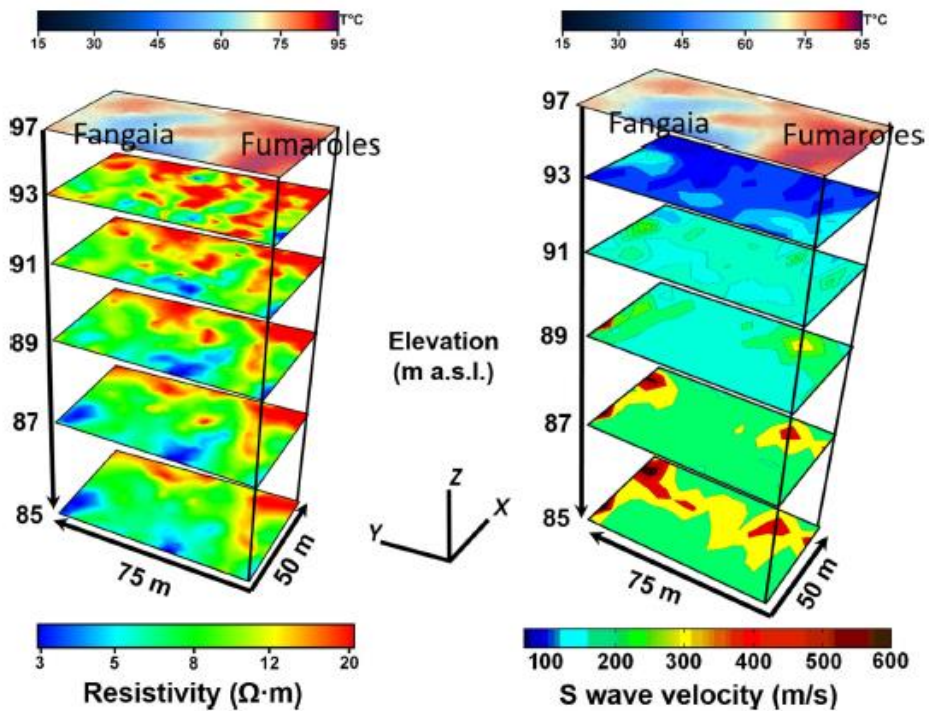


Figure 4-18: Resistivity model (on the left) and the S-wave model (on the right) obtained with data acquired during the same experiment. On the top of each model, there is the thermal map. The shallowest features can be associated with thermal ones, whereas results at depth show the presence of a water-saturated medium.

In general in all the one-dimensional profiles we observe a very shallow layer, whose depth is always well constrained and it reaches a maximum value of 4 m. A second layer is more variable and it has depths ranging between 4 m and 8 m. Finally, the depth of the last interface and the velocity below it are not well constrained. This layer could be the interface between the unconsolidated shallow deposits and the aquifer beneath the Solfatara that emerges in the Fangaia. This indetermination could be also due to the very low velocity of seismic waves and to the considered range of frequencies, which limit the penetration of waves. The comparison of our results with other seismic acquisitions, (Petrosino et al., 2012), even if those are based on a larger space scale, lower frequency range and consequently larger penetration depth, are in agreement with ours. They also recover a shallower interface at about 5 m, which could correspond on average to the variation of S-wave velocity in the first two layers of our model. The uncertainty is given by the larger wavelengths that smoothen the medium, whereas we are able to distinguish also smaller shallower interfaces.

We retrieved a relationship between the two NW and SE anomalies observed in the phase-velocity maps, and the region where we recovered higher velocity values. The NW anomaly can be associated to the spot that emerges at 4 m, and becomes more evident in terms of a velocity contrast at greater depths, whereas the SE anomaly appears at 8 m and remains unchanged at higher depths. One of the most important features which was recovered also in other works, and was also clear in the phase and group velocity maps, is the division of the investigated domain in two subareas: the SW domain is slower at all depths, as compared to the NE domain. This can be associated with a more water saturated medium, since the slower side is close to the Fangaia, where the water outcrops. . The geoelectric model obtained for the same area corroborates such an interpretation. This result comes from an acquisition performed during the RICEN experiment by means of direct current resistivity profiles, with sixteen, 115 m long profiles with NW–SE orientation and twenty-four, 75 m long orthogonal NE–SW profiles, all with 5 m spacing between the electrodes. The same Wenner–Schlumberger configuration was used for all of the profiles, and the three dimensional inversion was obtained using the algorithm detailed by Loke & Barker (Loke, et al., 1996) and implemented in the RES3DINV software (Loke, et

al., 2002). The normalized root mean square error of the resulting three-dimensional model was 7.5%, and the data quality allows for a high-resolution resistivity model down to 15 m depth. Also, acquisition of the soil temperature at 30 cm depth was performed at each electrode during the experiment. The geoelectric results are interesting for our purpose since they have good resolution in the discrimination of media that are richer or poorer in water. There is a correlation between the shallower slice and the temperature profile. High velocity values are linked to high temperature (here the temperature reaches 90-95 °C) where gas emissions are observed. Indeed, as interpreted by other authors the gas presence reduces the water saturation allowing an increase in the S-wave velocity. The slower areas are related to colder zones having temperature at about 50-60 °C, that are also rich in water content.

The influence of the water content or over pressured gas can be highlighted plotting the isosurfaces of velocity (100, 150, 200, 300 m/s) and on the same figure the isosurface of the resistivity at 8.5 $\Omega\cdot\text{m}$ (Figure 4-19). The resistivity surface shows a low level near the Fangaia, and at the same time the velocity surfaces deepen toward the Fangaia. For sake of completeness, the isosurfaces are obtained using the velocity values coming from the inversion with a spatial filter that smoothens the smallest velocity variations, and allows to be more focused on the general trend of the velocity gradient.

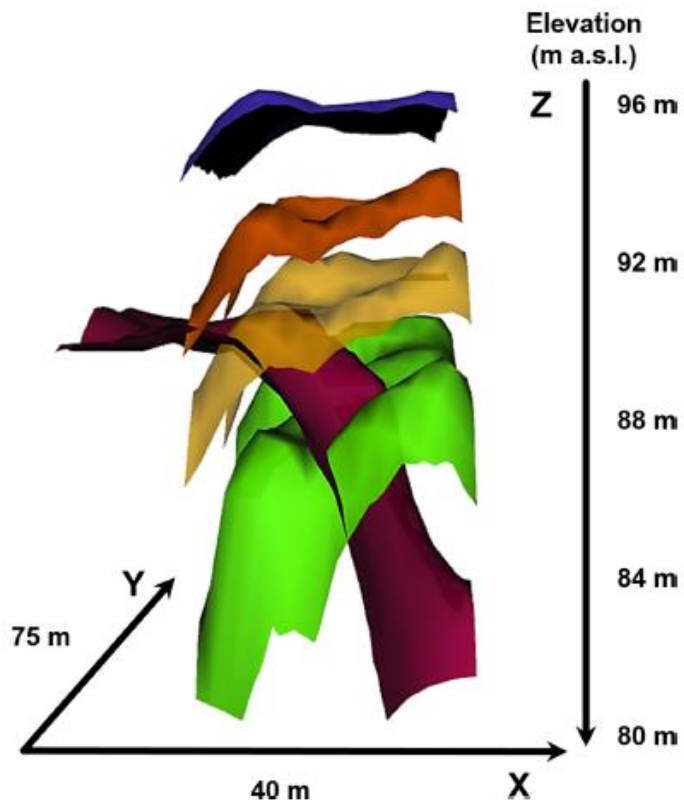


Figure 4-19: Isosurfaces of resistivity (magenta) and S-wave velocity (the other colors). The behavior of such surfaces show an another point of view about the duality of the investigated region. On the left, close to the Fangaia, there is more water, therefore lower shear velocities and resistivity are measured.

Below we present the paper deriving from this work as it has been published on the journal: Geophysical Journal International

A strongly heterogeneous hydrothermal area imaged by surface waves: the case of Solfatara, Campi Flegrei, Italy

Marcello Serra,¹ Gaetano Festa,¹ Philippe Roux,² Marceau Gresse,³
Jean Vandemeulebrouck³ and Aldo Zollo¹

¹*Dipartimento di Fisica, Università degli Studi di Napoli Federico II, Via Cinthia I-80126, Napoli, Italy. E-mail: serra@fisica.unina.it*

²*ISTerre, Université Grenoble Alpes Joseph Fourier, Rue de la Piscine 1381, F-38058, Grenoble, France*

³*ISTerre, Université Savoie Mont Blanc, Avenue du Lac d'Annecy, Batiment Belledonne 24-28, F-73370 Le Bourget-du-Lac, France*

Accepted 2016 March 29. Received 2016 March 21; in original form 2016 January 4

SUMMARY

We investigated the shallow structure of the Solfatara, a volcano within the Campi Flegrei caldera, southern Italy, using surface waves as a diagnostic tool. We analysed data collected during the RICEN campaign, where a 3-D active seismic experiment was performed on a dense regular grid of 90 m × 115 m using a Vibroseis as the seismic source. After removal of the source time function, we analysed the surface wave contribution to the Green's function. Here, a 1-D approximation can hold for subgrids of 40 m × 40 m. Moreover, we stacked all of the signals in the subgrid according to source–receiver distance bins, despite the absolute location of the source and the receiver, to reduce the small-scale variability in the data. We then analysed the resulting seismic sections in narrow frequency bands between 7 and 25 Hz. We obtained phase and group velocities from a grid search, and a cost function based on the spatial coherence of both the waveforms and their envelopes. We finally jointly inverted the dispersion curves of the phase and group velocities to retrieve a 1-D *S*-wave model local to the subgrid. Together, the models provided a 3-D description of the *S*-wave model in the area. We found that the maximum penetration depth is 15 m. In the first 4 m, we can associate the changes in the *S*-wave field to the temperature gradient, while at greater depths, the seismic images correlate with the resistivity maps, which indicate the water layer close to the Fangaia area and an abrupt variation moving towards the northeast.

Key words: Hydrothermal systems; Surface waves and free oscillations; Seismic tomography; Volcano seismology.

1 INTRODUCTION

This study is aimed at imaging the shallow structure of the Solfatara, one of the craters in the Campi Flegrei large volcanic caldera located in southern Italy, near the city of Naples. The volcanic structure of Campi Flegrei was mainly determined by two major historic eruptions: the Campanian Ignimbrite (39 kyr) and the Neapolitan Yellow Tuff (15 kyr), which created most of the present landscape of the region (Di Vito *et al.* 1999; Pappalardo & Mastrolorenzo 2012). After these two main events, dozens of smaller eruptions affected the area, the last of which was the 1538 Monte Nuovo eruption (Guidoboni & Ciuccarelli 2011). The area is also characterized by strong bradyseism. During the last century, three main episodes occurred in the area (1950–1952, 1969–1972, 1982–1984), with the most recent resulting in an uplift of about 1.80 m (Del Gaudio *et al.* 2010).

The deep structure of this caldera is mainly known through seismic imaging methods that have been obtained from both active and

passive data (Judenherc & Zollo 2004; Vanorio *et al.* 2005; Zollo *et al.* 2008). Analysis of reflected waves by the amplitude *versus* offset technique revealed two distinct interfaces beneath Campi Flegrei (Zollo *et al.* 2008). The deeper of these is located at a depth of ~8 km, and is characterized by a strong increase in the V_p/V_s ratio. This was interpreted as the deep magma layer that feeds the caldera and that is responsible for eruptions in the area. This interpretation is consistent with geochemical investigations on melt inclusions from Campi Flegrei shoshonites (Mangiacapra *et al.* 2008). The shallow interface is at ~3 km in depth, and is instead associated with a discontinuity between the older caldera deposits and a fluid-saturated metamorphic rock layer (Zollo *et al.* 2008), which can provide a shallow magma chamber before medium- or small-scale eruptions. This interface also separates the shallow hydrothermal system from the deeper magmatic one. The root of the bradyseism is commonly associated with this shallow layer, and has been ascribed to the intrusion of magma (D'Auria *et al.* 2015; Trasatti *et al.* 2015) or to the deformation of a concrete-like caprock due to the high

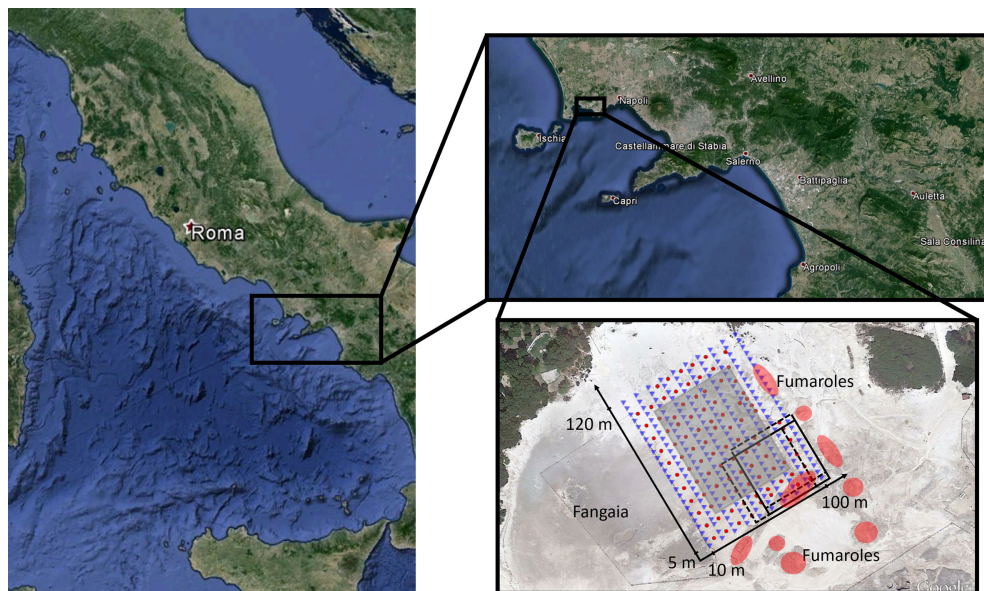


Figure 1. Satellite image of the Campi Flegrei region and zoom-in on the investigated area during the RICEN experiment, showing geometrical distribution of the sources (red circles) and receivers (blue triangles). The dimension of the subgrid used for the analysis is represented with the solid black square and the shifted overlapping subgrids are indicated with the dashed squares. The area for which the *S*-wave model is obtained is represented by the shaded grey box. In figure, Fangaia indicated the region at the boundary of the investigated area, where the water outcrops at the surface and the red points the fumaroles where high temperature is recorded.

pressure of the underlying gases (Vanorio & Kanitpanyacharoen 2015).

The shallow hydrothermal system of the Campi Flegrei is associated with the interaction of meteoric water and the heat and fluid transfer from greater depths. Within the hydrothermal system, the Solfatara is assumed to be the top of a hydrothermal plume (Chiodini *et al.* 2001) and it experiences large episodes of degassing, with very intense emissions of hydrothermal–magmatic gases and high heat flow (Chiodini *et al.* 2001). The Solfatara is a crater of about 0.6 km in diameter that is bounded by normal faults, along which geothermal fluids can ascend (Bianco *et al.* 2004). The surficial expression of these pathways are the fumaroles that are located within or at the boundaries of the crater. Several geophysical analyses have investigated the shallow structure of the Solfatara, including seismic (Bruno *et al.* 2007), resistivity (Byrdina *et al.* 2014) and magnetotelluric (Siniscalchi *et al.* 2015) surveys. Tomographic images have revealed a very complex structure, with alternation of positive and negative resistive bodies, which indicates the presence of water separated by gas sacks. Additionally, ambient noise was recorded in the crater from three-component stations and data were inverted to retrieve the phase velocity of the Rayleigh waves (Petrosino *et al.* 2012). Stable features are obtained in the frequency range 2–15 Hz; when retrieving the *S*-wave model from modelling of the dispersion curves, the resulting penetration depth is several tens of metres. A very shallow analysis based only on the measurement of group velocities of Rayleigh waves was also performed in the Fangaia mud pool using surface waves (Letort *et al.* 2012), which revealed a penetration depth of a few metres.

The shallow structure below the Solfatara is also subjected to seasonal changes due to variations in the meteoric contribution to the hydrothermal system (Chiodini *et al.* 2007). Over the last several years, the Solfatara has also experienced increases in pressure,

temperature and heat flow, and significant changes in the composition and pattern of the degassing, and in its distribution through the vents (Chiodini *et al.* 2011). Over the same period, a new uplift started after 20 yr of subsidence, with sporadic episodes of shallow seismicity beneath the Solfatara (at depths between 2 and 3 km; D’Auria *et al.* 2015).

To provide high-resolution images of the structure beneath the Solfatara, and to detect and track changes in the medium in the shallow parts of the Solfatara area, the ‘Repeated Induced Earthquake and Noise’ (RICEN) experiment was organized in the framework of the European ‘Mediterranean Supersite Volcanoes’ (MED-SUV) project. This consisted of three campaigns that were carried out in 2013 September, 2014 May and 2014 November, each of which lasted 1 week. A large data set with more than 75 000 seismograms was recorded during the soil energization of these campaigns, along with several days of continuous ambient noise. The active sources were the vibrations generated by a Vibroseis truck.

This study is limited to analysis of the active data acquired during the first campaign. This covered an area of 90 m × 115 m, on which a regular grid of 240 vertical sensors was positioned on the ground. The station geometry was a 2-D grid with 10 lines of 24 sensors, with the station in-line interdistance of 5 m. The distance between two contiguous lines (i.e. cross-line distance) was 10 m. The velocity sensors were GS-11D 4.5 Hz vertical-component geophones. About 100 shotpoints were energized on a staggered grid with respect to the receiver grid. For the vibrations, both the in-line and cross-line interdistances were 10 m. The source–station distribution is shown in Fig. 1.

A Geode G24 acquisition system was used, with a dynamic range of 24 bits, a full-scale voltage of 2.8 V and a sampling rate of 1 kHz. The trigger for the system was radio-controlled, to ensure correct timing for all of the sensors. When the Vibroseis was activated

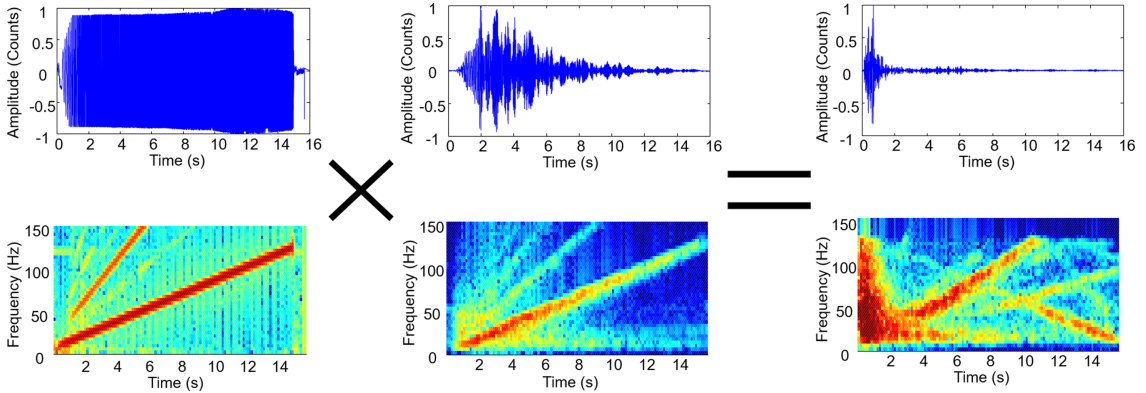


Figure 2. Examples of raw sweep data recorded during the experiment, with the results after the cross-correlation and the minimum phase filter, and their respective spectrograms. The first panel on the left shows the sweep function, the middle one displays the seismogram as recorded by the instrument and the right-hand panel shows the retrieved Green's function after correlation and filtering. All of the traces are normalized by their maximum. The panels on the right show that the largest part of the energy is concentrated in the first seconds of acquisition.

(i.e. lowered its mass to produce the energization), a radio signal was sent to the data logger, to open all of the recording channels. This guaranteed that the differences in the P -wave arrival times between close stations were due to the propagation of the seismic waves across the array. For each source position, three energizations were performed, and they were automatically stacked to increase the signal-to-noise ratio.

The Vibroseis produces vibrations in the frequency band of 5–125 Hz, with a 15-s-long linear sweep that is a signal where the dominant frequency increases linearly with time. Fig. 2 shows an example of the source signal recorded on the vibrating plate, and the associated spectrogram. It is worth noting that the spectrum of the source depended on the coupling of the mass with the ground, and it was usually not flat in the frequency range of 5–125 Hz. We observe that for frequencies > 40 Hz, the source behaves as a high-pass filter with a flat level and a ratio of about 4:1 between the flat level and the amplitude of the spectrum, at 7 Hz.

In this study, we investigate the shallow structure of the Solfatara using the surface waves as the diagnostic tool. In the next section, we discuss the data processing used to extract the Green's functions from the Vibroseis records. In the following section, we investigate the variability in the surface waves as a function of the frequency and the distance. After partitioning the investigated area into subgrids, we estimate the phase and group velocities using the coherence of the Rayleigh waves along the sections. We finally invert the dispersion curves to obtain a 3-D S -wave model for the area.

2 DATA PROCESSING

Velocity records are the convolution of the instrumental response by the source time function and the Green's function of the medium. The instrumental response is almost flat above the corner frequency of the sensor (4.5 Hz). We do not have a response curve for each single sensor, but only an average curve for all of the instruments, as furnished by the manufacturer. As the source has an additional cut-off at 5 Hz, we assumed a flat response in the investigated frequency range (7–25 Hz) and only converted the signal by multiplying it by the analog-to-digital conversion factor and by dividing it by the transduction factor, to get the appropriate units for the data. In the selected frequency range, the signal $v(\mathbf{x}, t)$ at position \mathbf{x} can be assumed to be the convolution of the source time function

$S(\bar{\xi}, t)$ acting at the location $\bar{\xi}$, and the medium Green's function $G(\mathbf{x}, t; \bar{\xi})$, such that

$$v(\mathbf{x}, t) = S(\bar{\xi}, t) * G(\mathbf{x}, t; \bar{\xi}), \quad (1)$$

where the symbol $*$ denotes time convolution. To obtain the Green's function, the correct removal of the source time function from the velocity records requires a deconvolution operation, which is usually performed in the frequency domain. This can be evaluated as the spectral ratio between the recorded signal spectrum and the spectrum of the source. A water level constraint is also added to avoid divergences in the amplitude spectrum of the Green's function. For specific source time functions, the associated autocorrelation is a well-known wavelet. In the case of the linear sweep as used in this study, the autocorrelation of the source is the Klauder wavelet $K(t)$ (Robinson & Saggaf 2001)

$$S(\xi, t) \times S(\xi, t) = K(\xi, t), \quad (2)$$

where the symbol \times now denotes time correlation. Indeed, when the original signal is cross-correlated with the sweep that generated it, we retrieve the Green's function filtered by the Klauder wavelet

$$\bar{v}(\mathbf{x}, t) = K(\bar{\xi}, t) \times v(\mathbf{x}, t) = K(\bar{\xi}, t) * G(\mathbf{x}, t; \bar{\xi}). \quad (3)$$

The filter parameters depend on the shape of the sweep, which results in a specific Klauder filter function (Brittle *et al.* 2001). Moreover, any autocorrelation function is a zero-phase filter, and its application to the Green's function yields a modification of the arrival times of the seismic waves, to produce a non-causal signal. To preserve causality in the data, an additional minimum phase filter is applied after cross-correlation (Gibson & Lerner 1984).

Here, we therefore cross-correlate the data with the sweep source function, which were recorded on a specific channel of the acquisition system. An example of input and cross-correlated signals is shown in Fig. 2. Although the input sweep is expected to be the same for all of the vibrations, some differences arise from the different coupling of the Vibroseis plate with the soil. We checked the quality of all of the sweeps by comparison of the observed spectrograms with the expected spectrograms. In most cases, we get consistent source spectrograms. There are very few cases for which a different spectrogram is observed, due either to an error in the radio communication of the sweep or to bad coupling between the plate and

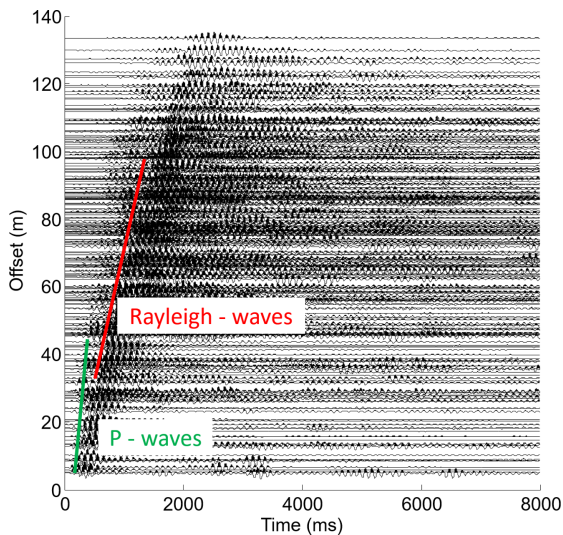


Figure 3. Filtered (7–10 Hz) seismic section of one shot recorded at all of the stations. The traces are ordered by distance from the source. The arrival times of the *P* waves and Rayleigh waves are indicated with two solid lines (green and red, respectively). Signals that deviate from these lines show the great spatial heterogeneity in the medium.

the soil. In this case, we did not use the specific sweep function for cross-correlation, but we used the average of all of the consistent sweep functions.

We also checked the effect of the minimum phase filter on the data. We did not observe any significant changes after applying the minimum phase, neither in the first *P*-wave arrival time nor in the arrival time of the largest amplitude wave train. However, to preserve causality, we applied the minimum phase filter. Finally, each trace is normalized by the maximum of its absolute value.

3 PHASE AND GROUP VELOCITY ESTIMATION

For the estimation of the phase and group velocities associated with the Rayleigh waves, we want to use the coherence of surface wave propagation along seismic sections and the stack of the signals in the same distance range, to increase the signal-to-noise ratio and to reduce the small-scale variability that cannot be resolved by the data.

The coherence of the waveforms in the same distance range is enhanced for a 1-D horizontally layered structure and an isotropic source, with this latter condition almost satisfied by the Vibroseis. Under these assumptions, the signal is independent of the azimuth of the receiver and only changes as a function of the source–receiver distance, regardless of the absolute locations of both source and receiver.

Fig. 3 shows a seismic section associated with a single shot, where the data are filtered in the frequency band of 7–10 Hz. The largest amplitude in the data corresponds to the Rayleigh waves. Although we can follow the surface waves that propagate along the section at an almost constant velocity, there is also a general smearing of this wave packet, a transfer of energy from ballistic to coda waves as the distance increases, and a strong variability in the surface wave signals, as also for traces recorded at similar distances from the source. This variability indicates that a 1-D model does

not provide a suitable description of the structure for interpretation of the surface wave propagation. Nevertheless, the coherence of the signal at short distances indicates that a 1-D model approximation holds locally, over a smaller space scale.

We then subdivide the receiver grid into smaller size subgrids, and determine whether there is any specific space length at which the signal remains coherent as a function of the distance. We thus recursively analyse squared overlapping subgrids, the sizes of which range from $20\text{ m} \times 20\text{ m}$ up to $90\text{ m} \times 90\text{ m}$ (the maximum allowed size for this experiment). We also subdivide the distance range into bins where we average all of the traces with sources and receivers in the same subgrid and the distance between them in the same bin, where the average is computed as the algebraic mean point-by-point along the trace. For each size, we investigate how coherent the signal remains along the section for several narrow frequency bands between 7 and 25 Hz. This lower limit is selected as the minimum frequency at which the energy radiated by the Vibroseis source can be clearly observed over the whole investigated area, regardless of the location of the source. This maximum frequency is chosen, instead, as the upper limit at which the energy coherently propagates across the Solfatara.

The maximum grid size at which the signal remains coherent along the section is $40\text{ m} \times 40\text{ m}$, as a subgrid that contains 9×5 receivers, and at a maximum of 5×4 shot locations. As we allow for the maximum overlap, the nearby grids are either shifted by 5 m along the in-line direction, or by 10 m along the cross-line direction, which leads to a total number of 96 subgrids. Within this partition, we obtain a coherent profile up to 20 m.

Finally, after selecting a subgrid partitioning of $40\text{ m} \times 40\text{ m}$, we also investigate the size of the bin according to which all of the source–receiver pairs that fall into the same distance range are stacked. This choice represents a compromise between a sufficient number of traces to be stacked to provide reliable averages, and the possibility to follow the surface wave features along the section with continuity. The best compromise is a binning of 1 m. An example related to one subgrid and containing the number of traces that are stacked in each bin is shown in Fig. 4. We have >10 traces to be stacked for most of the bins. The variability depends on the rectangular grid associated with the experiment.

Within this selection, we proceed to the estimation of phase and group velocities in each subgrid. For this goal, we filter the signal in 14 narrow overlapping bands between 7 and 25 Hz. We select the frequency bands using the criterion that the ratio between the width and the central frequency of the band is preserved. After filtering, we normalize each signal to its maximum.

To compute the phase velocity in a subgrid, we first gather the data into distance bins. An example of the resulting section is shown in Fig. 5(a), for the frequency band of 8.6–12.4 Hz, centred at 12 Hz. For the computation of the velocity, we perform a grid search with the velocity spanning the interval of $35\text{--}300\text{ m s}^{-1}$, with a step of 5 m s^{-1} . For each velocity v , we shift back in time the traces of the value given by the ratio between the source–receiver distance and v . We then stack the moved out section up to 20 m. We expected that in agreement with the effective value of the velocity, the amplitude of the stack function would be large, because the waveforms along the section are almost in phase, while the amplitude of the stack is likely to decrease for velocities further and further from the effective velocity. Therefore, we use the maximum of the envelope of the stack signal as the fitness function. An example of this function is shown in Fig. 5(c), as associated with a section of Fig. 5(a). That function can have several local maxima, with oscillations for low velocities. Nevertheless, the absolute maximum is well resolved in

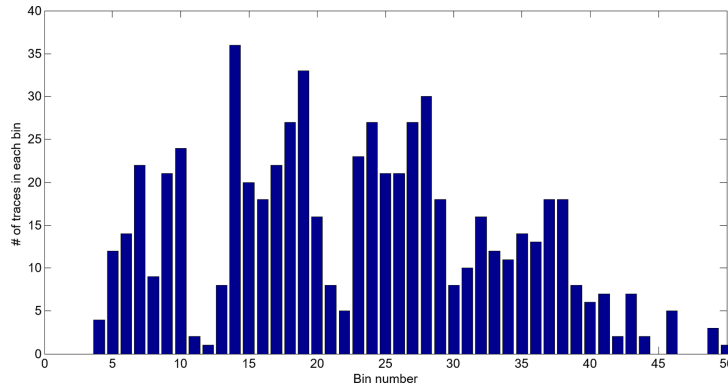


Figure 4. Number of source–receiver traces spatially averaged in each 1-m spatial bin for the subgrid used in Fig. 5. Due to the geometry of the experiment, we have not a uniform distribution of records with distance, but the selected sizes of subgrids and bins allow us to have a sufficient number of records for most of the bins.

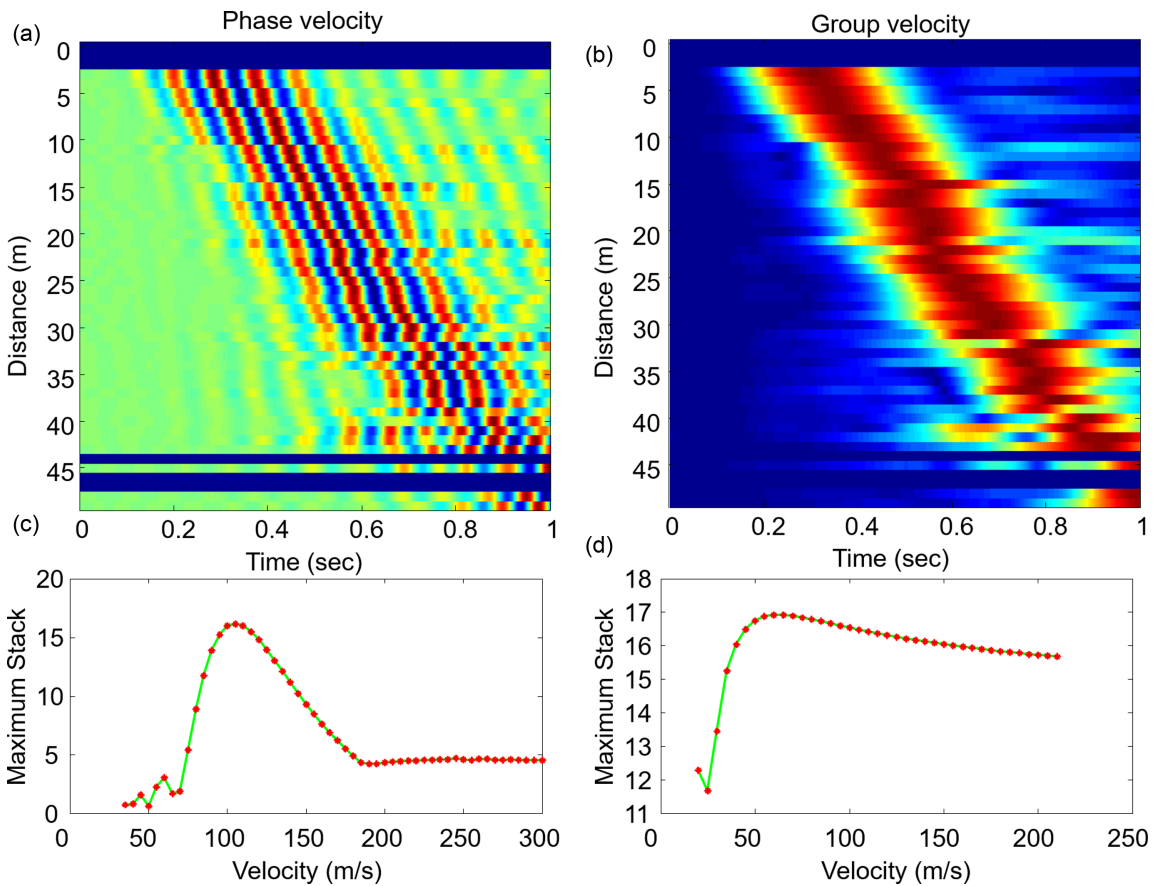


Figure 5. Filtered (8.6–12.4 Hz) average seismic section for sources and receivers selected in one squared subgrid (see Fig. 1). (a) Coherent average centred at 10.5 Hz, from which the phase velocity can be extracted. (b) Envelope of the coherent average from which the group velocity can be extracted. (c) and (d) Stack function for different velocity values used to realign the seismic sections in (a) and (b), and consequently to obtain the phase (c) and group (d) velocities. The blue lines in the panels (a) and (b) represent bins for which we have no records.

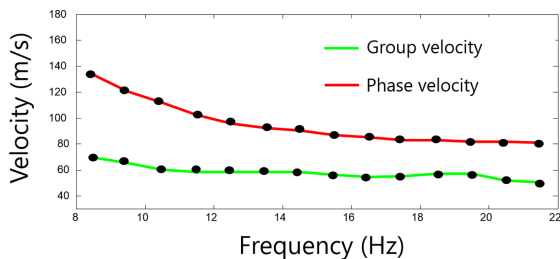


Figure 6. Representative data for phase and group velocity dispersion curves. On the horizontal axis, the central frequency for each band is reported. The curves generally show a decreasing trend with the frequency.

almost all of the cases, although the quality degrades as the central frequency of the band increases.

For the computation of the group velocity, we apply a similar technique, although we compute the envelope of the signals before building the binned seismic section for each subgrid. An example of this section is shown in Fig. 5(b). For computation of the velocity, we also perform a grid search, although we investigated a lower velocity range (20–210 m s^{-1} , with a step of 5 m s^{-1}). For each value, we align the traces, we compute the stack on the moveout section, and we use the maximum of the positive definite stack function as the fitness function. An example of the function is shown in Fig. 5(d), as associated with a section of Fig. 5(b). The absolute maximum of the function is smoother compared to the phase velocity. When increasing the frequency, bimodal or multimodal fitness functions occur for some subgrids, with comparable amplitudes of the maxima. In this case, we add a smoothness condition on the velocity as an additional constraint that penalizes significant jumps in the group velocity between consecutive frequency bands and contiguous subgrids in space. From this analysis, we get the dispersion curves in each subgrid. An example of this curve is shown in Fig. 6. As a general trend, the group velocity is always smaller than the phase velocity. While the phase velocity always decreases with frequency, the group velocity is almost constant, with local maxima and minima in several subgrids and different frequency bands.

Fig. 7(a) shows the maps of the phase velocity for the different frequencies. They are plotted at different depths, because we use the implicit association that lower frequencies or longer wavelengths correspond to deeper regions. There are two anomalies at the boundaries of the investigated region. The NW anomaly also corresponds to the largest phase velocity measured in the area (250 m s^{-1}), and it has a cross-line size of about 50 m, while it is thinner along the in-line direction. The SE anomaly has almost the same shape, although with smaller velocity values. The root of the NW anomaly can be seen in the whole frequency range, while the SE anomaly almost disappears at 17.5 Hz. Moreover, for frequencies >15 Hz, a faster velocity is observed in the SW part of the area, close to the Fangaia mud pool, compared to the NE domain. The retrieved velocities well superimpose on average to the values of the phase velocity, as obtained by Petrosino *et al.* (2012), in the overlapping frequency range (7–12 Hz), although the space scale at which they resolved the model is significantly larger than the space discretization used in this work.

The group velocity in Fig. 7(b) also has a maximum at low frequency that corresponds with the SE anomaly retrieved for the phase velocity, although it shows a minimum for the NW anomaly. These features do not have roots as deep as for the phase velocity. At higher frequencies, the main peculiarity is the separation between the SW domain, which is slightly faster than the NE region, as also observed for the phase velocity. Finally, in the last frequency band (17.7–25.3 Hz, centred at 21.5 Hz), very small velocities (i.e. $\sim 30 \text{ m s}^{-1}$) are obtained corresponding to the NW anomaly.

4 S-WAVE VELOCITY MODEL FROM INVERSION OF THE DISPERSION CURVES

The phase and group velocity dispersion curves were jointly inverted to determine a velocity model of the whole area. We first inverted the dispersion curves in each subgrid, to compute a 1-D velocity model local to the subgrid. Then the combination of the models for all of the subgrids provides us with a 3-D model. For the inversion, we use the Geopsy software (Wathelet *et al.* 2004), which searches for the best horizontally layered *P*-wave and *S*-wave models that fit

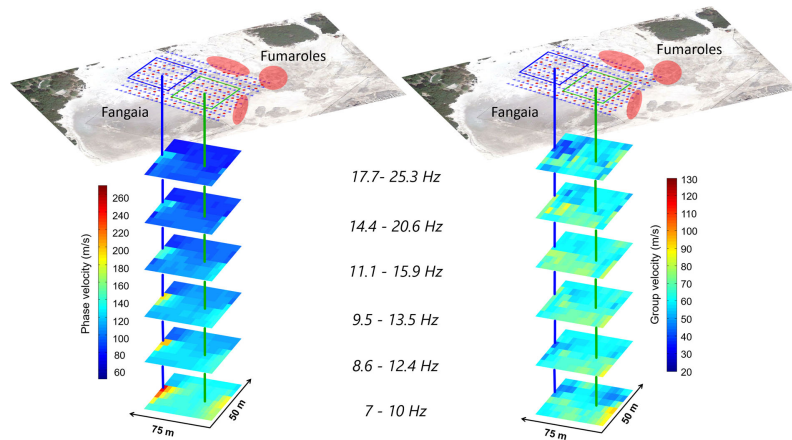


Figure 7. Spatial versus frequency representation of phase (a) and group (b) velocity maps. Different frequency bands classically investigate different depths for surface waves. Colour bars, variation of the phase and group velocities for the two different subgrids; blue and green squares at the surface, spatial extension of the subgrids; vertical lines (blue and green), centre of the two subgrids and associated to one pixel of the velocity maps. The overall map of the Solfatara is superimposed on the set of sources (red) and receivers (blue), where the location of the Fangaia and fumaroles (red points) is also indicated.

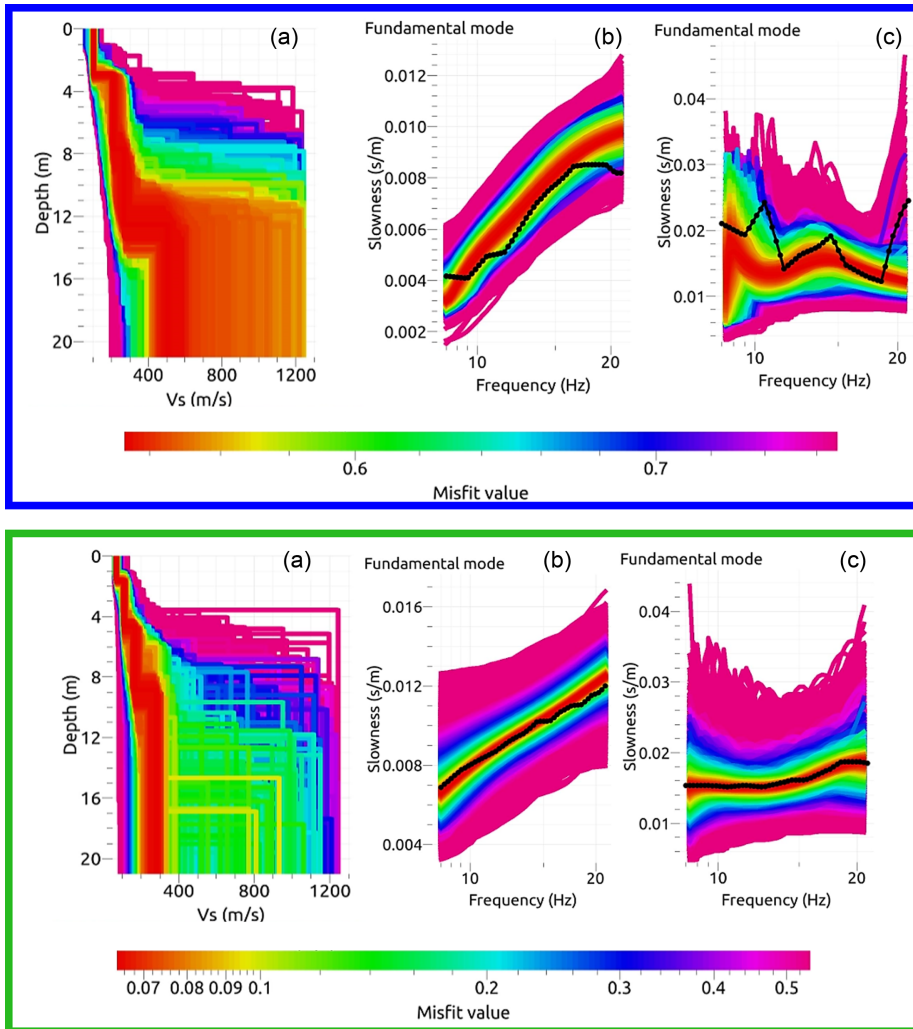


Figure 8. (a) Representations of the inverted layered model for the two subgrids indicated by the same colours in Fig. 7 (blue, top panel and green, green panel). (b) Phase velocity. (c) Group velocity. Black lines, experimental dispersion curves; coloured curves, numerical dispersion curves for a wide distribution of layered models.

the dispersion curves. To retrieve the velocity structure, the number of layers, the range of variability for the P -wave and S -wave speeds and the density are required. We first observe that the results are relatively insensitive to the P -wave model and the density. Hence, we limit the exploration to the S -wave velocities and to the depth of the interfaces.

We perform several tests to correctly set the number of layers and the maximum penetration depth of the Rayleigh waves. We consider a four-layered model as the best choice, because the misfit between the simulated and expected dispersion curves significantly reduces up to four layers, while there is no further large reduction when the number of layers is increased beyond this value. The range for the S -wave speed was selected as between 50 and 1250 m s⁻¹ (Letort *et al.* 2012).

An example of the S -wave models obtained from inversion of the dispersion curves is shown in Fig. 8. From Fig. 8, we see that

several models provide very similar fits for the dispersion curves. A four-layer model still provides a smooth dispersion curve that cannot match all of the slope breaks that we can observe in the real dispersion curves. This is the case of the dispersion curves plotted as solid black lines in the upper part of Fig. 8, which correspond to the largest phase-velocity region. When the dispersion curve is smoother, this is well retrieved by the model, as for the example shown in the bottom part of Fig. 8. This latter region is related to a subgrid in which a low phase velocity is measured. For the sake of completeness, the dispersion curves for the phase and group velocities, with the misfit, are also shown. As a general comment, the first very shallow layer is always well constrained and reaches a maximum depth of 4 m. A second layer has depths between 4 and 8 m. Finally, the depth of the last interface and the velocity below it are not well constrained. This layer could be the interface between the unconsolidated shallow deposits and the aquifer beneath the

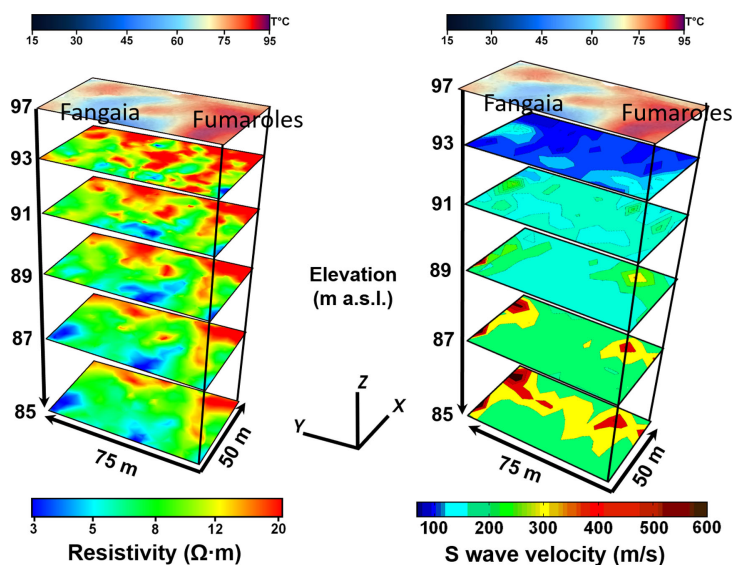


Figure 9. Spatial versus depth representation of S -wave velocity map (right) and comparison with geoelectric resistivity measurements (left) on the same spatial grid. The altitude of the Solfatara area is 97 m and the depth is plotted downwards from this reference. The temperature map with the position of mud pool and fumaroles is shown at the top.

Solfatara that clearly emerges in the Fangaia mud pool. Although the study of Petrosino *et al.* (2012) was based on a larger space scale, lower frequency range and consequently larger penetration depth, the interface that they retrieved at about 5 m well corresponds on average to the variation of S -wave velocity in the first two layers of the model obtained in this work.

From the analysis, we did not select the single best-fit model, but we decided to extract all of the profiles from the exploration ensemble with misfit <15 per cent, compared to the minimum value. We assume as best model the average of the selected models. The average models are no longer layered; they are instead characterized by the almost continuous variation of the wave velocity with depth. We finally combine the 96 velocity profiles to retrieve lateral 3-D variations in the S -wave velocity within the medium.

Fig. 9 (right-hand panel) shows the velocity model for fixed depths, from 4 to 12 m below the Solfatara surface (at an altitude of 97 m) with a step of 2 m. This model is compared with the resistivity model obtained on the same area (see below). We do not represent the velocity model above 4 m because with this range of velocities (100–600 m s^{-1}), we do not have a good resolution of the lateral variation.

We note that the two NW and SE anomalies observed in the phase-velocity maps, clearly appear as high-velocity bodies at all depths. Specifically, the NW anomaly is a clear spot that emerges at 4 m and becomes more evident in terms of the velocity contrast at greater depths. The SE anomaly appears at 8 m and preserves its shape with increasing depth. We also note that the SW domain is slower at all depths, compared to the NE domain. This area is the side closest to the Fangaia, where the water outcrops, and it might be the manifestation of an unconsolidated layer at shallow depths and of a water aquifer at greater depths. This statement is confirmed by Fig. 10, where we plot different isosurfaces of velocity (100, 150, 200 and 300 m s^{-1}) and an isosurface of resistivity at 8.5 $\Omega\text{-m}$. The isoresistivity surface shows low-level resistivity near the Fangaia,

which therefore indicates a soil rich in water. Indeed, at the same time, the isovelocity surfaces show a clear decreasing gradient toward the Fangaia side. As the resistivity curve goes down following the aquifer, the shear wave velocity decreases close to the surface, due to the presence of water. Fig. 10 is obtained using the same data as in Fig. 9, with a spatial filter that smooths the short-range velocity contrast. This filter allows us to focus on the average trend observed with the velocity gradient at lower frequencies toward the Fangaia mud pool.

5 DISCUSSION

The goal of the RICEN experiment at Solfatara is to determine whether combined active and passive seismic measurements can be used to accurately characterize the structure of an active hydrothermal area and its changes with time. This first study is aimed at defining the very shallow structure of the area, down to 12–15 m, using Rayleigh waves. These data are complementary to velocity models obtained from the inversion of P -wave traveltimes, which explore greater depths. The P waves generated by active experiments in the area (Bruno *et al.* 2007; Festa *et al.* 2015) cannot define the features of this very shallow region, because body-wave rays have an almost vertical incidence below the stations, due to the strong velocity gradient. The time delay is indeed integrated over the first 10–15 m beneath the station, independent of the source position, and it eventually appears as a residual contribution in the traveltime difference between synthetics and observations. Moreover, the measure of the P wave at very short source–station distances (<10 m) is not accurate, because the minimum wavelength in the source time function is comparable with such a distance. On the contrary, the surface waves can correctly explore the features of this shallow region. Due to the strong velocity gradient, the low-frequency (7–25 Hz) Rayleigh waves are trapped in this very shallow domain beneath the Solfatara. Additionally, the criss-crossing of the seismic rays from

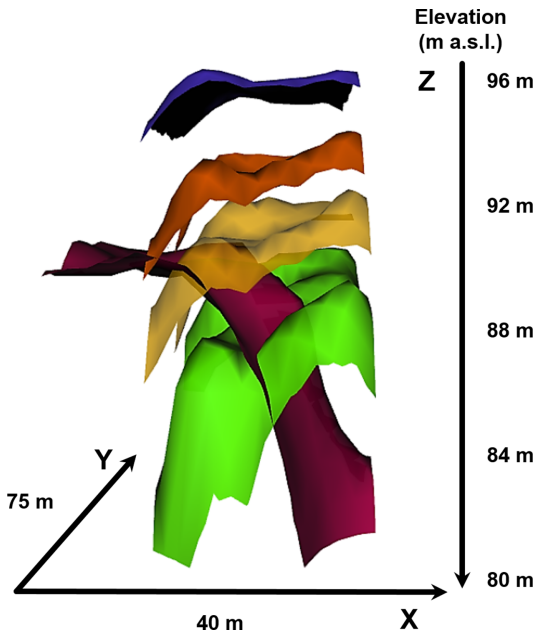


Figure 10. Representation of the isovelocity surfaces for velocities of 100 m s^{-1} (blue), 150 m s^{-1} (orange), 200 m s^{-1} (yellow) and 300 m s^{-1} (green). Purple surface, isoresistivity at $8.5 \Omega\text{-m}$. The same low-order spatial filter was applied to smooth the short-scale spatial heterogeneities (see Fig. 9) and to reveal any global trend of the shear velocity and resistivity gradients. This figure has the same orientation of Fig. 9.

the large number of stations and the source position increases the horizontal resolution in the models.

To have a complete description of the investigated area, seismic models are compared to the results from the electrical resistivity tomography, which has good resolution in the discrimination of media that are rich or poor in water and gas. The electrical resistivity tomography is obtained performing direct-current resistivity profiles, with sixteen 115-m-long profiles with NW–SE orientation and twenty-four 75-m-long orthogonal NE–SW profiles, all with 5 m spacing between the electrodes. The same Wenner–Schlumberger configuration is used for all of the profiles, and the 3-D inversion is obtained using an algorithm as detailed by Loke & Barker (1996) and implemented in the RES3DINV software (Loke & Dahlin 2002). The normalized root mean square error of the resulting 3-D model is 7.5 per cent, and the data quality allows for a high-resolution resistivity model down to 15 m in depth. Also, acquisition of the soil temperature at 30 cm in depth is performed at each electrode during the experiment. Resistivity maps are represented on the left side of Fig. 9, at the same depths as the S -wave velocity maps. The temperature field is added on the top of the resistivity and seismic profiles.

In the temperature field, there is a cold region at about $50\text{--}60^\circ\text{C}$ in the central part of the area, beside the Fangaia, which is surrounded by a hot domain with spots that reach $90\text{--}95^\circ\text{C}$, where the fumaroles emerge at the surface. The resistivity model in the first 4 m is correlated with the temperature field, with resistive bodies that correspond to high-temperature regions. Hence, high-temperature regions/high resistive bodies are likely to be related to the presence of rock filled with high-temperature gases. These regions also correspond to low-velocity domains very close to the surface in the

seismic model, although there is no clear correlation between the S -wave model at 4 m with the temperature field, as can be seen in the resistivity map at the same depth. Nevertheless, shallow velocity anomalies are mostly related to the temperature gradient. Hence, a change in the temperature can be associated with a rheological/lithological transition between rocks with different properties, such as with different degrees of water or vapor saturation. Between 8 and 10 m in depth, there are two strong anomalies at the boundary of the model, with an increase in the S -wave velocity by a factor of 2–3. These two anomalies also appear in the resistivity maps as a transition between an upper resistive, probably gas-rich, domain to a less resistive region, which appears to be representative of rock with significantly lower gas content. At greater depths, this anomaly appears to extend over a broader region, although it is probably a smearing effect due to loss of resolution as the investigation depth increases. Finally, at 12 m in depth, we observe a separation of the SW domain from the NE domain, with the NE domain significantly faster in terms of S -wave velocity. This boundary clearly appears in the resistivity profile as a transition to a conductive region ($5 \Omega\text{-m}$) close to the Fangaia mud pool, which is interpreted as a water-saturated layer (Byrdina *et al.* 2014). As the water emerges at the Fangaia, we expect that the water layer at depths of 10–12 m in the SW domain of the investigated area stops or sharply deepens when moving towards the NE. This is also observed clearly by the isosurfaces of the velocity and resistivity that show a complementary trend; in the area where there is low resistivity, the S waves are slower than where there is high resistivity.

6 CONCLUSIONS

In this study, we analysed active data recorded during the first stage of the RICEN experiment at the Solfatara, Campi Flegrei, Italy. After processing the data to remove the source time function of the Vibroseis, we investigated the Rayleigh wave dispersion in terms of both phase and group velocities in the frequency range 7–25 Hz. To have a robust estimate of the wave speed as a function of the frequency, we first investigate the maximum size for which the assumption of a 1-D velocity structure with depth is reliable. A 1-D approximation holds up to distances of 40 m within the investigated area. Then, we subdivide the area in squared subgrids with sides of 40 m, and within each subgrid we stack all the signals in the same source–receiver distance, independent of the absolute positions of the sources and stations. We estimate the phase and group velocities for each subgrid, to search for the maximum of the stack function after aligning the traces for the selected velocity. The stack is computed on the traces for the phase velocity and on the envelope of the traces for the group velocity. Finally, the phase and group velocities are jointly inverted to provide a 3-D S -wave model for the Solfatara area. We find that the maximum penetration depth is 12–15 m for the selected frequency range. At shallow depths, there are velocity anomalies that are correlated with the temperature gradient measured close to the surface, while at greater depths the anomalies correspond to transition between a gas-rich region to a water-saturated layer, which is outcropping SW outside of the analysed domain.

ACKNOWLEDGEMENTS

We acknowledge Marc Wathelet for his help in the use of the Geopsy software, and for providing us with scripts for the analysis of Geopsy outputs. ISTerre is part of Labex OSUG@2020. This study was

carried out within the framework of the MedSuv project, which received funding from the European Union Seventh Programme for research, technological development and demonstration, under grant agreement no. 308665.

We are grateful to two anonymous reviewers that contributed in improving the manuscript.

REFERENCES

- Bianco, F., Del Pezzo, E., Saccorotti, G. & Ventura, G., 2004. The role of hydrothermal fluids in triggering the July–August 2000 seismic swarm at Campi Flegrei, Italy: evidence from seismological and mesostructural data, *J. Volc. Geotherm. Res.*, **133**(1–4), 229–246.
- Brittle, K.F., Lines, L.R. & Dey, A.K., 2001. Vibroseis deconvolution: a comparison of cross-correlation and frequency-domain sweep deconvolution, *Geophys. Prospect.*, **49**, 675–686.
- Bruno, P.P., Ricciardi, G.P., Petrillo, Z., Di Fiore, V., Troiano, A. & Chiodini, G., 2007. Geophysical and hydrogeological experiments from a shallow hydrothermal system at Solfatara Volcano, Campi Flegrei, Italy: response to caldera unrest, *J. geophys. Res.*, **112**, B06201, doi:10.1029/2006JB004383.
- Byrdina, S. et al., 2014. Relations between electrical resistivity, carbon dioxide flux, and self-potential in the shallow hydrothermal system of Solfatara (Phlegrean Fields, Italy), *J. Volc. Geotherm. Res.*, **283**, 172–182.
- Chiodini, G., Avino, R., Caliro, S. & Minopoli, C., 2011. Temperature and pressure gas geoidicators at the Solfatara fumaroles (Campi Flegrei), *Ann. Geophys.*, **54**(2), 151–160.
- Chiodini, G., Frondini, F., Cardellini, C., Granieri, D., Marini, L. & Ventura, G., 2001. CO₂ degassing and energy release at Solfatara volcano, Campi Flegrei, Italy, *J. geophys. Res.*, **106**, doi:10.1029/2001JB000246.
- Chiodini, G., Vilardo, G., Augusti, V., Granieri, D., Caliro, S., Minopoli, C. & Terranova, C., 2007. Thermal monitoring of hydrothermal activity by permanent infrared automatic stations. Results obtained at Solfatara di Pozzuoli, Campi Flegrei (Italy), *J. geophys. Res.*, **112**, B12206, doi:10.1029/2007JB005140.
- D’Auria, L. et al., 2015. Magma injection beneath the urban area of Naples: a new mechanism for the 2012–2013 volcanic unrest at Campi Flegrei caldera, *Sci. Rep.*, **5**, 13100, doi:10.1038/srep13100.
- Del Gaudio, C., Aquino, I., Ricciardi, G.P., Ricco, C. & Scandone, R., 2010. Unrest episodes at Campi Flegrei: a reconstruction of vertical ground movements during 1905–2009, *J. Volc. Geotherm. Res.*, **195**, 48–56.
- Di Vito, M.A., Isaia, R., Orsi, G., Sounthon, J., de Vita, S., D’Antonio, M., Pappalardo, L. & Piochi, M., 1999. Volcanism and deformation since 12,000 years at the Campi Flegrei caldera (Italy), *J. Volc. Geotherm. Res.*, **91**, 221–246.
- Festa, G. et al., 2015. RICEN: Repeated Induced Earthquakes and Noise @Solfatara, Campi Flegrei, in AGU Fall Meeting, San Francisco, pp. 14–18.
- Gibson, B. & Larner, K., 1984. Predictive deconvolution and the zero-phase source, *Geophysics*, **49**, 379–397.
- Guidoboni, E. & Ciuccarelli, C., 2011. The Campi Flegrei caldera: historical revision and new data on seismic crises, bradyseisms, the Monte Nuovo eruption and ensuing earthquakes (twelfth century 1582 AD), *Bull. Volc.*, **73**, 655–677.
- Judenherc, S. & Zollo, A., 2004. The Bay of Naples (southern Italy): constraints on the volcanic structures inferred from a dense seismic survey, *J. geophys. Res.*, **109**, doi:10.1029/2003JB002876.
- Letort, J., Roux, P., Vandemeulebrouck, J., Coutant, O., Cros, E., Wathelet, M., Cardellini, C. & Avino, R., 2012. High-resolution shallow seismic tomography of a hydrothermal area: application to the Solfatara, Pozzuoli, *Geophys. J. Int.*, **189**, 1725–1733.
- Loke, M.H. & Barker, R.D., 1996. Rapid least-squares inversion of apparent resistivity pseudosections by a quasi-Newton method, *Geophys. Prospect.*, **44**, 131–152.
- Loke, M.H. & Dahlin, T., 2002. A comparison of Gauss-Newton and quasi-Newton methods in resistivity imaging inversion, *J. app. Geophys.*, **49**, 149–162.
- Mangiacapra, A., Moretti, R., Rutherford, M., Civetta, L., Orsi, G. & Papale, P., 2008. The deep magmatic system of the Campi Flegrei caldera (Italy), *Geophys. Res. Lett.*, **35**, L21304, doi:10.1029/2008GL035550.
- Pappalardo, L. & Mastrolorenzo, G., 2012. Rapid differentiation in a sill-like magma reservoir: a case study from the Campi Flegrei caldera, *Sci. Rep.*, **2**, doi:10.1038/srep00712.
- Petrosino, S., Damiano, N., Cusano, P., Di Vito, M., A., de Vita, S. & Del Pezzo, E., 2012. Subsurface structure of the Solfatara volcano (Campi Flegrei caldera, Italy) as deduced from joint seismic-noise array, volcanological and morphostructural analysis, *Geochem. Geophys. Geosyst.*, **13**, Q07006, doi:10.1029/2011GC004030.
- Robinson, E.A. & Saggaf, M., 2001. Klaunder wavelet removal before vibroseis deconvolution, *Geophys. Prospect.*, **49**, 335–340.
- Siniscalchi, A., Carlucci, M., D’Auria, L., Petrillo, Z., Romano, G. & Tripaldi, S., 2015. AMT investigation in the Solfatara-Pisciarelli-Agnano area: results and further outlook, in *EGU, Geophysical Research Abstracts*, Vol. 17, EGU2015-9540.
- Trasatti, E., Polcari, M., Bonafede, M. & Stramondo, S., 2015. Geodetic constraints to the source mechanism of the 2011–2013 unrest at Campi Flegrei (Italy) caldera, *Geophys. Res. Lett.*, **42**, 3847–3854.
- Vanorio, T. & Kanitpanyacharoen, W., 2015. Rock physics of fibrous rocks akin to Roman concrete explains uplifts at Campi Flegrei caldera, *Science*, **349**(6248), 617–621.
- Vanorio, T., Virieux, J., Capuano, P. & Russo, G., 2005. Three-dimensional seismic tomography from P-wave and S-wave microearthquake travel times and rock physics characterization of the Campi Flegrei caldera, *J. geophys. Res.*, **110**, doi:10.1029/2004JB003102.
- Wathelet, M., Jongmans, D. & Ohrnberger, M., 2004. Surface-wave inversion using a direct search algorithm and its application to ambient vibration measurements, *Near Surf. Geophys.*, **2**, 211–221.
- Zollo, A., Maercklin, N., Vassallo, M., Dello Iacono, D., Virieux, J. & Gasparini, P., 2008. Seismic reflections reveal a massive melt layer feeding Campi Flegrei caldera, *Geophys. Res. Lett.*, **35**, doi:10.1029/2008GL034242.

4.3 Scattering properties at Solfatara

Waves propagating in a strongly heterogeneous medium lose their coherence owing to the interaction with anomalies and scatterers at different scales. The energy of the incident wave-front is transferred from the ballistic part of the signal to the coda through multiple scattering events. Waves are converted in other seismic phases in order to preserve the continuity of the displacement and the stress at the interface with the anomalies, they are attenuated due to the elastomechanical properties of the medium, or they can be trapped in layers or into anomalies producing resonance effects. In such a kind of medium, the higher frequency content is rapidly lost and therefore the details of the real geological structure are no more recoverable. As a consequence, classical imaging methods based on the arrival times or on the waveform of the ballistic waves might provide too smooth images as compared to real medium. Techniques based on multiple scattering approach can provide a description of the medium in term of its scattering properties (Campillo et al., 2010; Poli et al., 2012; Chaput et al., 2012; Obermann et al., 2014). Such methods do not allow for localizing and characterizing precisely the single scatterers, they rather provide a statistical description of the medium in terms of some relevant parameters such as the mean free path (MFP) and the radiative transport mean free path (TMFP). Nevertheless, in the last years, more accurate and refined techniques, based on the principles of the previous mentioned works, provided surprising results. This is possible because, today, we are experiencing a revolution, thanks to the development of new acquisition systems, which make available a large number of instruments, recording high quality data. A richer and larger amount of data allows for observing particular trends and phenomena and therefore new interpretations can be made.

The MFP is defined as the average distance travelled by a wave between two scattering events. To estimate the MFP we can measure the decay of a seismic wave passing from one receiver to another one. To avoid problems linked to the geometrical spreading, for short distance, it is possible making use of a regular dense array to reconstruct a plane wave and to measure its decay across the receiver grid (Gouédard et al., 2011) (Figure 4-20).

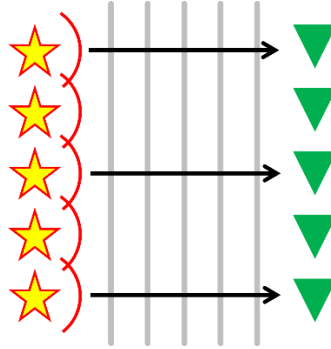


Figure 4-20: Schematic reconstruction of a plane-wave summing the spherical wave-fronts of many sources (stars) acquired at a regular array (triangles).

This approach is intuitive but it hides some drawbacks, such as the a-priori knowledge of the anelastic attenuation (Sato et al., 2012). In general, the anelastic attenuation is not always known and, in some cases, it is not simple to disaggregate the anelasticity from other attenuations effects. Indeed, it is more effective to calculate the MFP through the evaluation of the ratio between the coherent and incoherent intensities (Roux and De Rosny, 2001; Gouédard et al., 2011; Chaput et al., 2015).

In the De Rosny and Roux (2001) paper, the authors analyse the case of reflecting cavity containing fishes. They showed that if a transducer is located in the cavity and the backscattered wave field is averaged over a large number of realizations, the recovered waveform has a trend determined by the MFP, which is related to the density of the scatterers and to the number of independent realizations. The first parameter is linked to the decay of the curve: the higher the number of fishes the smaller the MFP and the faster the decay, whereas the second one is related to plateau of the curve (Figure 4-21). In this problem, we have moving scatterers, the fishes, that can move from one realization to another one, whereas the transducer is always at same position. In our case, we invert the roles between scatterers, sources and receivers. We have fixed anomalies but changing the source-receivers positions, we illuminate them under different views.

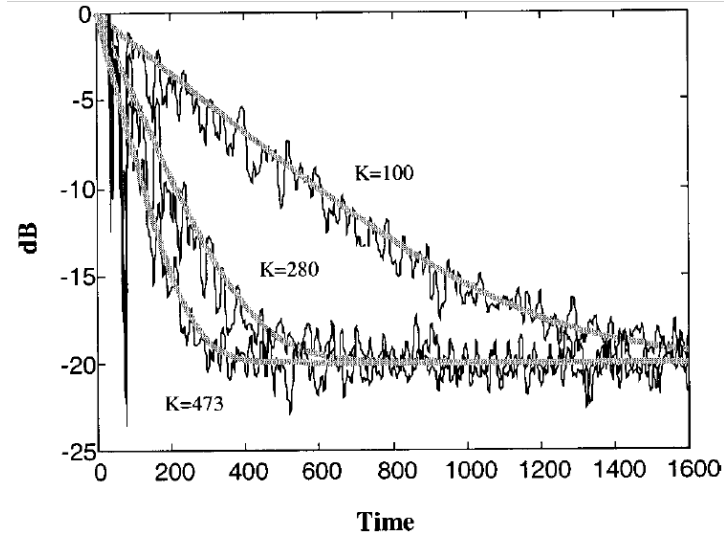


Figure 4-21: Numerical simulation from Roux and De Rosny (2001), where the average backscattered wavefield is represented for a different number of scatterers. The higher the scatterers number (K) the fastest the decay. All the curves reach the same final plateau since the same number of independent realization has been used for the simulation.

Heterogeneity in the structure of the Solfatara volcano is due to the stratification of the past eruptive products, permeated by fluids at different temperature and pressure conditions, moreover their interaction made more complicate the interpretation of their behavior. Such structural complexity is reflected in the recorded waveforms and in the arrival times of the ballistic waves. As the distance increases, the amount of energy in the coda increases and the arrival times are slightly different also for close stations. These effects are clear indicators of a highly scattering medium.

For the computation of the MFP, we evaluated the ratio between the coherent and incoherent intensities (Roux and De Rosny, 2001). The incoherent intensity I_i , defined classically as the average intensity of the velocity field, exponentially decays as the source-receiver distance increases:

$$I_i = \left\langle \left\langle G_n^2(t, r) \right\rangle_d \right\rangle_n = I_0 e^{(-r/l_a)} g(r) \quad (4.7)$$

Here, $G(t, r)$ is the Green's function, I_0 is the intensity of the velocity field at the source, r is source-receiver distance, $g(r)$ is the geometrical spreading, which is

specific to the wave that we are considering and l_a is the absorption mean free path that accounts for both dissipation and inelastic effects. The average is performed over the source–receiver distance for the same source and over all the sources, these averages being referred in the formula to the subscripts d and n respectively. The coherent intensity I_c is classically defined as the intensity of the averaged velocity field, it can be expressed as:

$$I_c = \left\langle \left\langle \mathbf{G}_n(t, \mathbf{r}) \right\rangle_d \right\rangle_n^2 = I_0 e^{(-\mathbf{r}/l_a)} e^{(-\mathbf{r}/l_s)} \mathbf{g}(\mathbf{r}) \quad (4.8)$$

Where l_s is the MFP that provides us with an estimate of the scattering behavior of the medium.

These relationships hold when the number of sources n is enough large that the average does not depend on the specific location of the scatterers and for a homogeneous or horizontally layered medium including scatterers of different size. In this case, the average elastic properties are invariant with respect to the absolute location of sources and receivers, when their distance is fixed. Therefore, the stack of traces having the same source–receiver distance but coming from absolute different positions rules out local-scale effects related to the single scatterers. This is in agreement with the assumption of not considering scatterers as single elements which interfere with the wave propagation, but we averaged over a large number of sources and at the same time on different paths allowing us to observe the global effects of the scatterers. Here, we do not expect a prevalently 1D propagation medium, indeed with the term scatterers we are gathering actually the presence of scatterers in the media as well as the 2D-3D structural effects. To implement the two formulas (4.7) and (4.8), we need to define the distance range in order to average signals on a rectangular source–receiver grid. This same problem arose before in the binning of the waveforms required to construct the seismic sections. The data binning was widely studied previously, therefore we use the same bins interval of 1 m.

Referring again to the formulas (4.7) and (4.8), it is immediate to show that the ratio of the coherent I_c and incoherent intensity I_t only depends on the MFP:

$$H = \frac{I_c}{I_t} = e^{(-\mathbf{r}/l_s)} \quad (4.9)$$

For the more generic case of a finite number of source positions, the above equation writes:

$$H_N(\mathbf{r}) = e^{\left(\frac{\mathbf{r}}{l_s}\right)} + \frac{1}{N} \left(1 - e^{\left(\frac{\mathbf{r}}{l_s}\right)} \right) \quad (4.10)$$

N represents the number of independent realizations and may depend on the scatterer distribution, on the source location and on the investigated frequency (Roux and De Rosny, 2001; Chaput et al., 2015). Using a characteristic wave velocity c and defining the mean free time τ_s as the average time between two scattering events, we can represent the intensity ratio as a function of time:

$$H_N(t) = e^{\left(\frac{-t}{\tau_s}\right)} + \frac{1}{N} \left(1 - e^{\left(\frac{-t}{\tau_s}\right)} \right) \quad (4.11)$$

In our work, we applied this second formulation because we deal with the binned traces as a function of the distance. Therefore, we are able to observe how the energy propagates inside the considered seismic section. We estimated the velocity value to 65 m/s (Figure 4-22), as the best fit line crossing the maxima of the intensity ratio at different distances. This value is almost independent of the frequency and it is worth to note that this value is compatible with the group velocity of the Rayleigh waves travelling across the network. Serra et al. (2016) showed that the group velocity dispersion curves exhibit a behavior independent of the frequency, therefore a single velocity value is able to describe the propagation of the energy in the grid.

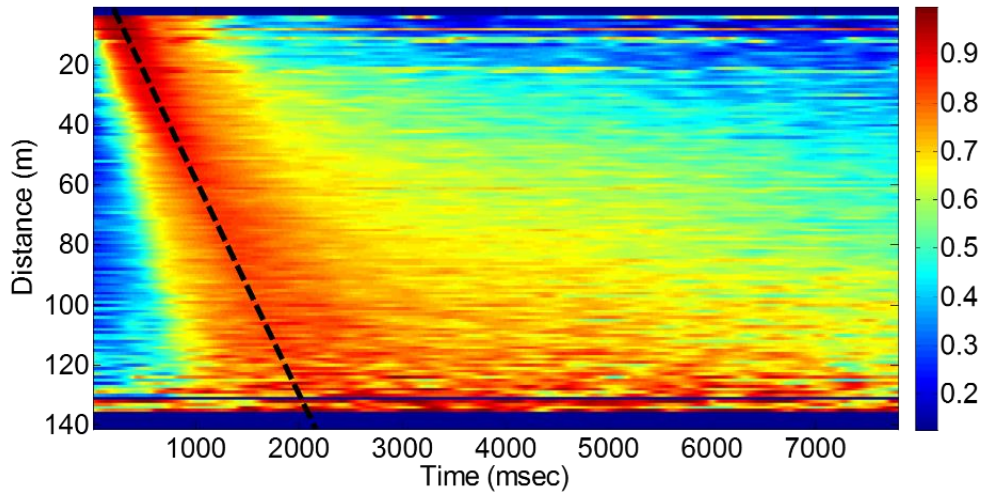


Figure 4-22: Ratio between the coherent and incoherent phases for the frequency band 7-10 Hz. The black dashed line represents the velocity of 65 m/s used for the extraction of the points used to compute the MFP.

At this point, we investigated how many sources and receivers are needed in order to achieve a suitable average in each bin and to have a reliable estimate of the ratio between the coherent and incoherent intensities in agreement with the formula (4.11). We started with a grid of $40 \times 40 \text{ m}^2$, as suggested by Serra et al. (2016), this grid size being the biggest one for which the one-dimensional approximation holds. We enlarged progressively it to $60 \times 60 \text{ m}^2$, $80 \times 80 \text{ m}^2$ and finally $90 \times 115 \text{ m}^2$ (the whole network) (Figure 4-23).

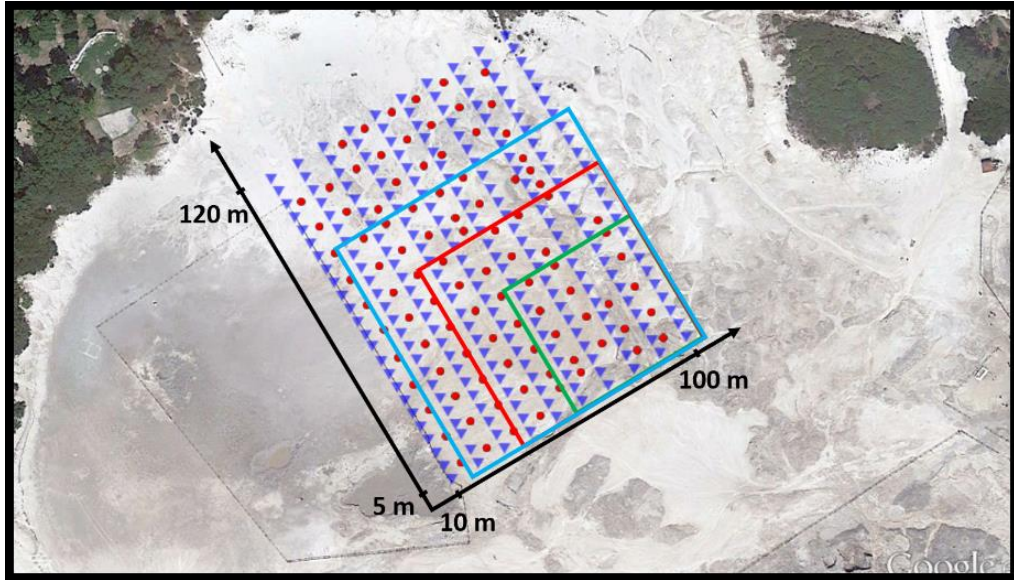


Figure 4-23: Source-receiver configuration for the RICEN experiment. The different sized grids represent the subgrids used to test the goodness of the approximation to the formula 1.178 for the MFP estimation. The blue one is $80 \times 80 \text{ m}^2$, the red one is $60 \times 60 \text{ m}^2$ and the green one is $40 \times 40 \text{ m}^2$.

To understand which grid size can be considered as a good solution, we plotted the intensity ratios and their values in correspondence of the extraction time associated with the velocity $c=65 \text{ m/s}$, for each of the considered grids. The choice was made considering the lowest frequency band 7-10 Hz, which is the most critical in the evaluation of the MFP because it involves the largest wavelengths in the analysis and therefore, it is insensitive to the smallest anomalies of the medium. In such a case, few scattering events may occur and therefore the assumptions of the MFP theory might be not met. In general, we do not recover any particular trend for the smallest grid, nevertheless the alignment of the points becomes more evident when increasing the grid size. The expected exponential behavior clearly appears only when the data are averaged over the whole grid (Figure 4-24). This is representative of the large number of scatterers that are in the medium, or in general, it is indicative that the Solfatara is a three-dimensional medium with strong lateral variations.

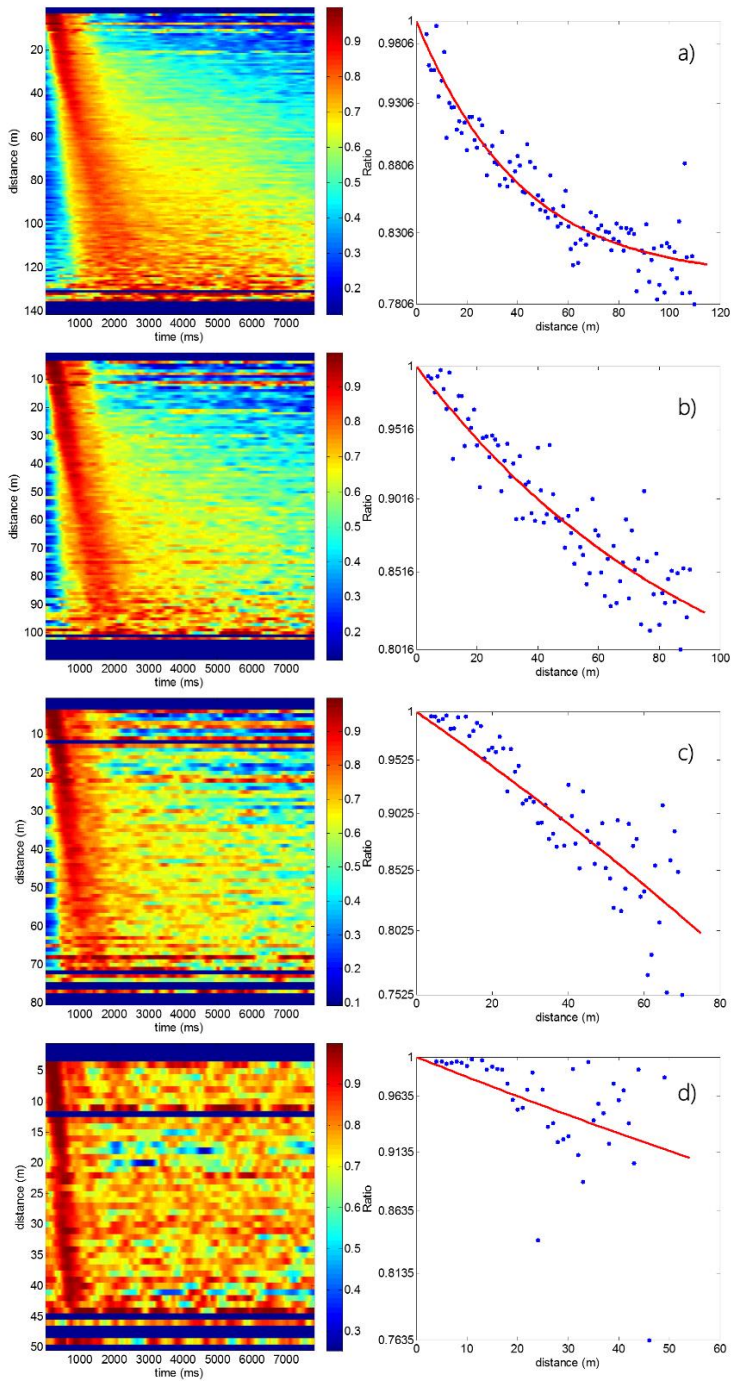


Figure 4-24: Ratios (on the left) between the coherent and incoherent intensities for the different subgrids showed in the figure 4-23. On the right, there are the extracted points for the related ratio and the curve of best fit in red. The size of the grid is increasing starting from the bottom to the top d, c, b, a. It is evident that the best result is obtained for the whole grid (a).

Of course, we repeated the extraction of the ratio values in different frequency bands, with their central frequency ranging from 8.5 Hz up to 21.5 Hz. The frequencies bands were selected maintaining constant the ratio between the central frequency and the width of the band. Looking at different figures of the ratio as a function of the distance in several frequency bands, going toward higher frequencies, we can better recognize the exponential trend in the data, with the final plateau level clearer identified. We see a more evident decay and plateau with increasing frequencies, because smaller and smaller wavelengths are involved in the analyses. Therefore, the wave field becomes more sensitive to the smallest heterogeneities of the medium and a higher number of scattering events are expected (Figure 4-25).

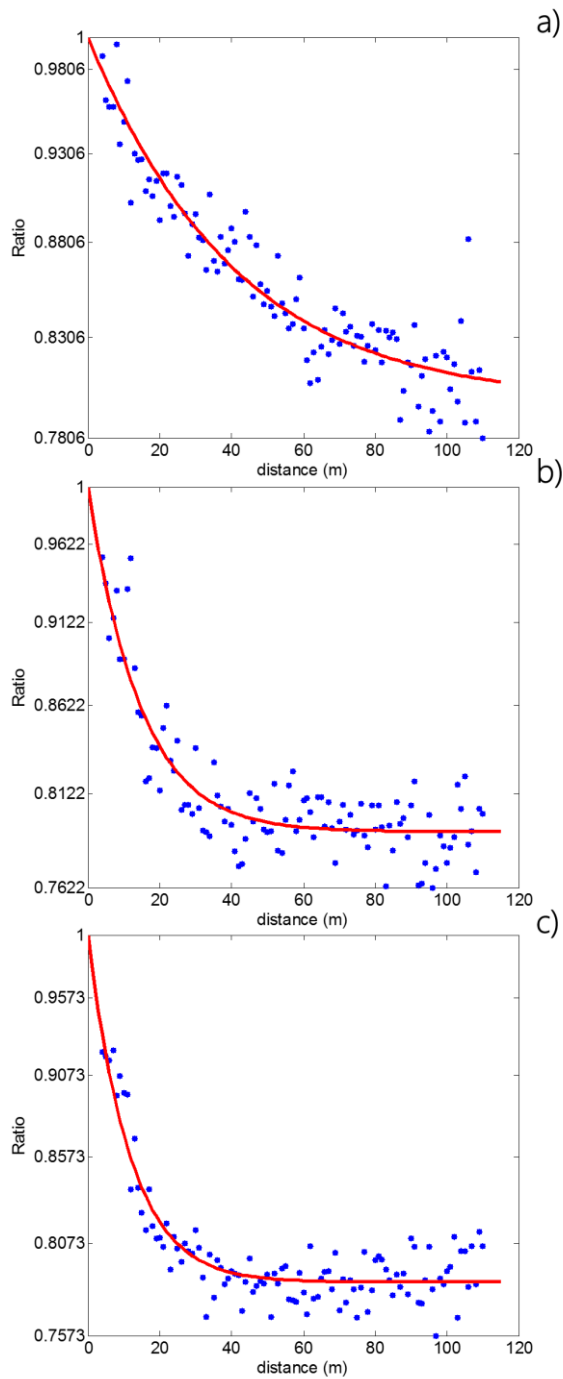


Figure 4-25: Exponential fits derived from the ratio between the coherent and incoherent intensities for the whole grid in the lowest 7-10 Hz (a), the middle 11.9-17.1 Hz (b) and the highest 17.7-25.3 Hz (c) frequency band. It is clear the exponential decay and also the plateau level.

To determine the two parameters N and τ_S of each experimental curve, we used a tool to perform inversions in order to achieve the best fit between the theoretical and experimental curves. From the inversion we determined a characteristic time, and assuming the velocity of 65 m/s we obtained the MFP. The hypothesis that looking at small scale the medium appears more heterogeneous is corroborated by the curve of the MFP as a function of the frequency (Figure 4-26); it shows a decaying trend as typically observed in strongly heterogeneous areas such as volcanic regions (Yamamoto et al., 2010; Chaput et al., 2015; Obermann et al., 2014).

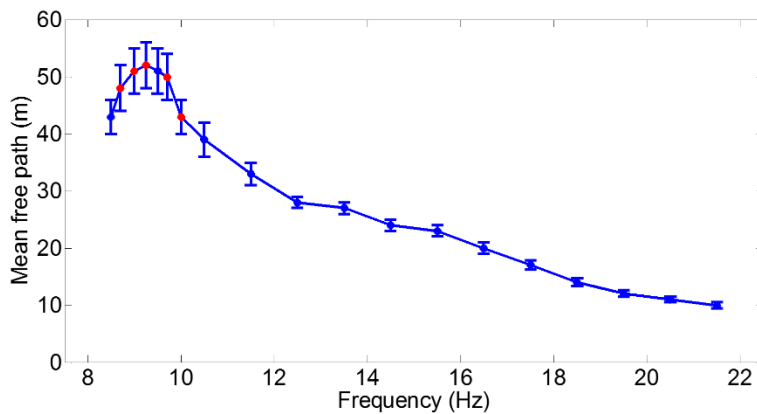


Figure 4-26: The MFP measured in different frequency bands and its associated error (blue curve). The red points indicate the measurement of the MFP in finest frequency bands in order to understand the nature of the initial hump.

The curve shows also an initial increase of the MFP, between 8.5-9.5 Hz, therefore we went deeper in the questions investigating in detail the initial small bump, to understand if it is real or it is linked to the processing. We performed a finer sampling in this frequency interval and the analysis confirmed the presence of the small hump in the MFP (Figure 4-26). In addition to the MFP, we also recovered the parameter N , that corresponds to the number of independent realizations. Despite the large number of source and receivers involved in the experiment, it is small ($N \approx 1.2-1.3$) and it is independent of the considered frequency band. This

might be related to the interaction of the surface waves with other body waves, such as reflected/ multiple waves in the shallow layering, preventing the intensity ratio to be representative of a single wave. Such small values are comparable with those retrieved in other active seismic experiments, where the measured MFP is at maximum one order of magnitude smaller than the size of the survey- In our case the grid has the size of hundreds of meters whereas the MFP is of tens of meters (Gouédard et al., 2011).

The MFP curve as a function of the frequency may provide information about the statistical properties of the scatterers, such as their density, velocity and average size. For the goal we model the scattering cross-section (σ) for a single anomaly of a given size a and determine the backscattered wavefield. Since we are investigating the scattering of the Rayleigh waves that propagate along the free surface, we assumed a cylindrical anomaly embedded in a homogeneous medium. We also investigated the behavior of a spherical anomaly in a homogeneous medium, which is more representative of the scattered field from body waves, but the data fit is significantly worse than the one obtained with a 2D cylindrical anomaly. We additionally considered a fluid-fluid interaction, assuming limited conversion between P and S waves. The mean free path can be related to the scattering cross-section σ by the relationship:

$$l_s = \frac{1}{n\sigma} \quad (4.12)$$

where n is the number of scatterers by surface unit (or volume unit for a 3D spherical anomaly). The computation of the MFP is strictly dependent on the used approximation for the medium through the parameter:

$$\sigma = \int_0^{2\pi} \sigma_\theta d\theta \quad (4.13)$$

σ_θ , the differential scattering cross section, contains the physics of the problem and it varies if we consider a penetrable or an impenetrable anomaly. Initially, we tried to model the MFP curve performing inversions with the simplest model of an impenetrable cylindrical anomaly having hard or soft boundary (Morse et al., 1968). In such a kind of approximation, the crucial parameter to set is the size of

the scatterer, on which the interaction between the incident waves and the scattered ones depends. The cylindrical anomaly reproduces a MFP curve monotonically decreasing, changing the radius of the scatterer, we can retrieve a good agreement only in the first points of the two curves or in the final ones, but we never obtained a global satisfactory matching between the theoretical and experimental MFP curves. Then the condition of penetrable cylinder was introduced. In this situation, we obtained a better data fit. In general, it is possible to demonstrate that changing the size of the scatterers, the density ratio, and the velocity contrast between the medium and the scatterer, we can reproduce theoretical curves having a spike located at different frequencies; it could be interpreted as a resonance effect of waves trapped inside the anomaly. To model the shape of the curve and its decay, due to the above mentioned parameters, we used an optimization algorithm able to invert at the same time the density ratio between the anomaly and the surrounding medium, the velocity of the anomaly and the size of the anomaly. The velocity of the embedding medium was fixed at 65 m/s, since this parameter can be directly constrained from the measure of the intensity ratio. We performed several tests imposing different initial conditions. We found that the problem has not a unique solution but the misfit function has several minima. Therefore, we did not focus on the search of the absolute minimum but we selected the solutions for which we observed the smallest misfit. As a criterion, we maintained all the solutions which differ at maximum of the: 8% from the minimum one and we looked at the common features of these solutions (Figure 4-27).

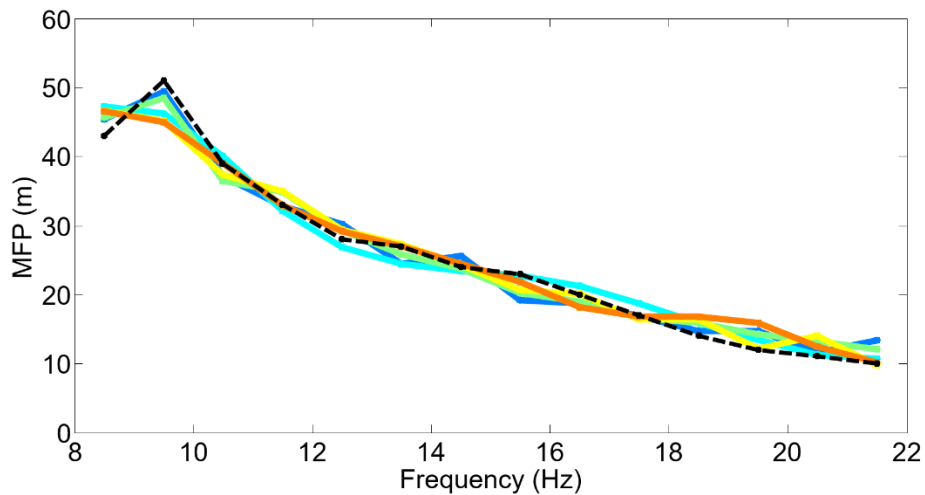


Figure 4-27: Some MFP curves obtained from the inversions to recover the characteristics of the scatterers. The black dashed line is the measure MFP curve. In general is clear a good matching between the real and the recovered curves.

Generally these solutions are representative of a medium having a small density contrast with the anomalies, the radius of the scatterers is smaller than 5 m, and the density per unit of surface ranges between 0.01 and 0.08 that, when referred to our experimental setup, it corresponds to a total number of scatterers between 100 and 800. The last issue to be addressed is the importance of that initial hump. In the inversions fitting the hump, we still retrieved , small contrasts of velocity and density, but the scatterers per volume unit significantly changes. Since the parameter n corresponds in the formulation to a scaling factor, therefore looking at the theoretical curve of the MFP as retrieved from the total scattering cross-section, if we fit the initial part of the curve where there are higher amplitudes, the scatterers density will be small, if we fit the final part a great density is expected. Anyway, we are analyzing data averaged on the whole grid where we tried to remove the small-scale heterogeneities and to observe and interpret the emergent average behavior. With this purpose, we imaged the medium using a very simple model, for example with our assumptions, we do not take into account the effects due to different anomalies shapes, to the non-horizontal structure or to the propagation of the energy associated to the transversal waves. These deviations from this simple model could interact constructively or destructively

and produce effects that we are not able to interpret. Nevertheless, we found some general characteristics such as the small density contrast, the large number of scatterers. This peculiarity can be interpreted as small sacks partially or totally saturated by fluids or gas, where of course, the seismic waves can propagate having slightly smaller or higher velocity values.

The TMFP is defined as the minimum distance beyond which a wave loses memory of the source. The seismic waves travel in the medium for very long distances, therefore they undergo a large number of scattering events and at each collision they change their propagation direction. After a certain number of events, there is no more a preferential propagation direction in the medium, it is not possible to recover an energy flux between source and receivers but energy seems to propagate from all the directions. Being the TMFP connected to later arrivals in the seismogram, it can be estimated from the coda of the seismic records (Margerin et al., 2000; Hennino et al., 2001; Lobkis et al., 2001; Campillo et al., 2003; Gouédard et al., 2008; Margerin et al. 2009). In this framework, since we can consider the medium as homogenous and isotropic, the waves belonging to the coda attenuate independently of the distance from the source, but their decay is related to the geometrical spreading and to the scattering properties of the medium. Following this approach in highly heterogeneous region, such as the volcanic ones, scattering effects are enhanced and therefore a stronger coda excitation is expected while equipartition of the energy is reached faster (Yamamoto et al., 2010; Gouédard et al., 2011; Chaput et al., 2015; Obermann et al., 2014).

The capability of the waves to propagate for long distances is strongly diminished by the anelastic attenuation properties of the medium. The anelastic attenuation converts the mechanical energy in thermal energy. In strong scattering media, as volcanic areas, phenomena of multiple scattering clearly occur, especially for acquisitions at small-scales, where the recorded signals exhibit the peculiar trend of the transition from a single scattering regime to a multiple scattering regime and in some cases, when the scattering is very there is also a transition to the diffusive regime. For example, the seismograms on the Moon show a greater coda when compared to those acquired on the Earth, due to the different scattering properties of the medium but also to the small attenuation on the

Moon (Dainty, et al., 1981). In this context, we cannot neglect the small-scale heterogeneities, because they are responsible of the mentioned regimes, as well as we cannot know their positions, although from the properties of the coda we can characterize them. The propagation regime can be inferred looking at the coda of the seismograms and therefore modeling the coda, we would be able to measure the TMFP. On the basis of the previous description a strong coda excitation should be visible, in our data. Furthermore this idea would be corroborated by the measured MFP that indicates a characteristic length of tens of meters, so a large number of scattering events are expected. Nevertheless, we do not observe an energetic coda and data show the largest part of the energy localized in the first seconds of acquisition, after which there is a strong decay of the signal amplitude. To explain this unexpected trend we performed some analysis on the incoherent intensity since it represents the energy propagation in the seismic section. Since we are working with surface waves, we tried to model the energy with analytic solutions in a 2D medium. To model the different regimes, we refer to the equations showed in the paragraph 2.6 and relative subparagraphs. We started trying the solution for the diffusive regime; we discarded it because the mismatch was clear at visual inspection (Figure 4-28). The diffusive solution shows a not well-identified ballistic phase in the signal, because in such regime a very large number of scattering events are expected and even the first wave front is almost unrecognizable. Therefore, we used the solution of the transport equation (Paasschens, 1997). In this case, the matching between the theoretical curve and the experimental one shows a clear improvement. But, the retrieved TMFP was too large (several hundreds of meters). Moreover, repeating the estimation of the TMFP for different distances and for different frequency bands, the results were irreconcilable with the scattering properties of the medium. The larger the distance and the frequencies the bigger the TMFP. The TMFP, as the MFP, is a typical length of the investigated medium representative of the time required to reach the equipartition of the energy. Therefore, it cannot be dependent on the distances and, moreover, if the investigated medium has not scale-invariant distribution of scatterers, of course it has to be decreasing with the frequency: the smaller the considered wavelengths, the faster the loss of source-wave direction correlation.

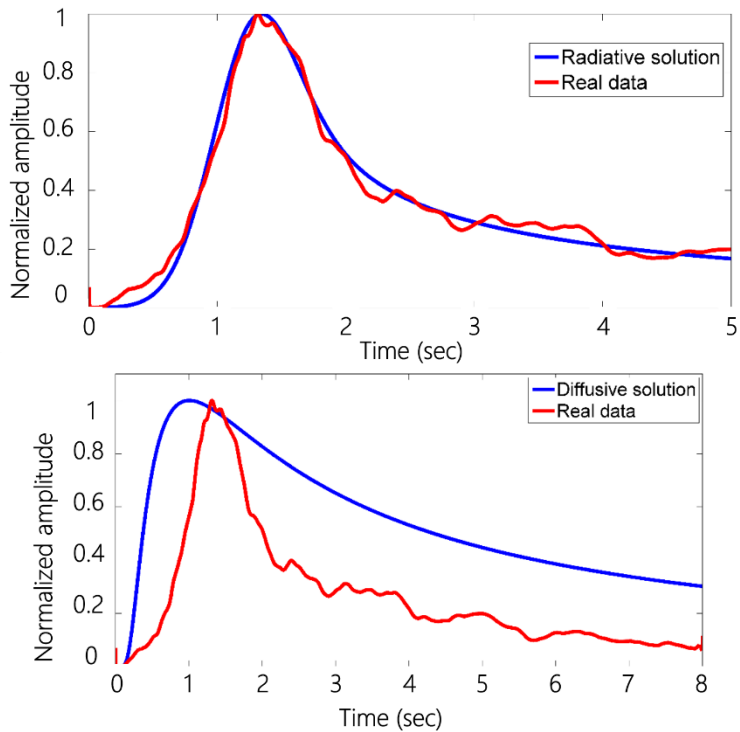


Figure 4-28: Comparison between the incoherent intensity for a given distance from the source (blue curves) and the theoretical solutions for the radiative regime (on the top) and the diffusive one (on the bottom). The radiative regime seems to fit better the experimental curve also if produces unrealistic results. The diffusive regime has a smoother ballistic arrivals and a larger coda excitation.

This behavior of the shape of the coda can be explained taking into account of the anelastic attenuation. The anelastic attenuation increases with the frequency, indeed, filtering signals in higher and higher frequency bands they show a shorter coda, because the high frequencies are rapidly absorbed. The Solfatara is composed by material with low mechanical properties: the most are sands and clays, indeed, very low Q factor values were obtained (Serlenga et al. 2016).

In the MFP determination this drawback was overcome thanks to the ratio which erased the effects not correlated with the scattering. If we model the coda without any correction, and the anelastic effects are not negligible, the scattering signature in the coda is completely hidden and no more trackable. The TMFP, in the description of the radiative transport equation, plays a fundamental role in

the modeling of the part of the signal that links the ballistic waves with the multiple scattered ones. The lack of the higher frequencies is reflected in the transition phase, producing unrealistic values in the fitting procedure. Therefore, none of previous models is suitable for such description.

Anyway, we tried to infer some coda characteristics, plotting the logarithm of the energy at different distances. We observed a linear decay and in general, this trend was observable for all the acquired signals, therefore it is possible to superimpose all of the envelopes by means of a shifting procedure and retrieve a common slope. To achieve this result, we implemented a common inversion where the linear part of each envelope was fitted by means of a linear regression, at this point each envelope was shifted adding its respective intercept value. After this step, the envelopes acquired at different distances are superimposed and it is now possible to recover a common slope (Figure 4-29). The same procedure was repeated for all the frequency bands for which we measured the MFP. We recovered a single length for each frequency band, decreasing as a function of the frequency. This processing was applied considering the curves from 2.5 s up to 5.5 s, in order to avoid the initial bump, which is composed by a mixture of phases relative to the ballistic waves and the transition from single scattering regime to the multiple one. The second limit is to discard the final plateau, which is reasonably associated to the noise amplitude.

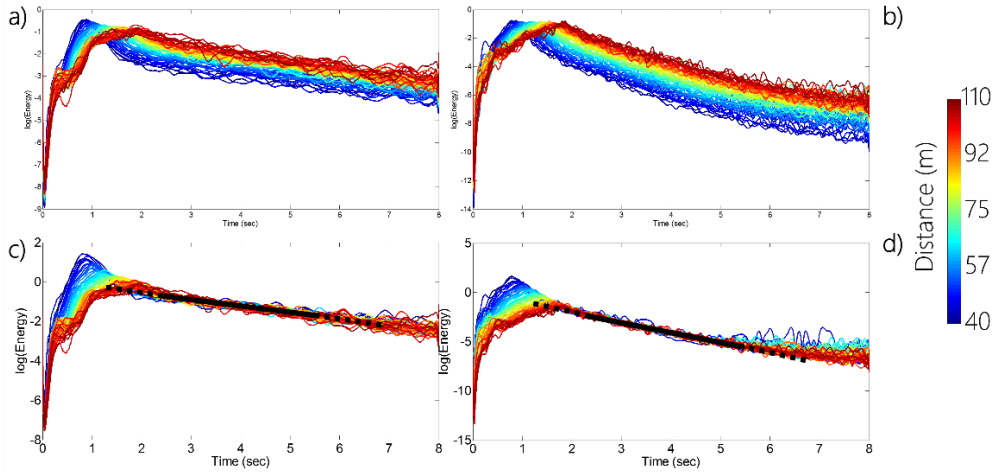


Figure 4-29: Incoherent intensities for different distances in the lowest (a) and the highest (b) frequency bands, and the associated realignments (c) and (d) in order to measure the common slope. The best fit lines are represented with the black solid lines. It is clear the linear decay of the coda.

In general, as showed in the section 2.6.4, the attenuation of the propagation medium is referred with the Q-value, which involves both the scattering and the anelastic terms. We can associate it the characteristic length derived from the fitting procedure. The relationship we used to associate at each slope a length is:

$$Q = \frac{\pi v}{S} \Rightarrow L = \frac{Qc}{\pi v} \quad (4.14)$$

where S is the slope recovered by the linear regression and c is the characteristic velocity of the medium, that in our case is 65 m/s. This assumption is supported by the linear decay observed in the logarithm of the incoherent energy. Finally, for sake of comparison, we can plot in same graphic the MFP and the values just recovered (Figure 4-30). The last ones are 3.5-4 times larger than the MFP values, as expected by the theory, nevertheless these values cannot be considered as the classical TMFP because we are interpreting them as the sum of two effects.

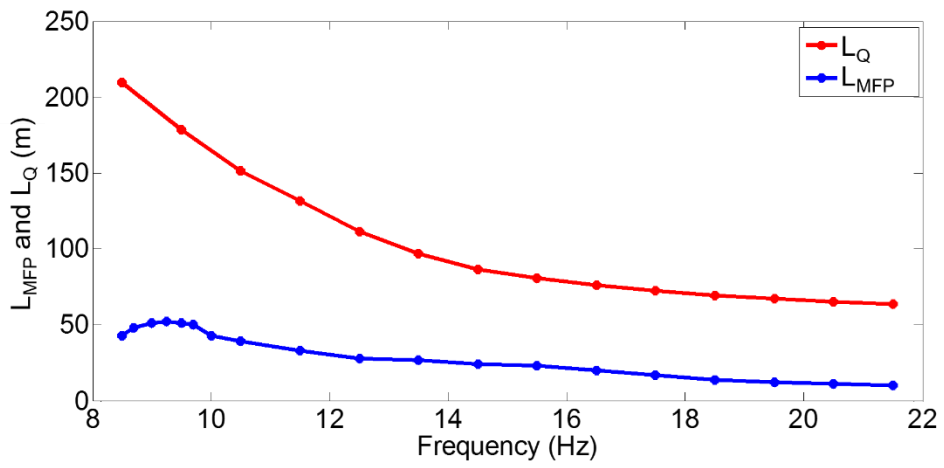


Figure 4-30: Plot of the measured MFP (blue curve) through the ratio between the coherent and incoherent intensities and the characteristic length derived from the Q-value associated to the decay of the coda (red curve).

5 Interferometry

As seen in the first section, when an earthquake occurs a wave field is generated. It is composed by the so-called near field and far field, the first is a not separable combination of P- and S-waves detectable close enough the source, the latter is interpretable as a separable superimposition of the P- and S-waves fields contributions. After these waves, all the other ones are generated by the interaction with the propagation medium: converted, reflected, refracted waves and from the interaction with the surface, we retrieve the surface waves. Each wave follows a different path from the source to the receiver and therefore it will be heard by the geophone at a different time, the first direct waves are, as suggested by the name, the P-waves and of course, the second ones are the S-waves. After that, in the seismograms there are a series of arrivals of P- and S-waves which have interacted with the medium several times, the ensemble of such waves shows a decaying behavior due to the attenuation; they form the so-called seismic coda. Today the ballistic arrivals are completely understood, and they are used in all the classical imaging methods in order to recover information about the medium. Also some of the later arrivals are interpret as the interaction with the most important Earth interfaces i.e. the Moho, the Gutenberg and the Lehman, but most of the subsequent arrivals are today object of study and they are revealing powerful instruments of investigation. We can image the generation of such kind of waves due to the multiple reflection of waves in a close medium, or surface waves which travelled around the Earth many times, thanks to their lower geometrical attenuation. Anyway, these arrivals have a clear nature and they leave a recognizable signature in the seismograms, they are periodic signals so we are able to track their passage. More interesting is the generation of the coda by means of the multiple scattering events with anomalies embedded in the propagation medium (Figure 5-1). Such kind of interactions make the propagation path of the waves more and more complicated but at the same time these waves sample the medium many times and they became more and more sensitive to the variations of the elastic properties of the medium as the time passes. We understand that dealing with these waves is harder to recognize some preferential pattern.

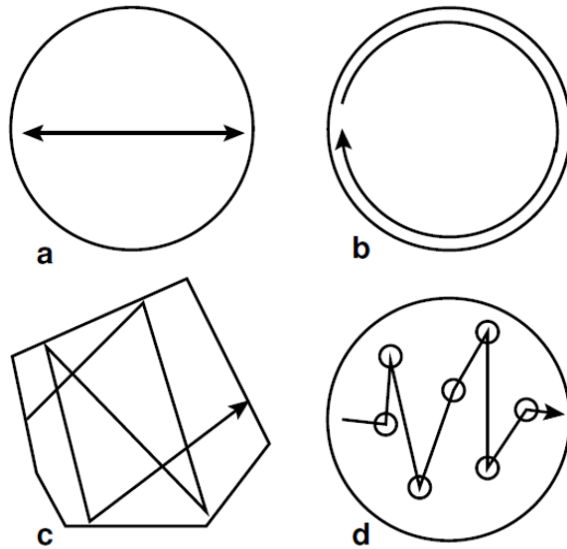


Figure 5-1: Schematic representation of a wave travelling in a close medium. a) shows the stationary bounce of a wave, b) shows the periodic passage of a surface wave, c) the more complicate path due to the rebound against irregular surfaces, and finally d) displays the path due to the scattering with some anomalies embedded in the medium.

In the past, the geophysicists have discarded the seismic coda and even more the noise for their purposes, because they thought that this parts of the signal were composed by completely random phenomena. Today we know that it is not true and a lot of work has be done e will be done in the future, since we have at our disposition a very large amount of data. Indeed, during a seismic survey or in general, the permanent seismic networks over the world acquire much more of these “meaningless” signals then Earthquakes (Figure 5-2).

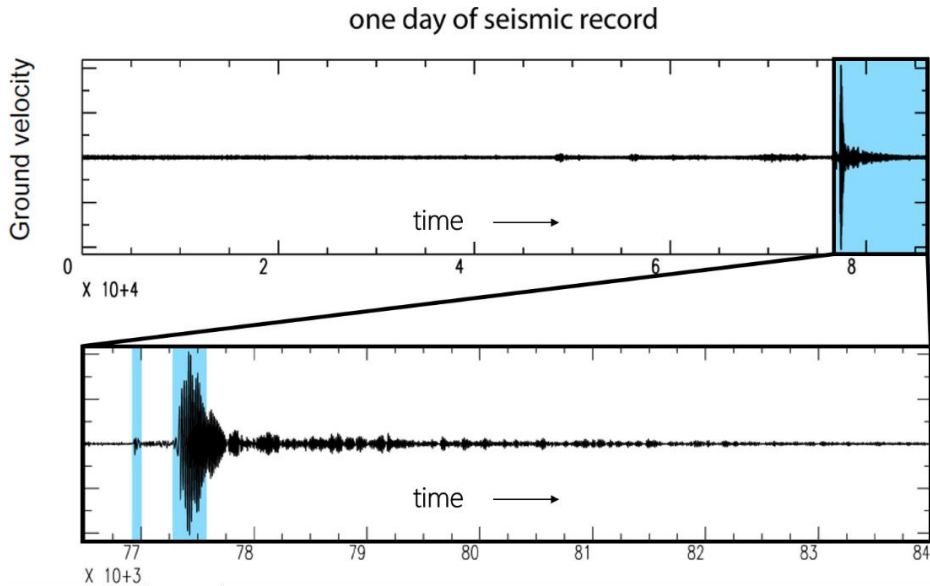


Figure 5-2: On the top, a seismogram for a day of acquisition is showed. The blue window is an earthquake occurred during the day. On bottom, there is a zoom of the previous selected window, and the areas, indicated again in blue, highlight the signal portions classically used in seismology.

The repeatability of the coda has been widely demonstrated by several authors, signals acquired at the same position and originated by the same source have almost the same waveform, but if the medium between one realization and another changes, we can observe some variations, this is the basis of the Coda Wave Interferometry, CWI (Snieder, 2002). It is worth to notice that if the variation in the elastic properties of the medium are very weak, the ballistic waves result insensitive to such variation with respect the coda waves, thank to their multiple sampling they accumulate delay or advance with respect the situation where the medium has not changed. Of course some differences could arise, they are easily connected to the random noise, but in laboratory experiment, it has been showed that repeating many realizations and averaging all of them, the noise contributions is completely removed and the traces became perfectly identical. Poupinet and Ratdomopurdo are considered the fathers of this technique, in their works (Poupinet et al., 1984), they showed that the time shift observed in the seismograms can be used to directly estimate the relative velocity variation. They detected a decrease of S-wave velocity by 0.2% in a region of 5-10 km around the hypocentral area of the Coyote Lake earthquake (M 5.9) in California. Similar analysis applied to the data acquired at Merapi volcano in Indonesia (Ratdomopurdo, et al., 1995), highlighted an 1% increase of seismic velocity several

months before the eruption occurred in 1992. Moreover, these analyses demonstrated high sensitivity of such technique that cannot be reached directly from the tomography using first arrivals. Today, an evolution of such method is extended to the ambient noise framework. Without loss of generality, the reasons which brings so high sensitivity and accuracy in the velocity variation measure, can easily understand making reference to the multiple passage for a fixed point of a surface wave around the Earth (Figure 5-3).

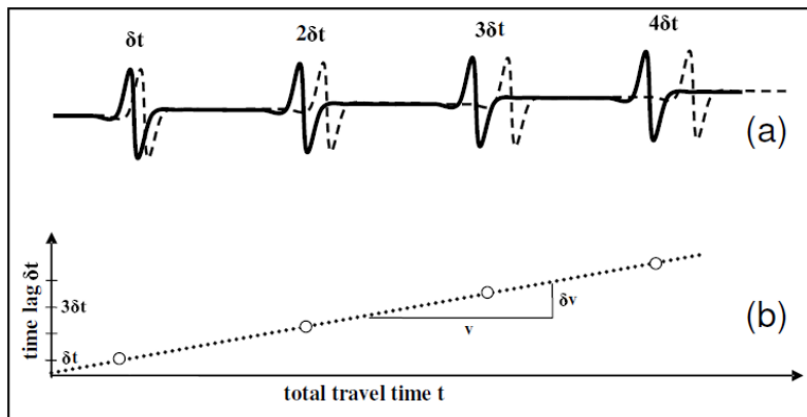


Figure 5-3: If in the propagation medium there is a velocity anomaly (a decreasing of velocity), at each passage the seismic waves accumulate a delay (a). There is a linear relationship between the lapsed time and the cumulative delay, which is also a measure of the relative velocity variation (b).

If in a given region of the the surface crossed by the waves we introduce a lower velocity anomaly, at each passage the wave accumulate a delay, the total delay is proportional to the number of passages. Since the higher is the velocity diminution the larger is the time shift, and vice versa, the relative time delay is exactly the measure of the relative velocity variation. From this simple example, we also understand that the resolution of such method increases with the passing time, because the smaller is the velocity difference the higher will be the number of passages in order to detect the time shift. In the case of the coda the measure is not limited to the surface waves that travelled around the world, but it is enough to consider waves which sampled the medium for longer times. Therefore, the CWI seems to be a perfect candidate to monitor the small changes in the medium, from the human constructions of different size up to volcanic edifices or also seismic faults. Finally, we want add that a lot of improvements have been

performed in this field, in some papers it has been demonstrated the use of the CWI also to localize the reason of the velocity change (Pacheco, 2004) or also the earthquakes location (Snieder et al., 2005).

As said before several times, the classical seismology is based on the analysis of the data coming from earthquakes or more generally from controlled seismic sources and from the interpretation of the first seconds of the acquisitions, i.e. the ballistic waves. The dependence on the earthquakes limits the investigation regions, since we know that seismic events are located in geologically active areas. Using active sources we could study also areas where no earthquakes occur but the energy emitted by artificial sources is not as great as that one of such big earthquakes therefore the same depth or the same excitation times cannot be reached. And, if we are interested in the temporal evolution of the elastic properties of the medium, another great limit is due to the source location repeatability, the occurrence of two earthquakes located at the same position and having the same source parameters is very rare. In the case of the geophysical prospecting, the number of the sources and receivers is of crucial importance in order to achieve a suitable spatial and temporal sampling. To achieve good results, long duration surveys are required with consequently high implementation costs. Today there are a lot of digital seismic networks spread all over the world, which acquire continuously the motion of the Earth, the largest part of the signals are made of seismic noise (Figure 5-2) and techniques, which are able to reconstruct the coherent content in the signals, have been developed.

The passive tomography is based on the extraction of the Green's function from the noise through cross-correlation method between a pair of stations. Typically, the two stations are located at the surface and therefore the content of surface waves is dominant. The seismic noise can be defined as the continuous motions of the Earth, which is not related to the Earthquakes occurrence or specific sources, also in the case of local surveys the noise could be strongly influenced by the human activity, while at larger scale the largest contribution to the noise is given by atmospheric and oceanic events. In the case of local surveys the noise is dominated by frequencies higher than 1 Hz, whereas global surveys the noise spectrum is characterized by two peaks in the so-called micro seismic band from 1-20 s, which are related to the action of the ocean owing to the interaction with the coast-lines or with storms (Longuet-Higgins, 1950). From the dispersion properties of such waves it is possible to determine images on scales ranging from

thousands of kilometers depth up to shorter distances. The basic idea of the noise cross-correlation is that the seismic noise is composed by randomly and homogeneously sources displaced all around the region we are investigating. If these assumptions are fulfilled the recovered Green's function by means of the cross-correlation converges toward the real propagation function between the two points including all the features due to the propagation in the medium.

The noise cross-correlation finds its root in the helioseismology (Duvall et al., 1997) where the scientists recovered the Green's function between two points reconstructing the velocity field as a function of the time associated at each position making use of the Doppler effect. Other laboratory experiments (Lobkis et al., 2001) highlighted that the thermal noise recorded on aluminum plate provide the exact Green's function between the two recording points. Mathematical studies showed that the cross-correlated wave field is the sum of the casual and acasual Green's function:

$$\frac{2i\omega}{|S(\omega)|^2} \langle u(\mathbf{r}_A, \omega) u^*(\mathbf{r}_B, \omega) \rangle = G(\mathbf{r}_A, \mathbf{r}_B, \omega) - G^*(\mathbf{r}_A, \mathbf{r}_B, \omega) \quad (5.1)$$

Where $u(\mathbf{r}_A, \omega)$ and $u(\mathbf{r}_B, \omega)$ are the displacement filed acquired at two stations A and B , $|S(\omega)|^2$ is the power spectrum of the noise sources, with the brackets $\langle \dots \rangle$ we are indicating the average over all the sources and with the symbol $*$ the complex conjugate in the frequency domain, which corresponds to the time-reversal in the time domain. If the conditions of uniformity and isotropic are respected the cross-correlation function is symmetric, otherwise some differences can occur. From the results obtained in the laboratory about the thermal noise, we understand that a similar result can be achieved in the Earth if the equipartition of the energy is reached, because it is indicative of the non-existence of a net energy flux coming from one direction and therefore the sources are isotropically distributed. For sake of completeness, the equipartition of the energy is achievable just in close medium, where after a certain time the normal modes of the considered body are excited. Otherwise, in opened medium, the equipartition of the energy is just an ideal concept, it cannot be never reached, but practical application show that a satisfactory convergence to the theoretical Green's function is possible.

The first application to the seismology were made by Shapiro and Campillo in the 2004 (Campillo and Shapiro, 2004), recovering the Green's function between two points located at hundreds of thousands km, and the relative measure of the dispersion curve. After this application a new seismological framework was born and long list of applications was realized. These new results showed higher resolution in space and in time and moreover, since such method is not connected to the specific source location, it allow to study areas where there is not an intense or there is not geological activity. The measure can be repeated over the time replacing a network of receivers in the same positions, so it is a suitable technique for the temporal monitoring (Brennguier et al., 2008). In literature, there are today many examples of the applications of seismic interferometry at different scales in order to investigate the velocity variation in the propagation in a fault zone, before and after an earthquake (Poupinet et al., 1984; Stähler et al., 2011;), volcanic structures (Brennguier et al., 2008; Miyazawa et al., 2008), or oil reservoirs (Mucciarelli et al., 2004). The observed relative changes in the velocity structure usually range below few percentage points, such variations are associated with the increasing damaging in the area around the fault zone, due to the increasing stress or the fluid injection that will culminate with an earthquake. At small scales laboratory experiments were performed about rock samples where temperature and deformation variation were applied (Snieder, 1999) but also to monitor structures such as buildings and bridges (Aki, 1985; Ratdomopurambo et al.; 1995).

We present now two works based on the previous exposed methods

5.1 Damage detection in a masonry bridge

Any building or infrastructure are subjected to natural phenomena that reduce or limit their usability. Structural degradation may occur over different timescales, as consequence of catastrophic events such as earthquakes, floods and fires, but also at long terms, because of the erosion by chemical agents, by the stiffness reduction of some elements of the structure. The long term damages deteriorate

structures without any visible signature of the damage, and when it is finally clear, in some cases is too late to perform restoring interventions or accidents occur.

Nowadays engineers have at their disposal different nondestructive techniques in order to supply information about the mechanical characteristics of masonry as a composite material and of its components (Binda et al., 2000). The aim is to improve the knowledge and to reduce the epistemic uncertainties affecting the whole construction in order to plan interventions or act promptly; it is well known that an early and planned measure is easier and cheaper than an urgent one.

The method of the past provided information referred to a limited portion of the structure, whereas the modern diagnostic monitoring systems were born with the prerogative to overcome these limitations providing an exhaustive depiction of the whole structural health state (Shull, 2007; Worden et al., 2004; Brownjohn, 2007). These techniques are either visual or based on localized experimental investigations such as acoustic, ultrasonic, magnetic field, radiography, eddy current, and thermal field methods. These methods are nondestructive techniques and are classified as local methods because they are generally carried out in some limited portions of the structure. All of them require an a priori knowledge of the damage location because they need to be applied in the proximity of damage and therefore the interesting portion of the structure has to be accessible. Nevertheless, these experimental techniques are very reliable to provide the assessment of the structure in terms of damage extent and estimated residual operating life. Therefore in the last years, the scientific community is focusing its efforts in the development of some methodologies which can evaluate the global health state of a structure without any a priori knowledge.

In this work, we will focus on very old and traditional buildings, they were built without strict geometric tolerances, and many hidden small defects could be present since the construction time, or some long term effects were not taking into account. Since we do not have idea where the damage could occur or where multiple imperfections could be present, the diagnosis of such kind of masonry constructions must be differentiated from that usually performed on other engineering structures (De Stefano et al., 2007). The development of methods based on the analysis of the changes in the vibration characteristics of the

structure can be seen as the answer to the need for quantitative global damage detection methods. The ability of a vibration-based damage identification method to distinguish between the damaged and undamaged states of a structure strongly depends on the data representation. Unfortunately, the best solutions to detect changes in the dynamic properties of a structure are target oriented (Ceravolo et al., 2011; Bonessio et al., 2012). They can be developed either in time, or in frequency, or in time-frequency domains depending on the employed level of data condensation. For instance, damage can be detected by the comparison of the flexibility matrix estimated from the mode shapes of the damaged and undamaged structures. Modal flexibility is a robust damage index for constructed facilities. However, classical flexibility methods suffer from low sensitivity to small and multiple damages and high sensitivity to ambient noise. Another limitation is represented by the requirement of mass-normalized modal parameters. More sensitive flexibility methods for damage identification have been recently proposed, but they often require distributed strain measurements (Adewuyi et al., 2011). As widely explained above, in the last decade, interferometric techniques, that are based on the recording of ambient noise or coda waves, have become very popular detecting changes in the elastic properties of natural structures and human buildings (Farrar et al., 1999; Tarchi et al., 2000; Snieder et al., 2006; Kohler et al., 2007; Todorovska et al., 2008; Bartoli et al., 2008; Gentile, 2010; Prieto et al., 2010; Trifunac et al., 2010). Such techniques correlate two or more signals acquired in the same source–receiver configuration making use of electromagnetic, acoustic, or seismic waves, since sources and receivers are located at the same position among the different surveys, the observable changes in the waveforms are due to some alterations of the propagation medium. We will use the seismic interferometry, specifically, we will adopt the CWI from repeated hits on a bridge artificially damaged in the laboratory. Sophisticated techniques based on the estimation of a time-windowed cross-correlation coefficient, which measures the similarities and time lag between portions of signals (Matsumoto et al., 2001), are able discriminate among changes related to the source location and to the scatterer's distribution. These analysis need of high-quality records, showing a large signal to noise ratio, and for strongly heterogeneous media for which a large amount of energy is transferred in the coda waves. In this way the signals can be compared for longer times and since the paths become longer and longer they

sample more accurately the medium allowing to recognize particular features for such deep interpretation (Snieder, 2006). In our case, as we will see, owing to the wavelengths involved in the problem, we have a global view of the structure and all of its variations in the mechanical properties will appear as spread over the whole structure. Our data allow to measure the time shifts directly on the seismograms, by comparing the arrival times of the waveform maximum (or minimum) amplitudes between two records in a narrow frequency range (Poupinet et al., 1984). When the time shift is related to a change in the medium wave velocity, the relative time shift $\Delta\tau/\tau$ can be written as a function of the relative change in the wave speed (Grêt et al., 2005) $\Delta v/v$:

$$\frac{\Delta\tau}{\tau} = -\frac{\Delta v}{v} \quad (5.2)$$

$\Delta\tau$ is defined as $\tau_0 - \tau_1$, where τ_0 is the arrival time of maxima (or minima) on the trace assumed as a reference and τ_1 is the arrival time of the same maxima (or minima) on the traces to be compared. Since the selected filtered portion of the coda contain several oscillations, to provide a robust estimate of the relative velocity changes, we recursively measure the time shifts $\Delta\tau$ as a function of the time along the seismogram. From the above relation, we expect that the time shifts change linearly with time. The slope of the expected trend can be then estimated by a least squares linear-fitting procedure. Similar measurements can be also performed in the frequency domain, where the cumulated delay appears as a shift of the predominant signal frequency (Grêt et al., 2006), we can understand that an increasing damage in the structure can be revealed as a diminution of the stiffness and it is reflected in its dominant frequency.

The object of our study is a masonry arch bridge model built in the laboratory of the Department of Structural, Geotechnical and Building Engineering at the Politecnico di Torino. The bridge is not a miniature of some existing bridge, but it reproduces the characteristics of a typical masonry bridge that can be found throughout Italy (Figure 1 in the paper attached below) in the scale 1:2. The model is a twin arch bridge with a length of 5.90 m, a width of 1.60 m, and a height of 1.75 m. Each span is 2.00 m long between the supports, and the thickness of the arch is equal to 0.20 m. The handmade clay bricks were also scaled to 130×65×30 mm to follow the adopted modelling scale law. For the determination of the

elastic properties of the materials that build up the structure, the elastic moduli, the Poisson coefficient, and the density were measured in the laboratory (Ruocci et al., 2013) and following the known mathematical relationships both P- and S-wave velocities were obtained. The parameters are:

Material	$E(N/m^2)$	ν	ρ	$V_p(m/s)$	$V_s(m/s)$
Reinforced concrete	$3.0 \cdot 10^{10}$	0.15	2400	3633	2331
Masonry	$1.5 \cdot 10^9$	0.20	1900	937	574
Backfill material	$5.0 \cdot 10^7$	0.1	2000	160	107
Concrete	$0.5 \cdot 10^{10}$	0.15	2200	1549	994

Low-velocity values arise from the choice of low-compressive strength elements bound by a mortar with poor mechanical properties in order to reproduce the typical materials of historical constructions.

The experiment was aimed at studying the changes in the elastic properties of the bridge, as a result of a progressive damage undergone by the structure. The damage mimics the erosion effect due to the slow removal of sediments from the base of the pier by the water flow that could generate the slipping off in the riverbed, possibly inducing severe damage up to the bridge collapse. To experimentally reproduce the erosion phenomenon, the central pier was erect on a polystyrene layer overlying a platform, and the tilt of this platform could be changed. The layer of polyester simulated the sediments in the bed of the river, and the progressive removal of parts of this layer simulated the early stage of damaging. The platform reproduced the effect of scour, in agreement with the results of hydraulic tests conducted in the laboratory (Ruocci et al., 2013). By lowering this latter, a failure of the central pillar occurred. In our case, the failure of the central pillar has to be considered a very important damage, since the stability of the structure depends on it. All the weight is loaded on it, therefore also a small variation in the load distribution can compromise dramatically the entire structure.

The structure started from an undamaged condition and progressively moved toward a final stage (also indicated as "severe damage") corresponding to a lowering of the platform of 2.5 mm and a removal of 75 cm of polystyrene. Data

were collected during the initial undamaged stage, an intermediate state (indicated as "moderate damage"), and the final severely damaged stage of the structure (Figure 2, of the attached paper below). The intermediate damage stage was reproduced with a lowering of 1.5 mm and a polystyrene removal of 60 cm. The change in the inclination of the central pier finally produced the opening of cracks in the arches and the disconnection between the arches and the lateral containment barriers. It is worth to note that the damage did not occur immediately but after a time needed for mass redistribution.

As active sources were used hammer bumps on specific points of the structure and seismic signals were collected by a multichannel acquisition system connected to 18 uniaxial capacitive accelerometers with a sensitivity of 1 V/g, dynamic range of ± 3 g, and a resolution of 30 μ g. It is worth to note that data from 8 stations were available, but just some of them were located in positions which produces data suitable to apply the over exposed technique. Therefore we will continue the analysis using data from 6 stations. The accelerometers were fixed to the bridge by an adhesive wax on an aluminum plate embedded in the structure. We selected just the sensors were fixed perpendicularly to the arches of the bridge from the bottom, to avoid the development of transverse normal modes. For such accelerometers, the average interstation distance is about 80 cm along the bridge and 1.60 along the transversal direction. The sampling rate of the data logger is 400 Hz, which corresponds to a bandwidth of 175 Hz when accounting for antialiasing low-pass filters. Hammer tests where repeated 8 times for each position to increase the statistical significance of the data. The velocity values showed in the table allow us to make some considerations: if we consider the lowest wave speed and the maximum frequency available in the records, we have a minimum wavelength propagating along the bridge about 60 cm. For lower frequencies, i.e. about 30 Hz, which is the frequency around which we performed the analysis, the wavelength is about 3 m. When considering the material with the highest speed, the wavelength associated to the maximum frequency in the data is about 12 m. Hence, the wavelengths associated to the seismic records are comparable to the size of the bridge, therefore the coda is expected to be dominated by standing waves exciting modal vibrations in the structure, and clearly we cannot use these signals to locate the regions where the

changes in the elastic properties occurred during the experiment. These elements lead us to conclusion that we are authorized to apply the formula (5.2) to investigate the variation in the medium that is more suitable for the average variations.

In order to increase the signal to noise ratio, in each source position 8 hammered were realized (Figure 5-4), and for each source–receiver couple and for the three acquisition stages, we cross-correlated the records for the different bumps and we use the time lag recovered from the cross-correlation procedure to properly align the traces.

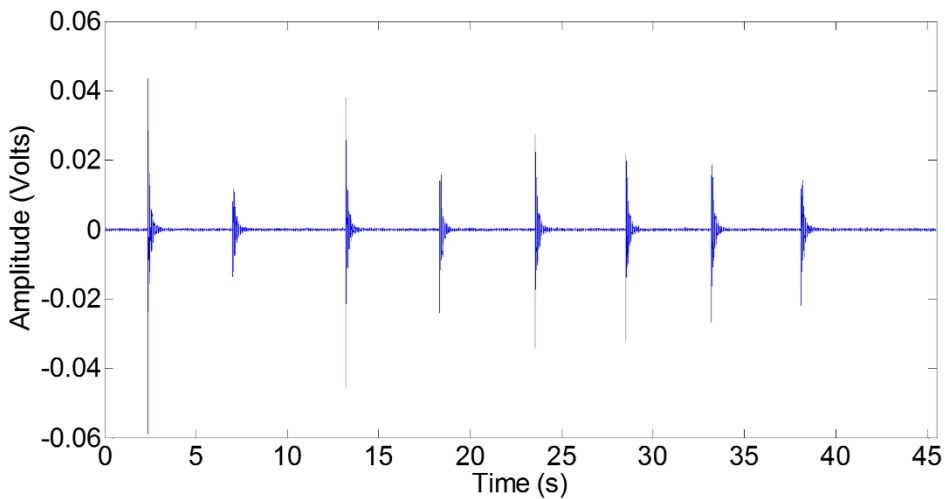


Figure 5-4: The 8 hammered acquired at one station. They have different amplitude because of the different amplitude of the hammered, but it is possible correctly to stack all of them by means of a normalization of the amplitude.

Then the stack is performed, in such way we also remove some aleatory effect that could diminish the quality of the dataset (Figure 5-5). All the following analyses were indeed performed on the stacked traces.

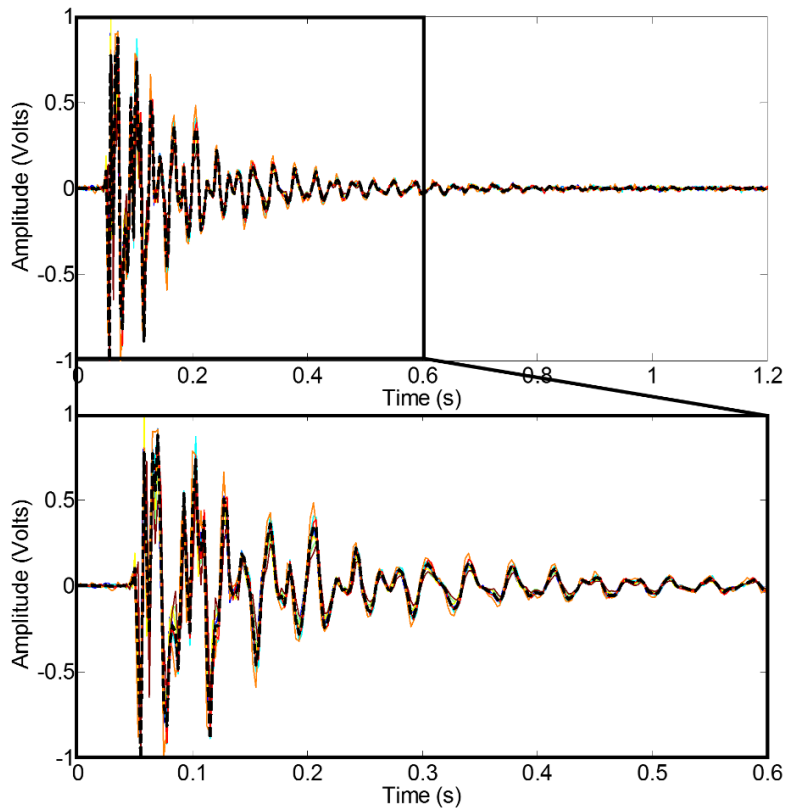


Figure 5-5: Superimposition of the hammered acquired at one station. The dotted black line is normalized stacked trace. From a simple visual inspection is clear the good phase alignment both in the ballistic that in coda waves.

After that, we obtained a single stacked trace for each acquisition position we can compare among the different damaging stages.

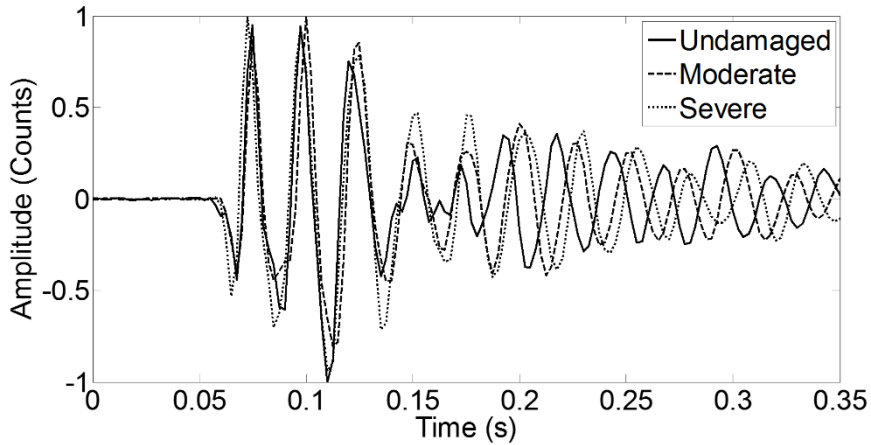


Figure 5-6: Superimposition of the traces associated to the different damage stages of the structure. For the realignment is used the assumption that the ballistic wave are not effected by the variation in the propagation medium and therefore they have to be almost in phase. Small variation are due to the sampling frequency.

In agreement with the theory of the CWI, if we look at the records in different damage condition but at the same source-receiver position (Figure 5-6), we clearly observe that ballistic waves mostly superimpose for the three damage steps, while in the late coda waves, we observe an increasing time shift. Moreover, at the same time the higher is damaged condition the higher is the phase shift.

To properly investigate the delay between the undamaged and the two damaged steps, we analysed the frequency content of the coda waves. Since the coda is composed by waves which travel for longer time in the medium, we want to be sure to look at the difference in the traces owing to the effective cumulative delay caused by the velocity variation and not because there are differences in the frequency content. In Figure 5 (see the paper attached below), we represent the amplitude spectrum of the signals recorded under the different damage conditions; the spectra are characterized by several peaks between 10 and 60 Hz, but the most interesting features is the frequency shift in the largest amplitude peak that can be seen among the three conditions, moving from about 31 Hz for the undamaged state to about 30 and 29 Hz for the moderate and severe stages respectively. This frequency variation was associated through the use of numerical simulations to the first vibration mode along the longitudinal direction of the

bridge (Ruocci et al., 2011) and it consists in a counterphase displacement of the arch barrels. Beyond 45 Hz, the spectrum of the signal related to the undamaged stage of the bridge decreases while the spectra related to the two damaged cases have several late peaks up to 90 Hz, which are smaller in amplitude than the peak around about 30 Hz.

For the reasons exposed before is fundamental look at the spectrograms of the different damage conditions (Figure 7 see the paper attached below); in this way we can observe which frequencies are excited for longer times, therefore are more sensitive to the elastic variations and are associated to the normal modes of the bridge. We observe that only the energy between 20 and 40 Hz survives in the late coda waves, where we expect multiple scattering effects, although several frequencies were excited in the initial part of the records by the source. For this reason, data were filtered in a narrow band around 30 Hz (27.5–32.5 Hz), to guarantee the equipartition of energy and then to measure the relative change in the wave speed. The CWI finds its natural application field in such experiment, because the equipartition of the energy and therefore the thermalization of the wave field can be really reached just in close structures, in all other cases, where anyway such kind of techniques are also applicable and recover excellent results, are limit case of the theory (Snieder, 2002).

In Figure 8 (see the paper attached below) we show an example of filtered data at different damage steps, where it is clear the initial superimposition and the consequent shift, at around 0.3 s. A further investigation is required to estimate the robustness of the method applied to our dataset. We compared the signals recorded in the same stage of damaging (either damaged or undamaged for different shots) to understand if the recovered shift was effectively imputable to the variation of the mechanoelastic properties of the structure and not to some random factors which could produce also intra-event differences. In reality, we do not expect this kind of pollution, because from the comparison among the stacked signals in the different damage steps, we observe the time shift goes in one direction and no uncontrolled oscillations occur. Anyway, for sake of example we present the results deriving from the superimposition of the traces for two sources hitting in the same location and recorded at the same receiver in the undamaged state, in the whole frequency range (Figure 9-Panel a, see the paper

attached below), or filtered in the selected frequency band (Figure 9-Panel b, see the paper attached below). For both cases, the two traces are completely superimposed and no shift can be observed from visual inspection. To evaluate the time shift, we computed the cross-correlation along the whole signal for the filtered trace (Figure 9-Panel c, see the paper attached below) and we picked the maximum amplitude, which is representative of the time shift for the best traces matching. For all cases, we found that the relative time shift is always smaller than three time steps, hence below the time associated with the largest frequency represented in the data. This shift is significantly smaller than the one measured when comparing the records in the two stages of the bridge. Hence, we can neglect the variability in the data related to the source time function and location and interpret the variation as completely due to changes in the elastic properties of the structure.

In order to measure the time shift we performed the described processing, so we measure the relative time shift, normalized to the velocity of the undamaged stage. The acquired data have different time lengths, and the hits were not given at a precise time, therefore we have not possibility to cut from the origin time of the shot, but we can align the traces for the different stages of damage on the ballistic portion of the signal by cross-correlation. We used the undamaged condition as a reference with respect to which we computed the time shifts and then the velocity changes. We compare each trace recorded during the intermediate and the final stage of damage with the trace recorded initially in the undamaged state of the bridge, for the same source–receiver couple. To reduce the uncertainty in the estimate of the time shift, we recursively measured the time shift $\Delta\tau$ as the time increases along the record, comparing the position of consecutive maxima for the two traces. Then we plotted the time shift $\Delta\tau$ as a function of time, assuming as the starting time, the time of the first sample on the trace related to the undamaged case (Figure 10, see the paper attached below). Anyway, for sake of completeness we want to note that the relative time shift is associated to the slope of the curve, independently of the choice of the offset on the abscissa of the plot. Finally, the slope was estimated by a linear fit, and the uncertainty in the slope was assumed as the error associated with the relative time shift. To reduce possible bias due to the coupling of the source with the structure,

we averaged all the estimates for the same shot position at different receivers and represent the results through a histogram (Figure 11, see the paper attached below). The distribution of the time shifts exhibits a peaked Gaussian behaviour when comparing the intact bridge to the moderate damage condition, while the distribution shows a longer tail, when analysing the final stage of the bridge. To give an overall measure of the variations relatively to the two damage stages, we chose the mean value as the final estimate and the standard deviation of the distribution as the associated uncertainty. We found that the average relative time shifts are $\Delta\tau/\tau=5.08\pm 0.08\%$ for the moderate damage condition and $\Delta\tau/\tau=8.2\pm 0.6\%$ for the severe damage condition, we remember that we are authorized to present an average value for each step since the investigated frequency band is associate to the whole structure. In agreement with our assumptions, the time shifts correspond to the relative velocity changes of the medium, that can be ascribed to the whole structure. The velocity variations are representative of a velocity diminution, also indicated by the reduction of the dominant peak in the frequency domain.

Making reference to the figure 11, we notice that in the case of the intermediate damage the histogram distribution looks like a Gaussian, as expected for an experiment where no bias intervenes. Therefore, we could explain the tail in the second histogram with the non perfect agreement between the theory and experimental condition. The damage was mimicked titling of the central, therefore the induced damage in the final step is not so small, therefore its effect could appear more localized, also at the investigated frequencies, in some points of the structure and produces some deviations from the theoretical approach. To finely locate the regions of the bridge that suffered effective damage or to reconstruct a tomographic image of the velocity changes in the structure, we should have recorded data with a dominant frequency larger than 10 KHz. This idea is corroborated by results esteemed from other authors, indeed, our velocity change, in the intermediate step, is of the same order of magnitude as retrieved in other studies performed on similar structures (Snieder, 2006). Nevertheless the last step is higher, we are around the 10%, it is indicative of a very strong velocity reduction where the efficiency of the structure is seriously compromised.

Anyway, the results relative to masonries are significantly larger (at least one order of magnitude) than velocity changes observed in natural environment, that is, Earth's crust in the post seismic phase of an earthquake (Poupinet, et al., 1984) or in volcanic areas (Brenquier, et al., 2011). This is mainly related to the severity of the damage but also to the source–receiver geometry as compared to the space scale at which the damage occurs. In this case, the scale of the damage is comparable to the source–receiver distances. For the Earth, the changes in the wave velocity are observed to occur mainly within or nearby the fault zones, for earthquakes, or close to the magma chamber for volcanic areas. Hence, only a small fraction of the ray path-connecting sources and receivers is sensitive to such velocity changes.

Coming back to the frequency domain, the inferred velocity changes could be also retrieved by an accurate measurement of the peak shifts in the frequency domain. Indeed, such an estimate is comparable with the relative difference between the frequency peaks (-5% and -7.5%), which is also responsible for the increasing of the time shift in the coda waves (Ruocci, et al., 2011). Nevertheless, the CWI allows to quantify the relative velocity change for the investigated structure with an associated uncertainty and better accuracy. The use of the coda waves allows to isolate the contribution of the scattered wave field, making the relative time shift measurement almost independent of the source–receiver location. Moreover, recursive measurements of the delay in the time domain lead to small uncertainties in the estimate of the relative time shifts by constraining the slope of delay as a function of time, while peak measurements in the frequency domain are an averaged information over the investigated portion of the signal. Eventually, combination of both information, with the use of time–frequency diagrams, may help in further improving the accuracy of the estimate.

Finally, we want say that such kind of investigation could be performed by means of the ambient noise. The use of ambient noise records at the top and bottom of a structure and the changes in the first modal frequency as an indicator of the damage within the structure are suggested by Ponzio (Ponzio et al., 2010). It is worth to note that velocity changes could be also ascribed to changes in ambient conditions, for instance, related to the temperature and the moisture. Such variations measured in rock samples result in lower values of the relative velocity

changes, for example, 0.3% for a partially water-saturated sandstone sample; 0.15% for a change in temperature of 5 °C (Grêt et al., 2006). Such variations estimated on rock samples are more extreme than the ones expected in real structures; hence, they are expected to be negligible as compared to the velocity changes estimated here. Nevertheless, variations in ambient parameters may limit the resolution in the estimation of these latter, averages of measurements performed under different ambient conditions are required to reduce the epistemic uncertainty. We also processed the ambient noise records related to the three stages of the bridge by cross-correlation of records at couples of stations in order to compute the Green's function between the stations (Shapiro et al., 2004). Noise records were continuous signals acquired during a time window of 180 s. In contrast with the CWI, when comparing the original noise spectra and the cross-correlated records in both time and frequency domains, we observed very different waveforms and spectra depending on the damage state, indicating that the variability of the noise sources in terms of excited frequencies is dominant as compared to the changes in the velocity structure. This effect is almost independent of the specific processing of the data, with or without the addition of spectral whitening and 1-bit normalization (Bensen et al., 2007). Changes in the noise structure might be related to the fact that the acquisition time is significantly smaller than the timescale at which the damage occurred and the seismic noise around the bridge are likely to be not stationary. In this case, since no stabilization in data is reached, we are not guaranteed to respect the hypothesis under which we can converge to the Green's function of the medium. Hence, we presented and conducted the analysis by means of the CWI interferometry.

For sake of completeness, we said that we discarded some accelerometers, because the measure was not repeated maintaining them in the same position or because they were not perpendicularly to the arch of the bridge. In the first case, it is clear that the data are not usable for such kind of analysis, but in the second case we notice that data present waveforms and spectra not easily interpretable and understandable at least in the light of the exposed theory. Several peaks of high amplitude were in the spectrum, probably associated to the transversal

modes (Figure 5-7), and also after the filtering procedure no characteristic similar features were recognized (Figure 5-8).

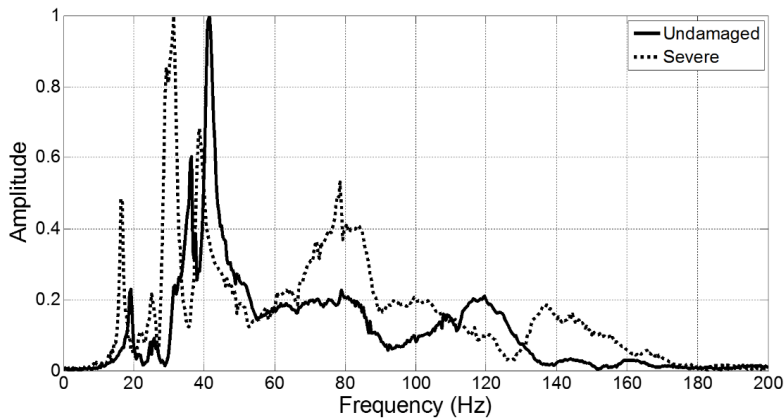


Figure 5-7: Examples of spectra related to traces acquired in not-perpendicular position with respect the arches of the ridge. It is evident that more frequencies are excited and in the case of the severe damage the other frequencies peaks are comparable among them.

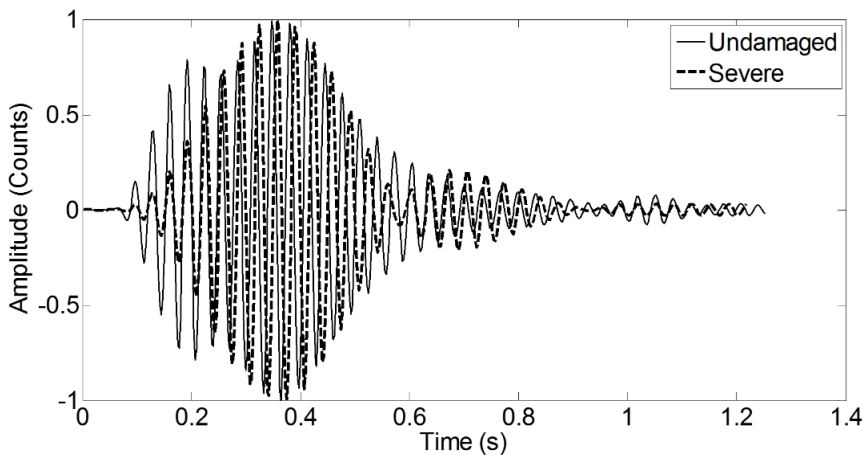


Figure 5-8: Signals filtered in the same frequency band where we measured the relative velocity variation. In such case, the measure cannot be considered reliable since traces don't follow similar amplitude patterns. Such variations could bias the measure.

Below we present this work as it has been published on the journal: Structural Control and Health Monitoring

RESEARCH ARTICLE

Damage detection in elastic properties of masonry bridges using coda wave interferometry

Marcello Serra¹ | Gaetano Festa¹ | Maurizio Vassallo² | Aldo Zollo¹  | Antonino Quattrone^{3,4} | Rosario Ceravolo⁴

¹Università degli Studi di Napoli “Federico” II, Dipartimento di Fisica “Ettore Pancini”, Naples, Italy

²Istituto Nazionale di Geofisica e Vulcanologia (INGV), L’Aquila, Italy

³College of Engineering, Mathematics and Physical Sciences, Harrison Building, Streatham Campus, University of Exeter, Exeter, UK

⁴Dipartimento di Ingegneria Strutturale, Edile e Geotecnica, Politecnico di Torino, Turin, Italy

Correspondence

Marcello Serra, Università degli Studi di Napoli “Federico” II, Dipartimento di Fisica “Ettore Pancini”, Complesso Universitario di Monte Sant’Angelo, Via Cinthia I-80126 Naples, Italy. Email: serra@fisica.unina.it

Summary

Structures may be subjected to damage and deterioration over different timescales, and monitoring their health status may allow to perform maintenance actions before the functionality limit is reached. Masonry arch bridges, in particular, are sensitive to the bearings loss produced by scour of the streambed soil at the pier foundations. In this study, we measured the changes in the elastic properties of a 1:2 scaled model of a masonry arch bridge built in the laboratory to study the evolution of the damage mechanism related to the application of foundation movements. Specifically, the bridge is realized to model the effect of erosion of the ground underneath the central pier. We analysed the accelerometric records acquired along the structure generated by a sledgehammer hitting the bridge walls. We used the method of coda wave interferometry to detect the changes in the elastic properties of the medium. After selecting the specific frequency band exciting coda waves, we progressively measured the time lag between signals acquired in the intact and two damaged stages of the bridge for each source–receiver couple, and we fit the data to get the relative wave velocity changes. We found that the average relative velocity changes for the two damaged steps are $\Delta v/v = -5.08 \pm 0.08\%$ and $\Delta v/v = -8.2 \pm 0.6\%$, consistently measured at all the analysed source–receiver couples. These values correspond to an average estimation of the velocity changes occurred within the structure, because the associated wavelengths are comparable with the bridge size and the damage is spread over a large portion of the structure.

KEYWORDS

bridge, damage, elastic waves, health monitoring, interferometry

1 | INTRODUCTION

Any building or infrastructure can be subjected to phenomena that reduce or limit their usability. Structural degradation may occur over different timescales, after catastrophic events such as earthquakes or floods, but also in the medium and long terms, because of the erosion by chemical agents or by the natural flow of water. In these latter cases, the structure often deteriorates without any visible signature of the damage. A complete classification of the damage effects detected on masonry arch bridges can be found in some reports of the European railway administrations on assessment, inspection, and maintenance of masonry arch railway bridges.^[1,2] In this

respect, a proposal for the terminology unification of the damage effects detected on masonry arch bridges has also been presented.^[3]

Local inspection on masonry structures is carried out by a destructive survey and a nondestructive evaluation in order to supply information about the mechanical characteristics of masonry as a composite material and of its components.^[4] The aim is to improve the knowledge and to reduce the epistemic uncertainties affecting the whole construction.

Often nondestructive estimations are locally performed, and they provide useful information referred to a limited portion of the structure. Modern diagnostic monitoring systems were born with the prerogative to overcome these

limitations providing an exhaustive depiction of the structural health state and easing the maintenance plan and restoring interventions.^[5–7]

The traditional damage detection methods have been reviewed in the work of Doherty.^[8] These techniques are either visual or based on localized experimental investigations such as acoustic, ultrasonic, magnetic field, radiography, eddy current, and thermal field methods. These methods are commonly known as nondestructive evaluation or techniques and are classified as local methods because they are generally carried out in some limited portions of the structure. All of them require an a priori knowledge of the damage location because they need to be applied in the proximity of damage. For the same reason, it is also essential that the portion of the structure being inspected is readily accessible. Nevertheless, these experimental techniques are capable to provide a reliable assessment of the structure or of its components in terms of damage extent and estimated residual operating life. They can also point out whether the damaged elements need to be replaced.

Indeed, traditional masonry structures were built without strict geometric tolerances, and many hidden local defects are present since the construction time. The scattering of the mechanical properties along the structure hides the presence of damage distributed over large volumes, which may potentially affect the structural integrity. Therefore, the diagnosis of old masonry constructions must be differentiated from that usually performed on other engineering structures.^[9] The development of methods based on the analysis of the changes in the vibration characteristics of the structure can be seen as the answer to the need for quantitative global damage detection methods.

The ability of a vibration-based damage identification method to distinguish between the damaged and undamaged states of a structure strongly depends on the data representation. Unfortunately, the best solutions to detect changes in the dynamic properties of a structure are target oriented (e.g., in the work of Ceravolo et al.^[10] and Bonessio et al.^[11]). They can be developed either in time, or in frequency, or in time-frequency domains depending on the employed level of data condensation. For instance, damage can be detected by the comparison of the flexibility matrix estimated from the mode shapes of the damaged and undamaged structures.

Modal flexibility is a robust damage index for constructed facilities. However, classical flexibility methods suffer from low sensitivity to small and multiple damages and high sensitivity to ambient noise. Another limitation is represented by the requirement of mass-normalized modal parameters. More sensitive flexibility methods for damage identification have been recently proposed, but they often require distributed strain measurements.^[12]

In the last decade, interferometric techniques have become very popular detecting changes in the elastic properties of a building,^[13–21] by correlation of two or more signals acquired in the same source–receiver configuration.

Such methods make use of electromagnetic, acoustic, or seismic waves to extract the properties of the medium crossed by waves and their possible variation with time. Seismic interferometry, specifically, is based on the recording of ambient noise or coda waves from natural earthquakes, artificial shots, or hits. First applications of seismic coda wave interferometry (CWI) were oriented to detect changes in the Earth's structure induced by the earthquake occurrence. They were based on parameters extracted from the coda shape such as the energy^[22] and the anelastic attenuation quality factor.^[23] More recently, interferometric techniques based on coda waves used the strong similarity in the waveforms to detect changes in the elastic properties of the medium.^[24] This method has become very popular in Earth Science, because it is a valid alternative to the more expensive active seismic exploration, it can be efficient also in regions where no earthquakes occur, and it allows for a continuous low-cost, noninvasive monitoring of structures and subsoil.^[25,26] CWI was then applied to infer variations in fault zones,^[27] volcanic structures,^[28,29] and rock samples due to temperature and deformation^[30] but also to monitor structures such as buildings and bridges.^[23,31] The observed relative changes in the velocity structure usually range below few percentage points. Applications of seismic interferometry at a larger scale were done in tectonic environments, with the use of ambient noise, to investigate postseismic relaxation of faults^[32] or oil reservoirs.^[33] In these cases, the observed velocity changes are of the same magnitude order. In this study, we applied the seismic CWI to a bridge artificially damaged in the laboratory. After describing the experiment setup, we analysed the coda waves obtained from hitting the walls of the bridge with a hammer. We recognized the frequency range in which the waveform similarity still holds after damage. We finally peaked the maxima in the records and estimated the velocity changes from the relative time shifts.

2 | SEISMIC INTERFEROMETRY FOR DAMAGE DETECTION

Coda waves are late arrivals on seismograms, originated by multiple scattering phenomena in the medium at different space scales. Indeed, they reach the receivers after a longer path than the ballistic waves, and then they are more sensitive to small changes in the elastic properties of the medium, even when the initial part of the signal remains unchanged.

When repeating the same experiment in an unchanged elastic medium with the same source time function and location, the seismic records remain unchanged. Indeed, any change in the signals from a repeated experiment can be ascribed to small variations either in the elastic properties of the crossed structure or in the location, mechanism, and energy release rate of the source. Ballistic waves, which travel directly from the source to the receiver, are poorly sensitive to

such small changes. Late coda waves, generated by multiple scatterings, sample the medium several times and cumulate time shifts (delays or anticipations) on seismograms as the time increases from the first P-wave arrival.

Usually, the time shifts can be directly measured on the seismograms, by comparing the arrival times of the waveform maximum (or minimum) amplitudes between two records in a narrow frequency range.^[32] More sophisticated techniques are based on the estimation of a time-windowed cross-correlation coefficient, which measures the similarities and time shifts between portions of signals.^[34] Since the time window should contain several oscillations, to provide a robust estimate of the correlation coefficient, the latter technique is well suitable for high-quality records, showing a large signal to noise ratio, and for strongly heterogeneous media for which a large amount of energy is transferred in the coda waves. Anyway, this technique allows to discriminate among changes related to the source location, to the scatterer's distribution, or to the medium average wave speed.^[24] When the time shift is related to a change in the medium wave velocity, the relative time shift $\Delta\tau/\tau$ can be written as a function of the relative change in the wave speed^[35] $\Delta v/v$:

$$\frac{\Delta\tau}{\tau} = -\frac{\Delta v}{v}.$$

$\Delta\tau$ is defined as $\tau_0 - \tau_1$, where τ_0 is the arrival time of maxima (or minima) on the trace assumed as a reference and τ_1 is the arrival time of the same maxima (or minima) on the traces to be compared. To improve the estimate of the relative velocity changes, we recursively measure the time shifts $\Delta\tau$ as a function of the time along the seismogram. From the above relation, we expect that the time shifts change linearly with time. The slope of the expected trend can be then estimated by a least squares linear-fitting procedure. Similar measurements can be also performed in the frequency domain, where the cumulated delay appears as a shift of the predominant signal frequency.^[36]

3 | BRIDGE DAMAGING AND COLLECTED DATA

The experiment was performed on a masonry arch bridge model built in the laboratory of the Department of Structural, Geotechnical and Building Engineering at the Politecnico di Torino. The bridge reproduces the characteristics of a typical masonry bridge that can be found throughout Italy (Figure 1) in the scale 1:2. The model is a twin arch bridge with a length of 5.90 m, a width of 1.60 m, and a height of 1.75 m. Each span is 2.00 m long between the supports, and the thickness of the arch is equal to 0.20 m.

The handmade clay bricks were also scaled to $130 \times 65 \times 30$ mm to follow the adopted modelling scale law.



FIGURE 1 Model of the bridge used for the experiment. Here, we show the bridge in the undamaged condition; at the base of the central pillar, we can observe the structure that can be tilted to mimic the effect of the erosion and the layer of polyester that simulates the sediments in the bed of the river

For the determination of the elastic properties of the materials that build up the structure, the elastic moduli, the Poisson coefficient, and the density were measured in the laboratory,^[37] and both P- and S wave velocities were obtained. The parameters are listed in Table 1 for all the materials composing the bridge. Low-velocity values arise from the choice of low-compressive strength elements bound by a mortar with poor mechanical properties in order to reproduce the typical materials of historical constructions.

The experiment was aimed at studying the changes in the elastic properties of the bridge, as a result of a progressive damage undergone by the structure. The damage mimics the erosion effect due to the slow removal of sediments from the base of the pier by the water flow that could generate the slipping off in the riverbed, possibly inducing severe damage up to the bridge collapse. To experimentally reproduce the erosion phenomenon, we erect the central pier on a polystyrene layer overlying a platform, and the tilt of this platform could be changed. The layer of polyester simulated the sediments in the bed of the river, and the progressive removal of parts of this layer simulated the early stage of damaging. The platform reproduced the effect of scour, in agreement with the results of hydraulic tests conducted in the laboratory.^[37] By lowering this latter, a failure of the central pillar occurred.

The structure started from an undamaged condition and progressively moved toward a final stage (hereafter indicated as “severe damage”) corresponding to a lowering of the platform of 2.5 mm and a removal of 75 cm of polystyrene: Data were collected during the initial undamaged stage, an

TABLE 1 Elastic parameters related to the materials in the bridge: the Young's modulus (E), the Poisson's ratio (ν), the density (ρ), the P-wave (V_p), and S wave (V_s) velocities.

Material	E (N/m ²)	ν	ρ (kg/m ³)	V_p (m/s)	V_s (m/s)
Reinforced concrete	$3.0 \cdot 10^{10}$	0.15	2400	3633	2331
Masonry	$1.5 \cdot 10^9$	0.20	1900	937	574
Backfill material	$5.0 \cdot 10^7$	0.1	2000	160	107
Concrete	$0.5 \cdot 10^{10}$	0.15	2200	1549	994

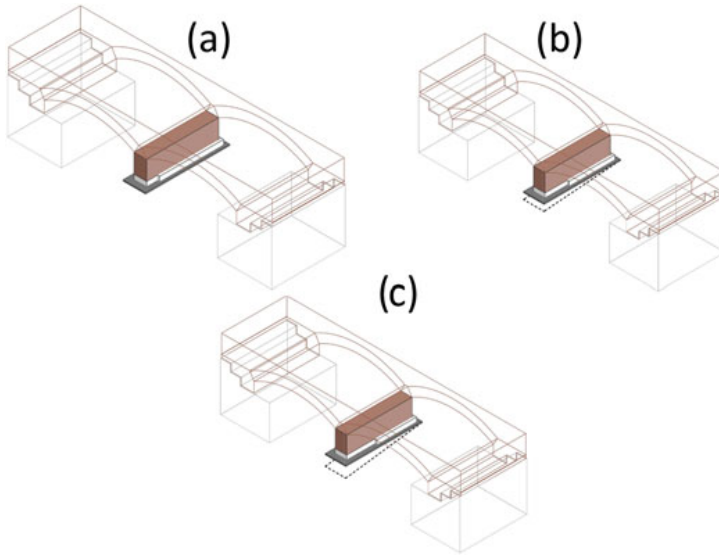


FIGURE 2 A simplified representation of the bridge and of the lowering of the platform in the three steps is shown: panel (a) undamaged step, (b) moderately damaged step, and (c) severely damaged step. The amplitude of the lowering is 1.5 and 2.5 mm, with 60 and 75 cm of polystyrene removed, for moderate and severe damage, respectively

intermediate state (indicated as “moderate damage”), and the final severely damaged stage of the structure (Figure 2). The intermediate damage stage was reproduced with a lowering of 1.5 mm and a polystyrene removal of 60 cm. The change in the inclination of the central pier finally produced the opening of cracks in the arches and the disconnection between the arches and the lateral containment barriers. It is worth to note that the damage did not occur immediately but after a time needed for mass redistribution.

For the undamaged and the two damaged stages, ambient noise and free decays were acquired. The free decays correspond to hammer bumps on specific points of the structure. Data were collected by a multichannel acquisition system connected to 18 uniaxial capacitive accelerometers with a sensitivity of 1 V/g, dynamic range of ± 3 g, and a resolution of 30 μ g. The location of receivers and the position of bumps are shown in Figure 3, and they remained unchanged during

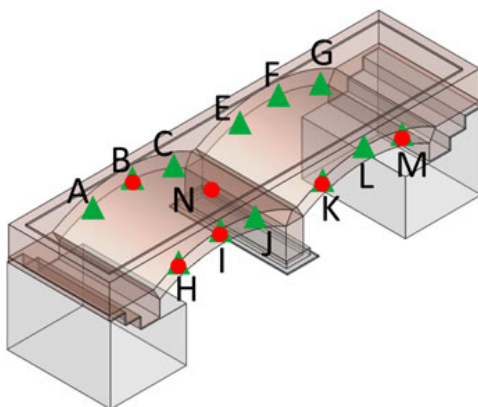


FIGURE 3 Three-dimensional representation of the bridge and the source—receiver configuration. The stations are marked with green triangles while positions of the hits are represented with red circles

the three acquisitions. The accelerometers were fixed to the bridge by an adhesive wax on an aluminium plate embedded in the structure. The plates were fixed perpendicularly to the arches of the bridge from the bottom. The average interstation distance is about 80 cm along the bridge and 1.60 along the transversal direction. The sampling rate of the data logger is 400 Hz, which corresponds to a bandwidth of 175 Hz when accounting for antialiasing low-pass filters. The ambient noise was recorded in consecutive time windows, whose duration ranges between 120 and 180 s. Hammer tests were repeated 10 times for each position to increase the statistical significance of the data.

Table 1 shows that, considering the lowest wave speed and the maximum frequency available in the records, the minimum wavelength propagating along the bridge is about 60 cm. For a central frequency of 30 Hz, around which we performed the analysis, the minimum wavelength is about 3 m. When considering the material with the highest speed, the wavelength associated to the maximum frequency in the data is about 12 m. Hence, the wavelengths associated to the seismic records are comparable to the size of the bridge, and we cannot use these signals to locate the regions where the changes in the elastic properties occurred during the experiment. Therefore, we limit the analysis to an average measurement of the velocity change across the whole structure. It is worth noting that this is not a limitation for this experiment, because the damage occurred over a large portion of the structure.

4 | WAVE SIGNAL PROCESSING

Because the investigated wavelengths are comparable or larger than the size of the bridge, coda waves are expected

to be dominated by standing waves exciting modal vibrations in the structure.

From the waveform database, we only selected the records for which both the hammer bump and the receiver were located perpendicularly to the arches, to avoid the development of transverse normal modes. For each source–receiver couple and for the three acquisition stages, we cross-correlated the records for the different bumps to properly align the traces. We then stacked the waveforms, to increase the signal to noise ratio. All the following analyses were indeed performed on the stacked traces. In Figure 4, we represent three records where the source position was in the location B and the receiver position in the location E, related to the undamaged, moderate, and severe damaged conditions of the bridge. We clearly observe that ballistic waves mostly superimpose for the three records, while in the late coda waves, we observe a phase shift. Signals in the damaged conditions are delayed as compared to signals recorded during the undamaged case, and the more severe the damage, the larger the time shift. We also observe a different frequency content in the signals, which would increase the uncertainty in the measure of the time shift.

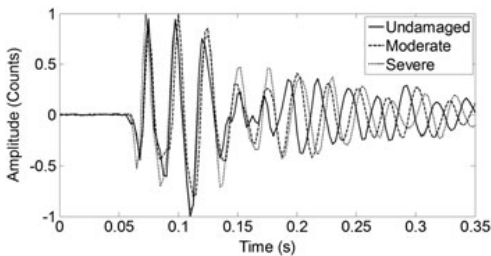


FIGURE 4 Data from three hits acquired at the same station but in different stages of the bridge are shown. In the initial part of the traces, the direct waves are clearly visible and they appear almost superimposed. We also observe the shift in the coda waves due to the velocity change occurred in the structure. The solid line refers to the undamaged stage, the dashed one to the moderate damage stage, and the dotted one to the severe damage stage

To properly investigate the delay between the undamaged and the two damaged steps, we analysed the frequency content of the coda waves. In Figure 5, we represent the amplitude spectrum of the signals recorded under the different damage conditions.

The spectra are characterized by several peaks between 10 and 60 Hz. A frequency shift in the largest amplitude peak can be seen between the three bridge conditions, moving from about 31 Hz for the undamaged state to about 30 and 29 Hz respectively for the two damaged cases. This frequency variation was also identified by Ruocci et al.,^[38] with a reduction of the peak from 29.9 to 28.3 Hz from the undamaged condition to the severely damaged one. This frequency was associated through the use of numerical simulations to the first vibration mode along the longitudinal direction of the bridge,^[30] and it consists in a counterphase displacement of the arch barrels (Figure 6).

Beyond 45 Hz, the spectrum of the signal related to the undamaged stage of the bridge decreases while the spectra related to the two damaged cases have several late peaks up to 90 Hz, which are smaller in amplitude than the peak around about 30 Hz. When looking at the spectrograms (Figure 7), we observe that only the energy between 20 and 40 Hz survives in the late coda waves, where we expect multiple scattering effects, although several frequencies were excited in the initial part of the records by the source. For this reason, data were filtered in a narrow band around 30 Hz (27.5–32.5 Hz), to guarantee the equipartition of energy and then to measure the relative change in the wave speed.^[39] The time shift in this frequency range can be therefore estimated for all the analysed source–receiver couples.

5 | TIME SHIFT MEASUREMENTS AND VELOCITY CHANGES

After filtering the data, we compared the signals during the damaged phases to the signals recorded while the structure

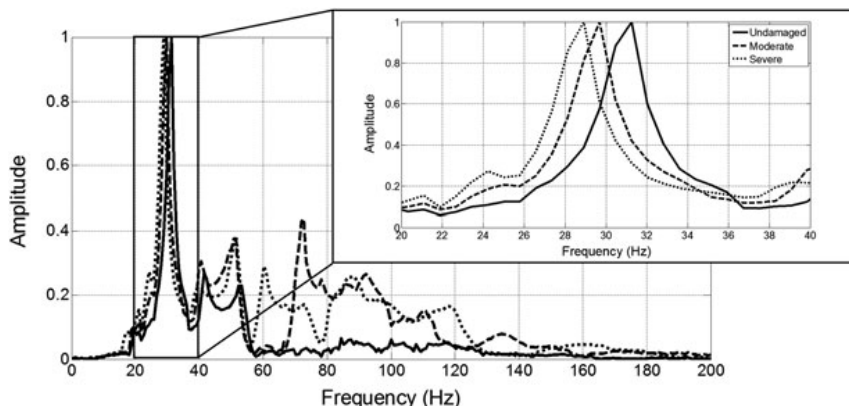


FIGURE 5 Normalized amplitude spectra of three accelerograms recorded, when the bridge is not damaged (solid line), moderately damaged (dashed line), and severely damaged (dotted line). We can see in the inset the shift in the dominant frequency

First Mode Longitudinal

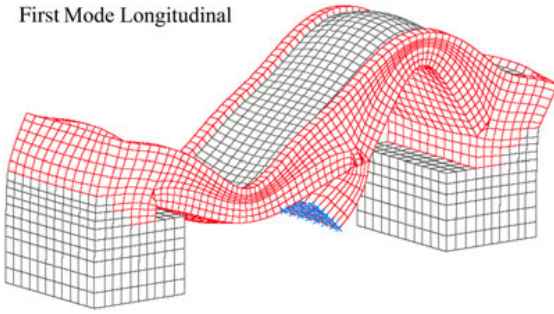


FIGURE 6 Three-dimensional representation of the shape of the first longitudinal mode (29.9 Hz) of the bridge. In the figure, the oscillations are clearly exaggerated

was still intact. An example of filtered records is shown in Figure 8, where each time series was normalized to its maximum amplitude. We observe that the traces are initially superimposed. Then after around 0.3 s, the signals related to the damaged conditions (represented with a dashed line for the moderate damage condition and with a dotted line for the severe damage condition) are delayed as compared to the undamaged condition (solid line). This behaviour is found for most of the couples, where no phase shift occurs for the ballistic waves while a clear time shift is observed in the later coda, thus indicating a decreasing of the average wave speed in the propagation medium.

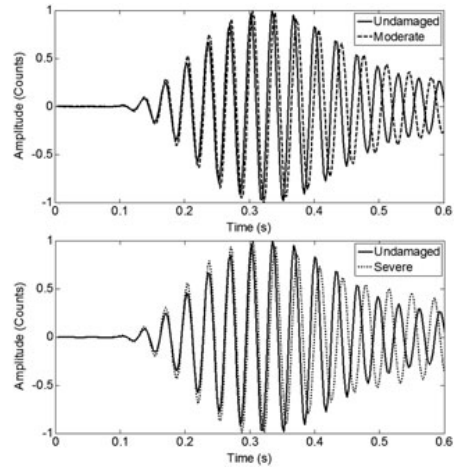


FIGURE 8 An example of filtered normalized signals used to measure the temporal shift. On the top, the comparison between the undamaged (solid line) and the moderate (dashed line) stages is represented. On the bottom, the superimposition between the undamaged (solid line) and severely damaged (dotted line) cases is plotted

To study the robustness of the time shift measure, we also compared the signals recorded in the same stage of damaging (either damaged or undamaged for different shots). In Figure 9, we superimpose the traces for two sources hitting in the same location and recorded at the same receiver in

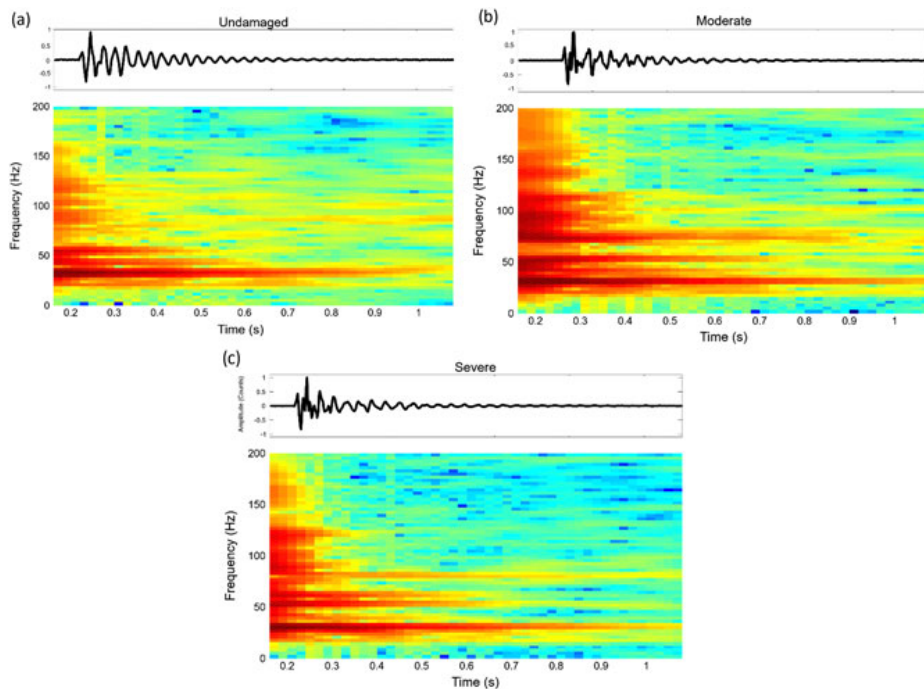


FIGURE 7 Spectrograms of the records represented in Figure 4. We recognize the variation in the frequency content over the time for the acquired data in the three cases: (a) undamaged, (b) moderate damage, and (c) severe damage. Only the frequencies that remain for a long time can be associated to the normal modes of the structure

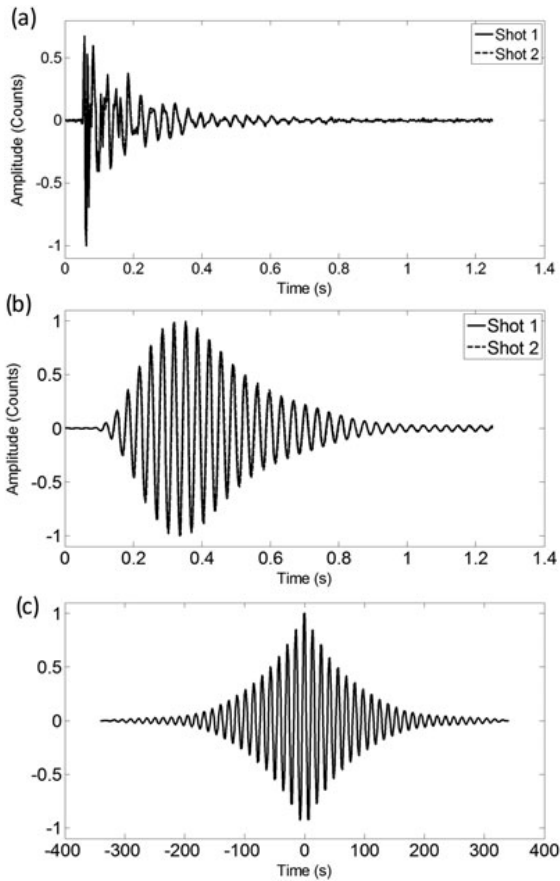


FIGURE 9 Here, we plot the traces of two hits for the same source, receiver, and damage condition. In the panel (a), we plot raw data; while in the panel (b), we represent filtered data. From a visual inspection, the superimposition of the two traces does not show any shift. In the panel (c), we plot the cross-correlation between the two signals: the maximum is reached very close to zero time, therefore, the two signals are really similar, and all the variations in the waveforms can be ascribed to the variations in the propagation medium

the undamaged state, in the whole frequency range (Panel a), or filtered in the selected frequency band (Panel b). For both cases, the two traces are completely superimposed and no shift can be observed from visual inspection. To evaluate the time shift, we computed the cross-correlation along the whole signal for the filtered trace (Panel c) and we picked the maximum amplitude. For all cases, we found that the relative time shift is always smaller than three time steps, hence below the time associated with the largest frequency represented in the data. This shift is significantly smaller than the one measured when comparing the records in the two stages of the bridge. Hence, we can neglect the variability in the data related to the source time function and location and interpret the variation as completely due to changes in the elastic properties of the structure.

We derived an estimate of the velocity change from the relative time shift, normalized to the velocity of the

undamaged stage. Since data were not cut from the origin time of the shot, we first aligned the traces for the different stages of damage on the ballistic portion of the signal by cross-correlation. We used the undamaged condition as a reference with respect to which we computed the time shifts and then the velocity changes. We compare each trace recorded during the intermediate stage of damage with the trace recorded initially in the undamaged state of the bridge, for the same source–receiver couple. To reduce the uncertainty in the estimate of the time shift, we recursively measured the time shift $\Delta\tau$ as the time increases along the record, comparing the position of consecutive maxima for the two traces. Then we plotted the time shift $\Delta\tau$ as a function of time, assuming as the starting time, the time of the first sample on the trace related to the undamaged case. The same comparison was performed using signals recorded during the final stage of the damage. Examples of the shift measurement with the associated uncertainties are shown in Figure 10. It is worth to note that the relative time shift is associated to the slope of the curve, independently of the choice of the offset on the abscissa of the plot. Finally, the slope was estimated by a linear fit, and the uncertainty in the slope was assumed as the error associated with the relative time shift.

For the curves shown in Figure 10, we found relative time shifts of $\frac{\Delta\tau}{\tau} = 5.202 \pm 0.002\%$ and $\frac{\Delta\tau}{\tau} = 7.881 \pm 0.002\%$ for the intermediate and final stages, respectively. This value is very consistent when selecting different source and receiver locations. We first averaged all the estimates for the same shot position at different receivers to reduce possible bias

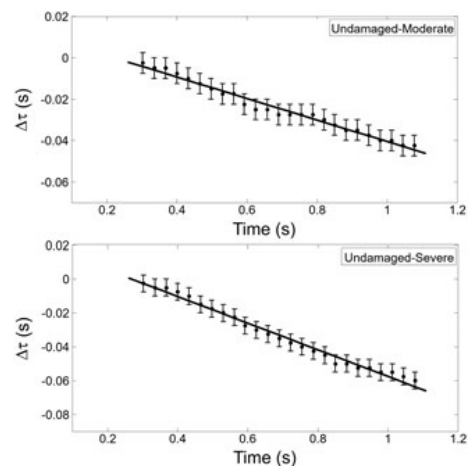


FIGURE 10 Temporal shift as a function of the time, where we assumed the time of the first sample on the undamaged trace as a starting time. The analysis refers to a shot in the position B and the station in the position H (Figure 3). The time shift $\Delta\tau$ is the time difference picked on consecutive maxima. From the slope of the linear regression, we estimated the relative velocity variation in the medium. On the top, we compare the undamaged and moderately damaged cases, on the bottom the undamaged and severely damaged stages

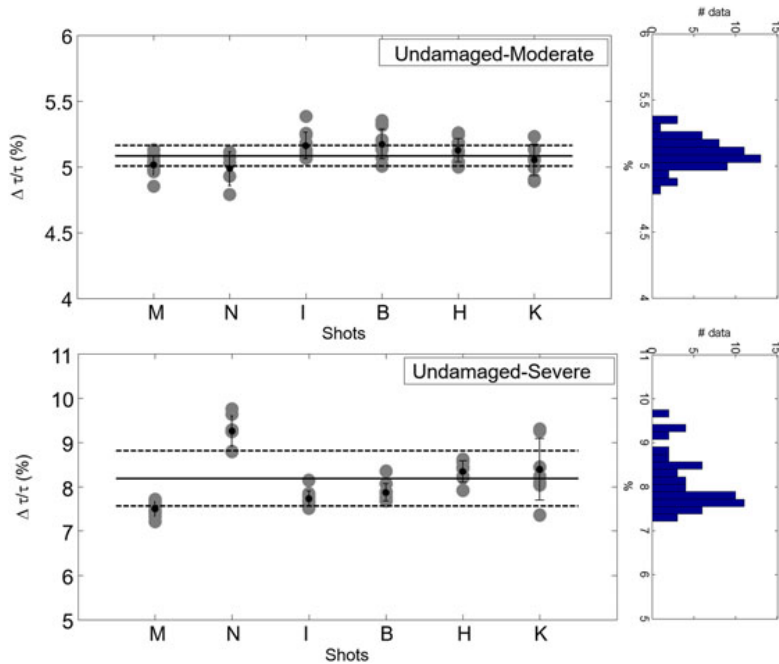


FIGURE 11 Average relative velocity change (black solid line) and its standard deviation (black dashed lines). Grey dots represent the relative time shifts for each source–receiver couple. On the right of each plot, the histogram of the distribution of $\Delta\tau/\tau$ is shown. On the top, we represent the relative velocity change between the undamaged and moderately damaged cases while on the bottom between undamaged and severely damaged cases

due to the coupling of the source with the structure. These estimates are represented as a function of the shot position in Figure 11 with the associated histogram. The distribution of the time shifts exhibits a peaked Gaussian behaviour when comparing the intact bridge to the moderate damage condition, while the distribution shows a longer tail for larger values of the relative time shift, when analysing the final stage of the bridge. We chose the mean value as the final estimate and the standard deviation of the distribution as the associated uncertainty. We found that the average relative time shifts are $\Delta\tau/\tau = 5.08 \pm 0.08\%$ for the moderate damage condition and $\Delta\tau/\tau = 8.2 \pm 0.6\%$ for the severe damage condition. The time shifts also correspond to the relative velocity changes of the medium.

It is worth to note that we also processed the ambient noise records related to the three stages of the bridge by cross-correlation of records at couples of stations.^[40] Noise records were continuous signals acquired during a time window of 3 min. In contrast with the CWI, when comparing the original noise spectra and the cross-correlated records in both time and frequency domains, we observed very different signals depending on the damage state, indicating that the variability of the noise sources in terms of excited frequencies is dominant as compared to the changes in the velocity structure. This effect is almost independent of the specific processing of the data, with or without the addition of spectral whitening and 1-bit normalization.^[41] In this case, we are not guaranteed to retrieve the effective Green function

of the medium, when cross-correlating the ambient noise at couples of stations.

6 | DISCUSSION

The relative velocity changes, which were estimated to be $-5.08 \pm 0.08\%$ and $-8.2 \pm 0.6\%$ for the two cases, were ascribed to an average estimate across the whole structure, because the selected frequency range, a narrow band around 30 Hz, corresponds to wavelengths that are comparable with the size of the bridge itself. This is due both to the sampling rate of the acquisition system and to the frequency range excited by the source. Indeed, to finely locate the regions of the bridge that suffered effective damage or to reconstruct a tomographic image of the velocity changes in the structure, we should have recorded data with a dominant frequency larger than 10 KHz.

We found that the estimated velocity changes in this study are of the same order as retrieved in other studies, performed on similar structures.^[24] Nevertheless, they are significantly larger (at least one order of magnitude) than velocity changes observed in the Earth's crust in the postseismic phase of an earthquake^[32] or in volcanic areas.^[42] This is mainly related to the severity of the damage but also to the source–receiver geometry as compared to the space scale at which the damage occurs. In this case, the scale of the damage is comparable to the source–receiver distances. For the Earth, the changes in

the wave velocity are observed to occur mainly within or nearby the fault zones, for earthquakes, or close to the magma chamber for volcanic areas. Hence, only a small fraction of the ray path-connecting sources and receivers is sensitive to such velocity changes.

We note that the inferred velocity changes could be also retrieved by an accurate measurement of the peak shifts in the frequency domain. Indeed, such an estimate is comparable with the relative difference between the frequency peaks (-5% and -7.5%), which is also responsible for the increasing of the time shift in the coda waves, as obtained by Ruocci et al.^[38] The use of ambient noise records at the top and bottom of a structure and the changes in the first modal frequency as an indicator of the damage within the structure are suggested by Ponzo et al.,^[43] while Ruocci et al.^[38] used the relative frequency shift as indication of damage without any distinction between ballistic and coda waves.

In this study, we propose an extension of the above indicator, which allows to quantify the relative velocity change for the investigated structure with an associated uncertainty and better accuracy. The use of the coda waves allows to isolate the contribution of the scattered wave field, making the relative time shift measurement almost independent of the source–receiver location. Moreover, recursive measurements of the delay in the time domain lead to small uncertainties in the estimate of the relative time shifts by constraining the slope of delay as a function of time, while peak measurements in the frequency domain are an averaged information over the investigated portion of the signal. Eventually, combination of both information, with the use of time–frequency diagrams, may help in further improving the accuracy of the estimate.

It is worth to note that velocity changes could be also ascribed to changes in ambient conditions, for instance, related to the temperature and the moisture. Such variations measured in rock samples result in lower values of the relative velocity changes (0.3% for a partially water-saturated sandstone sample; 0.15% for a change in temperature of 5 °C).^[36] Such variations estimated on rock samples are more extreme than the ones expected in real structures; hence, they are expected to be negligible as compared to the velocity changes estimated here. Nevertheless, variations in ambient parameters may limit the resolution in the estimation of velocity changes due to the damage. For smaller values of these latter, averages of measurements performed under different ambient conditions are required to reduce the epistemic uncertainty.

Several studies make use of ambient noise to monitor the velocity changes within structures and the Earth. In this case, we also compared the ambient noise cross-correlated traces at couples of stations for the three stages of the bridge. We found very different waveforms and spectra, indicating that the variability of the noise sources in terms of excited frequencies is dominant as compared to the changes in the elastic properties of the bridge and that it

cannot be de-aggregated from the records. Possible changes in the noise structure might be related to the fact that the acquisition time is significantly smaller than the timescale at which the damage occurred and the seismic noise around the bridge are likely to be not stationary. Hence, CWI is a valid alternative to the use of passive recording for building health monitoring also for real structures. The use of appropriate energetic sources, such as hits, shots, or Mini-Vib vibrations, warrants the repeatability of the experiments and allows to directly ascribe the difference in the waveforms to the variations in the elastic properties of the structure. Although passive techniques are cheaper and provide longer records, whose stack would improve in principle the signal to noise ratio, noise stationarity and excitation of specific frequencies are not guaranteed.

7 | CONCLUSIONS

Structures require continuous or periodic monitoring to assess their health status and perform maintenance actions. In this study, we estimated the velocity changes undergone by a masonry bridge built in the laboratory, which moved from an intact condition to a severe damage. We analysed the relative time shifts in the coda waves, which are expected to be more sensitive to small changes in the elastic wave speed. We observed that the source excited a signal with a broad spectrum of frequencies, but the coda waves, where we expect energy equipartition from multiple scattering, were dominated by a single peak in frequency (around 30 Hz), corresponding approximately to the first longitudinal mode of the bridge. Hence, we found that a proper estimation of the velocity change requires a narrowband filtering of the data around the frequencies that still propagate long time after the source action. In this case, we selected a single frequency band centred at around 30 Hz. After filtering the records, we were able to recognize a time shift between traces collected in the three stages of the bridge, linearly increasing with time. Moreover, this result is consistent among all of the source–receiver couples.

From the average relative time shift estimates, we found that the velocity changes in the medium are $\frac{\Delta v}{v} = -5.08 \pm 0.08\%$ and $\frac{\Delta v}{v} = -8.2 \pm 0.6\%$ for the moderate and severe damage conditions, respectively.

ACKNOWLEDGMENTS

This work was developed within the activities of Rete dei Laboratori Universitari di Ingegneria Sismica—ReLUIS—funded by the Italian Department of Civil Protection.

REFERENCES

- [1] A. Brencich, L. Gambarotta, *Guide to the high level assessment of masonry bridges*. UIC Workshop on Masonry, Arch Bridges, Paris, France 9th May 2007.

- [2] Z. Orbán, M. Gutermann, *Eng. Struct.* **2009**, *31*, 2287, DOI: 10.1016/j.engstruct.2009.04.008
- [3] J. Bien, T. Kaminski, *Proceedings of 5th International Conference on Arch Bridges, ARCH'07*, Madeira, **2009**, 341.
- [4] L. Binda, A. Saisi, C. Tiraboschi, *Constr. Build. Mater.* **2000**, *14*, 199, DOI: 10.1016/S0950-0618(00)00018-0
- [5] P. J. Shull, *Nondestructive Evaluation Theory, Techniques, and Applications*, Marcel Dekker, Inc., New York, NY **2007**.
- [6] K. Worden, J. M. Dulieu-Barton, *Int. J. Struct. Health Monit.* **2004**, *3*, 85, DOI: 10.1177/1475921704041866
- [7] J. M. W. Brownjohn, *Phil. Trans. R. Soc. A.* **2007**, *365*, 589, DOI: 10.1098/rsta.2006.1928
- [8] J. E. Doherty, in *Handbook on Experimental Mechanics*, (Ed: A. S. Kobayashi), Society for Experimental Mechanics, Englewood Cliffs, NJ **1987**.
- [9] A. De Stefano, R. Ceravolo, *J. Intell. Mater. Syst. Struct.* **2007**, *18*, 793, DOI: 10.1177/1045389X06074610
- [10] R. Ceravolo, N. Tondini, G. Abbiati, A. Kumar, *Struct. Control Health Monit.* **2012**, *19*(4), 511.
- [11] N. Bonessio, G. Lomiento, G. Benzoni, *Struct. Control Health Monit.* **2012**, *19*(5), dd565.
- [12] A. P. Adewuyi, Z. S. Wu, *Struct. Control Health Monit.* **2011**, *18*(3), 341.
- [13] C. R. Farrar, T. W. Darling, A. Migliori, W. E. Baker, *Mech. Syst. Signal Proc.* **1999**, *13*, 241, DOI: 10.1006/mssp.1998.1216
- [14] D. Tarchi, H. Rudolf, M. Pieraccini, C. Atzeni, *Int. J. Remote Sens.* **2000**, *21*, 3545, DOI: 10.1080/014311600750037561
- [15] R. Snieder, E. Safak, *Cal. Bull. Seismol. Soc. Am.* **2006**, *96*, 586, DOI: 10.1785/0120050109
- [16] M. D. Kohler, T. H. Heaton, S. C. Bradford, *Bull. Seismol. Soc. Am.* **2007**, *97*, 1334, DOI: 10.1785/0120060148
- [17] M. I. Todorovska, M. D. Trifunac, *Struct. Control Health Monit.* **2008**, *15*(1), 90, DOI: 10.1002/stc.208
- [18] G. Bartoli, L. Facchini, M. Pieraccini, M. Fratini, C. Atzeni, *Struct. Control Health Monit.* **2008**, *15*, 283, DOI: 10.1002/stc.252
- [19] C. Gentile, *NDT E Intern.* **2010**, *43*, 231, DOI: 10.1016/j.ndteint.2009.11.007
- [20] G. A. Prieto, J. F. Lawrence, A. I. Chung, M. D. Kohler, *Bull. Seismol. Soc. Am.* **2010**, *100*, 2322, DOI: 10.1785/0120090285
- [21] M. D. Trifunac, M. I. Todorovska, M. I. Manić, B. Đ. Bulajić, *Struct. Control Health Monit.* **2010**, *17*(2), 120, DOI: 10.1002/stc.277
- [22] B. Chouet, *Geophys. Res. Lett.* **1979**, *6*: ISSN: 0094-8276, DOI: 10.1029/GL006i003p00143
- [23] K. Aki. In: *Practical Approaches to Earthquake Prediction and Warning*. Springer Netherlands; **1985**, 219, DOI: 10.1007/978-94-017-2738-9_2
- [24] R. Snieder, *Pure Appl. Geophys.* **2006**, *163*, 455, DOI: 10.1007/s00024-005-0026-6
- [25] E. Larose, L. Margerin, B. A. van Tiggelen, M. Campillo, *Phys. Rev. Lett.* **2004**, *93*: 048501, DOI: 10.1103/PhysRevLett.93.048501
- [26] D. P. Schurr, J. Y. Kim, K. G. Sabra, L. J. Jacobs, *NDT & E Intern.* **2011**, *44*(8), 728, DOI: 10.1016/j.ndteint.2011.07.009
- [27] S. C. Stähler, C. Sens-Schönfelder, E. Niederleithinger, *J. Acoust. Soc. Am.* **2011**, *129*(4), 1945, DOI: 10.1121/1.3553226
- [28] F. Brenguier, M. Campillo, C. Hadziioannou, N. M. Shapiro, R. M. Nadeau, E. Larose, *Science* **2008**, *321*(5895), 1478, DOI: 10.1126/science.1160943
- [29] M. Miyazawa, A. Venkataraman, R. Snieder, M. A. Payne, *Geophysics* **2008**, *73*: O15, DOI: 10.1190/1.2901199
- [30] Snieder R., In: Fouque JP (ed), *Diffuse Waves in Complex Media*, Kluwer: Dordrecht; **1999**, 405–454, DOI: 10.1007/978-94-011-4572-5_14
- [31] A. Ratdomopurbo, G. Poupinet, *Geophys. Res. Lett.* **1995**, *22*: ISSN: 0094-8276, DOI: 10.1029/95GL00302
- [32] G. Poupinet, V. L. Ellsworth, J. Frechet, *J Geophys Res.* **1984**, *89*: ISSN: 0148-0227, DOI: 10.1029/JB089iB07p05719
- [33] M. Mucciarelli, A. Masi, M. R. Gallipoli, P. Harabaglia, M. Vona, F. Ponzio, M. Dolce, *Bull. Seismol. Soc. Am.* **2004**, *94*(5), 1943, DOI: 10.1785/012003186
- [34] S. Matsumoto, K. Obara, K. Yoshimoto, T. Saito, A. Ito, A. Hasegawa, *Geophys. J. Int.* **2001**, *145*, 48, DOI: 10.1111/j.1365-246X.2001.00339.x
- [35] A. Grêt, R. Snieder, R. C. Aster, P. R. Kyle, *Geophys. Res. Lett.* **2005**, *32*: L06304, DOI: 10.1029/2004GL021143
- [36] A. Grêt, R. Snieder, J. Scales, *J. Geophys. Res.* **2006**, *111*: B03305, DOI: 10.1029/2004JB003354
- [37] G. Ruocci, A. Quattrone, L. Zanotti Fragonara, R. Ceravolo, A. De Stefano, in *Industrial Safety and Life Cycle Engineering*, (Ed: H. Wenzel), Wien **2013** 107.
- [38] G. Ruocci, A. Quattrone, A. De Stefano, *J. Phys.* **2011**, *305*, 1. ISSN 1742-6588, DOI: 10.1088/1742-6596/305/1/012106
- [39] R. Snieder, *Phys. Rev. E.* **2002**, *66*, DOI: 10.1103/PhysRevE.66.0466150.046615-1,8
- [40] N. M. Shapiro, M. Campillo, *Geophys. Res. Lett.* **2004**, *31*: L07614, DOI: 10.1029/2004GL019491
- [41] G. D. Bensen, M. H. Ritzwoller, M. P. Barmin, A. L. Levshin, F. Lin, M. P. Moschetti, N. M. Shapiro, Y. Yang, *Geophys. J. Int.* **2007**, *169*(3), 1239, DOI: 10.1111/j.1365-246X.2007.03374.x
- [42] F. Brenguier, D. Clarke, Y. Aoki, N. M. Shapiro, M. Campillo, V. Ferrazzini, *C. R. Geosci.* **2011**, *343*, 633, DOI: 10.1016/j.crte.2010.12.010
- [43] F. C. Ponzio, R. Ditommaso, G. Auletta, A. Mossucca, *Bull Earthquake Eng.* **2010**, *8*(6), 1421, DOI: 10.1007/s10518-010-9194-6

How to cite this article: Serra M, Festa G, Vassallo M, Zollo A, Quattrone A, Ceravolo R. Damage detection in elastic properties of masonry bridges using coda wave interferometry. *Struct Control Health Monit.* 2016; e1976. doi: 10.1002/stc.1976

5.2 The Irpinia fault system

In this work, we present an application of the Green's functions extraction through the cross-correlation of the seismic noise acquired at couples of stations on the vertical component (Shapiro, et al., 2004). The interesting area is located in the South of Italy, more precisely, in the seismogenic region of the large earthquake occurred in Irpinia in 1980 (M_w 6.9). In this area are located 26 seismic stations, managed by the University of Napoli "Federico II" which acquire continuously, also for the experimentation of the earthquake early warning system PRESTo. In such application, three years of data were cross-correlated between all the possible couples of stations, it produced a variegated range of distances, the closest stations were at about 10 km whereas the farthest ones at about 140 km. The data were processed in agreement with the common practice, the whitening and the one-bit normalization was performed in order to weigh in the same way all the frequency and temporal contribution, in such way eventual spike or earthquakes were removed from the dataset (Shapiro, et al., 2006), (Larose, et al., 2004), (Shapiro, et al., 2005). Finally, data were filtered in the band 0.04-0.09 Hz where the largest amount of energy is concentrated. The results were encouraging, since they showed a satisfactory symmetry between the casual and acasual part of the signal, also if some differences in the amplitude of the signal arise over the year. It should be due to the no perfect isotropic distribution of the noise, in the southern Italy it is known that the source of noise are located along the coastline (Vassallo, et al., 2012), (Brzak, et al., 2009). Organizing the data in seismic section, we can more easily and more reliably pick the arrival times of the interesting phases. In our case, waveforms are dominated by Rayleigh waves, therefore we can filter signals in different frequency bands and pick the maximum of the wavelet. Since we are filtering the signals in narrow frequency bands, we see the emergence of a wave packet at which is associated the propagating energy, therefore the ratio between the interstation distance and the arrival time of the picked maximum furnishes the measure of the group velocity. In such way, it was possible to determine a dispersion curve for the group velocity for each couple of stations of the network. From the dispersion curves, as we did in the case of the Solfatara, it is possible to recover a tomographic model of the area (Wathelet,

et al., 2004). In the investigated area were computed at 400 control nodes the dispersion curves for the group velocity. This goal was reached by means of a software which starting from the real curves is able to recover the dispersion curves in other points taking into account the value of the contiguous nodes. Now following the same philosophy of the previous work, at each node a simple one-dimensional layered model was recovered, and from the collection of all of them the three-dimensional model was obtained. As before some input parameters are required, in such case the density of the medium was chose of 2700 Kg/m^3 , as typical of the rocks of the crust, and we set the minimum exploration value for the S-wave velocity 2500 m/s with a Poisson's coefficients varying from 0.2 up to 0.5. We were focused on the results in term of S-waves velocity since after several tests, it was clear that the P-wave velocity was not constrained as the S-wave one. Again, to understand which was the best-layered representation of the medium, we proceeded performing several inversion in different point of the nodes grid and systematically we increased the number of layers. At each inversion we take note of the misfit function to observe if there was important misfit drop or not. The best choice for all the nodes was a three-layered medium (Figure 5-9).

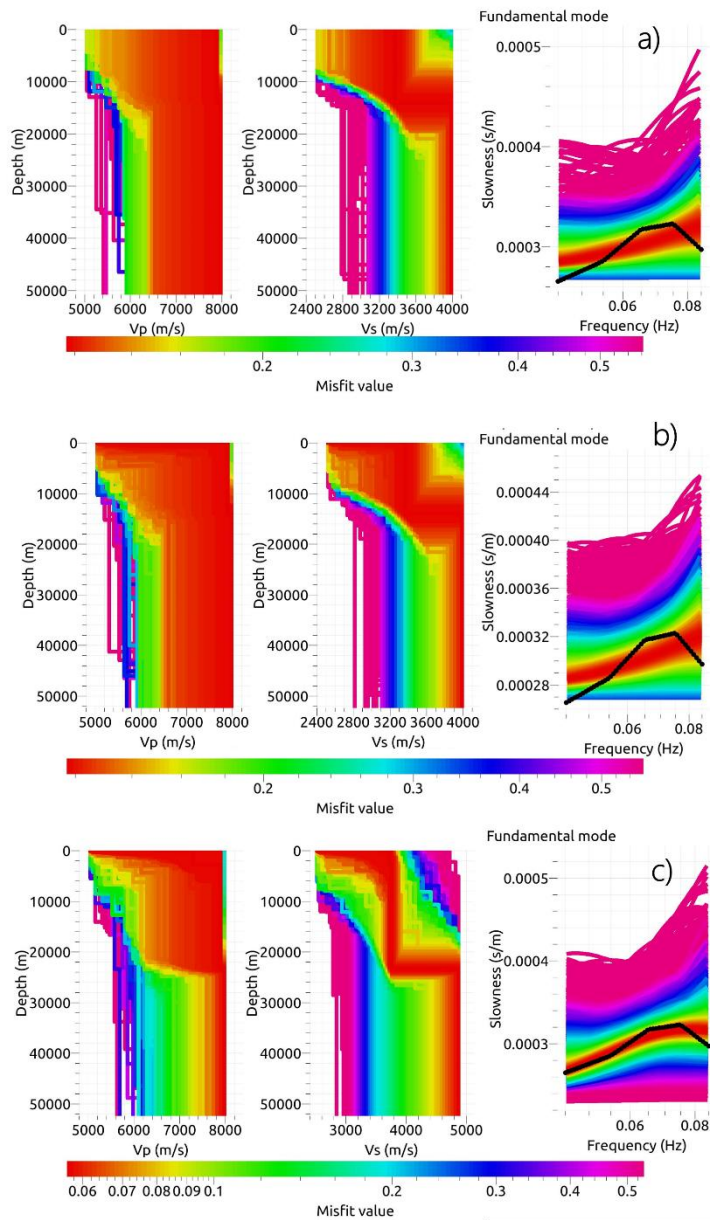


Figure 5-9: Example of the misfit reduction increasing the number of layers, passing from 1 layer (a), 2 layers (b) and 3 layers (c). As expected increasing the number of layers the measured group velocity dispersion curve (on the right) is well fitted. The solutions show a better resolution for the S-wave with respect the P model.

As expected we have not a single solution but there are several minima, therefore we can apply the same strategy, as seen for the computation of the S-wave model at the Solfatara. At each node, we selected a family of solutions around the minimum misfit and resampled the profile at step of 200 m giving as final value the mean among the chosen models and the associate standard deviation at each depth. Such procedure is possible also in this case since, the models having smallest misfit functions are superimposed and localized in a small region of the scheme where we show the solutions, and therefore the averaged solution will be again a model having the same misfit requirements of the initial ones. The final model clearly shows that the most important variations are along the Appennine direction and the most interesting feature is the low velocity anomaly bordered by the segments faults of the Irpinia earthquake.

The recovered low velocity values, associated with other works, which showed an higher V_P/V_S ratio and the location of the microseismicity in the area of the anomaly (Amoroso, et al., 2014), allow us to conclude that this could be a highly fractured zone where fluids can migrate. The value of the V_P/V_S ratio are indicative of a fluid saturated medium, and the velocity gradient could indicate the presence of a bimaterial interface.

Below we present the paper as it has been published in the journal: Journal of Geophysical research: Solid Earth

RESEARCH ARTICLE

10.1002/2015JB012410

Key Points:

- Ambient noise cross-correlation analysis in complex geological areas
- Study of normal active fault system by seismic ambient noise
- Role of fluids in nucleation and propagation of large earthquakes

Supporting Information:

- Supporting Information S1
- Figure S1
- Figure S2
- Movie S1

Correspondence to:

M. Vassallo,
maurizio.vassallo@ingv.it

Citation:

Vassallo, M., G. Festa, A. Bobbio, and M. Serra (2016), Low shear velocity in a normal fault system imaged by ambient noise cross correlation: The case of the Irpinia fault zone, Southern Italy, *J. Geophys. Res. Solid Earth*, 121, doi:10.1002/2015JB012410.

Received 4 AUG 2015

Accepted 29 APR 2016

Accepted article online 16 MAY 2016

Low shear velocity in a normal fault system imaged by ambient noise cross correlation: The case of the Irpinia fault zone, Southern Italy

Maurizio Vassallo¹, Gaetano Festa², Antonella Bobbio³, and Marcello Serra²

¹Istituto Nazionale di Geofisica e Vulcanologia, L'Aquila, Italy, ²Dipartimento di Fisica, Università di Napoli Federico II, Naples, Italy, ³Istituto Nazionale di Geofisica e Vulcanologia, Osservatorio Vesuviano, Naples, Italy

Abstract We extracted the Green's functions from cross correlation of ambient noise recorded at broadband stations located across the Apennine belt, Southern Italy. Continuous records at 26 seismic stations acquired for 3 years were analyzed. We found the emergence of surface waves in the whole range of the investigated distances (10–140 km) with energy confined in the frequency band 0.04–0.09 Hz. This phase reproduces Rayleigh waves generated by earthquakes in the same frequency range. Arrival time of Rayleigh waves was picked at all the couples of stations to obtain the average group velocity along the path connecting the two stations. The picks were inverted in separated frequency bands to get group velocity maps then used to obtain an *S* wave velocity model. Penetration depth of the model ranges between 12 and 25 km, depending on the velocity values and on the depth of the interfaces, here associated to strong velocity gradients. We found a low-velocity anomaly in the region bounded by the two main faults that generated the 1980, *M* 6.9 Irpinia earthquake. A second anomaly was retrieved in the southeast part of the region and can be ascribed to a reminiscence of the Adria slab under the Apennine Chain.

1. Introduction

In the last decade the use of passive methods based on ambient noise analysis has become very popular. The interest in their application is related to the possibility to reconstruct the properties of the propagation medium by ambient noise measurements, without the use of localized natural or artificial sources. Hence, they could be used as a cheap alternative to exploration methods based on the use of active seismic sources while providing useful information even in regions where earthquakes do not occur.

The passive seismic methods are based on the cross correlation of seismic signals recorded at couples of synchronized stations, located in different positions. It has been theoretically shown that the cross correlation of signals recorded at pairs of receivers is proportional to the imaginary part of the Green's function under the condition of energy equipartition [Sánchez-Sesma and Campillo, 2006]. Since energy equipartition is peculiar of multiple scattering, this condition can also hold for coda waves, whose cross correlation is still related to the medium Green's function [Campillo and Paul, 2003; Sneider, 2004]. Although in many cases energy equipartition condition is not completely fulfilled, the cross correlation may still approximate the Green's function of the medium. It has been shown both experimentally and numerically that an isotropic distribution of noise sources or scatterers around the receivers may allow to retrieve a coherent Green's function from cross correlation [e.g., Shapiro and Campillo, 2004; Paul et al., 2005].

The computed Green's functions are usually dominated by surface waves owing to the location of receivers at the surface. Its emergence originates from the fact that the seismic noise is preferentially excited by shallow sources [Shapiro et al., 2005]. Nevertheless, also body waves can be extracted from cross correlation of ambient noise both at short [Roux et al., 2005; Draganov et al., 2009], regional [Poli et al., 2012], and teleseismic [Boué et al., 2013] distances.

Passive seismic processing is mainly focused on two geophysical applications: imaging and monitoring. In the former case the Rayleigh and Love surface waves are extracted from the cross correlation of seismic noise to provide group and phase velocity maps at the surface and eventually tomographic images of the subsurface. Many studies provided accurate velocity models both at regional [Shapiro et al., 2005; Yang et al., 2007] and local scales [Roux, 2009; Picozzi et al., 2009; Pilz et al., 2013].

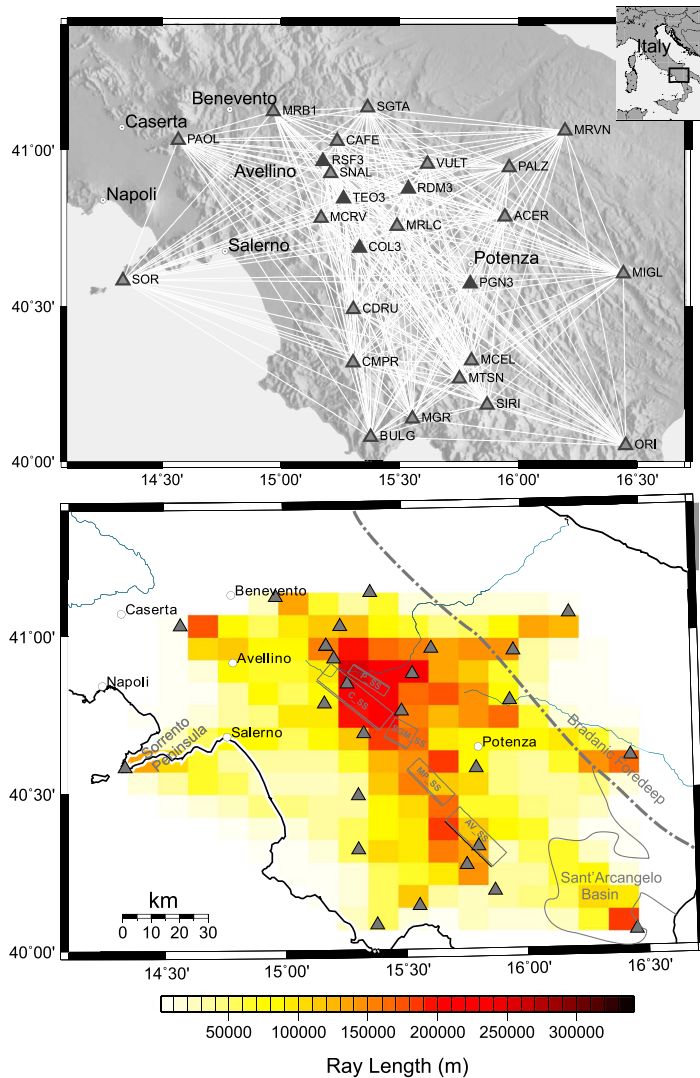


Figure 1. Seismic stations installed in Southern Italy and used for the cross-correlation analysis and total ray length in cells. (top) The dark gray triangles indicate the stations of ISNet, and the light gray triangles are the seismic stations of RSN (Rete Sismica Nazionale) managed by INGV. The white lines between each couple of stations indicate the ray coverage of the investigated area. (bottom) Total ray length (in m) in each cell (of size equal to 10 km × 7.5 km) of investigated area. The gray dashed lines show the main buried thrust front of the area which defines the western limit of Bradano Foredeep. The gray boxes indicate the positions of the main Seismogenic Sources of the investigated area: Colliano (C_SS), Pescopagano (P_SS), San Gregorio Magno (SGM_SS), Melandro-Pergola (MP_SS), and Agri-Valley (AV_SS) [Basilì et al., 2008].

In the latter case, the cross correlation extracted from the noise is used for the continuous monitoring of the velocity changes in the propagation medium. These variation can be observed in several fault areas after the occurrence of large earthquakes [Brenugier et al., 2008; Zaccarelli et al., 2011] and in volcanic regions, where the seismic velocity variations can suggest pre-eruptive inflation of the volcanic edifice [Duputel et al., 2009].

Extraction of Green's function requires summation of long time series of ambient noise cross correlation to improve the signal-to-noise ratio. Additional processing is required to reduce the weight of earthquakes

Table 1. List of Used Seismic Stations

#Station	Sensor	Network	Acquisition System
ACER	TRILLIUM 40 s	RSN	TRIDENT-NANOMETRICS
BULG	TRILLIUM 40 s	RSN	TRIDENT-NANOMETRICS
CAFÉ	TRILLIUM 40 s	RSN	GAIA2
CDRU	TRILLIUM 40 s	RSN	TRIDENT-NANOMETRICS
CMPR	TRILLIUM 40 s	RSN	TRIDENT-NANOMETRICS
MCEL	TRILLIUM 40 s	RSN	TRIDENT-NANOMETRICS
MCRV	TRILLIUM 40 s	RSN	TRIDENT-NANOMETRICS
MGR	TRILLIUM 40 s	RSN	TRIDENT-NANOMETRICS
MIGL	TRILLIUM 40 s	RSN	TRIDENT-NANOMETRICS
MRB1	TRILLIUM 40 s	RSN	TRIDENT-NANOMETRICS
MRLC	TRILLIUM 40 s	RSN	TRIDENT-NANOMETRICS
MRVN	TRILLIUM 40 s	RSN	TRIDENT-NANOMETRICS
MTSN	TRILLIUM 40 s	RSN	TRIDENT-NANOMETRICS
ORI	TRILLIUM 40 s	RSN	GAIA 2
PALZ	TRILLIUM 40 s	RSN	TRIDENT-NANOMETRICS
PAOL	TRILLIUM 120 s	RSN	GAIA 2
SGTA	TRILLIUM 40 s	RSN	GAIA 2
SIRI	TRILLIUM 40 s	RSN	TRIDENT-NANOMETRICS
SNAL	TRILLIUM 40 s	RSN	TRIDENT-NANOMETRICS
SOR	TRILLIUM 40 s	RSN	TRIDENT-NANOMETRICS
VULT	TRILLIUM 40 s	RSN	TRIDENT-NANOMETRICS
COL3	TRILLIUM 40 s	ISNet	OSIRIS-AGECODAGIS
PGN3	TRILLIUM 40 s	ISNet	OSIRIS-AGECODAGIS
RDM3	TRILLIUM 40 s	ISNet	OSIRIS-AGECODAGIS
RSF3	TRILLIUM 40 s	ISNet	OSIRIS-AGECODAGIS
TEO3	KS2000-EDU	ISNet	OSIRIS-AGECODAGIS

and coherent signals in the noise and to eliminate instrumental irregularities such as spikes. In this case, recursive filtering, spectral whitening [Shapiro et al., 2006], one-bit normalization [Larose et al., 2004; Shapiro et al., 2005], data clipping [Sabra et al., 2005], and running absolute mean normalization [Bensen et al., 2007] represent the common practice of single station processing before correlation and favor the emergence of the Green's function even for limited continuous time series of seismological data.

In this study, we computed the cross correlation of about 3 years of ambient noise acquired in the Campania-Lucania Apennine section of Southern Italy. The Campano-Lucano Apennine is characterized by normal direct and antithetic fault systems (these faults are indicated as C_SS, P_SS, SGM_SS, MP_SS, AV_SS in Figure 1) and extends over an area of

about $100 \times 100 \text{ km}^2$ in Southern Italy. The region experienced in last century three events of magnitude larger than 6 [Westaway, 1987; Emolo et al., 2004], the largest of which was the 1980, M 6.9, Irpinia earthquake, that occurred along three northwest-southeast oriented fault segments. Since 2007, the installation of the dense network ISNet as a prototype for an early warning system in Southern Italy [Iannaccone et al., 2010] allowed to develop near-fault observatory practices to characterize the geological structure [De Matteis et al., 2012; Amoroso et al., 2014] and to monitor the evolution of the microseismicity of the area [Bobbio et al., 2009; Stabile et al., 2012; Zollo et al., 2014]. Comparing the noise levels with the theoretical signature of small earthquakes based on the Brune model, the minimum magnitude of an event detectable in the region is 1.1, while the threshold for an accurate location is 1.3 [Bobbio et al., 2009; Vassallo et al., 2012].

In this study, we compute the cross correlation from ambient noise continuous records. After presenting the seismic networks and the data selected for this study, we discuss the specific data processing for single station that we applied before cross correlation. After retrieving the Green's functions from the stack of the cross-correlation functions, we compare the stacked functions to the low-frequency surface waves recorded during the largest earthquake occurred in the area. We then isolate the surface wave contribution from which we retrieve the dispersion curves in terms of group velocity. Finally, we invert the traveltimes to obtain a 2-D tomographic velocity model for the surface waves in the investigated area.

2. Seismic Stations and Data

For this study we used continuous data recorded by the broadband seismic stations located in the Irpinia region and belonging to two different seismic networks: the local network ISNet and the national network Rete Sismica Nazionale (RSN). The selected stations for the analysis are listed in Table 1, and their location is shown in the map of Figure 1.

ISNet, Irpinia Seismic Network, is a dense, local network of strong-motion, short-period, and broadband seismic stations displaced over an area of approximately $100 \times 70 \text{ km}^2$ along the southern Apennines chain [Iannaccone et al., 2010], around the fault system that generated the 1980, M 6.9 Irpinia earthquake. ISNet is managed by AMRA (Analisi e Monitoraggio del Rischio Ambientale) and University of Naples Federico II

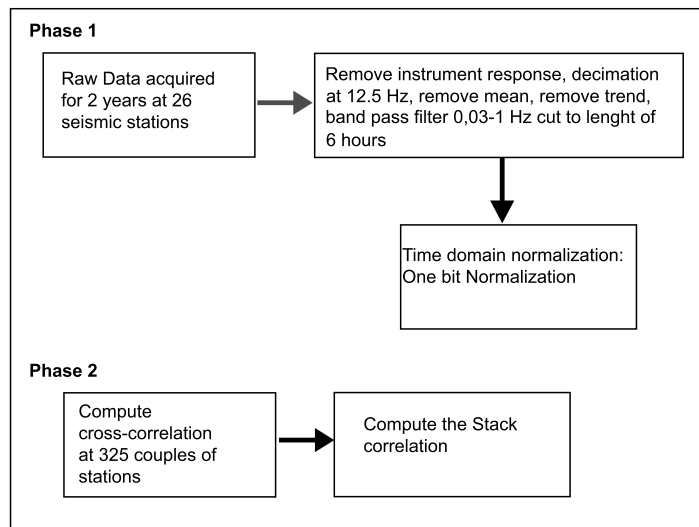


Figure 2. Block scheme for single station processing (Phase 1) and cross correlation (Phase 2). After data selection and filtering, data are equalized in time domain by one-bit normalization resulting into a barcode signal that keeps only phase information. In the Phase 2 normalized traces are cross correlated for couples of stations and stacked.

and is composed of 32 stations, equipped with two three-component instruments: an accelerometer (Güralp CMG-5 T) and a seismometer. Most of the seismometers are short-period velocimeters S-13 J from Geotech. At eight stations short-period instruments are replaced by broadband sensors (40 s from Nanometrics Trillium and Geotech) to better record regional and teleseismic events and to broaden the spectrum of the noise in the area at low frequency. The data acquisition is performed by the Osiris-6 data logger (Agecodagis), equipped with a Σ - Δ 24 bit analog to digital converter. Input signals entering the data logger are not amplified and are acquired by the analog-to-digital converter at 125 or 250 samples/second. The data sent by the stations to the control centers of the network are managed by the software Earthworm [Johnson *et al.*, 1995] that automatically picks the first arrivals and locates the events inside ISNet or on its outskirts.

The RSN (Rete Sismica Nazionale) is managed by Istituto Nazionale di Geofisica e Vulcanologia (INGV) and receives signals from more than 270 stations belonging to the Italian National Seismic Network, the MedNet Seismic Network, and several European and regional networks. The RSN collects data from more than 150 broadband and very broadband instruments (Streckeisen STS-1 and STS-2, Güralp CMG 40 and 360, Trillium 40 and 120) and from about 100 short-period instruments, in addition to several accelerometers. The acquisition system is mainly of two types, either realized by Nanometrics and or by INGV (GAIA system), with a sampling frequency ranging from 50 to 200 Hz. The acquisition system is fully operational since 2004 and is connected with digital terrestrial and satellite lines. It provides a first rapid location within 20–30 s from the origin time, a first evaluation of local magnitude M_L within 40 s, and updated location and magnitude estimations with a delay ranging from 3 to 5 min after the origin time [Amato and Mele, 2008; Schorlemmer *et al.*, 2010].

3. Data Processing and Cross Correlations

Continuous ambient noise records were collected and processed following the method described in Bensen *et al.* [2007]. The block diagram of the processing chain is shown in Figure 2. At a single station, the available vertical data stream was corrected for the instrumental response, decimated at 12.5 Hz, and cut in separated windows of duration of 6 h, starting from the midnight of each day. The mean and the trend were removed from the velocity traces, and the data were band pass filtered between 0.03 Hz and 1 Hz. When gaps occurred in the helicorder, data were further cut in smaller continuous time windows; each of them was used for the cross-correlation computation if its duration was at least 1 h.

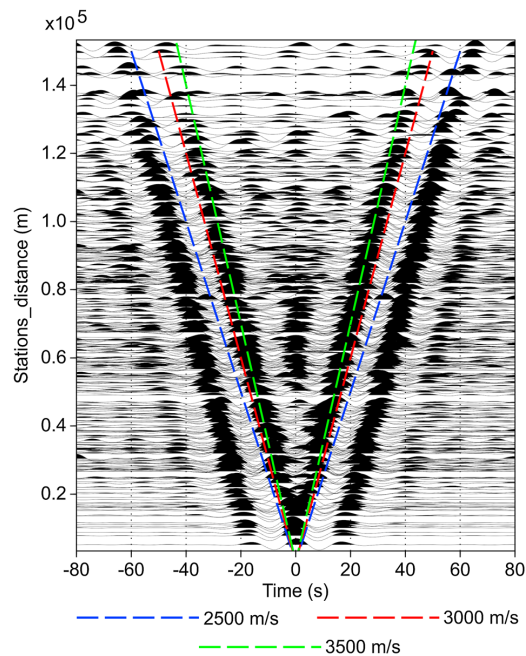


Figure 3. Cross-correlation stacks, organized for increasing interstation distance. The dashed blue, red, and green lines show the theoretical arrival times of a surface wave with velocity of 2.5, 3.0, and 3.5 km/s, respectively.

For the selected time windows, we applied the one-bit normalization [Bensen *et al.*, 2007], with the goal of equalizing the amplitude of the signal and taking care only of the phases. The one-bit normalization also reduces the weight of spikes and of seismic and anthropogenic events in the helicorder. We also tested the use of the spectral whitening in the same frequency range as selected for the filter. We applied the whitening either before or after the one-bit normalization. We did not observe any improvement in the final cross-correlation functions. Hence, the presented analysis was finally performed without any spectral amplitude equalization.

After the single station processing, data were cross correlated for couples of stations and stacked. When the complete data stream for both the selected stations was available, the cross correlation was performed over time windows of 6 h. When gaps occurred at one or both stations, we computed the cross correlation only in the case in which the two data streams superimpose in a continuous window of minimum duration of 1 h. A total number of 277,049 vertical cross-correlation functions were computed at 325 different couples of receivers extracted from the 26 seismic stations used in this study. The minimum number of cross-correlated traces before stacking spans from 42 (10 days of continuous data) to 2590 (647 days of continuous data), depending on the available data at the stations.

To check the quality of the resulting cross correlations and evaluate the upper frequency at which they are stable, we narrowed the band of the filter applied to the data, and we selected the cross-correlated records only when overcoming assigned values of the signal-to-noise ratio. We realized that no improvement larger than few percent was gained when such an ad hoc procedure was adopted, indicating that ambient noise features are pretty stable with time and automatic procedures are able to detect them. Hence, for further analysis we used the stack of all available cross-correlation functions at all the investigated couples of stations.

4. Cross-Correlation Analysis

The vertical cross-correlated stacked traces computed for all the available couples are shown in Figure 3. The correlations are represented in the section so that the positive time corresponds to waves propagating from the northernmost to southernmost station in the couple. Traces are then plotted as a function of the interstation distance. The cross correlations are filtered in the frequency band 0.04–0.09 Hz, and each trace in the section is normalized to its maximum value. We clearly observe energetic seismic phases symmetrically with respect to zero time, indicating that both “causal” and “anticausal” phases are retrieved by this analysis. The amplitude of the most energetic signal differs between the positive and the negative directions with the causal signal showing larger amplitudes than the anticausal one on average. It is worth to note that this difference between causal and anticausal portions of the cross correlations only affects the relative amplitudes while preserving the waveform and the arrival time of the most energetic phase. Hence, this asymmetry in the amplitudes does not affect the estimation of the arrival time associated with such a seismic phase. Nevertheless, this observation reveals a dominant direction of ambient noise propagation from north to

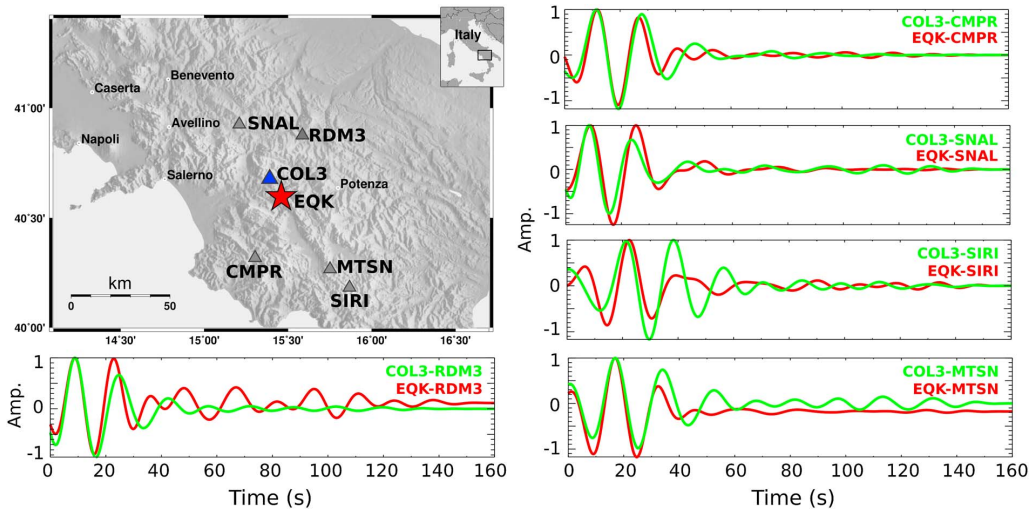


Figure 4. The map on the top left shows the location of the stations SNAL, RDM3, CMPR, MTSN, SIRI (gray triangles), and COL3 (blue triangle); this latter being installed very close to the epicenter of $M_L = 3.7$ earthquake (red star) occurred on 13 July 2010 at 03:36:13. In the other plots, the low-frequency records of the earthquake at the stations CMPR, SNAL, SIRI, MTSN, and RDM3 (red curves) are compared with the cross correlation computed between COL3 and the same stations (green curves). All waveforms are band pass filtered between 0.04 and 0.09 Hz.

south in this area. At both positive and negative times, the most energetic seismic phase travels with a seismic velocity of about 3–3.5 km/s that is compatible with crustal surface wave velocities observed in the area by previous studies in the same frequency range [Brzak *et al.*, 2009; Li *et al.*, 2010].

To further investigate the relationship of the cross-correlated signals with the Green’s functions of the medium, we compared them with data recorded for the largest earthquake occurred in this region since the installation of ISNet. The selected earthquake occurred on 13 March 2010 at 03:36:18 UTC, and its local magnitude was 3.7. The event occurred nearby COL3 station and was recorded all across the investigated area. In Figure 4 we compare the velocity records of the earthquake at five stations (CMPN, SNAL, SIRI, RDM3, and MTSN) with the cross-correlation functions between COL3 and one of the selected five stations. Both earthquake data and cross correlations are filtered in the frequency band 0.04–0.09 Hz and normalized. The earthquake data are corrected for the focal mechanism, while the causal and anticausal contributions to cross-correlation functions were stacked before normalization. We observe that the largest amplitude phase observed for the earthquake is well reproduced both in timing and shape at all the stations by the cross-correlation functions. Small differences and short time shifts might be ascribed to the different epicentral location and to the event focus. Hence, we may conclude that the cross-correlation functions well approximate Rayleigh wave Green’s functions between each pair of stations in the analyzed frequency band, independently of the distance and the relative location in the area.

In Figure 3 we can also recognize a coherent seismic phase near zero time between 40 km and 60 km. Although the limited distance range covered by the data does not allow to accurately characterize such a phase, we believe that it is associated with a body wave. Nevertheless, a better characterization of this phase requires larger distances and eventually longer time series, to improve the signal-to-noise ratio with the stack.

Finally, Figure 5 shows examples of cross correlations filtered in the 0.04–0.08 Hz, computed for three couples of stations (COL3-PGN3, ACER-SIRI, and MCEL-PALZ) using all the data acquired in 2009. For each couple, the horizontal axis represents the time lag of the cross-correlation function, while the vertical axis corresponds to the time in Julian days at which the ambient noise was recorded. The color scale is proportional to the amplitude of the cross-correlation function although each trace is normalized to its maximum value, positive and negative amplitudes being red and blue, respectively. The corresponding stack functions are shown at the top of each panel, while a map with the location of station pairs is shown at the bottom of the figure. For all the three couples we observe a good coherence over the whole analyzed year. One can observe that

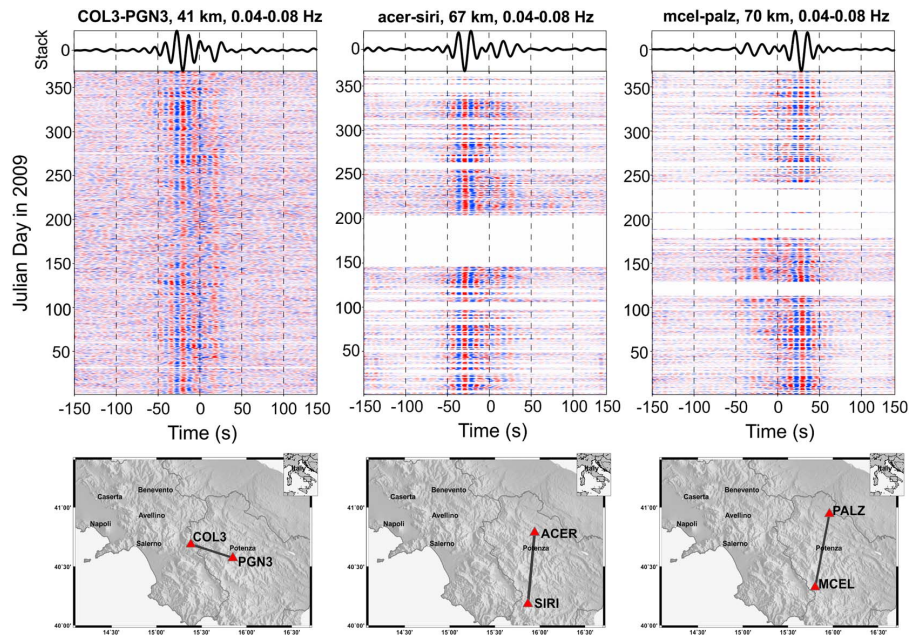


Figure 5. Cross correlation filtered between 0.04 and 0.09 Hz for three couples of stations (COL3-PGN3, acer-siri, and mcel-palz) as a function of time computed with data acquired in 2009. Each trace represents the cross correlation for 6 h long signals. The stack of all the cross-correlation functions is highlighted on top of the panels. The map at bottom shows the position of the couples. Cross correlation is almost stable with time.

the cross-correlation functions are asymmetric around zero. Specifically, for the couples COL3-PGN3 and ACER-SIRI anticausal signals show larger amplitudes, while the opposite behavior occurs for the couple MCEL-PALZ. Nevertheless, the presence of clear causal and anticausal signals, albeit with different amplitudes, evidences a wider azimuthal distribution of the noise sources. Although we observe a strong coherence in both the causal and anticausal phases during all the year, we clearly see a decrease of the amplitudes of both phases during summer time. This can be recognized in Figure 5, mainly in the first panel, between days 150 and 200, and it is a common feature of all the cross correlations. A decrease of the power spectral density computed on the ambient noise in the same area was observed in a slightly higher frequency range (0.1–0.5) Hz [Vassallo *et al.*, 2012], and it was correlated with the sea wave motion along the coast. We then argue that the amplitude decrease of the cross-correlated function during the summer season is related to a decrease in the wave motion; this hypothesis is also supported by the analysis of Brzak *et al.* [2009], who also located the sources of the ambient noise in Southern Italy along the coast.

5. Picking and Ambient Noise Tomography

5.1. Picking

The main target of this work is the reconstruction of tomographic images of the subsoil in southern Apennines from inversion of surface wave group velocity, as extracted from cross correlation of seismic noise. We inverted Rayleigh wave arrival time measurements performed on the cross-correlation functions in time domain. For the aim, the traces were filtered in different narrow bands applying a zero-phase, sine squared tapered filter. Then, the picking was performed on the symmetric component of cross correlations obtained by summing the causal part and the reversed anticausal part [Bensen *et al.*, 2007]. To maintain a coherence in the measurements of the arrival times, the traces were organized in seismic sections as a function of the station interdistance and picked on the maximum of the wavelet, corresponding to the surface wave phase along the section. In order to obtain reliable arrival time measurements, the picks are determined only for

Table 2. Number of Picked Traveltimes and Minimum Stations Interdistance (Offset) Used in Each Analyzed Frequency Band

Frequency Band	Number of Picks	Offset (m)
0.04–0.05 Hz	144	75,000
0.05–0.06 Hz	158	70,000
0.06–0.07 Hz	175	65,000
0.07–0.08 Hz	192	60,000
0.08–0.09 Hz	210	55,000

traces for which the distance between the stations is longer than one wavelength. The number of picks and the minimum stations interdistance (offset) used in each analyzed frequency band are listed in Table 2. Figure 6 shows the picks obtained in each frequency band. In the figure we superimpose the theoretical arrival times for different velocities

values with a red dashed line. The figure shows the surface wave dispersion, with a decrease in the group velocity as the frequency increases. Figure 7 shows the group velocity dispersion curves measured from four station pairs along different paths through the investigated area. For a fixed pair and frequency, the velocity is estimated by dividing the interstation distance for the measured arrival time. In Figure 7, we observe that dispersion curves measured from the pair MRVN-SOR, crossing the Apenninic chain in the upper part of the investigated region, show the largest velocity values. This can be ascribed to a larger velocity value in the northernmost part of the analyzed region, at least for frequencies smaller than 0.07 Hz. Conversely, the minimum of the group velocity is observed along the Apenninic path MRB1-ORI. This is a common feature of all of the Apenninic paths concerning the station ORI, indicating a low-velocity body in the vicinity of this station. The remaining two pairs (ACER-PAOL and MIGL-SOR) have intermediate dispersion curves between the first two cases.

5.2. Group Velocity Inversion and Resolution Analysis

The surface wave tomography of the investigated area was obtained using the Fast Marching Surface Tomography software (FMST) [Rawlinson and Sambridge, 2004]. This iterative nonlinear traveltime tomography code uses the fast marching method (FMM) for the forward prediction step, with traveltimes computed

in a 2-D spherical shell system and a subspace inversion scheme for the inversion step. The algorithm implements an iterative nonlinear method in which the inversion step assumes local linearity, but the repeated application of the FMM and the subspace inversion allows to account for the nonlinear relationship between velocities and traveltimes. In the inversion step both smoothing and damping regularizations are allowed in order to address the problem of nonuniqueness of the solution. The combination of the FMM and the subspace method provides stable and robust tomographic images; therefore, the FMST was widely used by several authors working with ambient noise tomography [Saygin and Kennett, 2010; Nicolson et al., 2012; Vuan et al., 2014].

For the computation of the tomographic images, the investigated area was subdivided in a 2-D regular grid of 10 × 10 velocity nodes. The nodes are not equally spaced along the longitude and latitude, with a relative distance of 0.115° and 0.065°, respectively. The damping factor ϵ and the smoothing

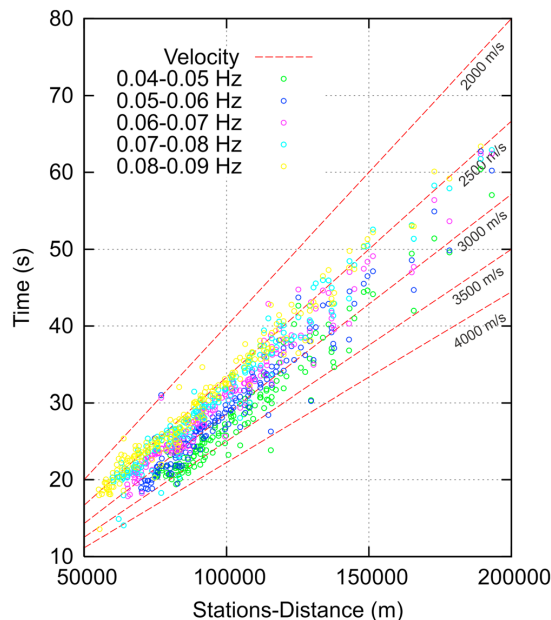


Figure 6. Picks of the arrival time of the Rayleigh wave, used for group velocity inversion, for data filtered in the bands 0.04–0.05 Hz, 0.05–0.06 Hz, 0.06–0.07 Hz, 0.07–0.08 Hz, and 0.08–0.09 Hz. The red dashed lines show the theoretical arrivals for surface wave traveling at velocity of 2.0, 2.5, 3.0, 3.5, and 4.0 km/s.

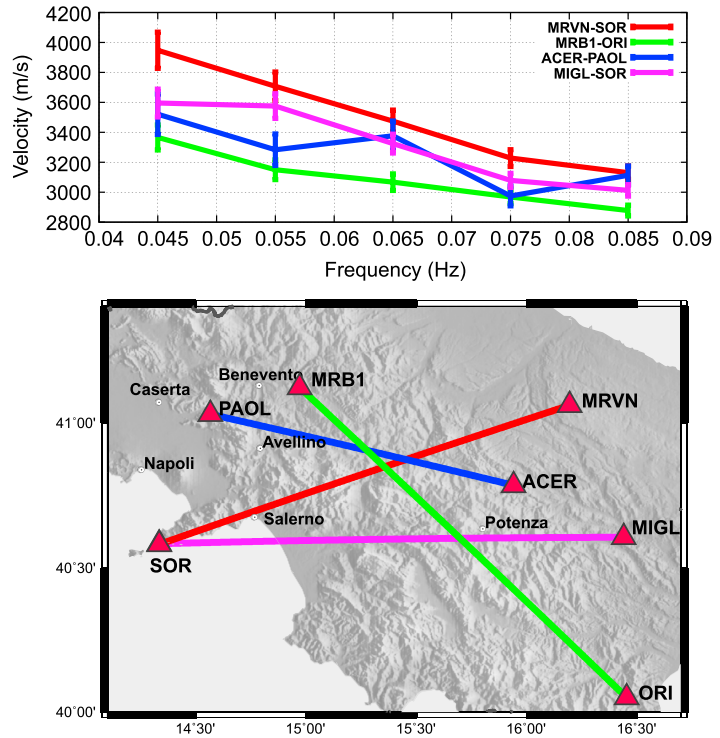


Figure 7. (top) Group velocity curves measured from the couples MRVN-SOR, MRB1-ORI, ACER-PAOL, and MIGL-SOR. (bottom) Interstation paths for group velocity measurements.

factor η are chosen following the approach of *Rawlinson and Sambridge* [2003]. It is based on a three-step procedure using the trade-off curves between the RMS function and the model roughness on the one hand and between the RMS function and the model variance on the other hand. We analyzed the trade-off curves between data fit and model roughness and data fit and model variance for different values of ε and η as shown in Figure 8. The optimal results were obtained when the decrease of the RMS started to slow down

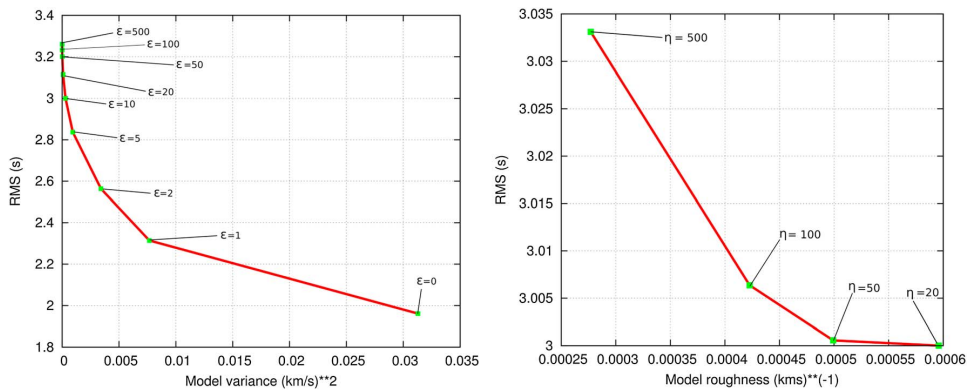


Figure 8. Trade-off curves used to choose the appropriate damping and smoothing parameters in the inversion. Several inversions with different values of such parameters are required in order to construct these curves. (left) Data fit versus model perturbation for different values of the damping factor ε . (right) Data fit versus model roughness for different values of the smoothing parameter η .

when decreasing the two different parameters. The choice of parameters which fix the misfit to a reasonable size allows to limit the contributions from data errors and rounding errors on the final solutions. Following the curves of Figure 8, the values of $\varepsilon=1$ and $\eta_l=100$ were selected.

The velocity models obtained from the inversion are shown in Figures 9a, 9c, 9e, 9g, 9i, and 9k. Rayleigh waves sample the crossed geological structure, at an average depth of about one third of its wavelength. Assuming this scaling, the images obtained for the investigated frequency scan the subsoil up to depths of about 14 and 18 km, respectively. The tomographic maps show frequency-dependent features. At low frequencies (between 0.04 and 0.07 Hz) a variation of seismic velocity clearly appears in the direction of the Apennine chain. The main feature at these frequencies is a high-velocity body in the northernmost part of the maps. It follows the Sorrento peninsula and cuts the Apennine chain from southwest to northeast. This change in the velocity is clearly visible in the first tomographic map (Figure 9c), but it can be retrieved also at higher frequencies, although the velocity anomaly is smoother. In the same frequency range a low-velocity anomaly is located in the southeast part of the region, below the Sant'Arcangelo basin. The contrast is more evident in the frequency range 0.05–0.07 Hz (Figures 9e and 9g) than at very low frequencies (Figure 9c), indicating a shallower anomaly, as compared to the previous one.

At higher frequencies, between 0.07 to 0.09 Hz (Figures 9i and 9k), the models show the occurrence of strong lateral variations of seismic velocity orthogonally to Apennine chain. In the well-resolved area, (a detailed discussion of which is present at the end of the section), inside the dashed black lines, we can recognize domains characterized by low and high velocities, respectively. These bodies appear very clearly in the 0.08–0.09 Hz (Figure 9k) tomographic image, but they start to emerge also in the frequency range 0.07–0.08 Hz (Figure 9i). These two maps correspond in depth to the region above 14 km where most of the present microseismicity occurs [Amoroso *et al.*, 2014]. The zone where the sharpest lateral transition occurs is well correlated with the location of the NW-SE oriented, primary normal faults associated with the 1980, M_s 6.9 earthquake. The surface trace of these faults is superimposed to the tomographic maps with solid black lines. This observation is in good agreement with other tomographic results obtained for the same area from the inversion of traveltimes of local events [Amoroso *et al.*, 2014] and of local/regional events [Di Stefano *et al.*, 2009]. The different characteristics of the tomographic models, with a transition between SW-NE oriented structures at low frequencies to NW-SE domains at higher frequencies, suggests a significant change in the structure.

A synthetic checkerboard test was used to investigate the resolution of the tomographic results. The checkerboard was built from the final retrieved model with a maximum velocity perturbation at the vertices of the grid of 0.2 km/s in order to ensure small perturbations for ray paths. The regularization parameters used during the checkerboard tests are the same as used for the reconstruction of final tomographic models. The checkerboard results (Figures 9b, 9d, 9f, 9h, 9j, and 9l) show that the regions where the checkerboard pattern is well reconstructed are located in the central part of investigated area where there is a large number of seismic stations and dense ray crossing.

We defined the well-resolved areas (represented by black dashed lines) using both the results of the checkerboard test and the distributions of available paths and azimuthal coverage in each cell of the velocity model. The resolved areas are those in which the perturbation retrieved by the checkerboard test has the same sign of the velocity anomaly introduced as input. Although in some areas the shape of the anomaly is not correctly reconstructed, the distribution of available paths from the cross-correlation analysis (Figure 1) provides a reasonable imaging of the gradient of the group velocity through the explored area. The size of resolved areas increases with frequency because the number of picks used for the tomographic inversion also increases with frequencies. This is also due to the selection of picks based on the signal wavelength as a function of source receiver distance.

5.3. S Wave Velocity Model

We obtained an S wave velocity model from inversion of the group velocity dispersion curves, using the software Geopsy [Wathelet *et al.*, 2004]. For each of the 400 control nodes in the group velocity map, as obtained in the previous section, we extracted a dispersion curve to get a local 1-D velocity profile with depth. To limit the model variation and avoid multiple solutions, we fixed the density to 2700 kg/m^3 , while the layer thicknesses and P and S wave velocity values within each layer were obtained from inversion. We also bounded the range of variation for the S wave speed from the minimum surface wave velocity value to 2.5 km/s and

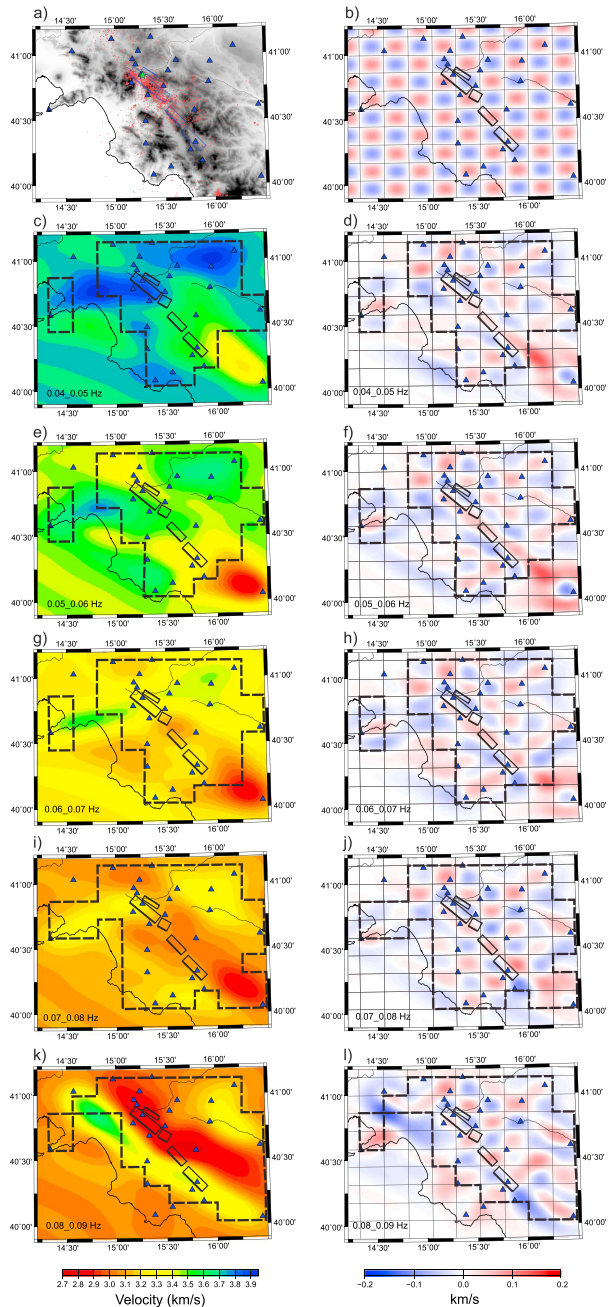


Figure 9. (c, e, g, i, and k) Group velocity maps in the frequency bands 0.04–0.05 Hz, 0.05–0.06 Hz, 0.06–0.07 Hz, 0.07–0.08 Hz, and 0.08–0.09 Hz. (d, f, h, j, and l) The results of checkerboard resolution test associated to each tomographic model. The black dashed lines, determined by the results of checkerboard test, limit the well-resolved areas in the tomographic models. (a) The investigated area with the recent seismicity (epicentral positions of seismic events occurred in the last 10 years) and the epicentral position of 6.9 M_w 1980 Irpinia earthquake and (b) the theoretical pattern of the perturbation used for the checkerboard tests.

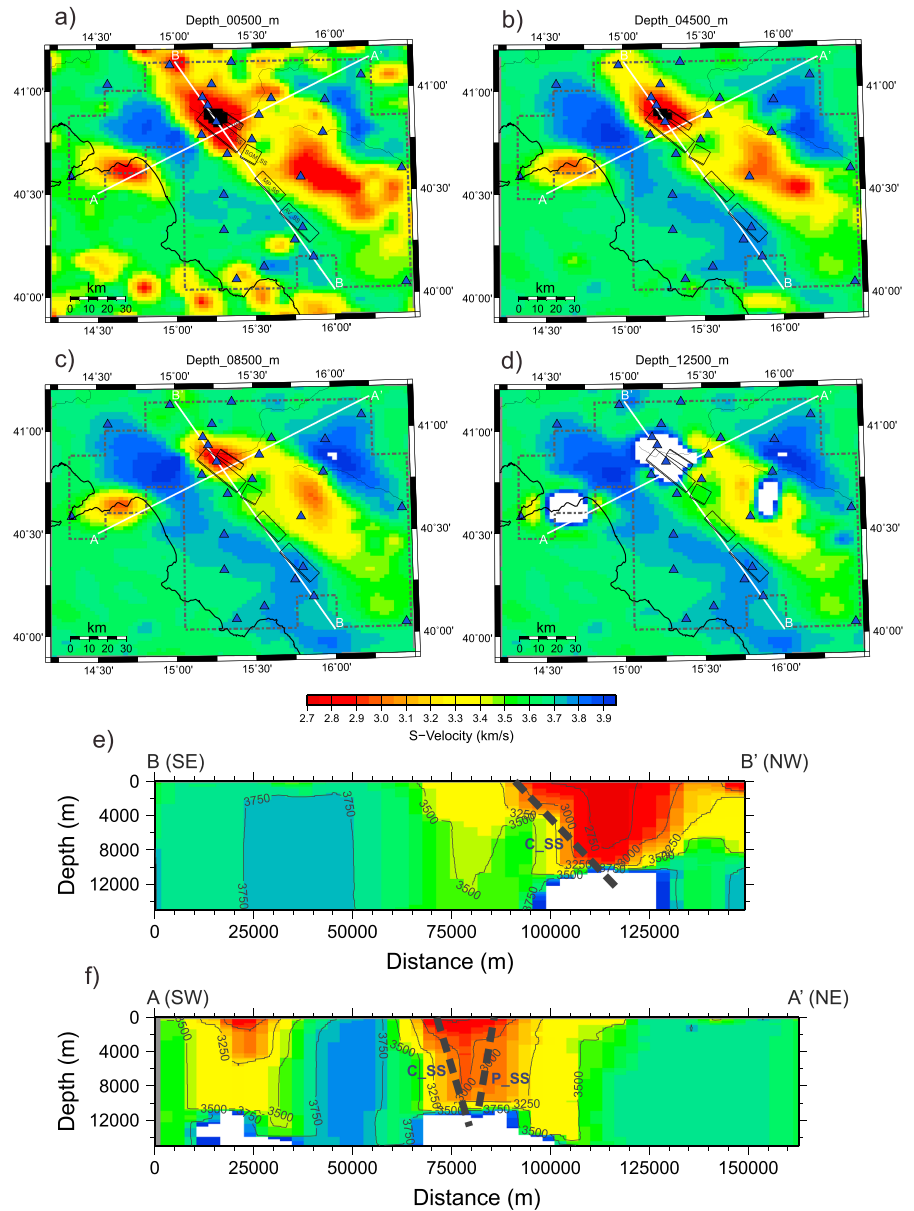


Figure 10. Horizontal and vertical sections of *S* wave velocity values obtained from the inversion of the dispersion curves. (a–d) The areal distribution of the *S* wave velocity field at four different depths (500 m, 4500 m, 8500 m, and 12500 m, respectively). The black boxes indicate the positions of the main seismicogenic sources of the investigated area, the white lines show the position of vertical section, and gray dashed lines delimit the well-resolved areas of the tomographic models on basis of the checkerboard tests. Cross sections along (e) Apennine and (f) anti-Apennine directions. The gray dashed lines show the positions of faults lines along the vertical section (from Database of Individual Seismicogenic Sources, <http://diss.rm.ingv.it/diss/>).

for the Poisson parameter from 0.2 to 0.5. For each dispersion curve, we performed three inversions fixing the number of layers from two up to four. To select the best representation in terms of number of layers, we studied the decrease in the misfit function, estimated as the L^2 norm between synthetic and measured dispersion curves, as the number of layers increases. Comparing the decrease in the misfit function, we concluded that a three-layer model is the best solution for all of the nodes, and moreover, we did not observe any significant improvement when increasing the number of layers beyond three. As expected we also found that such dispersion curves can only resolve the S wave model, because the P wave velocity values are completely unconstrained.

To smoothen the solution and study the uncertainty in the model, for each inversion we extracted a family of solutions around the minimum misfit. We then resampled the depth with a space step of 200 m, and we averaged the S wave velocity using all the models in the selected set. We also associated the standard deviation coming from the variability in the velocity values at the same depth as the uncertainty in the velocity at such a depth (the maps of the standard deviations are shown in Figure S2 in the supporting information). This strategy clearly generates a smoothly changing velocity profile with depth. After estimating the S wave velocity profile beneath each node of the grid, we interpolated the velocity values to obtain a 3-D model which allows us to follow the lateral variations of the medium.

The model is represented in Figure 10, as 2-D slices at constant depth or 2-D profiles, one along the Apennine (BB' line in Figure 10) direction and the second one almost orthogonal to the first one and crossing the faults traces (AA' in Figure 10). The dashed line in areal maps represents the boundary of well-resolved area obtained by adding all the resolved areas reconstructed for each frequency band (shown in Figure 9). Figure 10 also shows the position of the main seismogenic sources (black boxes) within the investigated area. The three northernmost faults (Colliano, C_SS; Pescopagano, P_SS; and San Gregorio Magno, SGM_SS seismogenic sources in Figure 10a) were the ones responsible for the 1980, M_w 6.9, Irpinia earthquake. The final S model ranges between 2.7 km/s and 4.0 km/s and the penetration depth between 10 km and 15 km, depending on the above velocity model. The larger the average S wave speed in the shallow crust, the larger the penetration depth. We observe that most of the variations occur along the anti-Apennine direction, while they look almost homogeneous along the Apennine chain. A low-velocity zone follows the Apennine Belt in the NW-SE direction and it lies, in the northernmost part, within the two segments of the Irpinia fault system (Colliano C_SS and Pescopagano P_SS seismogenic sources in Figures 10e and 10f) that generated the 1980 earthquake. We performed a shape test in order to check the reliability of low-velocity anomaly located between the two fault segments as retrieved in the final tomographic model. The test consists in computing the arrival times and then performing the inversion for a specific velocity pattern. The goal of the test is to check the ability of the inversion method to reconstruct the location, the shape, and the amplitude of a fixed anomaly, maintaining the station configuration unchanged. The comparison between the initial and the retrieved models can give information on the resolution of the tomographic image in specific areas and can also highlight any effect of smearing due to nonoptimal ray sampling. For the test, a low-velocity anomaly was added to a uniform velocity model. This anomaly has the same amplitude, geometry, and position of that retrieved in the 3-D tomographic model. In Figure S3, the results of the tests are shown for different frequency bands, according to the data selection specified in Table 2. The results clearly show that the area characterized by the low-velocity anomaly is well constrained by data. Indeed, the synthetic tests show that in all frequency bands the presence of the low anomaly is well reconstructed by the data inversion.

Low values of the S wave speed are also retrieved in the southeast part of the area, although the extension of the anomaly is less constrained because of the lower number of stations leading to less crossing rays through the model for this region. Moving from the 1980 Irpinia fault along the chain border and hence along the fault system, as reported by the Database of Individual Seismogenic Sources group (<http://diss.rm.ingv.it/diss/>), we found an increase of the S wave speed, which reaches high values along the southernmost faults (3.5–4.0 km/s) at depth of 10–15 km. An additional low-velocity anomaly is retrieved beneath the Amalfi peninsula, but here the resolution rapidly degrades with depth.

6. Discussion

The S wave velocity model, as obtained from the inversion of the group velocity maps, shows a strong low-velocity anomaly along the Campania-Lucania belt, in the region where the 1980, M 6.9 Irpinia earthquake

occurred. When superimposing the fault segments associated with this earthquake, as obtained from *Bernard and Zollo* [1989], we clearly see that the anomaly is bounded by the first and last fault segments that were responsible for the Irpinia earthquake. This separation is clearly visible for depths larger than 5 km, in the 2-D sections of Figure 10. The two fault segments are NW-SE trending antithetic faults, with dipping angle of 60° and 70°, respectively, and they were activated with a delay of about 40 s during that earthquake. The second, shorter segment instead, located southward, lies in a region of transition between the anomaly and a high-velocity body. The *S* wave speed in the anomaly at depths between 5 km and 10 km ranges between 2.7 km/s and 3.0 km/s, while its value outside is about 3.5–3.8 km/s.

A local tomographic model of the area, obtained from inversion of *P* and *S* wave arrival times measured from earthquakes [*Amoroso et al.*, 2014], shows large values of *P* wave velocity, corresponding to a structural high and a large ratio between *P* and *S* wave speeds in correspondence of the low *S* wave anomaly retrieved in this study, although the maximum values of both *P* wave velocity and V_p over V_s are located more southward. Combining the tomographic results, with the location of the microseismicity and the quality factor anomalies, *Amoroso et al.* [2014] interpreted this volume as a fluid-rich reservoir, where prevention of the fluid diffusion across the main structures is likely due to the low permeability of the fault core, while the internal region is a highly damaged fault zone, where fluids can migrate along fractures. Although the tomographic model is smooth, a strong velocity gradient is retrieved across the two bordering faults, indicating possible bimaterial interfaces. We estimated a shear wave velocity contrast up to 15–20% across the main fault that generated the 1980 Irpinia earthquake. We argue that this contrast is mainly due to a lithological discontinuity, although we might expect also a contribution owing to fluid saturated damage materials, as also suggested by *Amoroso et al.* [2014]. Indeed, laboratory measurements on fluid-saturated limestones require large values of the porosity ($> \sim 10\%$) to justify such a contrast [*Assefa et al.*, 2003].

An in-plane rupture propagating along a bimaterial interface may grow faster for slip in the direction of the more compliant medium [*Rubin and Ampuero*, 2007]. In-plane rupture is coupled to antiplane propagation for normal faults in the initial stage of the rupture, while most of the later rupture propagation only occurs in mode III. In its initial stage, hence, a rupture along a bimaterial interface loaded with a homogeneous stress, is favored to propagate downdip. Nevertheless, as pointed out by *Andrews and Ben-Zion* [1997], the stress variation with depth usually controls the rupture initiation, and then most of the normal fault ruptures propagate updip even in the case when the hanging wall is softer than the footwall. However, also in the presence of heterogeneous stress loading, the bimaterial effect for these faults hinders the updip propagation. This is also the case of the 1980 Irpinia earthquake, which nucleated at depth and propagated up to the surface [*Westaway and Jackson*, 1987] and of the recent moderate magnitude events occurred along the Apennine chain, such as the 2009 L'Aquila earthquake [*Cirella et al.*, 2009] and the 1997 Colfiorito earthquake [*Zollo et al.*, 1999]. The resolution in depth of the model obtained from this study is velocity dependent. The larger the average velocity values in the model, the better resolved the depth. Moreover, the resolution in depth could also be influenced by the depth of interfaces separating high-velocity from low-velocity shallow layers. Although the average depth resolution of model is around 12–15 km (see Movie S1 in the supporting information), the small area located in the southeast part of the model is resolved up to depth about 20–25 km with almost uniform velocity (3.5–3.7 km/s). This area is the region below the Sant'Arcangelo marine basin, one of the largest basins of the Apennines located close to the outer portion of the Lucano Apennine, west of the Bradanic Foredeep [*Caputo et al.*, 2007]. Its occurrence at the rear of the leading edge of the chain implies a complex stratigraphic and tectonic control. On the basis of the available deep wells for hydrocarbon research, the upper Pliocene-Pleistocene succession of the basin was interpreted as the continuation of the external foredeep basin.

The geophysical investigations of the area revealed a magnetic positive anomaly [*Speranza and Chiappini*, 2002] and low Bouguer gravity anomalies [*Tiberti et al.*, 2005] that could represent the effect of the northern lateral edge of the slab existing beneath the Calabrian arc [*Selvaggi and Chiarabba*, 1995]. The presence of a low-gravimetric anomaly in the area suggests the presence of deep bodies having lower density than the surrounding region, which is in good agreement with the presence of a deep body characterized by a low *S* wave velocity as retrieved in this work.

Finally, another low-velocity anomaly is observed south of the Sorrento peninsula. This latter could be due to the presence of extensional faults located along the southern part of peninsula [*Casciello et al.*, 2005], associated to the accumulation of a thick layer of sediments. Together with other extensional structures along

the Tyrrhenian margin of the Campania region, these faults are reminiscent of the complex patterns of subsidence and uplift that characterized the area during the Pleistocene while fitting well within the regional geodynamic framework of the southern Tyrrhenian Sea.

7. Conclusions

Cross-correlation analysis of 3 years of ambient seismic noise was used to reconstruct Rayleigh waves traveling between couples of stations and a high-resolution 3-D shear wave tomographic model in Southern Italy. Coherent Rayleigh waves extracted from cross correlations at couple of stations exhibit a significant energy in the frequency range 0.04–0.09 Hz, this band being related to the particular noise sources possibly due to the interactions of the marine waves along the coasts of Italy.

Compared to the results obtained from earthquake tomography, the shear wave images reconstructed in this work provided complementary information on the investigated area and its geological structures. The main normal faults associated to the Irpinia 1980 earthquake show a good spatial correlation with a clear low V_s anomaly. The strong velocity gradient in the fault region well fits the parameters of seismogenic sources (depth and dip), indicating that fault may be bimaterial interfaces that could hinder the nucleation and propagation of large earthquakes.

This study also highlighted the opportunity to study the rich Italian catalog of geological, volcanic, and seismogenic structures through tomographic analysis performed on the ambient seismic noise at low frequency acquired by broadband sensors. Future work will explore the possibility to reconstruct new 3-D and 4-D seismic models for different areas of the Italian peninsula taking advantage of the huge number (more than 300 stations) of broadband seismic stations of Italian Rete Sismica Nazionale (RSN) and other local/regional seismic networks that continuously acquire the ground motion.

Acknowledgments

The authors gratefully thank P. Brondi who helped in the development of software for data analysis and S. Mazza who provided seismic data acquired by Italian Rete Sismica Nazionale (RSN) and A. Zollo, L. Cantore and G. Di Giulio for helpful discussions and suggestions. Continuous seismic data used in this work were collected by the Irpinia Seismic NETWORK (ISNet); continuous waveform are available upon request, for contact <http://isnet.fisica.unina.it/>, last access 30 July 2015) and by Italian Rete Sismica Nazionale (RSN), continuous waveform are available online at link: <http://eida.mn.ingv.it/>, last access 30 July 2015).

References

- Amato, A., and F. Mele (2008), Performance of the INGV National Seismic Network from 1997 to 2007, *Ann. Geophys.*, *51*(2/3), 417–431.
- Amoroso, O., A. Ascione, S. Mazzoli, J. Virieux, and A. Zollo (2014), Seismic imaging of a fluid storage in the actively extending Apennine mountain belt, Southern Italy, *Geophys. Res. Lett.*, *41*, 3802–3809, doi:10.1002/2014GL060070.
- Andrews, D. J., and Y. Ben-Zion (1997), Wrinkle-like slip pulse on a fault between different materials, *J. Geophys. Res.*, *102*(B1), 553–571, doi:10.1029/96JB02856.
- Assefa, S., C. McCann, and J. Sothcott (2003), Velocities of compressional and shear waves in limestones, *Geophys. Prospect.*, *51*(1), 1–13.
- Basilii, R., G. Valensise, P. Vannoli, P. Burrato, U. Fracassi, S. Mariano, M. M. Tiberti, and E. Boschi (2008), The database of Individual Seismogenic Sources (DISS), version 3: Summarizing 20 years of research on Italy's earthquake geology, *Tectonophysics*, *453*, 20–43, doi:10.1016/j.tecto.2007.04.014.
- Bensen, G. D., M. H. Ritzwoller, M. P. Barmin, A. L. Levshin, F. Lin, M. P. Moschetti, N. M. Shapiro, and Y. Yang (2007), Processing seismic ambient noise data to obtain reliable broad-band surface wave dispersion measurement, *Geophys. J. Int.*, *169*, 1239–1260.
- Bernard, P., and A. Zollo (1989), The Irpinia (Italy) 1980 earthquake: Detailed analysis of a complex normal fault, *J. Geophys. Res.*, *94*, 1631–1648, doi:10.1029/JB094iB02p01631.
- Bobbio, A., M. Vassallo, and G. Festa (2009), A local magnitude scale for Southern Italy, *Bull. Seismol. Soc. Am.*, *99*(4), 2461–2470, doi:10.1785/0120080364.
- Boué, P., P. Poli, M. Campillo, H. Pedersen, X. Briand, and P. Roux (2013), Teleseismic correlations of ambient seismic noise for deep global imaging of the Earth, *Geophys. J. Int.*, *194*(2), 844–848, doi:10.1093/gji/ggt160.
- Brenguier, F., N. M. Shapiro, M. Campillo, V. Ferrazzini, Z. Duputel, O. Coutant, and A. Nercessian (2008), Towards forecasting volcanic eruptions using seismic noise, *Nat. Geosci.*, *1*, 126–130, doi:10.1038/ngeo104.
- Brzak, K., Y. J. Gu, A. Okeler, M. Steckler, and A. Lerner-Lam (2009), Migration imaging and forward modeling of microseismic noise sources near Southern Italy, *Geochem. Geophys. Geosyst.*, *10*, Q01012, doi:10.1029/2008GC002234.
- Campillo, M., and A. Paul (2003), Long-range correlations in the diffuse seismic coda, *Science*, *299*, 547–549, doi:10.1126/science.1078551.
- Caputo, R., L. Salviulo, S. Piscitelli, and A. Loperte (2007), Late Quaternary activity along the Scoriabuoi Fault (Southern Italy) as inferred from electrical resistivity tomographies, *Ann. Geophys.*, *50*(2), doi:10.4401/ag-3078.
- Casciello, E., M. Cesarano, and G. Pappone (2005), Extensional detachment faulting on the Tyrrhenian margin of the southern Apennines contractional belt (Italy), *J. Geol. Soc.*, *163*, 617–629, doi:10.1144/0016-764905-054.
- Cirella, A., A. Piatanesi, M. Cocco, E. Tinti, L. Scognamiglio, A. Michelini, A. Lomax, and E. Boschi (2009), Rupture history of the 2009 L'Aquila (Italy) earthquake from non-linear joint inversion of strong motion and GPS data, *Geophys. Res. Lett.*, *36*, L19304, doi:10.1029/2009GL039795.
- De Matteis, R., E. Matruolo, L. Rivera, T. A. Stabile, G. Pasquale, and A. Zollo (2012), Fault delineation and regional stress direction from the analysis of background microseismicity in the southern Apennines, Italy, *Bull. Seismol. Soc. Am.*, *102*(4), 1899–1907.
- Di Stefano, R., E. Kissling, C. Chiarabba, A. Amato, and D. Giardini (2009), Shallow subduction beneath Italy: Three-dimensional images of the Adriatic-European-Tyrrhenian lithosphere system based on high-quality P wave arrival times, *J. Geophys. Res.*, *114*, B05305, doi:10.1029/2008JB005641.
- Draganov, D., X. Campman, J. Thorbecke, A. Verdel, and K. Wapenaar (2009), Reflection images from ambient seismic noise, *Geophysics*, *74*, A63–A67.
- Duputel, Z., V. Ferrazzini, F. Brenguier, N. M. Shapiro, M. Campillo, and A. Nercessian (2009), Real time monitoring of relative velocity changes using ambient seismic noise at the Piton de la Fournaise Volcano (La Réunion) from January 2006 to June 2007, *J. Volcanol. Geotherm. Res.*, *184*, 164–173.

- Emolo, A., G. Iannaccone, A. Zollo, and A. Gorini (2004), Inferences on the source mechanisms of the 1930 Irpinia (Southern Italy) earthquake from simulations of the kinematic rupture process, *Ann. Geophys.*, *47*(6), 1743–1754.
- Iannaccone, G., et al. (2010), A prototype system for earthquake early-warning and alert management Southern Italy, *Bull. Earthquake Eng.*, *8*(5), 1105–1129.
- Johnson, C. E., A. Bittenbinder, B. Bogaert, L. Dietz, and W. Kohler (1995), Earthworm: A flexible approach to seismic network processing, *IRIS Newslett.*, *14*(2), 1–4.
- Larose, E., A. Derode, M. Campillo, and M. Fink (2004), Imaging from one-bit correlations of wide-band diffuse wavefields, *J. Appl. Phys.*, *95*(12), 8393–8399.
- Li, H., F. Bernardi, and A. Michelini (2010), Surface wave dispersion measurements from ambient seismic noise analysis in Italy, *Geophys. J. Int.*, *180*(3), 1242–1252.
- Nicolson, A., A. Curtis, B. Baptie, and E. Galetti (2012), Seismic interferometry and ambient noise tomography in the British Isles, *Proc. Geol. Assoc.*, *123*(1), 74–86, doi:10.1016/j.pgeola.2011.04.002.
- Paul, A., M. Campillo, L. Margerin, E. Larose, and A. Derode (2005), Empirical synthesis of time-asymmetrical Green functions from the correlation of coda waves, *J. Geophys. Res.*, *110*, B08302, doi:10.1029/2004JB003521.
- Piccozzi, M., S. Parolai, D. Bindi, and A. Strollo (2009), Characterization of shallow geology by high-frequency seismic noise tomography, *Geophys. J. Int.*, *176*, 164–174.
- Pilz, M., S. Parolai, and D. Bindi (2013), Three-dimensional passive imaging of complex seismic fault systems: Evidence of surface traces of the Issyk-Ata fault (Kyrgyzstan), *Geophys. J. Int.*, *194*, 1955–1965.
- Poli, P., H. A. Pedersen, M. Campillo, and the POLENET/LAPNET Working Group (2012), Emergence of body waves from cross-correlation of short period seismic noise, *Geophys. J. Int.*, *188*, 549–558.
- Rawlinson, N., and M. Sambridge (2003), Seismic traveltimes tomography of the crust and lithosphere, *Adv. Geophys.*, *46*, 81–198.
- Rawlinson, N., and M. Sambridge (2004), Wave front evolution in strongly heterogeneous layered media using the fast marching method, *Geophys. J. Int.*, *156*, 631–647.
- Roux, P. (2009), Passive seismic imaging with directive ambient noise: Application to surface waves and the San Andreas Fault in Parkfield, CA, *Geophys. J. Int.*, *367*–373.
- Roux, P., K. G. Sabra, P. Gerstoft, and W. Kuperman (2005), P-waves from cross-correlation of seismic ambient noise, *Geophys. Res. Lett.*, *32*, L19303, doi:10.1029/2005GL023803.
- Rubin, A. M., and J. P. Ampuero (2007), Aftershock asymmetry on a bimaterial interface, *J. Geophys. Res.*, *112*, B05307, doi:10.1029/2006JB004337.
- Sabra, K. G., P. Gerstoft, P. Roux, W. A. Kuperman, and M. C. Fehler (2005), Extracting time-domain Green's function estimates from ambient seismic noise, *Geophys. Res. Lett.*, *32*, L03310, doi:10.1029/2004GL021862.
- Sánchez-Sesma, F. J., and M. Campillo (2006), Retrieval of the Green's function from cross correlation: The canonical elastic problem, *Bull. Seismol. Soc. Am.*, *96*(3), 1182–1191.
- Saygin, E., and B. L. N. Kennett (2010), Ambient seismic noise tomography of Australian continent, *Tectonophysics*, *481*(1), 116–125, doi:10.1016/j.tecto.2008.11.013.
- Schorlemmer, D., F. Mele, and W. Marzocchi (2010), A completeness analysis of the National Seismic Network of Italy, *J. Geophys. Res.*, *115*, B04308, doi:10.1029/2008JB006097.
- Selvaggi, G., and C. Chiarabba (1995), Seismicity and P-wave velocity image of the southern Tyrrhenian subduction zone, *Geophys. J. Int.*, *121*, 818–826, doi:10.1111/j.1365-246X.1995.tb06441.x.
- Shapiro, N. M., and M. Campillo (2004), Emergence of broadband Rayleigh waves from correlations of the ambient seismic noise, *Geophys. Res. Lett.*, *31*, L07614, doi:10.1029/2004GL019491.
- Shapiro, N. M., M. Campillo, L. Stehly, and M. H. Ritzwoller (2005), High-resolution surface-wave tomography from ambient seismic noise, *Science*, *307*, 1615–1618.
- Shapiro, N. M., M. H. Ritzwoller, and G. D. Bensen (2006), Source location of the 26 sec microseism from cross-correlations of ambient seismic noise, *Geophys. Res. Lett.*, *33*, L18310, doi:10.1029/2006GL027010.
- Sneider, R. (2004), Extracting the Green's function from the correlation of coda waves: A derivation based on stationary phase, *Phys. Rev. E*, *69*(4), 046610.
- Speranza, F., and M. Chiappini (2002), Thick-skinned tectonics in the external Apennines, Italy: New evidence from magnetic anomaly analysis, *J. Geophys. Res.*, *107*(B11), 2290, doi:10.1029/2000JB000027.
- Stabile, T. A., C. Satriano, A. Orefice, G. Festa, and A. Zollo (2012), Anatomy of a microearthquake sequence on an active normal fault, *Sci. Rep.*, *2*(410), 1–7, doi:10.1038/srep00410.
- Tiberti, M. M., L. Orlando, D. Di Bucci, M. Bernabini, and M. Parotto (2005), Regional gravity anomaly map and crustal model of the central-southern Apennines (Italy), *J. Geodyn.*, *40*(1), 73–91, doi:10.1016/j.jog.2005.07.014.
- Vassallo, M., G. Festa, and A. Bobbio (2012), Seismic ambient noise analysis in Southern Italy, *Bull. Seismol. Soc. Am.*, *102*(2), 574–586, doi:10.1785/0120110018.
- Vuan, A., M. Sagan, and M. P. Plasenci Linares (2014), A reappraisal of surface wave group velocity tomography in the subantarctic Scotia Sea and surrounding ridges, *Global Planet. Change*, *123*, 223–238, doi:10.1016/j.gloplacha.2014.07.020.
- Wathelet, M., D. Jongmans, and M. Ohrnberger (2004), Surface wave inversion using a direct search algorithm and its application to ambient vibration measurements, *Near Surf. Geophys.*, *2*, 211–221.
- Westaway, R. (1987), The Campania, Southern Italy, earthquake of 1962 August 21, *Geophys. J. R. Astron. Soc.*, *88*, 1–24.
- Westaway, R., and J. Jackson (1987), The earthquake of 1980 November 23 in Campania-Basilicata (Southern Italy), *Geophys. J. Int.*, *90*(2), 375–443.
- Yang, Y., M. H. Ritzwoller, A. L. Levshin, and N. M. Shapiro (2007), Ambient noise Rayleigh wave tomography across Europe, *Geophys. J. Int.*, *168*, 259–274.
- Zaccarelli, L., N. M. Shapiro, L. Faenza, G. Soldati, and A. Michelini (2011), Variations of crustal elastic properties during the 2009 L'Aquila earthquake inferred from cross-correlations of ambient seismic noise, *Geophys. Res. Lett.*, *38*, L24304, doi:10.1029/2011GL049750.
- Zollo, A., S. Marucci, G. Milana, and P. Capuano (1999), The 1997 Umbria-Marche (central Italy) earthquake sequence: Insights on the mainshock ruptures from near source strong motion records, *Geophys. Res. Lett.*, *26*(20), 3165–3168, doi:10.1029/1998GL005285.
- Zollo, A., A. Orefice, and V. Convertito (2014), Source parameter scaling and radiation efficiency of microearthquakes along the Irpinia fault zone in southern Apennines, Italy, *J. Geophys. Res. Solid Earth*, *119*, 3256–3275, doi:10.1002/2013JB010116.

6 Conclusion

In this thesis, we focused on the analysis of the seismic waves propagating at different scales, analyzing data from experimental applications involving different places and contexts. The largest scale analysis was the determination of the S-wave model for the Irpinia fault system (≈ 100 km), then we analyzed the mechanical properties from data acquired at Solfatara (≈ 100 m), and finally at the smallest scale, we discussed how the damage affects the wave propagation in a bridge (≈ 10 m).

In the work, a first part was devoted to the development of the theoretical tools and concepts used during the remaining part of the thesis. We treated briefly the theory of the linear elasticity, within body and surface waves. We characterized such kind of waves through the definition of the phase and the group velocities and their dispersion curves. We finally addressed the problem of the attenuation of the seismic waves owing to scattering or inelastic phenomena.

A first part of the thesis was focused on the RICEN experiment. After the determination of the Green's function, we recovered the S-wave model of the investigated area from surface wave dispersion curves. We decomposed the domain in smaller subgrids, where the 1D approximation holds, and we locally measured the phase and the group velocities in different frequency bands in order to compute the dispersion curves. From the joint inversion of the dispersion curves, we obtained 96 one-dimensional S-wave velocity models, and from interpolation, we recovered a three-dimensional model for the area. We found that very low velocity values due to the poor mechanical properties of the rocks beneath the Solfatara, and the decrease of the S-wave velocity toward the *Fangaia*. We justified such a decreasing with the hypothesis of water saturated rocks. Such model is also corroborated by geoelectric measurements, simultaneously performed during RICEN, which show a decreasing of the resistivity near the *Fangaia*.

We also gave a statistical depiction of the scatterers embedded in the medium. We measured the MFP by means of the ratio between the coherent and

incoherent intensities, and the TMFP through the coda decay. We repeated the measurements in different frequency bands, recovering the typical trend observed in volcanic areas. Finally, we inverted the MFP curve as a function of the frequency to infer some properties of the scatterers. We found scatterers with size smaller than 5 m. Moreover, the density and the velocity close to the ones of the medium suggest that such scatterers are related to sacks having higher or lower presence of gas and water. In the fourth chapter, we applied the coda wave interferometry (CWI) to quantify the relative velocity variation in a progressively damaged bridge. The estimate is performed from the time delay measure in the seismic coda. Since the coda is composed by phases which travelled for longer time in the medium, they are more sensitive to the medium variations. We investigated three set of data, acquired when the bridge was intact, moderately damaged and severely damaged. We were able to detect the increasing damage, with about 5% and 8% of relative velocity variation. Therefore, we proved that such method can be used as a diagnostic tool for the monitoring of the health state of buildings.

Finally, we analyzed the Green's functions computed from the cross-correlation of the ambient noise acquired at the stations of the ISNet network. We measured the dispersion curves for the group velocity and from them we recovered a three-dimensional model in term of S-waves of the area crossed by the paths connecting the couple of stations. We found that the volume bounded by the faults of the 1980 earthquake has low S-wave velocity values. Superimposing such results with other images from previous works, it is possible to correlate this velocity anomaly with a fractured volume rich in fluids, which would have favored the earthquake generation in the past.

7 References

Acocella V. Activating and reactivating pairs of nested collapses during caldera-forming eruptions: Campi Flegrei (Italy). *Geophysical Research Letters*. AGU Journal, September 6, 2008. - Vol. 35, 17. Doi: 10.1029/2008GL035078

Adewuyi A., P. and Wu Z., S. Modal macro-strain flexibility methods for damage localization in flexural structures using long-gage FBG sensors. *Structural Control and Health Monitoring*. 2011. 3. Vol. 18. - pp. 341-360.

Aki K., and Chouet, B. Origin of coda waves: Source, attenuation, and scattering effects. *Journal of Geophysical Research*. August 10, 1975. Vol. 80. – pp. – 3322-3342. Doi: 10.1029/JB080i023p03322

Aki K. Space and time spectra of stationary stochastic waves, with special reference to microtremors. *Bull. Earthq. Res. Inst.* June 30, 1957. - 35. - pp. 415-457.

Aki Keiiti and Richards Paul, G. *Quantitative Seismology*. Sausalito: University Science Books, 2002. - second edition.

Aki Keiiti. Practical Approaches to Earthquake Prediction and Warning. Springer, 1985. - Vol. Theory of Earthquake Prediction with Special Reference to Monitoring of the Quality Factor of Lithosphere by the Coda Method : pp. 219-230. Doi: 10.1007/978-94-017-2738-9_2

Amato A. and Mele F. Performance of the INGV National Seismic Network from 1997 to 2007. *Annals of Geophysics*. 2008. Vol. 51. - 2/3 - pp. 417-431. Doi: 10.4401/ag-4454

Amoroso O., Ascione A., Mazzoli S., Virieux J., Zollo A. Seismic imaging of a fluid storage in the actively extending Apennine mountain belt, Southern Italy. *Geophysical Research Letters*. 2014 - Vol. 41. - pp. 3802–3809. Doi: 10.1002/2014GL060070

Andrews D., J. and Ben-Zion Y. Wrinkle-like slip pulse on a fault between different materials. *Journal of Geophysical Research: Solid Earth*. AGU Journal, January 10, 1997. - B1 - Vol. 102. - pp. 553-571. Doi: 10.1029/96JB02856

Assefa S., McCann C. and Sothcott J. Velocities of compressional and shear waves in limestones. *Geophysical Prospecting*. January 2003. - 1 - Vol. 51. - pp. 1-13. Doi: 10.1046/j.1365-2478.2003.00349.x

Bartoli, G., L. Facchini, M. Pieraccini, M. Fratini, and C. Atzeni. Experimental utilization of interferometric radar techniques for structural monitoring. *Structural Control and Health Monitoring*. March 28, 2008. Vol. 15. – 3 -pp. 283-298. Doi: 10.1002/stc.252

Basili, R., Valensise, G., Vannoli, P., Burrato, P., Fracassi, U., Mariano, S., Tiberti, M., M., Boschi, E. The database of Individual Seismogenic Sources (DISS), version 3: Summarizing 20 years of research on Italy's earthquake geology. *Tectonophysics* (Elsevier) 453, no. 1-4 (June 2008): 20-43. Doi: 10.1016/j.tecto.2007.04.014

Bensen, G., D., Ritzwoller, M., H., Barmin, M., P., Levshin, A., L., Lin, F., Moschetti, M., P., Shapiro, N., M., Yang, Y. Processing seismic ambient noise data to obtain reliable broad-band surface wave dispersion measurements. *Geophysical Journal International* 169, no. 3 (June 2007): 1239-1260. Doi: 10.1111/j.1365-246X.2007.03374.x

Bernard, P., and A. Zollo. The Irpinia (Italy) 1980 earthquake: Detailed analysis of a complex normal fault. *Journal of Geophysical Research: Solid Earth*. February 10, 1989. Vol. 94. - B2 - pp. 1631-1648. Doi: 10.1029/JB094iB02p01631

Bianco, F., E. Del Pezzo, G. Saccorotti, and G. Ventura. The role of hydrothermal fluids in triggering the July-August 2000 seismic swarm at Campi Flegrei, Italy: evidence from seismological and mesostructural data. *Journal of Volcanology and Geothermal Research*. May 2004. - Vol. 133. - pp. 229-246. Doi: 10.1016/S0377-0273(03)00400-1

Bien, J., and T. Kaminski. Proceedings of 5th International Conference on Arch Bridges. ARCH'07 - Madeira, 2009. - Vol. 341.

Binda, L., A., A. Saisi, and C. Tiraboschi. Investigation procedures for the diagnosis of historic masonries. *Construction and Building Materials*. June 2000. - 199 : Vol. 14. Doi: 10.1016/S0950-0618(00)00018-0

Bobbio, A., M. Vassallo, and G. Festa. A local magnitude scale for Southern Italy. *Bulletin of the Seismological Society of America.* August 2009. Vol. 99. - 4 - pp. 2461-2470. Doi: 10.1785/0120080364

Bonessio, N., G. Lomiento, and Benzoni G. Damage Identification Procedure for Seismically Isolated Bridges. *Structural Control and Health Monitoring.*2012. Vol. 19. --5 - pp. 565-578. Doi: 10.1002/stc.448

Boué, P., P. Poli, M. Campillo, H. Pedersen, X. Briand, and P. Roux. Teleseismic correlations of ambient seismic noise for deep global imaging of the Earth. *Geophysical Journal International.* May 15, 2013. Vol. 194. - 2 - pp. 844-848. Doi: 10.1093/gji/ggt160

Brencich, A., and L. Gambarotta. Guide to the high level assessment of masonry bridges. UIC Workshop on Masonry, Arch Bridges. - Paris, France 2007.

Brenguier F., Shapiro, N., M., Campillo, M., Ferrazzini, V., Duputel, Z., Coutant, O., Nercessian, A. Towards forecasting volcanic eruptions using seismic noise. *Nature geosciences.* January 20, 2008. - Vol. 1. - pp. 126-130. Doi: 10.1038/ngeo104

Brenguier, F., Campillo, M., Hadziioannou, C., Shapiro, N., M., Nadeau, R., M., Larose, E. Postseismic Relaxation Along the San Andreas Fault at Parkfield from Continuous Seismological Observations. *Science.* September 12, 2008. - Vol. 321. - pp. 1478-1481. Doi: 10.1126/science.1160943

Brenguier, F., D. Clarke, Y. Aoki, and V. Ferrazzini. Monitoring volcanoes using seismic noise correlations. *Comptes Rendus Geosciences.* September 2011. Vol. 343. - 8-9 - pp. 633-638. Doi: 10.1016/j.crte.2010.12.010

Brittle, K.F., L.R. Lines, and A.K. Dey. Vibroseis deconvolution: a comparison of cross-correlation and frequency-domain sweep deconvolution. *Geophysical Prospecting.* July 2001. - Vol. 49. - pp. 675-686.

Brownjohn, J., M., W. Structural health monitoring of civil infrastructure. *Philosophical Transactions of the Royal Society A.* The Royal Society, February 15, 2007. - 589-622 : Vol. 365. Doi: 10.1098/rsta.2006.1925

Bruno, Pier Paolo, G., Giovanni, P. Ricciardi, Zaccaria Petrillo, Vincenzo Di Fiore, Antonio Troiano, and Giovanni Chiodini. Geophysical and hydrogeological

experiments from a shallow hydrothermal system at Solfatara Volcano, Campi Flegrei, Italy: Response to caldera unrest. *JOURNAL OF GEOPHYSICAL RESEARCH*. June 05, 2007. - B06201 : Vol. 112. Doi: 10.1029/2006JB004383

Brzak, K., Y., J., Gu, A. Okeler, M. Steckler, and A. Lerner-Lam. Migration imaging and forward modeling of microseismic noise sources near Southern Italy. *Geochemistry Geophysics Geosystems*. 2009 - Q01012: Vol. 10. Doi: 10.1029/2008GC002234

Byrdina, S., Vandemeulebrouck, J., Cardellini, C., Legaz, A., Camerlynck, C., Chiodini, G., Lebourg, T., Gresse, M., Bascou, P., Motos, G., Carrier, A., Caliro, S. Relations between electrical resistivity, carbon dioxide flux, and self-potential in the shallow hydrothermal system of Solfatara (Phlegrean Fields, Italy). *Journal of Volcanology and Geothermal Research*. Elsevier, August 15, 2014. - Vol. 283. - pp. 172-182. Doi: 10.1016/j.jvolgeores.2014.07.010

Campillo, M., and L. Margerin. Mesoscopic seismic waves. Ed. Weaver Richard and Wright Matthew. 2010. - Vol. 11.

Campillo, M., and A. Paul. Long-range correlations in the diffuse seismic coda. *Science*. January 24, 2003. - 5606 : Vol. 299 - pp. 547-549. Doi: 10.1126/science.1078551

Capuano, Paolo, Guido Russo, Lucia Civetta, and Roberta Moretti. The active portion of the Campi Flegrei caldera structure imaged by 3-D inversion of gravity data: The Campi Flegrei Caldera Structure. *Geochemistry Geophysics Geosystems*. AGU Journal, October 24, 2013. Vol. 14. - 10 - pp. 4681-4697. Doi: 10.1002/ggge.20276

Caputo, R., L. Salviulo, S. Piscitelli, and A. Loperte. Late Quaternary activity along the Scorciabuoi Fault (Southern Italy) as inferred from electrical resistivity tomographies. *Annals of Geophysics*. 2007. Vol. 50 – 2. Doi: 10.4401/ag-3078

Casciello, E., M. Cesarano, and G. Pappone. Extensional detachment faulting on the Tyrrhenian margin of the southern Apennines contractional belt (Italy). *Journal of the Geological Society*. July 2005. - Vol. 163 - pp. 617-629. Doi: 10.1144/0016-764905-054

Ceravolo, R., N. Tondini, G. Abbiati, and A. Kumar. Dynamic characterization of complex bridge structures with passive control systems. *Structural Control and Health Monitoring*. March 23, 2011. Vol. 19. - 4 - pp. 511-534. Doi: 10.1002/stc.450

Chaput, J., Zandomeneghi, D., Aster, R., C., Knox, H., Kyle, P., R. Imaging of Erebus volcano using body wave seismic interferometry of Strombolian eruption coda. *Geophysical Research Letters*. April 14, 2012. Vol. 39 - 7 - Doi: 10.1029/2012GL050956

Chaput, J., Campillo, M., R., C. Aster, Roux, P., Kyle, P., R., Knox, H., Czoski, P. Multiple scattering from icequakes at Erebus volcano, Antarctica: Implications for imaging at glaciated volcanoes. *Journal of Geophysical Research*. February 24, 2015. Vol. 120 - 2 - pp. 1129-1141. Doi: 10.1002/2014JB011278

Chiodini, G., R. Avino, S. Caliro, and S. Minopoli. Temperature and pressure gas geoindicators at the Solfatara fumaroles (Campi Flegrei). *Annals of Geophysics*. - 2011. Vol. 54. - 2 - pp. 151-160.

Chiodini, G., G. Vilardo, V. Augusti, D. Granieri, S. Caliro, and C. Minopoli. Temperature and pressure gas geoindicators at the Solfatara fumaroles (Campi Flegrei). *Annals of Geophysics*. - 2011. Vol. 54. - 2 - pp. 151-160. Thermal monitoring of hydrothermal activity by permanent infrared automatic stations: Results obtained at Solfatara di Pozzuoli, Campi Flegrei (Italy). *JOURNAL OF GEOPHYSICAL RESEARCH*. December 28, 2007. - B12206 : Vol. 112. Doi: 10.1029/2007JB005140

Chiodini, G., Frondini, F., Cardellini, C., Granieri, D., Marini, L., Ventura, G. CO₂ degassing and energy release at Solfatara volcano, Campi Flegrei, Italy. *Journal of Geophysical Research*. *AGU Journal*, August 10, 2001. Vol. 106. - B8 - pp. 16213-16221. Doi: 10.1029/2001JB000246

Chiodini, G., Paonita, A., Aiuppa, A., Costa, A., Caliro, S., De Martino, P., Acocella, V., Vandemeulebrouck, J. Magmas near the critical degassing pressure drive volcanic unrest towards a critical state. *Nature communications*. *Nature*, December 20, 2016. Doi: 10.1038/ncomms13712

Chouet, B. Temporal variation in the attenuation of earthquake coda near Stone Canyon, California. *Geophysical Research Letters*. AGU Journal, March 1979. Vol. 6. - 3 - pp. 143-146. Doi: 10.1029/ GL006i003p00143

Cirella, A., A. Piatanesi, Cocco, M., E. Tinti, L. Scognamiglio, A. Michelini, A. Lomax, and E. Boschi. Rupture history of the 2009 L'Aquila (Italy) earthquake from non-linear joint inversion of strong motion and GPS data. *Geophysical Research Letters*. October 06, 2009. Vol. 36. L19304 . Doi: 10.1029/2009GL039795

Costa, A., A. Folco, G. Macedonio, B. Giaccio, R. Isaia, and V., C. Smith. Quantifying volcanic ash dispersal and impact of the Campanian Ignimbrite super-eruption. *Geophysical research Letters*. AGU Journal, May 28, 2012. Vol. 39. 10. Doi: 10.1029/2012GL051605

Dainty, Anton, M., and M.Nafi Toksoz. Seismic codas on the Earth and the Moon: a comparison. *Physics of the Earth and Planetary Interiors*. Elsevier, September 1981. Vol. 26. - 4 - pp. 250-260. Doi: 10.1016/0031-9201(81)90029-7

D'Auria, L., Pepe, S., Castaldo, R., Giudicepietro, F., Macedonio, G., Ricciolino, P., Tizzani, P., Casu, F., Lanari, R., Manzo, M., Martini, M., Sansosti, E., Zinno, I. Magma injection beneath the urban area of Naples: a new mechanism for the 2012–2013 volcanic unrest at Campi Flegrei caldera. *Scientific Reports*. Nature, August 17, 2015. - 13100 : Vol. 5. Doi: 10.1038/srep13100

De Landro, G., Serlenga, V., Russo, G., Amoroso, O., Festa, G., Bruno, P., P., Gresse, M., Vandemeulebrouck, J., Zollo, A. 3D ultra-high resolution seismic imaging of shallow Solfatara crater in Campi Flegrei (Italy): new insights on deep hydrothermal fluid circulation processes (under review).

de Lorenzo, Salvatore, Aldo Zollo, and Francesco Mongelli. Source parameters and three-dimensional attenuation structure from the inversion of microearthquake pulse width data: Qp imaging and inferences on the thermal state of the Campi Flegrei caldera (southern Italy). *Journal of Geophysical Research: Solid Earth*. AGU Journal, August 10, 2001. Vol. 106. - B8 - pp. 16265–16286. Doi: 10.1029/2000JB900462

de Lorenzo, Salvatore, V. Di Rienzo, Lucia Civetta, M. D'Antonio, and Paolo Gasparini. Thermal model of the Vesuvius magma chamber. *GEOPHYSICAL*

RESEARCH LETTERS. September 02, 2006. Vol. 33. L17302. Doi: 10.1029/2006GL026587

De Matteis, R., E. Matrullo, L. Rivera, T., A. Stabile, G. Pasquale, and A. Zollo. Fault delineation and regional stress direction from the analysis of background microseismicity in the southern Apennines, Italy. *Bulletin of the Seismological Society of America.* August 2012. Vol. 102. - 4 - pp. 899-1907. Doi: 10.1785/0120110225

De Stefano, A., and R. Ceravolo. Assessing the health state of ancient structures: the role of vibrational tests. *Journal of Intelligent Material Systems and Structures.* August 01, 2007. Vol. 18. - 8 - pp. 793-807. Doi: 10.1177/1045389X06074610

Del Gaudio, Carlo, Ida Aquino, G. P. Ricciardi, and Roberto Scandone. Unrest episodes at Campi Flegrei: A reconstruction of vertical ground movements during 1905–2009. *Journal of Volcanology and Geothermal Research.* Elsevier, August 2010. - 195. - pp. 48-56. Doi: 10.1016/j.jvolgeores.2010.05.014

Di Renzo, V., Civetta L., D'Antonio M., S. Tonarini, M. A. Di Vito, and G. Orsi. The magmatic feeding system of the Campi Flegrei caldera: Architecture and temporal evolution. *Chemical Geology.* Elsevier, 2011. - 281. - pp. 227-241. Doi: 10.1016/j.chemgeo.2010.12.010

Di Stefano, R., E. Kissling, C. Chiarabba, A. Amato, and D. Giardini. Shallow subduction beneath Italy: Three-dimensional images of the Adriatic-European-Tyrrhenian lithosphere system based on high-quality P wave arrival times. *Journal of Geophysical Research.* AGU Journal, May 2009. - B5 : Vol. 114. Doi: 10.1029/2008JB005641

Di Vito, M., Isaia, R., Orsi, G., Southon, J., de Vita, S., D'Antonio, M., Pappalardo, M., Piochi, M. Volcanic and deformational history of the Campi Flegrei caldera in the past 12 ka at the Campi Flegrei Caldera (Italy). *Journal of Volcanology and Geothermal Research.* - 1999. - 91. - pp. 221-246.

Doherty, J., Draganov, D., X. Campman, J. Thorbecke, A. Verdel, and K. Wapenaar. *Handbook on Experimental Mechanics.* Englewood Cliffs : Kobayashi, A., S. , 1987.

Duputel, Z., V. Ferrazzini, F. Brenguier, N., M. Shapiro, M. Campillo, and A. Nercessian. Real time monitoring of relative velocity changes using ambient seismic noise at the Piton de la Fournaise Volcano (La Réunion) from January 2006 to June 2007. *Journal of Volcanology and Geothermal Research*. July 01, 2009. - 1-2 : Vol. 184. - pp. 164-173. Doi: 10.1016/j.jvolgeores.2008.11.024

Duvall, T., L., Kosovichev, A., G., Scherrer, P., H., Bogart, R., S., Bush, R., I., De Forest, C., Hoeksema, J., T., Schou, J., Saba, J., L., R., Tarbell, T., D., Title, A., M., Wolfson C., J., Milford, P., N. TIME-DISTANCE HELIOSEISMOLOGY WITH THE MDI INSTRUMENT: INITIAL RESULTS. *Solar Physics*. January 1997. - 1 : Vol. 170. - pp. 63-73. Doi: 10.1023/A:1004907220393

Emolo, A., G. Iannaccone, A. Zollo, and A. Gorini. Inferences on the source mechanisms of the 1930 Irpinia (Southern Italy) earthquake from simulations of the kinematic rupture process. *Annals of Geophysics*. - 2004. - 6 : Vol. 47. - pp. 1743-1754.

Farrar, C., T. Darling, A. Migliori, and W., E. Baker. Microwave interferometer for non-contact vibration measurements on large structures. *Mechanical Systems and Signal Processing*. March 1999. - 2 : Vol. 13. - pp. 241-253. Doi: 10.1006/mssp.1998.1216

Fedele, F., G., Biagio Giaccio, and Hajdas Irka. Timescales and cultural process at 40,000 BP in the light of the Campanian Ignimbrite eruption, Western Eurasia. *Journal of Human Evolution*. 2008. - 5 : Vol. 55. - pp. 834-857. Doi: 10.1016/j.jhevol.2008.08.012

Fedi, M., C. Nunziata, and A. Rapolla. The Campania-Campi Flegrei area: a contribution to discern the best structural model from gravity interpretation. *Journal of Volcanology and Geothermal Research*. Elsevier Science Publishers B.V., February 09, 1991. - Vol. 48. - pp. 51-59.

Festa, G. Repeated Induced Earthquakes and Noise @Solfatara, Campi Flegrei. AGU Fall Meeting. - San Francisco, 2015. - pp. 14-18.

Gentile, C. Deflection measurement on vibrating stay cables by non-contact microwave interferometer. *NDT & International*. Elsevier, April 2010. - 3 : Vol. 43. - pp. 231-240. Doi: 10.1016/j.ndteint.2009.11.007

Gibson, B., and K. Larner. Predictive deconvolution and the zero-phase source. *Geophysics*. April 1984. - 49. - pp. 379-397. Doi: 10.1190/1.1441832

Gouédard, P., P. Roux, M. Campillo, and A. Verdel. Convergence of the two-point correlation function toward the Green's function in the context of a seismic-prospecting data set. *GEOPHYSICS*. November-December 2008. - 6 : Vol. 73. - pp. 47-53. Doi: 10.1190/1.2985822

Gouédard, P., P. Roux, M. Campillo, A. Verdel, H. Yao, and R. D. van der Hilst. Source depopulation potential and surface-wave tomography using a crosscorrelation method in a scattering medium. *Geophysics*. Society of Exploration Geophysicists, 2011. - 2 : Vol. 76. Doi: 10.1190/1.3535443

Grêt, A., R. Snieder, and J. Scales. Time-lapse monitoring of rock properties with coda wave interferometry. *Journal of Geophysical Research*. AGU Journal, March 09, 2006. - B3 : Vol. 111. Doi: 10.1029/2004JB003354

Grêt, A., Snieder, R., R., C. Aster, and P., R. Kyle. Monitoring rapid temporal change in a volcano with coda wave interferometry. *Geophysical Research Letters*. AGU Journal, March 18, 2005. - 6 : Vol. 32. Doi: 10.1029/2004GL021143

Guidoboni, E., and C. Ciuccarelli. The Campi Flegreicaldera: Historical revision and new data on seismic crises, bradyseisms, the Monte Nuovo eruption and ensuing earthquakes (twelfth century 1582 AD). *Bulletin of Volcanology*. - [s.l.] : Springer, 2011. - 73 : Vol. 6. - pp. 655-677.

Hemmer, P., Chr. *Physica* (Amsterdam). 27, 79, 1961.

Hennino, R., N., M. Trégourés, L. Margerin, M. Campillo, B., A. van Tiggelen, and R., L. Weaver. Observation of Equipartition of Seismic Waves. *PHYSICAL REVIEW LETTERS*. 2001. - 15 : Vol. 86. - pp. 3447-3450. Doi: 10.1103/PhysRevLett.86.3447

Iannaccone, G., Zollo, A., Elia, L., Convertito, V., Satriano, C., Martino, C., Festa, G., Lancieri, M., Bobbio, A., Stabile, T., A., Vassallo, M., Emolo, A. A prototype system for earthquake early-warning and alert management Southern Italy. *Bulletin of Earthquake Engineering*. Springer, October 2010. - 5 : Vol. 8. - pp. 1105-1129. Doi: 10.1007/s10518-009-9131-8

Johnson, C., E., A. Bittenbinder, B. Bogaert, L. Dietz, and W. Kohler. Earthworm: A flexible approach to seismic network processing. IRIS Newsletter. - 1995. - 2 : Vol. 14. - pp. 1-4.

Judenherc, S., and Aldo Zollo. The Bay of Naples (southern Italy): Constraints on the volcanic structures inferred from a dense seismic survey. JOURNAL OF GEOPHYSICAL RESEARCH. October 26, 2004. - B10312 : Vol. 109. Doi: 10.1029/2003JB002876

Kohler, M., D., T., H. Heaton, and S., C. Bradford. Propagating Waves in the Steel, Moment-Frame Factor Building Recorded during Earthquakes. Bulletin of the Seismological Society of America. August 2007. - 4 : Vol. 97. - pp. 1334-1345. Doi: 10.1785/0120060148

Larose, E., A. Derode, M. Campillo, and M. Fink. Imaging from one-bit correlations of wide-band diffuse wavefields. Journal of Applied Geophysics. June 2004. - 12 : Vol. 95. - pp. 8393–8399. Doi: 10.1063/1.1739529

Larose, E., L. Margerin, B., A. van Tiggelen, and M. Campillo. Weak Localization of Seismic Waves. Physical Review Letters. July 23, 2004. - 4 : Vol. 93. Doi: 10.1103/PhysRevLett.93.048501

Lay, Thorne, and Terry, C. Wallace. Modern Global Geismology. Ed. Elsevier An Imprint of. - San Diego : Academic Press, 1995. - Vol. 58.

Letort, J., Roux, P., Vandemeulebrouck, J., Coutant, O., Cros, E., Whathelet, M., Cardellini, C., Avino, R. High-resolution shallow seismic tomography of a hydrothermal area: application to the Solfatara, Pozzuoli. Geophysical Journal International. June 01, 2012. - 3 : Vol. 189. - pp. 1725-1733. Doi: 10.1111/j.1365-246X.2012.05451.x

Li, H., F. Bernardi, and A. Micheleni. Surface wave dispersion measurements from ambient seismic noise analysis in Italy. Geophysical Journal International. March 2010. - 3 : Vol. 180. - pp. 1242-1252. Doi: 10.1111/j.1365-246X.2009.04476.x

Lobkis, O., and R., L. Weaver. On the emergence of the Green's function in the correlations of a diffuse field. The Journal of the Acoustical Society of America. December 2001. - Vol. 110. - pp. 3011-3017. Doi: 10.1121/1.1417528

Loke, M., H., and R., D. Barker. Rapid least-squares inversion of apparent resistivity pseudosections by a quasi-Newton method. *Geophysical Prospecting*. January 1996. - 1 : Vol. 44. - pp. 131-152. Doi: 10.1111/j.1365-2478.1996.tb00142.x

Loke, M., H., and T. Dahlin. A comparison of the Gauss–Newton and quasi-Newton methods in resistivity imaging inversion. *Journal of Applied Geophysics*. Elsevier, 2002. - 49. - pp. 149-162. Doi: 10.1016/S0926-9851(01)00106-9

Longuet-Higgins, M., S. A Theory of the Origin of Microseisms. *Philosophical Transactions of the Royal Society of London. Series A, Mathematical and Physical Sciences*. The Royal Society, September 27, 1950. - 857 : Vol. 243. - pp. 1-35. Doi: 10.1098/rsta.1950.0012

Mangiacapra, A., R. Moretti, M. Rutherford, L. Civetta, G. Orsi, and P. Papale. The deep magmatic system of the Campi Flegrei caldera (Italy). *GEOPHYSICAL RESEARCH LETTERS*. November 06, 2008. - L21304 : Vol. 35. Doi: 10.1029/2008GL035550

Margerin, L., M. Campillo, B. van Tiggelen, and R. Hennino. Energy partition of seismic coda waves in layered media: theory and application to Pinyon Flats Observatory. *Geophysical Journal International*. March 12, 2009. - 2 : Vol. 177. - pp. 571-585. Doi: 10.1111/j.1365-246X.2008.04068.x

Margerin, L., M. Campillo, and B. Van Tiggelen. Monte Carlo simulation of multiple scattering of elastic waves. *JOURNAL OF GEOPHYSICAL RESEARCH*. - April 10, 2000. - B4 : Vol. 105. - pp. 7873-7892.

Matsumoto, S., K. Obara, K. Yoshimoto, T. Saito, A. Ito, and A. Hasegawa. Temporal change in P-wave scatterer distribution associated with the M6.1 earthquake near Iwate volcano, northeastern Japan. *Geophysical Journal International*. April 01, 2001. - 1 : Vol. 145. - pp. 48-58. Doi: 10.1111/j.1365-246X.2001.00339.x

Miyazawa, M., Venkataraman A., R. Snieder, and M. A. Payne. Analysis of micro-earthquake data at Cold Lake and its applications to reservoir monitoring. *Geophysics*. May-June 2008. - 3 : Vol. 73. - pp. 15-21. Doi: 10.1190/1.2901199

Morse, P., and K.U. Ingard. Theoretical acoustics. New York : McGraw-Hill, 1968. - Vol. 8.

Mucciarelli, M., Masi, A., Gallipoli, M., R., Harabaglia, P., Vona, M., Ponzo, F., Dolce, M. Analysis of RC Building Dynamic Response and Soil-Building Resonance Based on Data Recorded during a Damaging Earthquake (Molise, Italy, 2002). Bulletin of the Seismological Society of America. October 2004. - 5 : Vol. 94. - pp. 1943-1953. Doi: 10.1785/012003186

Nicolson, A., A. Curtis, B. Baptie, and Galetti E. Seismic interferometry and ambient noise tomography in the British Isles. Proceedings of the Geologists' Association. Elsevier, January 01, 2012. - 1 : Vol. 123. - pp. 74-86. Doi: 10.1016/j.pgeola.2011.04.002

Obermann, A., E. Larose, L. Margerin, and V. Ressetto. Measuring the scattering mean free path of Rayleigh waves on a volcano from spatial phase decoherence. Geophysical Journal International. January 22, 2014. - 1 : Vol. 197. - pp. 435-442. Doi: 10.1093/gji/ggt514

Orsi, Giovanni, mauro, Antonio Di Vito, and Roberto Isaia. Volcanic hazard assessment at the restless Campi Flegrei Caldera. Bulletin of Volcanology. Springer-verlag, April 2, 2004. - pp. 514-530. Doi: 10.1007/s00445-003-0336-4

Paasschens, J., C., J. Solution of the time-dependent Boltzmann equation. Physical Review E: Statistical, Nonlinear, Biological, and Soft Matter Physics. American Physical Society, July 1997. - 1 : Vol. 56. Doi: 10.1103/PhysRevE.56.1135

Pacheco, C. Time-lapse monitoring with multiply scattered waves [Book] / ed. Mines Colorado School of. Center for Wave Phenomena, 2004.

Pappalardo, Lucia, and Giuseppe Mastrolorenzo. Rapid differentiation in a sill-like magma reservoir: a case study from the campi flegrei caldera. Scientific Reports. Nature, October 5, 2012. - 712 : Vol. 2. Doi: 10.1038/srep00712

Paul, A., M. Campillo, L. Margerin, E. Larose, and A. Derode. Empirical synthesis of time-asymmetrical Green functions from the corcorrelation of coda waves.

Journal of Geophysical Research. AGU Journal, August 2005. - B08302 : Vol. 110.
Doi: 10.1029/2004JB003521

Petrosino, Simona, Norma Damiano, Paola Cusano, Antonio Di Vito, Sandro de Vita, and Edoardo Del Pezzo. Subsurface structure of the Solfatara volcano (Campi Flegrei caldera, Italy) as deduced from joint seismic-noise array, volcanological and morphostructural analysis. *Geochemistry Geophysics Geosystems*. AGU and Geochemical Society, July 13, 2012. - 7 : Vol. 13. - pp. 1525-2027. Doi: 10.1029/2011GC004030

Picozzi, M., S. Parolai, D. Bindi, and Strollo A. Characterization of shallow geology by high-frequency seismic noise tomography. *Geophysical Journal International*. January 2009. - 1 : Vol. 176. - pp. 164-174. Doi: 10.1111/j.1365-246X.2008.03966.x

Pilz, M., S. Parolai, and D. Bindi. Three-dimensional passive imaging of complex seismic fault systems: Evidence of surface traces of the Issyk-Ata fault (Kyrgyzstan). *Geophysical Journal International*. June 18, 2013. - 1955-1965 : Vol. 194. Doi: 10.1093/gji/ggt214

Pilz, M., Parolai, S., Woith, H., Gresse, Marceau, G., Vandemeulebrouck, J. 4-D imaging and monitoring of the Solfatara crater (Italy) by ambient noise tomography. *EGU General Assembly 2016*. Vol. 18, EGU2016-11719, 2016.

Poli, P., H. A. Pedersen, M. Campillo, and POLENET/LAPNET Working Group. Emergence of body waves from cross-correlation of short period seismic noise. *Geophysical Journal International*. February 2012. - 2 : Vol. 188. - pp. 549-558. Doi: 10.1111/j.1365-246X.2011.05271.x

Poli, P., M. Campillo, and H. Pedersen. Body-Wave Imaging of Earth's Mantle Discontinuities from Ambient Seismic Noise. *Science*. November 23, 2012. - Vol. 338. - pp. 1063-1065. Doi: 10.1126/science.1228194

Ponzo, F., C., R. Ditommaso, G. Auletta, and A. Mossucca. A fast method for structural health monitoring of Italian reinforced concrete strategic buildings. *Bulletin of Earthquake Engineering*. December 2010. - 6 : Vol. 8. - pp. 1421-1434. Doi: 10.1007/s10518-010-9194-6

Poupinet, G., and W., L., Frechet Ellsworth. Monitoring Velocity Variations in the Crust Using Earthquake Doublets: An Application to the Calaveras Fault, California. JOURNAL OF GEOPHYSICAL RESEARCH, . - July 10, 1984. - B7 : Vol. 89. - pp. 5719-5731.

Prieto, G., A., J., F. Lawrence, A., I. Chung, and M., D. Kohler. Impulse Response of Civil Structures from Ambient Noise Analysis. Bulletin of the Seismological Society of America. October 2010. - 5A : Vol. 100. - pp. 2322-2328. Doi: 10.1785/0120090285

Ratdomopurbo, A., and G. Poupinet. Monitoring a temporal change of seismic velocity in a volcano: Application to the 1992 eruption of Mt. Merapi (Indonesia). Geophysical Research Letters. April 1, 1995. - 7 : Vol. 22. - pp. 775-778. Doi: 10.1029/95GL00302

Rawlinson, N., and M. Sambridge. Seismic travelttime tomography of the crust and lithosphere. Advances in Geophysics. - 2003. - Vol. 46. - pp. 81-197.

Rawlinson, N., and M. Sambridge. Wave front evolution in strongly heterogeneous layered media using the fast marching method. Geophysical Journal International. March 01, 2004. - Vol. 156. - pp. 631-647. Doi: 10.1111/j.1365-246X.2004.02153.x

Robinson, E., A., and M. Saggaf. Klauder wavelet removal before vibroseis deconvolution. Geophysical Prospecting. May 2001. - 3 : Vol. 49. - pp. 335-340. Doi: 10.1046/j.1365-2478.2001.00260.x

Roux, P, K., G. Sabra, P. Gerstoft, and W. Kuperman. P-waves from cross-correlation of seismic ambient noise. Geophysical Research Letters. AGU Journal, October 2005. - L19303 : Vol. 32. Doi: 10.1029/2005GL023803

Roux, P. Passive seismic imaging with directive ambient noise: Application to surface waves and the San Andreas Fault in Parkfield, CA. Geophysical Journal International. October 2009. - 1 : Vol. 179. - pp. 367-373. Doi: 10.1111/j.1365-246X.2009.04282.x

Roux, P., and J. De Rosny. Multiple scattering in a reflecting cavity: Application to fish counting in a tank. Acoustical Society of America. June 06, 2001. - 6 : Vol. 109. - p. 2587. Doi: 10.1121/1.1369101

Rubin, A., M., and J., P. Ampuero. Aftershock asymmetry on a bimaterial interface. *Journal of Geophysical Research: Solid Earth.* AGU Journal, May 18, 2007. - B5 : Vol. 112. Doi: 10.1029/2006JB004337

Ruocci, G., A. Quattrone, and A. De Stefano. Multi-domain feature selection aimed at the damage detection of historical bridges. *Journal of Physics Conference Series.* July 2011. - Vol. 305. - pp. 1-10. Doi: 10.1088/1742-6596/305/1/012106

Ruocci, G., L. Quattrone, L. Zanotti Fragonara, R. Ceravolo, and A. De Stefano. *Industrial Safety and Life Cycle Engineering.* - Wien : H. Wenzel, 2013. - Vol. 107.

Sabra, K., G., P. Gerstoft, P. Roux, W., A. Kuperman, and M., C. Fehler. Extracting time-domain Green's function estimates from ambient seismic noise. *Geophysical Research Letters.* AGU Journal, February 15, 2005. - L03310 : Vol. 32. Doi: 10.1029/2004GL021862

Sambridge, Malcolm. Geophysical inversion with a neighbourhood algorithm—I. Searching a parameter space. *Geophysical Journal International.* August 1999. - 2 : Vol. 138. - pp. 479-494. Doi: 10.1046/j.1365-246X.1999.00876.x

Sambridge, Malcolm. Geophysical inversion with a neighbourhood algorithm—II. Appraising the ensemble. *Geophysical Journal International.* September 1999. - 3 : Vol. 138. - pp. 727-746. Doi: 10.1046/j.1365-246x.1999.00900.x

Sánchez-Sesma, F., J., and M. Campillo. Retrieval of the Green's function from cross correlation: The canonical elastic problem. *Bulletin of the Seismological Society of America.* June 2006. - 3 : Vol. 96. - pp. 1182–1191. Doi: 10.1785/0120050181

Sato, Haruto, Michaela, C. Fehler, and Takuto Maeda. *Seismic Wave Propagation and Scattering.* Springer, 2012. - Second Edition. Doi: 10.1007/978-3-642-23029-5

Saygin, E., and B., N., L. Kennett. Ambient seismic noise tomography of Australian continent. *Tectonophysics.* Elsevier, January 15, 2010. - 1-4 : Vol. 481. - pp. 116-125. Doi: 10.1016/j.tecto.2008.11.013

Schorlemmer, D., F. Mele, and W. Marzocchi. A completeness analysis of the National Seismic Network of Italy. *Journal of Geophysical Research. AGU Journal*, April 2010. - B4 : Vol. 115. Doi: 10.1029/2008JB006097

Schurr, D., P., J., Y. Kim, K., G. Sabra, and J., J. Laurence. Damage detection in concrete using coda wave interferometry. *NDT & E International. Elsevier*, August 02, 2011. - Vol. 44. - pp. 728-735. Doi: 10.1016/j.ndteint.2011.07.009

Selvaggi, G., and C. Chiarabba. Seismicity and P-wave velocity image of the southern Tyrrhenian subduction zone. *Geophysical Journal International*. June 1995. - 3 : Vol. 121. - pp. 818-826. Doi: 10.1111/j.1365-246X.1995.tb06441.x

Serlenga, Vincenzo, Salvatore de Lorenzo, Guido Russo, Ortensia Amoroso, Stephane, Virieux, Jean Garambois, and Aldo Zollo. A three-dimensional QP imaging of the shallowest subsurface of Campi Flegrei offshore caldera, southern Italy. *Geophysical Research Letters. AGU Journal*, November 12, 2016. - 21 : Vol. 43. - pp. 11,209–11,218. Doi: 10.1002/2016GL071140

Serra, Marcello, Gaetano Festa, Philippe Roux, Marceau Gresse, Jean Vandemeulebrouck, and Aldo Zollo. A strongly heterogeneous hydrothermal area imaged by surfacewaves: the case of Solfatara, Campi Flegrei, Italy. *Geophysical Journal International*. April 07, 2016. - 205. - pp. 1813-1822. Doi: 10.1093/gji/ggw119

Shapiro, N. M., Campillo, M., L. Stehly, and M., H. Ritzwoller. High-resolution surface-wave tomography from ambient seismic noise. *Science*. March 11, 2005. - 5715 : Vol. 307. Doi: 10.1126/science.1108339

Shapiro, N. M., Ritzwoller M. H., and G., D. Bensen. Source location of the 26 sec microseism from cross-correlations of ambient seismic noise. *Geophysical Research Letters*. September 26, 2006. - L18310 : Vol. 33. Doi: 10.1029/2006GL027010

Shapiro, N., M., and M. Campillo. Emergence of broadband Rayleigh waves from correlations of the ambient seismic noise. *GEOPHYSICAL RESEARCH LETTERS*. April 08, 2004. - L07614 : Vol. 31. Doi: 10.1029/2004GL019491

Sheriff, R. E. Encyclopedic Dictionary of Exploration Geophysics. Tulsa : Society of Exploration Geophysicists, 1990.

Shull, P., J. Nondestructive Evaluation Theory, Techniques, and Applications. New York : Marcel Dekker Inc., 2007.

Siniscalchi, A., M. Carlucci, L. D'Auria, Z. Petrillo, G. Romano, and S. Tripaldi. AMT investigation in the Solfatara-Pisciarelli-Agnano area: results and further outlook. Geophysical Research Abstracts. - 2015. - EGU2015-9540 : Vol. 17.

Snieder, R. Imaging and Averaging in Complex Media. Ed. media Diffuse waves in complex. Fouque, J., P., 1999. - pp. 405-454.

Snieder, R. Coda wave interferometry and the equilibration of energy in elastic media. PHYSICAL REVIEW E. October 21, 2002. - 4 : Vol. 66. Doi: 10.1103/PhysRevE.66.046615

Snieder, R. Extracting the Green's function from the correlation of coda waves: A derivation based on stationary phase. PHYSICAL REVIEW E. April 29, 2004. - 046610 : Vol. 69. Doi: 10.1103/PhysRevE.69.046610

Snieder, R., and M. Vrijlandt. Constraining the source separation with coda wave interferometry: Theory and application to earthquake doublets in the Hayward fault, California. JOURNAL OF GEOPHYSICAL RESEARCH. April 02, 2005. - B04301 : Vol. 110. Doi: 10.1029/2004JB003317

Snieder, R. The Theory of Coda Wave Interferometry. Pure and applied geophysics. Springer, February 08, 2006. - 2 : Vol. 163. - pp. 455-473. Doi: 10.1007/s00024-005

Snieder, R., and E. Safak. Extracting the building response using seismic interferometry; Theory and application to the Millikan Library in Pasadena, California. Bulletin of the Seismological Society of America. April 2006. - 2 : Vol. 96. - pp. 586-598. Doi: 10.1785/0120050109

Speranza, F., and M. Chiappini. Thick-skinned tectonics in the external Apennines, Italy: New evidence from magnetic anomaly analysis. Journal of Geophysical Research: Solid Earth. AGU Journal, November 14, 2002. - B11 : Vol. 107. - pp. ETG 8-1–ETG 8-19. Doi: 10.1029/2000JB000027

Stabile, T., A., C. Satriano, A. Orefice, G. Festa, and A. Zollo. Anatomy of a microearthquake sequence on an active normal fault. Scientific reports. Nature, May 16, 2012. - 410 : Vol. 2. Doi: 10.1038/srep00410

Stähler, S., C., C. Sens-Schönfelder, and E. Niederleithinger. Monitoring stress changes in a concrete bridge with coda wave interferometry. The Journal of the Acoustical Society of America. April 2011. - 4 : Vol. 129. - pp. 1945-1952. Doi: 10.1121/1.3553226

Tarchi, D., H. Rudolf, M. Pieraccini, and C. Atzeni. Remote monitoring of buildings using a ground-based SAR: Application to cultural heritage survey. International Journal of Remote Sensing. December 15, 2000. - 18 : Vol. 21. - pp. 3545-3551. Doi: 10.1080/014311600750037561

Tiberti, M., M., L. Orlando, D. Di Bucci, M. Bernabini, and M. Parotto. Regional gravity anomaly map and crustal model of the central-southern Apennines (Italy). Journal of Geodynamics. Elsevier, August 2005. - 1 : Vol. 40. - pp. 73-91. Doi: 10.1016/j.jog.2005.07.014

Todorovska, M., I., and M., D. Trifunac. Impulse response analysis of the Van Nuys 7-story hotel during 11 earthquakes and earthquake damage detection. Structural Control and Health Monitoring. 2008. - 1 : Vol. 15. - pp. 90-116. Doi: 10.1002/stc.208

Trasatti, Elisa, Marco Polcari, Maurizio Bonafede, and Salvatore Stramondo. Geodetic constraints to the source mechanism of the 2011–2013 unrest at Campi Flegrei (Italy) caldera. Geophysical Research Letters. AGU Journal, May 26, 2015. - 10 : Vol. 42. - pp. 3847–3854. Doi: 10.1002/2015GL063621

Trifunac, M., D., M., I. Todorovska, M., I. Miodrag, and B., D. Borko. Variability of the fixed-base and soil-structure system frequencies of a building–The case of Borik-2 building. Structural Control and Health Monitoring. July 17, 2010. - 2 : Vol. 17. - pp. 120-151. Doi: 10.1002/stc.277

Vandemeulebrouck, Jean, Didier Stemmelen, Tony Hurst, and Jacques Grangeon. Analogue modeling of instabilities in crater lake hydrothermal systems. Journal of Geophysical Research. AGU Journal, February 25, 2005. - B2 : Vol. 110. Doi: 10.1029/2003JB002794

Vanorio, T., J. Virieux, P. Capuano, and G. Russo. Three-dimensional seismic tomography from P wave and S wave microearthquake travel times and rock physics characterization of the Campi Flegrei Caldera. *JOURNAL OF GEOPHYSICAL RESEARCH*. March 01, 2005. - B03201 : Vol. 110. Doi: 10.1029/2004JB003102

Vanorio, Tiziana, and W. Kanitpanyacharoen. Rock physics of fibrous rocks akin to Roman concrete explains uplifts at Campi Flegrei Caldera. *Science*. August 07, 2015. - 6248 : Vol. 349. - pp. 617-621. Doi: 10.1126/science.aab1292

Vassallo, M., G. Festa, and A. Bobbio. Seismic Ambient Noise Analysis in Southern Italy. *Bulletin of the Seismological Society of America*. 2012. - 2 : Vol. 102. - pp. 574-586. Doi: 10.1785/0120110018

Vuan, A., M. Sujan, and M., P. Plasenci Linares. A reappraisal of surface wave group velocity tomography in the subantarctic Scotia Sea and surrounding ridges. *Global and Planetary Change*. Elsevier, December 2014. - Part B : Vol. 123. - pp. 223-238. Doi: 10.1016/j.gloplacha.2014.07.020

Wathelet, M., D. Jongmans, and M. Ohrnberger. Surface-wave inversion using a direct search algorithm and its application to ambient vibration measurements. *Near Surface Geophysics*. November 2004. - Vol. 2. - pp. 211-221. Doi: 10.3997/1873-0604.2004018

Westaway, R., Jackson, J. The earthquake of 1980 November 23 in Campania-Basilicata (Southern Italy). *Geophysical Journal International*. August 1987. - 2 : Vol. 90. - pp. 375-443. Doi: 10.1111/j.1365-246X.1987.tb00733.x

Westaway, R. The Campania, Southern Italy, earthquake of 1962 August 21. *Geophysical Journal International*. January 1987. - 1 : Vol. 88. - pp. 1-24. Doi: 10.1111/j.1365-246X.1987.tb01366.x

Worden, K., and Dulieu-Barton, J., M. An Overview of Intelligent Fault Detection in Systems and Structures. *Structural Health Monitoring*. March 1, 2004. - 85 : Vol. 3. Doi: 10.1177/1475921704041866

Yamamoto, M., and H. Sato. Multiple scattering and mode conversion revealed by an active seismic experiment at Asama volcano, Japan. *JOURNAL OF*

GEOPHYSICAL RESEARCH. July 14, 2010. - B07304 : Vol. 115. Doi: 10.1029/2009JB007109

Yang, Y., M., H. Ritzwoller, A., L. Levshin, and N., M. Shapiro. Ambient noise Rayleigh wave tomography across Europe. *Geophysical Journal International*. January 2007. - 1 : Vol. 168. - pp. 259-274. Doi: 10.1111/j.1365-246X.2006.03203.x

Yilmaz, Öz. Seismic Data Analysis: Processing, Inversion, and Interpretation of Seismic Data. Society of Exploration Geophysicists, 2001. - p. 2065.

Zaccarelli, L., N., M. Shapiro, L. Faenza, G. Soldati, and A. Michelini. Variations of crustal elastic properties during the 2009 L'Aquila earthquake inferred from cross-correlations of ambient seismic noise. *GEOPHYSICAL RESEARCH LETTERS*. December 17, 2011. - L24304 : Vol. 38. Doi: 10.1029/2011GL049750

Zollo, A., A. Orefice, and V. Convertito. Source parameter scaling and radiation efficiency of microearthquakes along the Irpinia fault zone in southern Apennines, Italy. *Journal of Geophysical Research: Solid Earth*. April 2014. - 4 : Vol. 119. - pp. 3256-3275. Doi: 10.1002/2013JB010116

Zollo, A., S. Maruccci, G. Milana, and P. Capuano. The 1997 Umbria-Marche (central Italy) earthquake sequence: Insights on the mainshock ruptures from near source strong motion records. *Geophysical Research Letters*. AGU Journal, October 15, 1999. - 20 : Vol. 26. - pp. 3165-3168. Doi: 10.1029/1998GL005285

Zollo, Aldo, and Antonio Emolo. Terremoti e onde. Metodi e pratica della sismologia moderna. Liguori, 2011. - pp. XV-422.

Zollo, Aldo, Nils Maercklin, Maurizio Vassallo, Dario Dello Iacono, and Jean Virieux. Seismic reflections reveal a massive melt layer feeding Campi Flegrei caldera. *GEOPHYSICAL RESEARCH LETTERS*. June 21, 2008. - L12306 : Vol. 35. Doi: 10.1029/2008GL034242